

**Structural and Thermodynamic Characterization of
Inhibitor Binding to Aldose Reductase:
Insights into
Binding Modes, Driving Forces,
and Selectivity Determinants**

Dissertation
zur
Erlangung des **Doktorgrades**
der **Naturwissenschaften**
(**Dr. rer. nat.**)

dem
Fachbereich Pharmazie
der Philipps-Universität Marburg
vorgelegt von

Holger Steuber
aus Hagen/Westfalen

Marburg an der Lahn, 2007

Vom Fachbereich Pharmazie der Philipps-Universität Marburg als Dissertation
angenommen am: 05.06.2007

Erstgutachter: Prof. Dr. G. Klebe

Zweitgutachter: Prof. Dr. C. A. Sotriffer

Tag der mündlichen Prüfung: 05.06.2007

Die Untersuchungen zur vorliegenden Arbeit wurden auf Anregung und in der Arbeitsgruppe von Prof. Dr. G. Klebe am Institut für Pharmazeutische Chemie des Fachbereichs Pharmazie der Philipps-Universität Marburg in der Zeit von März 2003 bis Oktober 2006 durchgeführt.

*Der Fortgang der wissenschaftlichen Entwicklung
ist im Endeffekt
eine ständige Flucht vor dem Staunen.*

(Albert Einstein)

The following scientific contributions (ordered by type and date of publication) emanated from this thesis:

1. Journal Articles

- Petrova T., **Steuber H.**, Hazemann I., Cousido-Siah A., Mitschler A., Chung R., Oka M., Klebe G., El-Kabbani O., Joachimiak A., Podjarny A.,
Factorizing selectivity determinants of inhibitor binding toward aldose and aldehyde reductases: structural and thermodynamic properties of the aldose reductase mutant Leu300Pro-fidarestat complex
J. Med. Chem. 2005, 48, 18, 5659-5665
- **Steuber H.**, Zentgraf M., Podjarny A., Heine A., Klebe G.,
High resolution crystal structure of Aldose Reductase complexed with the novel sulfonyl-pyridazinone inhibitor exhibiting an alternative active site anchoring group
J. Mol. Biol., 2006, 356, 45-56
- **Steuber H.**, Zentgraf M., Gerlach C., Sotriffer C. A., Heine A., Klebe G.,
Expect the unexpected or caveat for drug designers: multiple structure determinations using Aldose Reductase crystals treated under varying conditions reveal surprising challenges for structure-based ligand design
J. Mol. Biol., 2006, 363, 174-187
- **Steuber H.**, Heine A., Klebe G.,
Structural and thermodynamic Study on Aldose Reductase: nitro-substituted inhibitors with strong enthalpic binding contributions
J. Mol. Biol., 2007, 368, 618-638
- **Steuber H.**, Zentgraf M., La Motta C., Sartini S., Heine A., Klebe G.,
Evidence for a novel binding site conformer of aldose reductase in ligand-bound state
J. Mol. Biol., in press
- Zentgraf M., **Steuber H.**, Koch C., La Motta C., Sartini S., Sotriffer C. A., Klebe, G.,
How reliable are current docking approaches for structure-based drug design? Lessons from aldose reductase
Angewandte Chemie Int. Ed. Engl., in press

- Gerlach C., Smolinski M., **Steuber H.**, Sotriffer C. A., Heine A., Hangauer D., Klebe G.,
Thermodynamic inhibition profile of a cyclopentyl- and a cyclohexyl derivative towards thrombin: The same, but for different reasons
Submitted
- **Steuber H.**, Czodrowski P., Sotriffer C. A., Klebe G.,
Tracing changes in protonation: A prerequisite to factorize thermodynamic data of inhibitor binding to aldose reductase
Submitted
- **Steuber H.**, Heine A., Podjarny A., Klebe G.,
Merging the binding sites of aldose and aldehyde reductase for detection of inhibitor selectivity-determining features
To be submitted
- Zentgraf M., **Steuber H.**, Klebe G. & Sotriffer C. A.,
Evaluating MM-PBSA in case of a flexible binding pocket: the Aldose Reductase test case. To be submitted.
- Zentgraf M., **Steuber H.**, Klebe G. & Sotriffer C. A.,
Extending charted space: comparative MD simulations of Aldose Reductase.
To be submitted.
- Eisenmann M., **Steuber H.**, Zentgraf M., Klebe G., Schlitzer M.,
Design, synthesis, biological and structural evaluation of novel aldose reductase inhibitors
Manuscript in preparation
- Silber K., **Steuber H.**, Jaeger R., Sohn C., Heine A., Klebe G.,
Successful lead identification for metalloproteinases: a fragment-based approach using virtual screening
Manuscript in preparation

2. Oral presentations

- **Steuber H.**, Sotriffer C. A., Klebe G.,
Aldose Reductase and Aldehyde Reductase - a model system for selectivity determinants involved in protein-ligand interactions
Meeting on experimental and computational approaches to understand protein-ligand interactions, BASF AG, Ludwigshafen, Germany, **2004**
- **Steuber H.**, Heine A., Sotriffer C., Klebe G.,
Aldose Reductase Inhibition from a structural and thermodynamic point of view
DFG-Evaluation of the Research Training Group “Protein function at the atomic level”, Marburg, Germany, **2004**
- **Steuber H.**, Heine A., Klebe G.,
Aldose reductase inhibition from the thermodynamic point of view
Bilateral Joint Aldose Reductase Meeting, IGBMC, Illkirch, France, **2005**

3. Posters

- **Steuber H.**, Sotriffer C., Heine A., Klebe G.,
How to design selective drugs? Aldose Reductase and Aldehyde Reductase as a model system
High Resolution Drug Design, Bischberg-Strasbourg, France, 2004
- Eisenmann M., **Steuber H.**, Zentgraf M., Klebe G., Schlitzer M.,
Structure-based drug design of Aldose Reductase inhibitors
Joint Meeting of the German Pharmaceutical Society (DPhG), Regensburg, Germany, 2004
- Silber K., **Steuber H.**, Reinscheid U., Klebe, G.:
A Fragment-based Screening Approach for Metalloproteinase Inhibitors,
Gordon Research Conference on Computer Aided Drug Design, Tilton, NH, USA, 2005
- Zentgraf M., Sotriffer C., **Steuber H.**, Klebe G.,
Thermodynamic characterization of Aldose Reductase inhibitors by comparative MD simulations
Gordon Research Conference on Computer Aided Drug Design, Tilton, NH, USA, 2005

- Gerlach C., **Steuber H.**, Velec H.F.G, Smolinski M., Hangauer D., Heine A., Klebe G.,
Docking and direct design in the binding pocket - libraries for serine protease inhibitors
Young Modellers` Forum, London, UK, 2005
- Eisenmann M., **Steuber H.**, Zentgraf M., Klebe G., Schlitzer M.,
Design of new Aldose Reductase inhibitors – a structure-based approach
Joint Meeting on Medicinal Chemistry, Vienna, Austria, 2005

Abbreviations

AKR	aldo-keto reductase
ALR1	Aldehyde Reductase
ALR2	Aldose Reductase
BSASA	Buried solvent accessible surface area
HTS	High Throughput Screening
IDD	Institute for Diabetes Discovery
ITC	Isothermal titration calorimetry
k_b	binding constant
MD	molecular dynamics simulation
n.d.	not determined
NMR	Nuclear Magnetic Resonance
PB	Poisson-Boltzman
PEOE	Partial Equalization of Orbital Electronegativities
PDB	Protein Data Bank
RMSD	Root mean square deviation
VS	Virtual Screening
WT	wild type

Table of Contents

1.	Introduction	1
1.1	Drug Design – an interdisciplinary, permanently renewing field of research	1
1.2	Thermodynamic implications of ligand binding and its consequences for lead optimization	3
1.3	Aldose Reductase – Structural and functional features	8
1.4	Aldose Reductase – Pathological relevance and inhibitor evaluation	10
1.5	Motivation of this Thesis	12
1.6	References	14
2.	Structural and Thermodynamic Study on Aldose Reductase: Nitro-substituted Inhibitors with Strong Enthalpic Binding Contribution	22
2.1	Introduction	22
2.2	Results and Discussion	26
2.2.1	Binding mode of the carboxylate head group	26
2.2.2	An interstitial water molecule picked up upon binding	28
2.2.3	Placement of the central heterocycle and the terminal nitro group	28
2.2.4	Binding mode differences of the two virtual screening hits	30
2.2.5	Comparison of docking-predicted and crystallographically determined binding modes	31
2.2.6	Binding mode of AR inhibitors lacking a terminal nitro group	33
2.2.7	Correlation of binding affinity with structural and thermodynamic properties	35
2.2.8	Enthalpic binding contributions of the nitro group	38
2.3	Summary and Conclusions	40
2.4	Materials and Methods	41
2.5	References	46

3.	High Resolution Crystal Structure of Aldose Reductase Complexed with the Novel Sulfonyl-Pyridazinone Inhibitor Exhibiting an Alternative Active Site Anchoring Group	54
3.1	Introduction	54
3.2	Results and Discussion	56
3.2.1	X-Ray crystallography	56
3.2.2	Isothermal titration calorimetry to determine binding constants	66
3.3	Summary and Conclusions	67
3.4	Materials and Methods	68
3.5	References	73
4.	Evidence for a Novel Binding Site Conformer of Aldose reductase in Ligand-Bound State	78
4.1	Introduction	78
4.2	Results and Discussion	80
4.3	Conclusions	88
4.4	Materials and Methods	90
4.5	References	93
5.	Tracing Changes in Protonation: A Prerequisite to Factorize Thermodynamic Data of Inhibitor Binding to Aldose Reductase	97
5.1	Introduction	97
5.2	Results and Discussion	100
5.2.1	Changes of the protonation inventory upon ligand binding	100
5.2.2	Factorization into enthalpic and entropic contributions	109
5.2.3	Correlation of thermodynamic and structural features	109
5.2.4	Thermodynamic consequences of substituent effects	112
5.3	Conclusions	116
5.4	Materials and Methods	117
5.5	References	120

6.	Merging the Binding Sites of Aldose and Aldehyde Reductase for Detection of Inhibitor Selectivity-Determining Features	125
6.1	Introduction	125
6.2	Results and Discussion	128
6.3	Summary and Conclusions	149
6.4	Materials and Methods	152
6.5	References	154
6.6	Appendix: Data collection and Refinement statistics	160
7.	Expect the Unexpected or Caveat for Drug Designers: Multiple Structure Determinations Using Aldose Reductase Crystals Treated under varying Soaking and Cocrystallization Conditions	170
7.1	Introduction	170
7.2	Results and Discussion	172
7.2.1	An unexpected backbone flip in the ALR2-zopolrestat complex . . .	172
7.2.2	ALR2 complexed with one or several tolrestat molecules	179
7.3	Conclusions	183
7.4	Materials and Methods	184
7.5	References	188
8.	Summary / Zusammenfassung	193

1. Introduction

1.1 Drug Design – an interdisciplinary, permanently renewing Field of Research

The establishment of “Life Sciences” comprising a broad variety of medicinal, biological and chemical research disciplines has generated increasing knowledge about the complex interplay of a phenotypical disease pattern and the pharmacological basis of the corresponding disease at the molecular level. Accordingly, the identification of putative small-molecule drug candidates was subjected to various shifts of paradigm: whereas in the early days drug discovery was mainly driven by serendipity-based attempts, meanwhile more rational and target-oriented approaches evolved as an effective strategy.¹⁻⁴ After appropriate target validation and characterization, several strategies can be followed in order to obtain putative lead compounds. The evaluation of large compound libraries for an effect towards the selected biological target is known as “High-throughput screening” (HTS), however this method suffers from poor success rates below 1%, high costs, and difficult hit optimization.⁵⁻⁷ In case natural or assay-confirmed ligands or substrates of the desired target are known, the design of ligand-analogues or mechanism-based inhibitors can be attempted. Furthermore, de-novo design of ligands can be performed to retrieve a putative lead compound. The success of these approaches can be enhanced effectively, if knowledge about the enzyme mechanism and, even more importantly, a model of the three-dimensional target structure, mostly derived from X-ray crystallographic analysis or NMR data, is available.^{1,5,8-10} Subsequent complex structure determination or reliable modelling efforts provide insights into the spatial interactions between lead molecule and target. These might stimulate further ligand modifications in order to enhance affinity and/or selectivity properties. This procedure usually embarks into a cyclic, iterative process until ligands have been identified which fulfil the desired prerequisites (or until academic/industrial funding for the corresponding design program becomes terminated). Such structure-guided or rational ligand design has been successfully applied for the development of various marketed drugs, e.g. the neuraminidase inhibitor

zanamivir, various HIV-protease inhibitors, the carbonic anhydrase ligand dorzolamide, the kinase inhibitor imatinib, and the inhibitor captopril which binds to the angiotensin-converting enzyme (ACE).^{1,11}

Despite the ~ 22,000 genes present in the human genome encode for estimated 3,000 gene products to be considered as “druggable”, only about 100 drug targets are responsible for the action of the currently marketed drugs.¹² The efforts of structural and functional genomics initiatives to provide structural information and validation of novel targets have to be complemented by efficient concepts assisting in the identification of appropriate lead compounds. If at least one binding pocket conformer resembling the in-vivo situation has been determined experimentally or is reliably represented by homology modelling, a virtual screening campaign can be performed *in-silicio* in order to identify putative hits from a virtual compound library.^{5,13-14} This procedure comprises, firstly, the appropriate generation of placements (docking solutions) of each compound to be evaluated within the expected target binding site (docking problem). Secondly, the thereby retrieved interaction geometries have to be scored in order to identify the most favourable binding geometry and to enrich the most active compounds from the original library (scoring problem). This issue is usually addressed by consultation of scoring functions.¹⁵ Even though the success of this VS approach has been demonstrated at a broad variety of targets exhibiting hit rates up to three orders of magnitude higher compared to HTS, various limitations prevent VS to be used as a standard application. As proteins are and have to be dynamic systems to fulfil their catalytic function, they are enabled to perform induced-fit adaptations with respect to natural substrates and small-molecule inhibitors.¹⁶⁻¹⁹ This complicates the reliable application of *in-silicio* approaches, as the prediction of the most relevant binding conformer in dependence of each particular ligand is difficult to achieve. Cross-docking approaches considering multiple binding site conformers have been recently developed, but also their results depend on the quality of the implemented scoring function.²⁰ In addition, in many cases ligand binding is accompanied by changes of the local electrostatic properties within the binding pocket. Accordingly, protonation states of titratable functional groups being part of the binding site or the ligand may change upon binding.^{21,22} Such proton transitions can clearly influence the hydrogen-bond inventory, but they are difficult to predict for a previously unknown system in absence of experimental data. Computational tools in order to fix these limitations are currently developed.²³ Furthermore, most association events take place

in an aqueous environment. Even though the role of water for protein folding, stability and participation at the target-ligand interface as well as its contribution to binding thermodynamics is widely known, the reliable prediction of these effects complicates the VS procedure. Whereas these limitations influence to large extent the generation of accurate docking poses, further weaknesses are caused by deficiencies of the scoring functions used for ranking of the suggested binding geometries. Despite extensive efforts in order to develop scoring functions for the correct identification of binding geometries and/or estimation of binding affinity, various aspects influencing the binding thermodynamics, enthalpic and entropic contributions, are usually insufficiently considered by the scoring functions used to date.^{5,15} However, the origin of this limitation is clearly attributed to the insufficient availability of experimental thermodynamic data for an appropriate number of model systems in order to derive the driving forces making a macromolecular binding pocket attractive for ligand association. Recently, attempts have been initiated to establish databases merging structural information of protein-ligand binding geometries with thermodynamic data (AffinDB,²⁴ PDBbind,²⁵ SCORPIO²⁶) and to derive scoring functions under enhanced consideration of thermodynamic parameters.²⁷

Our ability to predict ligand binding affinities and to develop appropriate scoring functions will presumably profit from a more profound understanding of the thermodynamic driving forces resulting in an association event.

1.2 Thermodynamic Implications of Ligand Binding and its Consequences for Lead Optimization

Binding affinity of non-covalent ligands originates from different types of interactions between the small-molecule lead compound and the macromolecular target as well as their interactions with solvent molecules, in most cases an aqueous buffered environment.^{28,29} Accordingly, in total, binding energy can be viewed as the difference between the interaction energy with the target and the desolvation energy of both binding partners. The binding affinity is represented by the Gibbs free enthalpy of binding (ΔG_{bind}^0), which is a function of two terms, the standard enthalpy (ΔH_{bind}^0) and the standard entropy (ΔS_{bind}^0) related to the association event.

According to the Gibbs-Helmholtz equation

$$\Delta G_{\text{bind}}^0 = \Delta H_{\text{bind}}^0 - T \Delta S_{\text{bind}}^0,$$

both terms contribute to binding affinity in an additive fashion.

Roughly, the binding enthalpy can be thought of as a “structural” component of the association, whereas the binding entropy represents the “dynamic” component.³⁰ In more detail, the classical, to some extent simplifying interpretation of enthalpic contributions reflects the strength of directed ligand-target interactions in relation to those with the solvent. The favourable term arises primarily from hydrogen bonding, salt bridges and van der Waals interactions between ligand and target. Unfavourable enthalpic contributions originate from the desolvation of polar groups of both partners. Two major terms contribute to the binding entropy:²⁹ first, the (de-)solvation entropy associated with the burial of polar and unpolar surfaces of ligand and protein accompanied by a release of solvent molecules into bulk solvent. Second, the conformational entropy reflects the loss of conformational degrees of freedom with respect to ligand and target upon binding. Due to availability of increasing experimental data, this classical picture of processes related to an association event becomes nowadays more extended. In particular, our imagination of the desolvation contribution currently experiences an alteration. To our present understanding burial of hydrophobic surface provokes a favourable contribution towards the binding affinity by two, to some extent converse effects:³¹⁻³³

- the “classical hydrophobic effect” contributes to ligand affinity by a favourable entropic contribution due to the release of water molecules which cage-like solvate hydrophobic areas of the binding site and the ligand before binding. The ordering of water molecules around hydrophobic hydrocarbon chains is e.g. reflected in the increasingly unfavourable entropic contribution for the solvation of the aliphatic alcohols methanol ($T\Delta S$ 20 kJ mol⁻¹) and hexanol ($T\Delta S$ 48 kJ mol⁻¹). Release of such immobilized water molecules should be associated with a favourable desolvation entropy.
- According to the “non-classical hydrophobic effect” water molecules solvating hydrophobic surfaces of ligand and binding site undergo fewer and geometrically restrained hydrogen bonds. In addition, the coordination sites of these water molecules pointing to the hydrophobic surface remain to some

extent unsaturated.³¹⁻³³ Thus, removal of hydrophobic surface is accompanied by a gain of binding enthalpy, as release of these water molecules in total leads to the formation of additional, previously unsaturated H-bonds.

Both types of desolvation contribution have been observed in protein-ligand interactions, however, experimental evidence increases that the “non-classical hydrophobic effect” appears more relevant for biological association processes.³¹ Despite the rather simple “oil and water do not mix” analogy, the hydrophobic effect exhibits remarkable complexity at molecular level.³⁴ Its quantitative evaluation turns out to be quite difficult, as it cannot be directly probed separately from other influences. The influence of the solvent towards hydrophobic associations has been found for the dimerization of cyclopentadiene: in water, the dimerization rate is remarkably increased compared to the situation in pure organic solvents or aqueous solution with organic cosolvents, as the hydrocarbon surface exposed to the solvent decreases upon formation of the transition state.³⁵ Similar observations suggested an “antihydrophobic effect” for protein-ligand interactions: increasing the percentage of ethanol in the assay buffer solution of 0-9 % provoked poorer inhibition constants by up to an order of magnitude for binding of hydrophobic macrocyclic inhibitors to thermolysin.³⁴

A favourable desolvation entropy of binding reflects a repulsion of the ligand from solvent rather than an attractive interaction with the target and is therefore a non-specific force proportional to the hydrophobicity of ligand and binding site.²⁹

The conformational entropy change of binding is usually related to a loss of conformational degrees of freedom in ligand and protein molecules, and thereby superimpose an unfavourable contribution onto the binding event. It should be noted that ligand binding may be accompanied by various (favourable or unfavourable) changes of the dynamic behaviour of the protein also contributing to the conformational entropy. Those changes of dynamic order parameters are nowadays accessible by intricate NMR relaxation experiments. Interestingly, protein regions concerned by these ligand binding-induced effects can be found far remote from the original binding site, as recently reported for binding of small heterocycles to mouse major urinary protein (MUP).³⁰ Clearly, these effects are difficult to predict and therefore complicate the reliable estimation of the binding properties of a given ligand molecule.

Strategies of affinity optimization aim to optimize either the binding enthalpy, or the entropy, or both contributing terms. Historically, it has been proven much simpler to optimize the binding entropy of putative leads by attaching hydrophobic, nonpolar

substituents enhancing binding affinity by means of the hydrophobic effect.²⁹ Over many years, this strategy led to an increasing hydrophobic character of drug candidates and turned out to be counterproductive to appropriate drug-like properties.^{36,37} In addition, this strategy exhibited various further limitations. As already mentioned, hydrophobic association is to large extent caused by a repulsion of hydrophobic surface from aqueous environment. Thus, in most cases, such an optimization was accompanied by a loss of binding selectivity.²⁹ It was almost not applicable to leads whose binding was already mainly driven by hydrophobic interactions. Furthermore, the favourable effect related to the attachment of hydrophobic groups appeared difficult to estimate, in particular, as hydrophobic substituents tend to occupy hydrophobic protein pockets via “induced fit” adaptations.^{16,17} Those pockets are usually closed prior to binding, and accordingly, they remain closed and, thus, undetected in presently known crystal structures. Such unexpected induced-fit adaptations resulting in novel protein-conformers stabilized by ligand molecules have been described for a broad variety of protein targets including stromelysin (MMP-3), HIV-protease, calmodulin, glycogen phosphorylase, and aldose reductase.¹⁷ A further strategy of optimizing the desolvation entropy consists in the attempt to displace ordered water molecules pre-organized within the binding pocket by an appropriate ligand decoration into the bulk phase. The unfavourable entropic contribution related to the immobilization of a water molecule is estimated to a maximum value of 8 kJ mol⁻¹ (at 300 K) for highly ordered water molecules.³⁸ Next to the desolvation contribution, optimization of the binding entropy can also be achieved by constraining the ligand to its bioactive conformation in order to obtain maximum shape complementarity of the ligand in unbound state, thereby decreasing the loss of conformational degrees of freedom upon binding. Appropriate immobilization of one rotatable ligand bond should be associated with about 2 kJ mol⁻¹ more favourable free enthalpy of binding.³⁹ Even though e.g. conventional inhibitors of HIV-protease combine rigidity and entropically driven binding, the effect of such ligand pre-organization strategies is not fully understood. Such conformational pre-organisation of the ligand is usually assumed to optimize the binding entropy,²⁹ however, a recent contribution systematically analysing the binding thermodynamics of constrained and non-constrained peptide ligands to the Grb2 SH2 domain suggested surprising experimental evidence that the binding superiority of the constrained ligands is mainly of enthalpic origin.⁴⁰ It might be further speculated that optimization of the conformational entropy obtained by freezing a ligand into its bioactive conformation

equipped with highest shape complementarity enhances its binding selectivity in comparison to putative concurrent, binding-competent target isoforms. On the other hand, such restrained ligands experience severe loss of affinity in case, mutations occur within the binding site, as their intentionally immobilized constitution makes the adoption of an appropriate compensating binding mode unfavourable.⁴¹

The other determinant to be optimized in order to enhance affinity is the binding enthalpy. A favourable enthalpic contribution is obtained (next to hydrophobic association according to the “non-classical hydrophobic effect”) from suitable geometric complementarity of polar interactions such as hydrogen bonds, salt bridges and further polar contacts such as halogen bonds or non-classical hydrogen bonds between polarized e.g. hydrogen-carbon bonds and appropriate acceptors. Depending on donor and acceptor properties as well as the local environment, a hydrogen bond implicates a favourable enthalpic contribution of about 5 – 32 kJ mol⁻¹.⁴² Naively considered, the enthalpic optimization appears rather simple as such an optimization requires “only” the placement of appropriate H-bond acceptors and donors or charged groups complementary to the polar equipment of the protein binding pocket. However, this simplistic concept is in practise difficult to realize. First, one has to assume, that the suggested ligand derivative adopts the expected binding geometry and no induced-fit adaptations occur on the side of the protein. However, even if this prerequisite is fulfilled, such a derivatisation does not necessarily lead to a more potent ligand, as the enthalpically favourable formation of the H-bond has to compensate for the unfavourable desolvation contribution of protein and ligand polar groups.^{21,29} Thus, the question whether a putative optimized ligand possesses an efficiently improved H-bond/polar contact inventory and thereby is equipped with higher affinity is difficult to answer without experimental evidence.

As optimization of the enthalpic contribution aims to maximize the spatial complementarity of polar interactions between ligand and binding pocket, such an optimization process may produce ligands with improved selectivity over protein isoforms with distinct polar properties compared to ligands optimized by the attachment of non-polar groups in order to obtain affinity by a favourable desolvation entropy.²⁹

It should be noticed that these concepts become further complicated as a phenomenon widely distributed to biomolecular association events referred to as “enthalpy-entropy compensation” may be superimposed.^{16,21,43,44} As the formation of directed interactions such as hydrogen bonds is accompanied by a loss in conformational and translational

degrees of freedom, the effect imposed onto the free enthalpy of binding is not of same size as the enthalpic enhancement, but accompanied by an entropic penalty. This is, e.g. observed, if water-mediated hydrogen bonds are established. Even though it is currently under discussion whether enthalpy and entropy relate in a linear or non-linear fashion, the occurrence of this mutually compensating phenomenon has to be considered with respect to the interpretation of thermodynamic data.

In summary, thermodynamic insights into protein-ligand interactions provide important information about the driving forces which make the association event favourable and pave the way for further optimization strategies of leads to drugs. In addition, binding thermodynamics can facilitate the interpretation of ligand electron density in crystal structures. As recently observed, an entropically more beneficial binding can result in less well defined difference density in certain regions of a ligand suggesting higher mobility or distribution over multiple conformational states compared to a more enthalpic analogue.⁴⁵ Those insights could be helpful to understand crystallographic results or to establish a screening protocol for ligands with binding properties mainly driven by directed interactions and, accordingly, more likely detectable in X-ray complex structures.

1.3 Aldose Reductase – Structural and Functional Features

The 36 kDa aldo-keto reductase aldose reductase (ALR2, E.C. 1.1.1.21) has been described firstly by Hers et al. in 1956 emphasizing its role as a mechanism of the glucose conversion to fructose in seminal vesicles.⁴⁶ The cytosolic and almost ubiquitous distributed enzyme utilizes NADPH to catalyse the reduction of a broad variety of aldehydes and certain ketones to their corresponding alcohols. Within the polyol pathway, ALR2 performs the rate-limiting conversion of glucose to sorbitol, which is subsequently oxidized NAD⁺-dependently to fructose by sorbitol dehydrogenase.⁴⁷⁻⁴⁹ The rate-limiting step of the ALR2 reduction mechanism has been demonstrated to comprise the exchange of the cofactor which is deeply buried and undergoes various interactions such as H-bonds, salt bridges and cation- π interactions.^{50,51} In addition, its exchange involves an extended induced-fit adaptation, (opening and closing) of the safety-belt loop, to some extent rationalizing the described kinetic observation. Even though the exact reaction mechanism is currently under

discussion, according to a broad consensus, NADPH donates a hydride ion to the carbonyl carbon of the aldehyde substrate. Most likely, this step is subsequently followed by the transfer of a proton from one of the neighbouring acidic protein residues to the intermediately formed substrate anion.^{52,53}

The first crystal structure determination of ALR2 at 2.5 Å was described by Rondeau et al. in 1992.⁵⁰ Meanwhile, 85 ALR2 crystal structures have been deposited at the Protein Data Bank (PDB), among them are 39, which evolved from the present thesis.

In 1992, the ALR2 crystal structure was of particular interest, as it exhibited a previously unknown cofactor binding site.⁵⁰ Up to the current knowledge, oxidoreductases belong either to long-chain alcohol dehydrogenases, short-chain dehydrogenases (which bind NADPH via a Rossmann fold), or the aldo-keto reductases.⁵¹ Currently, the latter superfamily includes more than hundred known members, which have been classified into 14 families, AKR 1-14, and subfamilies according to their degree in amino acid sequence identity. ALR2 belongs to the subfamily AKR1B (mammalian aldose reductases). Further well known members of the AKR superfamily are 3 α -hydroxy steroid dehydrogenase (3 α -HSD) and aldehyde reductase (ALR1). All members of the AKR superfamily possess remarkable similarities:⁵¹

- They consist of approximately the same number of residues.
- They share the well known (α/β)₈-triose phosphate isomerase (TIM)-barrel fold, which is widely distributed over a large number of other enzyme families.
- They have a similar reaction mechanism in common: the reduction process involves the transfer of the 4-*pro*-R hydride of NADPH, followed by protonation of the substrate anion by one of the acidic catalytic residues.
- A similar mode of cofactor binding is shared between all members. The nicotinamide moiety points towards the catalytic site located at the C-terminal side of the barrel. Binding of the negatively charged cofactor (and other ligands) is favoured by helix-induced dipole moments.⁵⁴
- The substrate specificity is mainly determined by the amino acid decoration of the A, B, and C loop, which are located at the C-terminal side and connect α -helices and β -strands.

Similar to the distribution of the TIM-barrel fold, which is the most prevalent folding pattern throughout all known enzyme crystal structures deposited in the PDB, thereby serving nature as a template to introduce a broad variety of distinct catalytic

activities,^{54,55} it is assumed also for the AKR members to have evolved from an ancestral TIM barrel with oxidoreductase activity via divergent evolution. Considering the catalytic mechanism and active site constellation of residues, the AKR superfamily represents an example of convergent evolution compared to the short-chain dehydrogenases, as both families are neither homologous nor share a similar three-dimensional fold, but catalyze NAD(P)H-dependent oxidoreduction reactions involving an active site tyrosine and lysine residue as key catalytic components located at virtually identical positions.⁵¹

1.4 Aldose Reductase – Pathological Relevance and Inhibitor Evaluation

Even though the physiological function of ALR2 is not completely understood, the enzyme might play a role as detoxifier of various aldehydes produced under conditions of cellular oxidative stress. Representatives of such substrates are, e.g. 4-hydroxy-2-nonenal, methylglyoxal as well as their glutathionylated derivatives.⁴⁷⁻⁴⁹

However, under diabetic conditions accompanied by high cellular levels of glucose, ALR2 is responsible for an enhanced conversion of glucose via the polyol pathway to fructose. The worldwide prevalence of diabetes mellitus has been estimated to 2.8 % in 2000 and is expected to raise by 4.4 – 9 % within the next two decades.^{56,57} Careful predictions anticipate 366 million people worldwide suffering from the “diabetes epidemic” in 2030. Even though various therapy options have been developed for the treatment of diabetes mellitus including compounds interfering with hydrocarbon digestion and glucose utilisation, insulines, insulin-releasing agents, and recently drugs compensating insulin resistance, a stringent blood glucose control as maintained under physiological conditions could not be achieved.⁵⁸⁻⁶⁰ In consequence, in diabetic patients non-physiological hyperglycaemic events are responsible for severe long-term complications including retinopathy, nephropathy, neuropathy, cataract and angiopathy.^{56,61,62} The increased flux of glucose via the polyol pathway induces various biochemical imbalances, thereby strongly contributing to the onset of diabetic complications. Such enhanced polyol pathway activity is accompanied by generation of osmotic and oxidative stress causing various pathological interferences with cytokine signalling, regulation of apoptosis as well as activation of kinase cascades.⁶³ For instance, recent experimental observations provided evidence that under increased

glucose metabolism via the polyol pathway p38-MAP kinase shows increased activity causing nerve conduction deficits and, thus, leads to neuropathy.⁶⁴ Secondly, increased protein kinase C activity under elevated polyol pathway flux has been shown to induce smooth muscle cell proliferation of blood vessels being in agreement with atherosclerosis. This also explains estimations that 75 – 80 % of adults with diabetes die from complications of atherosclerosis.^{65,66} In addition, extended polyol pathway activity has been shown to provoke endothelial cell damages by increased oxidative stress and thereby contribute to atherosclerotic complications.⁶⁷ In particular, a shift in the NAD⁺/NADH balance provoked by enhanced polyol pathway activity is accompanied by an increase in the mitochondrial proton gradient.⁶⁸ Increasing amounts of electrons are transferred to oxygen resulting in the production of reactive oxygen species. Aggravatingly enough, increasing amounts of fructose derived from the polyol pathway contribute to the formation of advanced glycosylated endproducts (AGEs) and thereby lead to pathological changes of proteins functionally affected by covalent modification.^{69,70}

Furthermore, it should be noted that ALR2 is susceptible to post-translational modifications such as nitrosation and glutathionylation, most likely at the active site residue Cys 298, thereby influencing the catalytic activity of ALR2 depending on the current oxidative-nitrosative stress.^{71,72}

Altogether, the pathological activity of ALR2 plays a key role in the development of diabetic complications and thereby represents an excellent drug target. In fact, *in vitro* and *in vivo* studies suggest a clear benefit of the administration of aldose reductase inhibitors (ARIs) in various model systems exposed to high glucose levels as well as during the therapy of diabetic patients.⁷³⁻⁷⁸

Thus, extensive efforts have been performed to develop appropriate drug candidates. Most of these inhibitors can be classified according to their negatively charged anchor groups into carboxylate-type or hydantoin-type inhibitors. Except the carboxylate epalrestat, which is currently marketed in Japan, most of the inhibitors evolved from these approaches failed in clinical trials either due to poor bioavailability or selectivity properties.^{56,79} It has been argued that carboxylate-type inhibitors are inappropriate due to their more acidic properties compared to hydantoins. Under physiological conditions carboxylate groups will be almost completely ionised impairing their ability to cross biological membranes.⁸⁰

Certain inhibitors exhibited further deficiencies during their clinical evaluation.^{81,82}

-
- Sorbinil, the first agent extensively studied, was associated with toxic epidermal necrolysis in two patients.
 - Statil failed to prove positive clinical effects. Later, it was demonstrated that statil is obviously able to penetrate the rat nerve confirming the expected in-vitro benefits, but not the human nerves. This explained its inefficiency in clinical trials.
 - Tolrestat appeared problematic as some patients developed hepatic side effects.
 - After zenarestat exhibited dose-dependent elevations in creatinine levels, clinical trials were immediately terminated.
 - Zopolrestat failed to demonstrate sufficient efficacy in phase 3, possibly due to a decreased dose compared to phase 2.

It should be remarked that various clinical studies of ALR2 inhibitors provoked some criticism, as some of them were either performed at an insufficient time scale to obtain a reliable final estimation, or insufficient doses of the putative agent were administered.

1.5 Motivation of this Thesis

This thesis aims to characterize the thermodynamic driving forces of inhibitor binding to human ALR2 correlated with structural features. As already mentioned above, ALR2 represents a promising drug target for the treatment of diabetic complications. In addition, its pronounced active-site susceptibility to undergo induced-fit adaptations upon ligand binding (see chapter 4.1) suggests ALR2 as an excellent evaluation system for structure-guided drug design and to gain insights into protein-ligand interactions in case of proteins equipped with extended binding site mobility.

After successful establishment of expression, purification and crystallisation protocols for ALR2 in our laboratory within the work of this thesis, high-quality protein preparations and well-diffracting crystals of a diffraction power beyond 1 Å at synchrotron sources as well as 1.4-1.6 Å at inhouse rotating anodes were achieved, facilitating the performance of extended experimental studies to characterize ligand binding in structural and thermodynamic terms.

-
- In particular, binding of ALR2 inhibitors identified by a previously performed virtual screening campaign⁸³ should be analysed to evaluate the structural basis for binding affinity and to suggest guidelines for a putative optimization (chapter 2).
 - Furthermore, an inhibitor with favourable inhibition and selectivity properties exhibiting an alternative anchor group was published in 2003 by Mylari et al.⁷⁷ In-vivo results suggested highly promising efficacy such as inhibition of cataract development, normalized sorbitol and fructose levels and protection against neuronal apoptosis in diabetic rats.⁸⁴ In this thesis we intended to follow the question for the experimental binding mode with particular emphasis to resolve the protonation states of this novel ligand head group and active site residues in complexed state (chapter 3).
 - As ALR2 is widely known for the pronounced mobility of its active site residues, it was probed with a recently published series of naphthoisothiazole acetic acid derivatives⁸⁵ designed as tolrestat analogues to study putative adaptation events (chapter 4).
 - A further aspect of this thesis concerns the detailed characterization and interpretation of changes in protonation states upon ligand binding in order to perform a meaningful factorization of thermodynamic data into enthalpic and entropic contributions (chapter 5).
 - As inhibitors of ALR2 should not only possess high affinity to the desired target, but should also be equipped with high selectivity, in particular with respect to the related isoform ALR1, the binding site of ALR2 should be probed for selectivity-determining features using site-directed mutagenesis. Structural and thermodynamic characterization of the corresponding mutants complexed with ALR2 inhibitors was intended to reveal new insights into selectivity discrimination of ligands towards both isoforms (chapter 6).
 - As various protocols for complex formation were applied during this study, a systematic comparative evaluation of these complexation protocols towards the crystallographically observed binding mode should be performed (chapter 7).

1.6 References

1. Kubinyi, H. (1998). Structure-based design of enzyme inhibitors and receptor ligands. *Curr. Opin. Drug Discov.* **1**, 4-15.
2. Lombardino, J. G. & Lowe III, J. A. (2004). The role of the medicinal chemist in drug discovery-then and now. *Nat. Rev. Drug Discov.* **3**, 853-862.
3. Poupaert, J. H. (2002). Design of drugs: Basic principles and applications. *Encyclopedia Pharm. Technol.* 708-716.
4. Anderson, A. C. (2003). The process of structure-based drug design. *Chem. Biol.* **10**, 787-797.
5. Klebe, G. (2006). Virtual ligand screening: strategies, perspectives and limitations. *Drug Discov. Today* **11**, 580-594.
6. Lahana, R. (1999). How many leads from HTS? *Drug Discov. Today* **4**, 447-448.
7. Ramesha, C. S. (2000). Comment: How many leads from HTS? *Drug Discov. Today* **5**, 43-44.
8. Blundell, T. L. & Patel, S. (2004). High-throughput X-ray crystallography for drug discovery. *Curr. Opin. Pharmacol.* **4**, 490-496.
9. Blundell, T. L., Jhoti, H. & Abell, C. (2002). High-throughput crystallography for lead discovery in drug design. *Nat. Rev. Drug Discov.* **1**, 45-54.
10. Davis, A. M., Teague, S. J. & Kleywegt, G. J. (2003). Applications and limitations of X-ray crystallographic data in structure-based ligand and drug design. *Angew. Chem. Int. Ed. Engl.* **42**, 2718-2736.
11. Gohle, H. & Klebe, G. (2002). Approaches to the description and prediction of the binding affinity of small-molecule ligands to macromolecular receptors. *Angew. Chem. Int. Ed. Engl.* **41**, 2644-2676.
12. Betz, U. A. K., Farquhar, R. & Ziegelbauer, K. (2005). Genomics: success or failure to deliver drug targets? *Curr. Opin. Chem. Biol.* **9**, 387-391.
13. Shoichet, B. K. (2004). Virtual screening of chemical libraries. *Nature* **432**, 862-865.
14. Gosh, S., Nie, A., An, J. & Huang, Z. (2006). Structure-based virtual screening of chemical libraries for drug discovery. *Curr. Opin. Chem. Biol.* **10**, 194-202.

15. Kitchen, D. B., Decornez, H., Furr, J. R. & Bajorath, J. (2004). Docking and scoring in virtual screening for drug discovery: methods and applications. *Nat. Rev. Drug Discov.* **3**, 935-949.
16. Teague, S. J. (2003). Implications of protein flexibility for drug discovery. *Nat. Rev. Drug Discov.* **2**, 527-539.
17. Davis, A. M. & Teague, S. J. (1999). Hydrogen bonding, hydrophobic interactions, and failure of the rigid receptor hypothesis. *Angew. Chem. Int. Ed. Engl.* **38**, 736-749.
18. Dodson, G. & Verma, C. S. (2006). Protein flexibility: its role in structure and mechanism revealed by molecular simulations. *Cell. Mol. Life Sci.* **63**, 207-219.
19. Karplus, M. & McCammon, J. A. (2002). Molecular dynamics simulations of biomolecules. *Nat. Struct. Biol.* **9**, 646-652.
20. Sotriffer, C. A. & Dramburg, I. (2005). "In situ cross-docking" to simultaneously address multiple targets. *J. Med Chem.* **48**, 3122-3126.
21. Dullweber, F., Stubbs, M. T., Musil, D., Stürzebecher, J. & Klebe, G. (2001). Factorizing ligand affinity: a combined thermodynamic and crystallographic study of trypsin and thrombin inhibition. *J. Mol. Biol.* **313**, 593-614.
22. Baker, B. M. & Murphy, K. P. (1996). Evaluation of linked protonation effects in protein binding reactions using isothermal titration calorimetry. *Biophys. J.* **71**, 2049-2055.
23. Czodrowski, P., Dramburg, I., Sotriffer, C. A. & Klebe, G. (2006). Development, Validation and application of adapted PEOE charges to estimate pKa values of functional groups in protein ligand complexes. *Proteins* **65**, 424-437.
24. Block, P., Sotriffer, C. A., Dramburg, I., Klebe, G. (2006). AffinDB: a freely accessible database of affinities for protein ligand complexes from the PDB. *Nucleic acids Res.* **34**, D522-526.
25. Wang, R., Fang, X., Lu, Y. & Wang, S. (2004). The PDBbind database: collection of binding affinities for protein-ligand complexes with known three-dimensional structures. *J. Med. Chem.* **47**, 2977-2980.
26. SCORPIO: Structure-calorimetry of reported protein interactions online.
<http://www.biochem.ucl.ac.uk/scorpio/scorpio.html>

-
27. Naim, M., Bhat, S., Rankin, K. N., Dennis, S. et al. (2007). Solvated interaction energy (SIE) for scoring protein-ligand binding affinities. 1. Exploring the parameter space. *J. Chem. Inf. Model.* **47**, 122-133.
 28. Holdgate, G. A. & Ward, W. H. J. (2005). Measurements of binding thermodynamics in drug discovery. *Drug Discov. Today* **10**, 1543-1550.
 29. Ruben, A. J. Kiso, Y. & Freire, E. (2006). Overcoming roadblocks in lead optimization: A thermodynamic perspective. *Chem. Biol. Drug Des.* **67**, 2-4.
 30. Homans, S. W. (2005). Probing the binding entropy of ligand-protein interactions by NMR. *ChemBioChem* **6**, 1-8.
 31. Meyer, E.A., Castellano, R.K. & Diederich, F. (2003). Interactions with aromatic rings in chemical and biological recognition. *Angew. Chem. Int. Ed.* **42**, 1210-1250.
 32. Barratt, E., Bingham, R. J., Warner, D. J., Laughton, C. A., Phillips, S. E. V. & Homans, S. W. (2005). Van der Waals interactions dominate ligand-protein association in a protein binding site occluded from solvent water. *J. Am. Chem. Soc.* **127**, 11827-11834.
 33. Chandler, D. (2005). Interfaces and the driving force of hydrophobic assembly. *Nature* **437**, 640-647.
 34. Bartlett, P. A., Yusuff, N., Rico, A. C. & Lindvall, M. K. (2002). Antihydrophobic solvent effects: An experimental probe for the hydrophobic contribution to enzyme-inhibitor binding. *J. Am. Chem. Soc.* **124**, 3853-3857.
 35. Breslow, R. & Zhu, Z. (1995). Quantitative antihydrophobic effects as probes for transition state structures. 2. Diels-Alder Reactions. *J. Am. Chem. Soc.* **117**, 9923-9924.
 36. Lipinski, C. A., Lombardo, F., Dominy, B. W., Feeney, P. J. (1997). Experimental and computational approaches to estimate solubility and permeability in drug discovery and development settings. *Adv. Drug Delivery Rev.* **23**, 3-25.
 37. Lipinski, C. A. (2000). Drug-like properties and the causes of poor solubility and poor permeability. *J. Pharmacol. and Toxicol. Methods* **44**, 235-249.
 38. Dunitz, J. D. (1994). The entropic cost of bound water in crystals and biomolecules. *Science* **264**, 670.

-
39. D'Aquino, J.A., Freire, E. & Amzel, L.M. (2000). Binding of small organic molecules to macromolecular targets: evaluation of conformational entropy changes. *Proteins Suppl.* **4**, 93-107.
 40. Benfield, A. P., Teresk, M. G., Plake, H. R., DeLorbe, J.E et al. (2006). Ligand preorganization may be accompanied by entropic penalties in protein-ligand interactions. *Angew. Chem. Int. Ed. Engl.* **118**, 6984-6989.
 41. Velazquez-Campoy, A., Todd, M. J. & Freire, E. (2000). HIV-1 protease inhibitors: enthalpic versus entropic optimization of the binding affinity. *Biochemistry* **39**, 2201-2207.
 42. Williams, M.A. & Ladbury, J.E. (2003). Hydrogen bonds in Protein-ligand complexes. In *Protein-Ligand interactions: From Molecular Recognition to Drug Design*. (Boehm, H.-J. & Schneider, G., eds), p. 137-161, Wiley-VCH, Weinheim.
 43. Dunitz, J. D. (1995). Win some, lose some: enthalpy-entropy compensation in weak intermolecular interactions. *Chem. Biol.* **2**, 709-712.
 44. Gilli, P., Ferretti, V., Gilli, G. & Borea, P. A. (1994). Enthalpy-entropy compensation in drug-receptor binding. *J. Phys. Chem.* **98**, 1515-1518.
 45. Gerlach, C., Smolinski, M., Steuber, H., Sottriffer, C. A. Heine, A., Hangauer, D. & Klebe, G. Thermodynamic inhibition profile of a cyclopentyl- and a cyclohexyl derivative towards thrombin: The same, but for different reasons. *Submitted*.
 46. Hers, H. G. (1956). The mechanism of the transformation of glucose in fructose in the seminal vesicles. *Biochim.Biophys. Acta* **22**, 202-203.
 47. Yabe-Nishimura, C. (1998). Aldose reductase in glucose toxicity: a potential target for the prevention of diabetic complications. *Pharmacol. Rev.* **50**, 21-33.
 48. Davydov, V. V., Dobaeva, N. M. & Bozhkov, A. I. (2004). Possible role of alteration of aldehyde`s scavenger enzymes during aging. *Exp. Gerontol.* **39**, 11-16.
 49. Brownlee, M. (2001). Biochemistry and molecular cell biology of diabetic complications. *Nature* **414**, 813-820.
 50. Rondeau, J. M., Tete-Favier, F., Podjarny, A., Reymann, J. M. et al. (1992). Novel NADPH-binding domain revealed by the crystal structure of aldose reductase. *Nature* **355**, 469-472.

-
51. Jez, J. M., Bennett, M. J., Schlegel, B. P., Lewis, M., Penning, T. M. (1997). Comparative anatomy of the aldo-keto reductase superfamily. *Biochem. J.* **326**, 625-636.
 52. Varnai, P., Richards, W. & Lyne, P.D. (1999). Modelling the catalytic reaction in human aldose reductase. *Proteins* **37**, 218-227.
 53. Cachau, R., Howard, E., Barth, P., Mitschler, A., Chevrier, B., Lamour, V., Joachimiak, A., Sanishvili, R., Van Zandt, M., Sibley, E., Moras, D. & Podjarny, A.D. (2000). Model of the catalytic mechanism of human aldose reductase based on quantum chemical calculations. *J. Phys. IV France* **10**, 3-13.
 54. Wierenga, R. K. (2001). The TIM-barrel fold: a versatile framework for efficient enzymes. *FEBS Lett.* **492**, 193-198.
 55. Sterner, R. & Höcker, B. (2005). Catalytic versatility, stability, and evolution of the $(\beta\alpha)_8$ -Barrel enzyme fold. *Chem. Rev.* **105**, 4038-4055.
 56. Miyamoto, S. (2002). Recent advances in aldose reductase inhibitors: potential agents for the treatment of diabetic complications. *Expert. Opin. Ther. Patents* **12**, 621-631.
 57. Wild, S., Roglic, G., Green, A., Sicree, R. & King, H. (2004). Global Prevalence of Diabetes. *Diabetes Care* **27**, 1047-1053.
 58. Skyler, J.S. (2004). Diabetes Mellitus: Pathogenesis and Treatment Strategies. *J. Med. Chem.* **47**, 4113-4117.
 59. Stumvoll, M. Goldstein, B.J. & van Haeften, T.W. (2005). Type 2 diabetes: principles of pathogenesis and therapy. *Lancet* **365**, 1333-1346.
 60. Ross, S. A., Gulve, E. A. & Wang, M. (2004). Chemistry and Biochemistry of Type 2 Diabetes. *Chem. Rev.* **104**, 1255-1282.
 61. Pfeifer, M. A. & Schumer, M. P. (1995). Clinical Trials of diabetic neuropathy: past, present and future. *Diabetes* **44**, 1355-1361.
 62. Suzen S. & Buyukbingol E. (2003). Recent studies of aldose reductase enzyme inhibition for diabetic complications. *Curr. Med. Chem.* **10**, 1329-1352.
 63. Evans, J. L., Goldfine, I. D., Maddux, B. A. & Grodsky, G.M. (2002). Oxidative stress and stress-activated signalling pathways: a unifying hypothesis of type 2 diabetes. *Endocrine Rev.* **23**, 599-622.
 64. Price, S. A., Agthong, S., Middlemas, A.B. & Tomlinson, D.R. (2004). Mitogen-activated protein kinase p38 mediates reduced nerve conduction

-
- velocity in experimental diabetic neuropathy. – Interactions with aldose reductase. *Diabetes* **53**, 1851-1856.
65. Suzuki, L. A., Poot, M., Gerrity, R.G. & Bornfeldt, K.E. (2001). Diabetes accelerates smooth muscle accumulation in lesions of atherosclerosis. Lack of direct growth-promoting effects of high glucose levels. *Diabetes* **50**, 851-860.
66. Nakamura, J., Kasuya, Y., Hamada, Y., Nakashima, E., Naruse, K., Yasuda, Y., Kato, K. & Hotta, N. (2001). Glucose-induced hyperproliferation of cultured rat aortic smooth muscle cells through polyol pathway hyperactivity. *Diabetologica* **44**, 480-487.
67. Oyama, T., Miyasita, Y., Watanabe, H. & Shirai, K. (2006). The role of polyol pathway in high glucose-induced endothelial cell damages. *Diabetes Res. Clin. Pract.* **73**, 227-234.
68. Ceriello, A. & Motz, E. (2004). Is oxidative stress the pathogenic mechanism underlying insulin resistance, diabetes, and cardiovascular disease? The common soil hypothesis revisited. *Arterioscler. Thromb. Vasc. Biol.* **24**, 816-823.
69. Dan, Q., Wong, R.L.C., Yin, S., Chung, S.K., Chung, S.S.M. & Lam, K.S.L. (2004). Interaction between the polyol pathway and non-enzymatic glycation on mesangial cell gene expression. *Nephron Exp. Nephrol.* **98**, e89-e99.
70. Jerums, G., Panagiotopoulos, S., Forbes, J., Osicka, T. & Cooper, M. (2003). Evolving concepts in advanced glycation, diabetic nephropathy, and diabetic vascular disease. *Arch Biochem Biophys.* **419**, 55-62.
71. Srivastava, S. K., Ramana, K. V., Chandra, D., Srivastava, S. & Bhatnagar, A. (2003). Regulation of aldose reductase and the polyol pathway activity by nitric oxide. *Chem. Biol. Interact.* **143-144**, 333-340.
72. Chandra, D., Jackson, E. B., Ramana, K. V., Kelley, R., Srivastava, S. K. & Bhatnagar, A. (2002). Nitric oxide prevents aldose reductase activation and sorbitol accumulation during diabetes. *Diabetes* **51**, 3095-3101.
73. Suzen S. & Buyukbingol E. (2003). Recent studies of aldose reductase enzyme inhibition for diabetic complications. *Curr. Med. Chem.* **10**, 1329-1352.
74. Greene, D. A., Arezzo, J. C. & Brown, M. B. (1999). Effect of aldose reductase inhibition on nerve conduction and morphometry in diabetic neuropathy. Zenarestat Study Group. *Neurology* **53**, 580-591.

-
75. Constantino, L., Rastelli, G., Vianello, P., Cignarella, G. & Barlocco, D. (1999). Diabetes Complications and their potential prevention: Aldose Reductase Inhibition and other Approaches. *Med. Res. Rev.* **19**, 3-23.
 76. Yagihashi, S., Yamagishi, S. I., Wada Ri, R., Baba, M., Hohman, T. C., Yabe-Nishimura, C. & Kokai, Y. (2001). Neuropathy in diabetic mice overexpressing human aldose reductase and effects of aldose reductase inhibitor. *Brain* **124**, 2448-2458.
 77. Mylari, B. L., Armento, S. J., Beebe, D. A., Conn, E. L., Coutcher, J. B., Dina, M. S., O'Gorman, M. T., Linhares, M. C., Martin, W. H., Oates, P. J., Tess, D. A., Withbroe, G. J. & Zembrowski, W. J. (2003). A highly selective, non-hydantoin, non-carboxylic acid inhibitor of aldose reductase with potent oral activity in diabetic rat models: 6-(5-chloro-3-methylbenzofuran-2-sulfonyl)-2-H-pyridazin-3-one. *J. Med. Chem.* **46**, 2283-2286.
 78. Baba, M., Kimura, K., Suda, T. & Yagihashi, S. (2006). Three-year inhibition of aldose reductase on development of symptomatic neuropathy in diabetic patients. *J. Peripher. Nerv. Syst.* **11**, 176-178.
 79. Constantino, L., Rastelli, G., Vianello, P., Cignarella, G. & Barlocco, D. (1999). Diabetes Complications and their potential prevention: Aldose Reductase Inhibition and other Approaches. *Med. Res. Rev.* **19**, 3-23.
 80. El-Kabbani, O., Darmanin, C., Schneider, T. R., Hazemann, I., Ruiz, F., Oka, M., Joachimiak, A., Schulze-Briese, C., Tomizaki, T., Mitschler, A. & Podjarny, A. (2004). Ultrahigh resolution drug design. II. Atomic resolution structures of human aldose reductase holoenzyme complexed with Fidarestat and Minalrestat: implications for the binding of cyclic imide inhibitors. *Proteins* **55**, 805-813.
 81. Bril, V. (2001). Status of current clinical trials in diabetic polyneuropathy. *Can. J. Neurol. Sci.* **28**, 191-198.
 82. Ziegler, D. (2004). Polyneuropathy in the diabetic patient – update on pathogenesis and management. *Nephrol. Dial. Transplant.* **19**, 2170-2175.
 83. Krämer, O., Hazemann, I., Podjarny, A.D. & Klebe, G. (2004). Virtual screening for inhibitors of human aldose reductase. *Proteins* **55**, 814-823.
 84. Sun, W., Oates, P. J., Coutcher, J. B., Gerhardinger, C. & Lorenzi, M. (2006). A selective aldose reductase inhibitor of a new structural class prevents or reverses

-
- early retinal abnormalities in experimental diabetic retinopathy. *Diabetes* **55**, 2757-2762.
85. Da Settimo, F., Primofiore, G., La Motta, C., Sartini, S., Taliani, S., Simorini, F., Marini, A.M., Laveccia, A., Novellino, E. & Boldrini, E. (2005). Naphtho[1,2-*d*]isothiazole acetic acid derivatives as a novel class of selective aldose reductase inhibitors. *J. Med. Chem.* **48**, 6897-6907.

2. Structural and Thermodynamic Study on Aldose Reductase: Nitro-substituted Inhibitors with Strong Enthalpic Binding Contribution

2.1 Introduction

The worldwide prevalence of diabetes mellitus has been estimated to 2.8 % in 2000 and is expected to raise by 4.4 – 9 % within the next two decades.^{1,2} Careful predictions anticipate 366 million people worldwide suffering from the “diabetes epidemic” in 2030. Even though various therapy options have been developed for the treatment of diabetes mellitus including compounds interfering with hydrocarbon digestion and glucose utilisation, insulines, insulin-releasing agents, and recently drugs compensating insulin resistance, a stringent blood glucose control as maintained under physiological conditions could not be achieved.³⁻⁵ In consequence, in diabetic patients non-physiological hyperglycaemic events are responsible for severe long-term complications including retinopathy, nephropathy, neuropathy, cataract and angiopathy.^{1,6,7} Under these elevated glucose levels an increased flux of glucose through the polyol pathway occurs inducing various biochemical imbalances, thereby strongly contributing to the onset of diabetic complications. In particular, the polyol pathway consists of two enzymes: the first and rate-limiting one, aldose reductase (ALR2) catalyses the conversion of glucose to sorbitol using NADPH as reducing cofactor, the second enzyme, sorbitol dehydrogenase, oxidizes sorbitol to fructose NAD⁺-dependently.^{8,9} Thus, increased polyol pathway activity is accompanied by generation of osmotic and oxidative stress causing various pathological interferences with cytokine signalling, regulation of apoptosis as well as activation of kinase cascades.¹⁰ For instance, recent experimental observations provided evidence that under increased glucose metabolism via the polyol pathway p38-MAP kinase shows increased activity causing nerve conduction deficits and, thus, leads to neuropathy.¹¹ Secondly, increased protein kinase C activity under elevated polyol pathway flux has been shown to induce smooth muscle cell proliferation of blood vessels being in agreement with atherosclerosis. This also explains estimations that 75 – 80 % of adults with diabetes die from complications of atherosclerosis.^{12,13} In addition, extended polyol pathway

activity has been shown to provoke endothelial cell damages by increased oxidative stress and thereby contribute to atherosclerotic complications.¹⁴ Aggravatingly enough, increasing amounts of fructose derived from the polyol pathway contribute to the formation of advanced glycosylated endproducts (AGEs) and thereby lead to pathological changes of proteins functionally affected by covalent modification.^{15,16}

Altogether, the pathological activity of ALR2 plays a key role in the development of diabetic complications and thereby represents an excellent drug target. In fact, in vitro and in vivo studies suggest a clear benefit of the administration of aldose reductase inhibitors (ARIs) in various model systems exposed to high glucose levels as well as during the therapy of diabetic patients.^{7,17-21} Thus, extensive efforts have been performed to develop appropriate drug candidates. Most of these inhibitors can be classified according to their negatively charged anchor groups into carboxylate-type or hydantoin-type inhibitors. However, most of the inhibitors evolved from these approaches failed in clinical trials either due to poor bioavailability or selectivity properties.^{1,22} It has been argued that carboxylate-type inhibitors are inappropriate due to their more acidic properties compared to hydantoins. Under physiological conditions carboxylate groups will be almost completely ionised impairing their ability to cross biological membranes.²³ Nevertheless, a recently published carboxylate-type ligand, lidorestat, exhibits a favourable pharmacokinetic profile resulting in desirable tissue penetration. Accordingly, even though possessing this ionisable group, ligands can be optimized with respect to sufficient penetration behaviour.²⁴ Besides an appropriate pharmacokinetic profile, potential drug candidates should also possess high selectivity to aldose reductase in comparison to the highly related aldehyde reductase (ALR1) which shares a sequence identity of about 65 %.²⁴⁻²⁸ As ALR1 detoxifies various aldehydes derived from oxidative stress including 3-deoxyglucosone and methylglyoxal by conversion to their corresponding non-reactive alcohols,²⁹ its reducing activity is of utmost physiological importance, in particular under increased oxidative conditions as experienced during a diabetic situation.

ALR2 (EC 1.1.1.21) is a 36 kDa (β/α)₈-TIM-barrel shaped aldo-keto reductase with the active site located at the C-terminal region of the enzyme.^{23,25,26,30,31} The deeply buried substrate binding pocket comprises residues presumably participating in the catalytic mechanism (Tyr 48, Lys 77, His 110). Furthermore, the nicotinamide moiety of NADP⁺ and Trp 111 interact with the head group of most described ligands. Additionally, hydrophobic contacts can be formed by the side-chains Trp 20, Val 47, Trp 79, and Trp

219. This catalytic site is usually addressed by hydrophilic, negatively charged building blocks. Ligands decorated at the opposing terminal end with appropriate hydrophobic groups exhibit to varying degree the ability to induce an opening of distinct pockets. They are referred to as “specificity pockets” formed in consequence of different rotameric states of Ala 299, Leu 300 and Phe 122 at the solvent-exposed face and the side chain of Trp 111 facing the center of the TIM-barrel.

ALR2 converts various aldehydes (including glucose under diabetic conditions) to their corresponding alcohols using NADPH as reducing cofactor. Even though the exact mechanism is currently under discussion, NADPH donates a hydride ion to the carbonyl carbon of the aldehyde. Most likely, this step is followed by a subsequent transfer of a proton from one of the neighbouring acidic protein residues to the intermediately formed substrate anion.^{32,33}

An ultra-high resolution structure of ALR2 in complex with the carboxylate-type inhibitor IDD 594 (analogue of **3**, Fig. 2.1 with a thioamide instead of an amide group and a chlorine atom replaced by fluorine) has been refined to a resolution of 0.66 Å. The crystal structure provides evidence for the protonation states of the titratable and catalytically relevant residues involved in inhibitor binding.²⁵

Four successful *in-silico* screening studies have been reported on ALR2 up to now to find novel lead compounds.³⁴⁻³⁷ Recently, a virtual screening study has been performed in our laboratory based on the coordinates and protonation states observed in the ultra-high resolution crystal structure. This computer screening resulted in six new carboxylate-type leads, among them two ligands in the low- and submicromolar affinity range.³⁷ Both ligands contain a nitro-substituted terminal moiety linked to a 5-membered heterocycle connected via an alkyl spacer to the carboxylic head group (**1**, **2**, Fig. 2.1). In all screening studies reported so far on ALR2, binding affinity of identified hits was discussed with respect to binding geometries obtained from docking with or without subsequent force-field minimization or molecular dynamics simulations. However, as could be demonstrated in several cases, surprising differences between the docking predictions and the subsequently determined crystal structures have been reported.³⁸⁻⁴⁰ Accordingly, it is highly advisable to determine the crystal structure of virtual screening hits in complex with the target protein prior to embarking into a synthesis program with the goal to optimize binding properties. Furthermore, detailed insight into the thermodynamic driving forces of inhibitor binding can be very supportive to select the best screening hit for a synthesis follow-up program.⁴¹

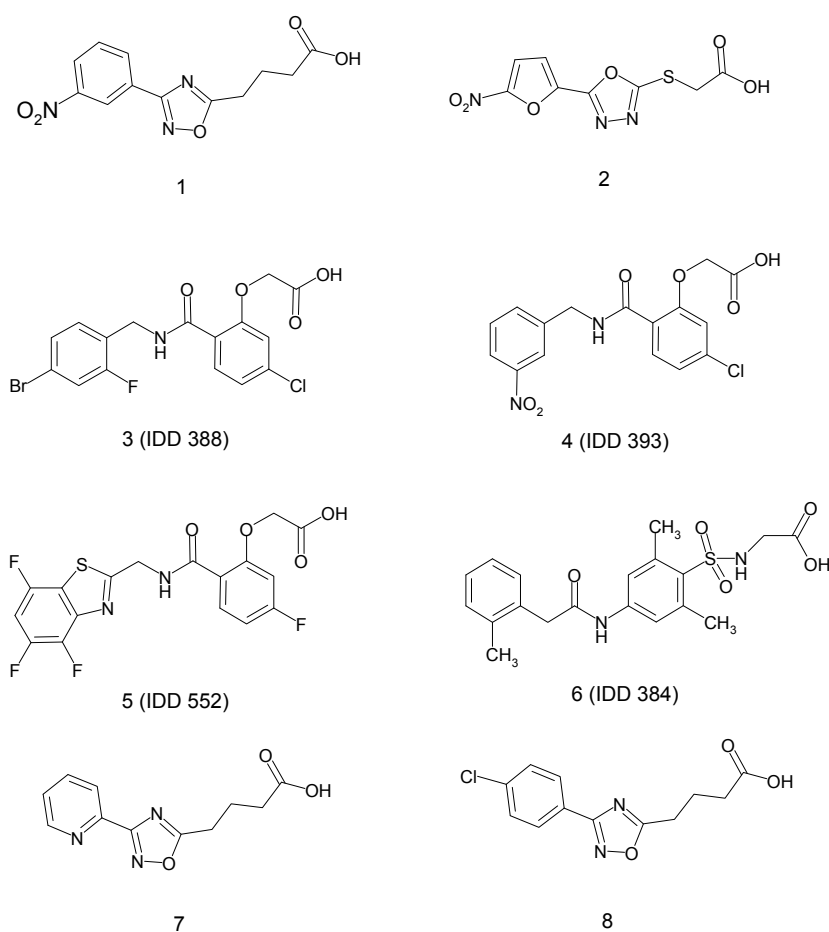


Figure 2.1. Chemical formulae of inhibitors discussed in this study. Ligands **1** and **2** have been identified by virtual screening. **3**: IDD 388, **4**: IDD 393, **5**: IDD 552, **6**: IDD 384. Ligands **7** and **8** were selected as analogues to **1** in order to evaluate the influence of the nitro substituent at the terminal aromatic moiety.

In the present study, we report on the crystallographically determined binding modes of **1** and **2** in complex with ALR2 together with the thermodynamic driving forces responsible for binding as available from isothermal titration calorimetry (ITC). Furthermore, we identified initial structure-activity relationships of both leads by facing their properties to two inhibitors of the IDD series (**3**, **4**, Fig. 2.1, respectively).

2.2 Results and Discussion

2.2.1 Binding mode of the carboxylate head group

The final model (1.43 Å resolution) of the ternary complex of human ALR2 with bound NADP⁺ and **1** shows the expected (β/α)₈-TIM barrel with the active site located at the C-terminal loop of the enzyme. The F_o-F_c density map clearly shows the location of the inhibitor (Fig. 2.2a). The inhibitor occupies the active site with its carboxylate head group located at the catalytic cavity. The aromatic portions are sandwiched by the indole moiety of Trp 111 forming a π–π stacking interaction, and the side chains of Phe 122, Leu 300 and Cys 302 lining the specificity pocket (Fig. 2.2b). The carboxylate is involved in a network of charge-assisted H-bonds interacting with Tyr 48 OH, His 110 Nε2 and, interestingly, to a water molecule mediating the contact to Trp 111 Nε1. Assuming identical protonation states as observed in the 0.66 Å resolution ALR2-IDD594 complex structure,²⁵ the carboxylate-type inhibitor binds deprotonated and acts via its carboxylate as H-bond acceptor. The deprotonated negatively charged ligand head group forms electrostatic interactions to the positively charged nicotinamide moiety of the cofactor. The incorporation of an interstitial water molecule is surprising as in all other ALR2 complexes with carboxylate-type inhibitors determined using crystals grown under the same conditions at pH 5 (including the 0.66 Å crystal structure) a direct H-bond between the carboxylate and Trp 111 Nε2 is formed. Obviously, in the present case, the distance of 4.3 Å between the carboxylate oxygen and Trp 111 Nε2 (compared to 3 Å in other structures) prevents a direct H-bond. Only, for the ALR2-IDD 552 complex the presence of a similar interstitial water molecule has been described, where a split conformation for the IDD 552 carboxylate group could be assigned (**5**, Fig. 2.1 and Fig. 2.3).⁴² However, this structure has been determined using crystals grown under different crystallisation conditions at pH 8, while neither split conformations nor a mediating water molecule have been detected for this complex crystallised at pH 5. The temperature factor for the interstitial water molecule in ALR2-**1** amounts to 31.2 Å², thus, slightly elevated in comparison to the average of its coordinating atoms (29.2 Å²). This value suggests full occupancy and low mobility of this water molecule.

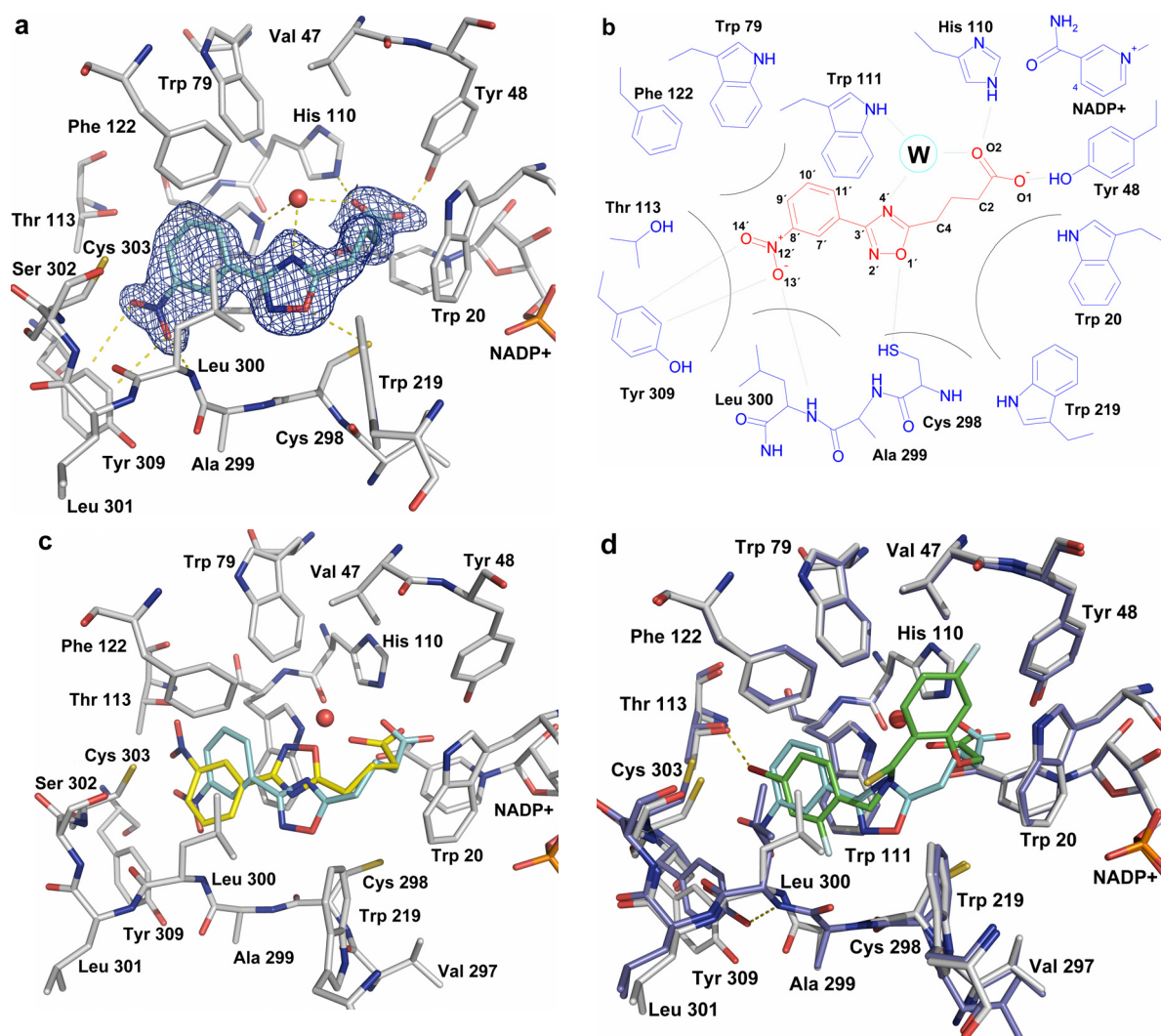


Figure 2.2. Binding pocket of ALR2 complexed with **1**. (a) Binding pocket residues are represented by silver sticks, the ligand is shown in cyan. The red sphere represents the interstitial water molecule mediating a hydrogen-bond contact between Trp 111 N ϵ 1 and the carboxylic group of the inhibitor. Hydrogen bonds and polar interactions are indicated as yellow dashed lines. The $F_o - F_c$ omit electron density is depicted in dark blue at 3σ . (b) Schematic representation of the binding mode of **1** (red). Hydrogen bonds and polar contacts are indicated as green dotted lines. (c) Superposition of the crystallographically determined ALR2-**1** complex (ligand in cyan) and the computationally predicted binding mode (yellow) generated by docking in the virtual screening campaign. (d) Superposition of the ALR2-**1** crystal structure (binding pocket represented in silver and ligand in cyan) and the 0.66 Å resolved ALR2 complex (dark blue) with IDD 594 (green) which served as template geometry in the virtual screening run. The short contact between the ligand's bromine atom and the Thr 113 O γ is shown as yellow dashes. A backbone flip of the Ala 299-Leu 300 peptide bond is observed. In the ALR2-IDD 594 complex (yellow dashes) the backbone NH group forms a hydrogen bond to Tyr 309 OH, whereas in the ALR2-**1** complex the NH group hydrogen-bonds to the nitro group of **1**. The rupture of the H-bond to Tyr 309 is accompanied by a displacement of the latter residue, which thereby enlarges the far end of the specificity pocket to accommodate the nitro group.

2.2.2 An interstitial water molecule picked up upon binding of 1

Accordingly, the question arises whether the presence of such a water molecule is simply pH-dependent, or whether it is reinforced by the geometry of the protein-ligand interface: even though in both complexes (ALR2-IDD 552, pH 8 and ALR2-1, pH 5) the observed water molecule mediates a hydrogen bond between the carboxylate oxygen and Trp 111 N ϵ 1, their spatial positions deviate by 2.5 Å in a C $_{\alpha}$ -superposition of both protein complexes. Both water molecules are involved in different local coordination geometry. In ALR2-IDD 552, it finds six adjacent interaction partners for putative hydrogen bond formation (as H-bond donors Trp 111 N ϵ 1 and the ligand's amide nitrogen; as H-bond acceptors the ether and carboxylate oxygens of the ligand, the amide carbonyl oxygen of the nicotinamide moiety, and the sulphur of Cys 298 either as donor or acceptor depending on its protonation state and orientation). The interstitial water in ALR2-1 shows three-fold coordination accepting an H-bond from Trp 111 N ϵ 1, and likely acting as a hydrogen-bond donor to the carboxylate oxygen and the nitrogen N4' of the ligand. Obviously, in case of **1**, the ligand provides appropriate coordination sites and, by means of the alkyl spacer, it adopts in a way to accommodate the additional water molecule. The placement of the carboxylic group seems to further depend on the constitution of the attached side chain, and the adopted binding mode of the ligand: as depicted in Fig. 2.3, the carboxylate anchor of IDD 384 (**6**, Fig. 2.1), crystallized at pH 5, adopts a further conformation coordinating to Tyr 48 and His 110, whereas its sulfonyl group present in the attached side chain places one of its oxygens in a position well-suited to hydrogen-bond to Trp 111 N ϵ 1.⁴³ It actually coincides with the water position in the complex with **1**.

2.2.3 Placement of the central heterocycle and the terminal nitro group of 1 and 2

The oxadiazol spacer of **1** forms van der Waals contacts to the indole moiety of Trp 111 and Trp 219 (Fig. 2.2a, 3.3 and 3.9 Å between C3' and O1' of the ligand and the Trp CZ2 atoms, respectively), and O1' approaches the sulfur of Cys 298 (3.6 Å). Furthermore, the side chain of Leu 300 forms hydrophobic contacts with the oxadiazole moiety (3.2 Å between Leu 300 CG and N2'). The three-membered alkyl chain of the ligand is flanked by Trp 20 and Trp 219 (3.3 Å between C4 of the ligand to Trp 20 CZ2 and 3.6 Å to Trp 219 CH2). The nitro-substituted phenyl moiety penetrates into the specificity pocket and forms a face-to-face-oriented π - π stacking with the side chain of

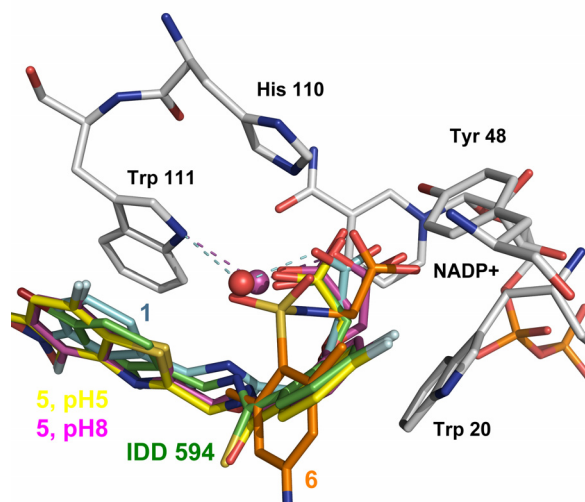


Figure 2.3. Interactions formed by carboxylic anchor groups in several distinct carboxylate-type inhibitors. The superposition is generated by a C_{α} fit of the corresponding crystal structure onto ALR2-1 (key interacting residues are shown in silver, **1** in cyan). Most carboxylate groups adopt an orientation similar to IDD 594 (green) and IDD 552 (**5**) (yellow), both crystallized at pH 5. The IDD 552 complex crystallized at pH 8 (magenta) exhibits two split conformations for the carboxymethylene moiety. One orients similarly as observed for this ligand at pH 5. The second conformation is shifted towards Tyr 48 and interacts with Trp 111 N ϵ 1 via H-bonds mediated by a water molecule (magenta sphere and dashes lines). The red sphere and cyan dashes represent the water-mediated interaction between **1** and Trp 111 observed at pH 5. A deviating placement of the carboxymethylene moiety is observed for IDD 384 (**6**, coloured in orange, crystallized at pH 5). Here, the adjacent sulfonamide group places one of its oxygens in similar position as the interstitial water molecule in ALR2-1.

Trp 111 via a distance of about 3.4 Å between both aromatic planes. Putatively this interaction is favoured by the electron-rich character of the indole moiety complemented by the electron-withdrawn properties of the nitro-phenyl ring. Further hydrophobic contacts to the side chains of Trp 79 and Phe 122 (3.7 Å between Trp 79 CH₂ and Phe 122 CZ to C11'), Cys 80 (4.1 Å between Cys 80 S and C10') and Leu 300 (3.7 Å between Leu 300 C γ and C7') are formed. The nitro oxygen O14' forms a van der Waals contact to Thr 113 O γ (4.1 Å). The Ala 299-Leu 300 peptide bond donates an H-bond via its nitrogen to O13' of the nitro group (3.3 Å). N2' of the oxadiazole ring is in 4 Å distance, thus excluding the formation of an effective H-bond. Remarkably, the nitro group orients its oxygens towards the aromatic side chain of Tyr 309 (3.3 and 3.4 Å between the oxygen atoms and the aromatic carbon atoms C δ 1 and C ϵ 1). Apart from pure van der Waals interactions these short distances suggests

additional electrostatic interactions between the negatively polarized nitro oxygens and the aromatic system.

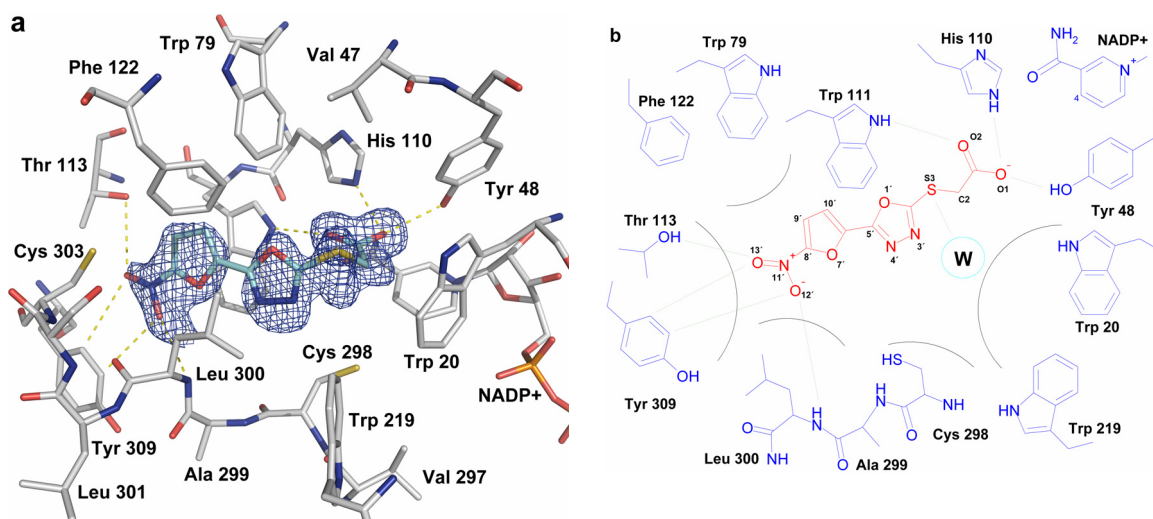


Figure 2.4. Representation of the binding mode observed for **2**. (a) Refined model of the binding pocket (shown in silver) complexed with the inhibitor (cyan). Polar contacts are depicted as yellow dashes. The $F_o - F_c$ omit electron density of the ligand is shown in dark blue contoured at 3σ . (b) Schematic representation of the binding mode of **2** (red) with ALR2 (blue). The thioether of **2** forms a hydrogen bond to a water molecule beyond the binding pocket, which further interacts with bulk water molecules.

2.2.4 Binding mode differences of the two virtual screening hits 1 and 2

The second inhibitor (**2**) identified by virtual screening, shares overall similarity with **1**. However, a comparison between both ligands reveals the following differences. (1) The three-membered alkyl chain bearing the terminal carboxylate group in **1** is replaced by a two-membered thiomethylene spacer. (2) The distribution of heteroatoms composing the five-membered ring is different. (3) The nitro-phenyl ring is replaced by a nitro-furyl group. Obviously, these differences modify the ligand's binding geometry (Fig. 2.4a, b): in ALR2-**2** the carboxylate head group is located nearly identically to the majority of the other carboxylate-type inhibitors. Accordingly, its O1 atom performs an H-bond to Tyr 48 and His 110 (2.9 and 2.8 Å, respectively), while O2 is hydrogen-bonded to Trp 111 N ϵ 1 (2.9 Å), remarkably without involving an interstitial water molecule as observed for ALR2-**1**. Probably due to the decreased adaptability of the two-membered spacer in **2**, its heterocycle experiences less stringent van der Waals contacts to Trp 20 (4.1 Å between Trp 20 CZ2 and the ligand's S3), Trp 219 (4.3 Å between Trp 219 CH2 and N3'), and Cys 298 (4.2 Å between Cys 298 S and N3') compared to ligand **1**. Similarly, less efficient contacts between the five-membered ring

and Leu 300 are observed (3.6 Å between Leu 300 C γ and the N4'). In both complexes, the nitro-substituted aromatic rings point similarly with their nitro oxygens towards Tyr 309 and intercalate between Trp 111 (3.3 – 3.5 Å in between both aromatic moieties) and Cys 302 (3.8 Å between the ligand's aromatic plane and the sulphur atom). They form interactions with Trp 79 (3.7 Å between the carbon atom C11' of **1** as well as C10' of **2** and Trp 79 CH₂) and Phe 122 (3.9 Å between the nitro-furyl moiety's C10' and Phe122 CZ in ALR2-**2** versus 3.7 Å to C11' in ALR2-**1**). However, some of the remaining interactions found for **2** are attenuated in comparison to **1**: the arene-sulfur contact between Cys 80 and the nitro-aromatic moiety is slightly decreased in ALR2-**2** suggested by the longer distance of 4.3 Å compared to 4.0 Å in ALR2-**1**. The contacts between the nitro group and the aromatic side chain of Tyr 309 seem to be less stringent in **2** compared to **1**: While both nitro oxygens of **1** are in close distance to the aromatic carbons (3.3 and 3.4 Å), the corresponding contacts in ALR2-**2** are longer (3.6 and 3.7 Å). Similar to ALR2-**1**, the backbone NH of Leu 300 donates a weak H-bond to the nitro oxygen O12' (3.5 Å distance) of **2**, whereas the distances to the furyl-O (3.9 Å) and the oxadiazole-N (4.2 Å) are too long to be classified as hydrogen bond. The other nitro oxygen O13' is involved in a weak H-bond to Thr 113 O γ via 3.5 Å in ALR2-**2**, where the corresponding contact in ALR2-**1** amounts to 4.1 Å.

Concluding by the number of short contacts formed, **1** exhibits better shape complementarity to the binding cavity, whereas such a 'snug fit' is not similarly observed for **2**. This observation is underlined by the amount of solvent-accessible surface (BSASA) that becomes buried upon ligand binding: while **1** buries in total 613.5 Å² with respect to both protein cavity and ligand itself, the corresponding value for **2** amounts only to 539.5 Å². Assuming full occupancy for both inhibitors their mobility in the binding pocket is virtually identical (average B-factors for ALR2-**1** 29.8 Å² versus 27.5 Å² in ALR2-**2**) indicating comparable spatial arrest.⁴⁴

2.2.5 Comparison of docking-predicted and crystallographically determined binding modes

Retrospectively, the binding geometries observed in the two crystal structures can be faced to the docking poses predicted in our virtual screening study³⁷ based on the 0.66 Å resolution IDD 594-NADP⁺ template structure (Fig. 2.2c). The carboxylate head group was forced to adopt the same geometry as previously observed for IDD 594, thus, all docking solutions based on this assumption and the coordinates of the

carboxylate substructure are virtually identical. This assumption may be justified for **2**, but not for **1**, as it picks up a water molecule upon binding. Even though the importance of water for the driving forces of ligand binding is widely known, the occurrence of water molecules contributing to the protein-ligand interface is difficult to predict and, thus, usually not assumed as putative binding partner in a docking run. While the overall binding pocket geometry and most of its side chain conformations are conserved throughout the complexes of **1**, **2** and IDD 594, two important deviations are detected between the crystal structure and the virtual screening prediction. First, in the IDD 594 complex, which served as docking template, the Ala 299-Leu 300 peptide bond adopts an orientation facilitating an H-bond to Tyr 309 OH via 3.1 Å. However, in ALR2-**1** and -**2**, a backbone flip occurs resulting in a rupture of this H-bond. In contrast, a new H-bond is donated to one of the ligand's nitro oxygens. Inhibitor IDD 594, which possesses only a fluorine atom as putative weak H-bond acceptor is obviously not able to induce a similar backbone flip in order to establish an H-bond to the Leu 300 backbone NH group. For **1** and **2**, the docking prediction suggested a flipped orientation of the terminal nitrophenyl portion placing the nitro group towards Thr 113 (shown for **1** in Fig. 2.2c). Did this deviating binding mode result in consequence of the disregarded peptide flip providing the option to form an additional hydrogen bond? We performed a GRID⁴⁵ analysis of both alternative pocket conformations, using a nitro probe.

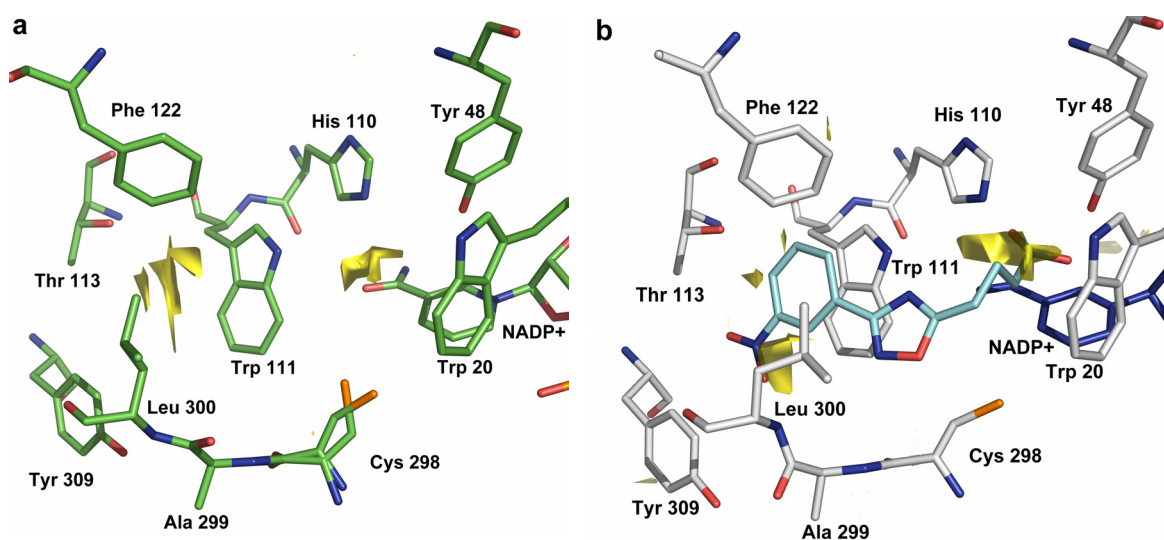


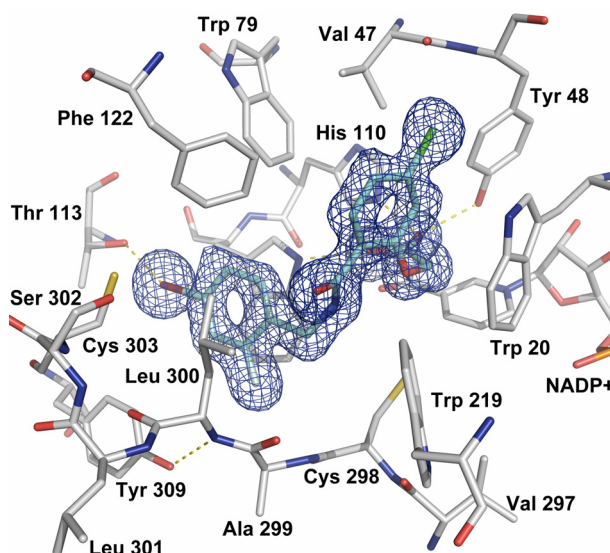
Figure 2.5. Analysis of the two binding pocket conformations with a nitro probe computed by the program GRID. Whereas the IDD 594 pocket conformation (a) which served as template for docking shows favourable interaction fields (yellow, contoured at an interaction energy of -4 kcal mol^{-1}) in a region next to Thr 113 O γ , the conformer in the crystal structure of ALR2-**1** (b) exhibits the most favourable interaction field contributions (contoured at -6 kcal mol^{-1}) at the bottom of the specificity pocket where actually the nitro group of the ligand is found in the crystal structure. In addition, favourable contours are found in the catalytic pocket which is usually occupied by carboxylic or hydantoin anchor groups.

Whereas the IDD 594 complex conformer shows the most favourable placement of a nitro probe near Thr 113 O γ (Fig. 2.5a), the corresponding optimum (at higher energy level) for the conformer actually adopted in ALR2-1 is found in the region next to Leu 300 NH at the bottom of the pocket (Fig. 2.5b). The former conformer served as template for docking, accordingly, the binding mode generated by docking has been found as the most reasonable solution (Fig. 2.2c). Secondly, binding of the meta-substituted nitrophenyl moiety is accompanied by a rotation of the χ_1 of Tyr 309 away from the binding pocket towards the solvent (compared to the corresponding docking template conformation). This rotation displaces the atoms C δ_1 and C ϵ_1 by 1.1 and 1.5 Å, respectively, thereby creating the space for the accommodation of the nitro group which would otherwise form a clash at the bottom of the specificity pocket (Fig. 2.2d).

2.2.6 Binding mode of AR inhibitors lacking a terminal nitro group

In order to obtain more profound insights into the binding features induced by the presence of the nitro group, the binding modes of **1** and **2** are faced to those of differently substituted derivatives of the IDD series.²⁸ IDD 388 and IDD 393 (**3** and **4**, Fig. 2.1, respectively) with similar scaffold to IDD 594 differ in the substitution pattern of the aromatic moiety penetrating into the specificity pocket: whereas **3** is ortho-substituted by a fluorine and para-substituted by a bromine, **4** possesses a nitro group in meta position, similarly to **1** and **2**. According to the similar scaffold and substitution pattern, **3** adopts a virtually identical binding mode as described for IDD 594 (Fig. 2.6). The carboxylate anchoring group occupies the catalytic site of the enzyme in the typical way, whereas the chloro-benzamide portion is surrounded by the residues Trp 20, Val 47, Phe 122, and Trp 219 forming hydrophobic contacts with distances in the range of 3.3 to 3.9 Å.

Figure 2.6. Binding pocket of ALR2 in complex with IDD 388 (**3**). Protein residues are shown in silver, the inhibitor is represented in cyan. The $F_o - F_c$ omit electron density contoured at 3σ clearly shows the location of the ligand. Whereas the bromine atom of the inhibitor forms a short contact of 2.9 Å to the Thr 113 O γ atom (similarly to IDD 594, Fig. 2.2d), the Ala 299-Leu 300 peptide bond donates a hydrogen bond to the side chain oxygen atom of Tyr 309 (both interactions depicted as yellow dashes).



The halogen-substituted phenyl moiety penetrates into the specificity pocket forming a stacking interaction to Trp 111 via a distance of 3.4 Å between both aromatic planes. Additional contacts are formed between this phenyl moiety and the phenyl ring of Phe 122 (3.9 Å), Leu 300 (3.5 Å between Leu 300 C β and the fluoro-substituted carbon), and Cys 303 (4.2 Å between the sulphur atom of the latter side chain and the bromo-substituted carbon). Similar to the ALR2-IDD 594 complex, the backbone NH group involved in the Ala 299-Leu 300 peptide bond forms an H-bond to the side chain oxygen of Tyr 309 via a distance of 3.1 Å.

A remarkable feature observed in the 0.66 Å resolution ALR2-IDD 594 complex²⁵ consists in the short distance between Thr 113 O γ and the bromine atom of the inhibitor (2.973 Å) which is significantly shorter than the sum of the van der Waals radii. Thus, additional electrostatic effects resulting from the polarizability of the bromine atom are assumed to contribute to binding affinity.^{25,46-48} Despite the lower resolution of our ALR2-3 complex and accordingly, the less precise determination of the atomic coordinates, the short distance of 2.9 Å between the ligand's bromine atom the Thr 113 O γ suggests similar polarisation effects in this complex as well. Remarkable differences are found for the binding geometry of the nitro derivative **4**. Similarly to ALR2-1, this ligand places its nitrophenyl group into the specificity pocket. In ALR2-4, this is accompanied by a 5° rotation of Tyr 309 χ 1 resulting in a displacement of the aromatic C δ 1 and C ϵ 2 carbon atoms by 1.3 and 1.6 Å, respectively (Fig. 2.7).

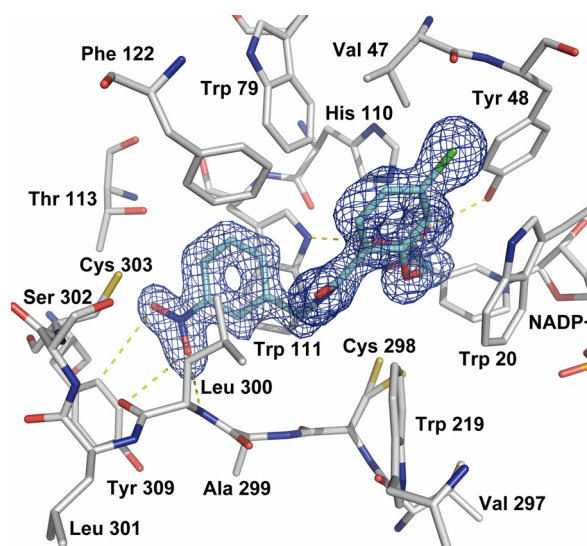


Figure 2.7. Refined model of the ALR2 binding pocket (silver) in complex with IDD 393 (**4**) (cyan). The $F_o - F_c$ omit electron density is represented in dark blue and contoured at 3σ . The terminal aromatic moiety equipped with a nitro group performs similar interactions to the specificity pocket as described for **1** (Fig. 2.2a).

The nitro oxygen atoms perform contacts via 3.4 and 3.6 Å to these two carbon atoms. The shift of the Tyr 309 side chain is accompanied by the rupture of the H-bond between Tyr 309 OH and Leu 300 NH. Instead, the latter NH group is now involved in an H-bond to one of the nitro oxygens (3.4 Å). The nitro groups of **1** and **4** occupy virtually the same position in the specificity pocket, whereas both nitro oxygens of **2** are shifted upwards in the pocket by 0.6 Å. This suggests less stringent interactions of **2** to Leu 300 NH and the side chain of Tyr 309. Nevertheless, the nitro oxygen O13' of **2** to forms instead a weak H-bond to Thr 113 O γ (3.5 Å). A similar interaction is unlikely for **1** (4.1 Å) or **4** (3.8 Å).

2.2.7 Correlation of binding affinity with structural and thermodynamic properties

The affinity data obtained by kinetic and ITC measurements are listed in Table 2.1.

Ligand	IC50 [μM]	K_b [10^6 L mol^{-1}]	$K_d (=K_b^{-1})$ [μM]	ΔG^0 [kJ mol^{-1}]	ΔH^0 [kJ mol^{-1}]	$-T\Delta S^0$ [kJ mol^{-1}]	BSASA _{polar} [\AA^2]	BSASA _{apol} ar [\AA^2]	BSASA _{total} [\AA^2]
1	0.53 +/- 0.08	1.65 +/- 0.34	0.61	-35.4	-25.6 +/- 1.2	-9.8	240.3	373.2	613.5
2	4.1 +/- 1.0	0.31 +/- 0.1	3.20	-31.3	-8.7 +/- 1.0	-22.6	264.8	274.7	539.5
3 , IDD 388	n.d.	31.5 +/- 8.45	0.032	-42.7	-62.1 +/- 1.4	19.4	142.0	609.7	751.7
4 , IDD 393	n.d.	25.0 +/- 4.1	0.040	-42.2	-79.1 +/- 1.4	36.9	220.0	513.2	733.2

Table 2.1. Kinetic and thermodynamic inhibition data. The enthalpic contribution was obtained by ITC measurements performed in Hepes buffer at pH 8. In order to correlate thermodynamic properties with the solvent-accessible surface area buried upon binding (BSASA), the latter value and its polar and apolar components have been calculated using the crystal structures of the four complexes.

Additionally, enthalpic and entropic contributions are given. Binding of the studied carboxylate-type inhibitors is superimposed by changes in protonation states. These, in principle, would have to be corrected before a meaningful factorization into absolute enthalpic and entropic contributions can be performed.⁴⁹ However, comparative measurements of different carboxylate-type inhibitors exhibited nearly identical protonation effects (Steuber, H. et al., unpublished results). Accordingly, a relative comparison of the thermodynamic differences and thus driving forces can be performed for each ligand.

As described, the nitro group is involved in multiple interactions with residues of the specificity pocket. In the complex with **1** and **4** they appear stronger compared to **2**. This observation prompted us to study the binding of two further ligands **7** and **8** (Fig. 2.1) with similar constitution, both lacking the nitro substituent: in **7** the nitrophenyl substituent is replaced by a pyridyl substituent with related electron-deficient properties. **8** contains a p-chloro-phenyl moiety as terminal aromatic substituent. The chloro-substituent is differently positioned compared to the nitro group in **1** and **4**, but as the ALR2-IDD 594 complex demonstrates, an even larger para-bromine substituent can be accommodated in the specificity pocket. Interestingly, the binding affinities of **7** and **8** are reduced by more than one order of magnitude compared to **1**, and about threefold compared to **2** (IC_{50} **7**: 12.4 +/- 2.5 μ M; **8**: 17.7 +/- 2.4 μ M). Assuming, that **7** and **8** are similarly accommodated, these results underline the special affinity-enhancing features of the nitro group. As expected, the pure electron-deficient pyridyl moiety or the sterically more demanding p-chloro-phenyl portion is obviously not capable to mimic these interactions in an equivalent way.

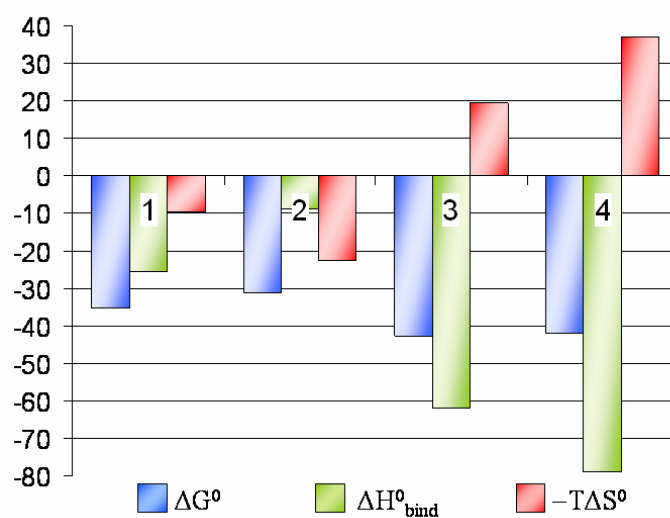


Figure 2.8. Thermodynamic data (Table 2) given in kJ mol^{-1} . The free energy of binding (ΔG^0 , blue) is factorized into enthalpic (ΔH^0 , green) and entropic ($-T\Delta S^0$, red) contributions. Whereas **1** and **2** possess a similar constitution, a different thermodynamic profile is observed: binding of **1** is more enthalpically driven, on the contrary, complex formation with **2** is stronger governed by entropy. A comparison of the enthalpic versus entropic partitioning of the equipotent ligands **3** (IDD 388) and **4** (IDD 393) reveals a stronger enthalpic contribution to binding of **4** probably determined by the nitro substituent. The enthalpic portion is compensated by a more unfavourable entropic penalty.

Interestingly, the affinities of **1** and **2** differ by a factor of about 5 (K_d values) or 8 (IC_{50} values), even though both possess similar constitution and a terminal nitro group. What are possible reasons for this affinity difference that translates into a Free Energy

difference of about 4 kJ mol⁻¹ (Table 2.1)? It factorizes into enthalpic and entropic contributions indicating different thermodynamic profiles for both ligands: whereas **1** shows a stronger enthalpy-driven binding (~ 17 kJ mol⁻¹ benefit), **2** reveals entropic advantages (22.6 kJ mol⁻¹ for **2** over **1**, Fig. 2.8).

The following considerations may explain the deviating thermodynamic profiles:

(1) **1** possesses one additional rotatable bond compared to **2**, thus, more degrees of freedom are lost upon immobilization in the bound conformation. Immobilization of a rotatable bond upon binding which is unrestrained under solvated conditions carries a Binding Free Energy penalty of about 2 kJ mol⁻¹ due to a loss of conformational entropy.⁵⁰

(2) Upon binding of **1**, an interstitial water molecule is accommodated lacking in ALR2-**2**. The isotropic B-factor of 31.1 Å² for this water amounts to the 1.3 fold value of the average B-value of the three coordinating atoms (24.3 Å³). This suggests low residual mobility for this water molecule. As generally estimated by Dunitz, fixing a water molecule at a protein binding site correlates with an entropic penalty of up to 8 kJ mol⁻¹ compared to its degrees of freedom in the bulk phase.⁵¹ However, the actual contribution depends on various influences such as the direct interaction partners, the burial, and the residual mobility. This complicates the estimation of the corresponding penalty in each particular case. In addition, the H-bond network formed by the interstitial water molecule, despite its entropically unfavourable contribution, could possibly contribute favourably to the binding enthalpy of **1**, thereby (over)-compensating for the entropic loss. The phenomenon known as enthalpy-entropy compensation is widely discussed for protein-ligand binding processes.⁵²⁻⁵⁵

(3) The nitro-phenyl moiety of **1** and the nitro-furan portion of **2** perform a π - π stacking interaction with the aromatic side chain of Trp 111. The strength of this interaction strongly depends on the electronic properties of the interacting partners: a more intense interaction is achieved, if one aromatic contributor possesses electron-withdrawing substituents and thus, decreases the electrostatic repulsion between the π -systems.⁵⁶ This criterion is better fulfilled in **1**, whereas in **2** the additional oxygen in the furan portion enhances the electron density and probably leads to a less efficient stacking. We assume that this also translates into an enthalpic advantage of **1** over **2**.

(4) Furthermore, different portions of polar and apolar surface areas are buried upon binding (Table 2.1), which have to be desolvated prior to binding. Upon formation of ALR2-**1** additional 98.5 Å² are buried compared to **2**, whereas binding of **2** is related to

a burial of additional 24.5 Å² polar surface area compared to **1**. In contrast to **1**, most of the heteroatoms present in **2** (except the nitro group) are not saturated by polar interaction partners at the binding site. This indicates that ligand binding involves an unfavourable desolvation without finding an appropriate compensation by polar contacts in the binding pocket. Obviously, binding of **2** suffers from an imbalanced hydrogen bond/polar interaction inventory, whereas that of **1** is better balanced. As the additional incorporation of an oxygen or a nitrogen involves additional solvation enthalpy,⁵⁷ a remarkable difference with respect to the enthalpic contribution probably derives from this solvation/desolvation balance. Furthermore, binding of **1** is accompanied by the burial of an additional surface contribution (s. above) compared to **2**. To our present understanding, burial of hydrophobic surfaces is beneficial for binding affinity. This is either related to the “classical hydrophobic effect” (entropically favourable) or to the “non-classical hydrophobic effect” (accompanied by a gain of binding enthalpy).^{56,58,59} Possibly, the latter provides an additional explanation for the stronger enthalpic binding of **1** compared to **2**.

However, these qualitative considerations are difficult to interpret on a quantitative level, as the different contributions will probably mutually compensate to some extent. Nevertheless, our comparison suggests that the incorporation of heteroatoms leading to an imbalanced H-bond inventory is accompanied by a drop of affinity. Once inhibitors are identified by virtual screening, these considerations should be included during subsequent optimization steps.

2.2.8 Enthalpic binding contributions of the nitro group

A further aspect concerns the presumably favourable contribution to binding enthalpy related to the presence of the nitro group. Assuming ligands **1**, **2**, **7**, and **8** adopt a similar binding mode (which appears justified considering their almost identical constitution), it is surprising that titration of **1** or **2** to the enzyme is accompanied by an explicit enthalpic signal (Table 2.1), whereas binding of **7** and **8**, under the same conditions, reveals only a marginal enthalpic signal, virtually undetectable. This observation prompted us to perform ITC measurements with **3** and **4**. Both ligands possess virtually the same Binding Free Energy of about 42 kJ mol⁻¹ (Table 2.1). Nevertheless, they factorize into enthalpic and entropic contributions quite differently.

Whereas **4** binds more enthalpically-driven ($\sim 17 \text{ kJ mol}^{-1}$) compared to **3**, the latter shows a more favourable entropic contribution (18 kJ mol^{-1} , Fig. 2.8).

Comparing the data collected for the pair **1**, **2** with those for **7**, **8** and values observed for **3** with those for **4** it becomes evident that occupation of the specificity pocket with an aromatic moiety equipped with a nitro group in appropriate position is in particular enthalpically driven. Accordingly, the question remains which interactions are performed by the nitro functionality in order to provoke this remarkable enthalpic contribution. The electron-withdrawing character of the nitro group enhances the stacking interaction⁵⁶ to the indole side chain of Trp 111 and thereby contributes to a favourable binding enthalpy. In addition, one nitro oxygen atom in all three presented crystal structures accepts an H-bond from Leu 300 NH via 3.3 to 3.4 Å. Its strength is probably enhanced as they are formed in a buried, water-excluding environment of low local dielectricity. However, are these observations sufficient to explain the deviation in binding enthalpy between the bromo derivative **3** and the nitro derivative **4**? All three nitro-substituted ligands (**1**, **2**, **4**) induce a shift of the aromatic side chain of Tyr 309 enlarging the specificity pocket to accommodate the nitro group. In consequence, the distance between the nitro group oxygen atoms and the two aromatic carbons of Tyr 309 amounts to 3.3 and 3.4 Å for **1**, 3.6 and 3.7 Å for **2**, and 3.4 and 3.6 Å for **4**. Is such an interaction capable to provoke any enthalpic contribution? A pure van der Waals interaction would probably result in slightly longer distances compared to the observed values. To address the question for the optimum interaction distance between a ligand's nitro group and an aromatic moiety on the side of the protein, a Relibase search was carried out.^{60,61} This search for similar nitro-to-phenyl contacts in the range between 2.7 to 4.0 Å retrieves 1282 contacts with a local maximum between 3.5 to 3.6 Å (14 %). Quantum mechanical calculations performed on the interaction of a carbonyl oxygen of formamide and benzene reveal as most favourable interaction geometry an in-plane approach of the carbonyl oxygen to the benzene carbon atoms along the C-H bond vector with a distance of about 3.5 Å.⁶² In agreement with this result, in all three complex structures reported here, the nitro group oxygens are located virtually coplanar to the aromatic moiety of Tyr 309. Obviously, polar interactions between the negatively polarized nitro oxygens and the positively polarized hydrogens, attached to the aromatic carbon atoms, are experienced which can be assigned to "non-classical hydrogen bonds". Interestingly, those non-classical hydrogen bonds formed within protein residues have been recently identified to contribute to the stability of cofactor-

binding Rossman folds. Here, distances in the range of 3.2 to 3.7 Å have been detected between the corresponding H-bonding partners, a C^α atom and a carbonyl oxygen atom of a GXXG/A motif.⁶³ This distance range is in agreement with our data observed between the nitro group of the ligand and the side chain of Tyr 309. A further study investigating the geometric properties of non-classical hydrogen bonds within protein-ligand complexes found a mean hydrogen-oxygen distance of 2.51 Å for CH[⋯]O contacts between a protein side chain carbon and an oxygen atom of a ligand.⁶⁴ Due to lack of experimental data, the extent of this polar contribution to the binding enthalpy is difficult to interpret quantitatively. In inert solvents, the contacts between polarized CH bonds and water molecules or accepting π-systems have been assigned to an enthalpic contribution of about 6-9 kJ mol⁻¹.⁶⁵ Possibly, also in the present case such polar contacts between the aromatic C-H bonds and the nitro group provide a significant contribution to binding enthalpy.

2.3 Summary and Conclusions

To identify novel leads for ALR2, we performed a virtual screening campaign in a previous study. In the present contribution, we report on the structural and thermodynamic characterization of the two most potent hits found by this screening.

Compared to the binding modes predicted previously by molecular docking some important deviations are detected. For both inhibitors, **1** and **2**, the orientation of their oxadiazole and nitro-aromatic moieties are flipped by about 180° compared to the docking mode. This places the terminal nitro group in a different environment. Furthermore, ligand binding of **1** is accompanied by incorporation of an interstitial water molecule next to the carboxylic head group binding to the catalytic center. This water was not considered in the docking attempts. Up to now only one other complex has been observed showing such a water molecule in the protein-ligand interface of a carboxylate-type ALR2 inhibitor. Also, the reversed orientation of the nitrophenyl group induces structural rearrangements not considered in docking. As they could be observed in three complexes (**1**, **2** and **4**) they appear of major importance. A slight reorientation of a peptide NH group, seen in other ALR2 complexes, ruptures a hydrogen bond to the neighbouring Tyr 309 OH. Instead, the NH involves in an H-bond to the nitro group, which, additionally, engages in polar, non-classical hydrogen bond contacts to the adjacent phenyl moiety of the tyrosine.

A crude estimate suggests that the presence of this nitro group corresponds to an affinity increase of about one order of magnitude. Thermodynamic analysis helps to elucidate the driving forces for binding and to correlate the latter with structural differences across the similarly constituted leads. The presence of polar heteroatoms incorporated within the initial leads which remain unsaturated by missing polar contacts in the complex is accompanied by an unfavourable desolvation enthalpy, and the imbalanced hydrogen bond inventory results in a less favourable binding enthalpy. These heteroatoms are present in the ligands without purpose for complex formation, simply because the initial virtual screening suggested them as hits from the list of commercially available compounds. In a subsequent lead optimization they should be replaced.

Furthermore, our thermodynamic data, collected for both lead compounds and two inhibitors of the IDD series, suggest a remarkable gain of binding enthalpy due to the presence of the nitro group. Usually, nitro groups are reluctantly considered in drug-like molecules mainly because of their putative mutagenic character.⁶⁶ However, in the present case it achieves an additional gain of binding enthalpy which can probably be exploited with respect to selectivity enhancement.

Comparing the thermodynamic data of **1** and **2** suggests stronger enthalpic binding for **1**, even though this ligand exhibits more rotatable bonds. Interestingly enough, **1** picks up a water molecule upon complexation in contrast to **2**. This observation likely results in an enthalpic advantage as immobilization of a water at the binding interface should be entropically disfavoured.

Structural and thermodynamic characterization of virtual screening hits at an early stage of lead optimization avoids false conclusions based on incorrectly predicted binding modes and helps to extract the features most relevant for enthalpic binding. These should be exploited in the subsequent optimization, as an increase in size, hydrophobic surface complementarity and rigidity of the lead structures will implicitly increase their entropic contribution to binding.

2.4 Materials and Methods

Compounds **1** (BTB02809), **2** (JFD00882), **7** (DP001247), and **8** (DP001236) were purchased from Chempur, Karlsruhe, Germany. IDD 388 (**3**) and IDD 393 (**4**) were kindly provided by Dr. A. Podjarny, IGBMC, Illkirch, France.

Cloning, expression, purification and crystallisation of Aldose Reductase have already been described elsewhere.^{23,25,30} Prior to crystallisation, ALR2 solutions were concentrated to 20 mg/ml in 50 mM di-ammonium hydrogen citrate at pH 5 and mixed with a solution of the cofactor in oxidized state to achieve a molar ratio of ALR2:NADP⁺ of 1:3. After an equilibration period of one week, a microseeding was performed. Crystals were grown at 293 K using the hanging drop vapor diffusion method. For soaking a saturated inhibitor solution in 50 mM di-ammonium hydrogen citrate, pH 5 containing 25 % (m/V) PEG 6000 was prepared. Crystals were obtained one day after microseeding.

Data Collection. Data were collected at 100 K using a cryoprotectant solution of 40 % (m/V) PEG 6000 in 50 mM di-ammonium hydrogen citrate at pH 5. The data sets were collected on a RIGAKU copper rotating anode (Molecular Structure Cooperation) at 50 kV, 90 mA using a R-AXIS IV++ image plate system. For each frame the exposure time and oscillation range were set to 5 min and 0.5°, respectively. Data processing and scaling were performed using the HKL2000 package.⁶⁷

Structure Determination and Refinement. The coordinates of human ALR2 (PDB code 1el3)⁴³ were used for initial rigid-body refinement of the protein atoms followed by repeated cycles of conjugate gradient energy minimization, simulated annealing and B-factor refinement using the CNS program package.⁶⁸ Refinement at later stages was performed with the program SHELXL.⁶⁹ Here, at least 20 cycles of conjugate gradient minimization were performed with default restraints on bonding geometry and B-values. Five percent of all data were used for R_{free} calculation. Amino acid side-chains were fitted into sigmaA-weighted $2F_o - F_c$ and $F_o - F_c$ electron density maps using O.⁷⁰ After the first refinement cycle, water molecules and subsequently cofactor and ligand were located in the electron density and added to the model. Restraints were applied to bond lengths and angles, chiral volume, planarity of aromatic rings and van der Waals contacts. Multiple side-chain conformations were built in case an appropriate electron density was observed and maintained during the refinement, and if the minor populated side-chain showed at least 10% occupancy. During the last refinement cycles, riding H atoms were introduced without using additional parameters. The final models were validated using PROCHECK.⁷¹ Data collection, unit cell parameters and refinement statistics are given in Table 2.2. Figures were prepared using Isis Draw (MDL, San Leandro, USA) and Pymol.⁷² Calculations of the solvent-accessible surface buried upon

complex formation was calculated with the web-accessible tool GETAREA 1.1⁷³ using an 1.4 Å probe and radii published by Shrake and Rupley.⁷⁴

complex	ALR2-1	ALR2-2	ALR2- IDD 388	ALR2- IDD 393
pdb entry	2IKG	2IKH	2IKI	2IKJ
Data collection and Processing				
No. of crystals used	1	1	1	1
Wavelength [Å]	1.5418	1.5418	1.5418	1.5418
Space group	P 2 ₁	P 2 ₁	P 2 ₁	P 2 ₁
Unit cell parameters				
a, b, c [Å]	49.3, 66.7, 47.2	49.4, 66.9, 47.3	49.4, 66.8, 47.3	49.4, 66.8, 47.4
β [°]	92.6	92.1	92.4	92.2
Matthews coefficient [Å ³ /Da]	2.15	2.16	2.16	2.16
Solvent content [%]	42.7	43.1	43.0	43.1
Diffraction data				
Resolution range [Å]	50 – 1.43 (1.45-1.43)	50 – 1.55 (1.58 – 1.55)	25 – 1.47 (1.5 – 1.47)	30 – 1.55 (1.58 – 1.55)
Unique reflections	51 269 (2 180)	41 286 (1 789)	46 959 (1 154)	40 334 (1 640)
R(I) _{sym} [%]	4.5 (46.1)	3.7 (12.4)	3.4 (13.0)	5.3 (12.2)
Completeness [%]	90.8 (77.8)	92.5 (80.7)	89.8 (44.0)	90.1 (74.5)
Redundancy	4.4 (4.0)	3.1 (3.0)	3.0 (1.8)	2.2 (1.9)
I/σ(I)	31.2 (2.5)	29.1 (9.0)	31.8 (6.0)	21.7 (7.7)
Refinement				
Resolution range [Å]	25 – 1.43	50 – 1.55	25 – 1.47	30 – 1.55
Reflections used in refinement (work/free)	48 014 / 2 546	38 875 / 2 035	44 334 / 2 324	37 995 / 1 998
Final R values for all reflections (work/free) [%]	13.3 / 20.4	16.8 / 20.9	14.8 / 18.3	16.2 / 21.3

Final R values for reflections with $F > 4 \sigma$ (work/free) [%]	12.7 / 19.4	16.5 / 20.4	14.4 / 17.7	15.8 / 20.7
Protein residues	316	315	311	315
Coenzyme	1	1	1	1
Inhibitor	1	1	1	1
Water molecules	323	268	406	347
RMSDs				
Bonds [Å]	0.01	0.009	0.011	0.01
Angles [°]	2.3	2.3	2.5	2.4
Ramachandran plot				
Residues in most favored regions [%]	91.7	88.8	91.9	92.1
Residues in additional allowed regions [%]	8.3	10.8	8.1	7.9
Residues in generously allowed regions [%]	-	0.4	-	-
Mean B factor [Å²]				
Protein	22.9	16.2	13.3	15.8
NADP ⁺	15.9	10.3	9.8	10.1
Inhibitor	29.9	27.9	9.6	12.1
Water molecules	31.5	22.7	23.1	24.8

Table 2.2 Data collection and Refinement statistics.

Enzymatic inhibition assay. The in-vitro inhibitory activity of the candidate molecules was determined by recording the decrease of the NADPH absorbance upon enzymatic reduction of xylitol. The absorbance at 340 nm was monitored at 25 °C with a BMG plate reader. The assay was performed using a polypropylene plate with 250 μ L reaction mixture of 100 mM sodium phosphate buffer (100 mM, pH 6.2) which contained 0.14 mM NADPH, 26.5 mM D-xylitol as substrate, and 0.28 μ M human ALR2. Test compounds were assayed for inhibition at concentrations ranging from 0.8 mM to 20 nM. The program GraFit⁷⁵ (Version 4.0) was used for fitting the IC₅₀ values. All kinetic measurements were carried out at least in duplicate. Given inhibition data and standard deviations have been obtained from data fitting and subsequent averaging.

Isothermal Titration Calorimetry. Calorimetric measurements⁷⁶ were carried out using a MCS ITC-instrument from MicroCal Inc. (Northampton, USA). In each experiment, the ligand was titrated to the protein solution present in the 1.4 mL sample cell. The reference cell contained 0.1 mM sodium azide dissolved in demineralised water. All measurements were carried out at 298 K. The protein was dissolved in 10 mM HEPES buffer at pH 8 to a concentration of 18.9 μ M for the titration of **3** and **4**, and 37.8 μ M for the measurement of **1** and **2**. Protein concentrations were determined by UV spectroscopy (280 nm) using the specific absorption calculated by the ProtParam tool (www.expasy.ch). The ligand solution contained 252 μ M of the corresponding inhibitor dissolved in the same buffer as the protein. The protein was saturated with an excess of NADP⁺ which was present at the same concentration in the ligand solution to avoid heat effects caused by diluting the cofactor. Solutions were degassed at 293 K under vacuum for 10 min. Upon experimental setup, the protein solution present in the sample cell was stirred at 400 rpm. After a stable baseline had been achieved the titration was initiated. The injection sequence started with an initial aliquot of 1.5 μ L (to preserve diffusion effects arising from the experimental setup, data not used for fitting) followed by injections of 10 μ L in time intervals of 300 s until complete saturation was obtained. Heat changes caused by each inhibitor injection were obtained from the integral of the calorimetric signal. Data were analysed using the ORIGIN software (MicroCal Inc.) for fitting the data points to a single-site binding model in agreement with the results from X-ray crystallography.

Experimental heats of the protein-inhibitor titration were corrected for heats of dilution by subtracting the average heat of the last three measurements after saturation of the

protein binding sites has occurred. All measurements have been carried out at least in duplicate. Given energy values, binding constants and standard deviations were derived from data fitting and subsequent averaging of the corresponding measurements. Standard Gibbs free energy values were calculated using the equation $\Delta G^0 = -RT \ln K_b$ (where $R=8.3144 \text{ J mol}^{-1}\text{K}^{-1}$, K_b binding constant).

Coordinates and structure factor amplitudes of the crystal structures have been deposited at the Protein DataBank. The corresponding PDB codes are given in Table 2.2.

2.5 References

1. Miyamoto, S. (2002). Recent advances in aldose reductase inhibitors: potential agents for the treatment of diabetic complications. *Expert. Opin. Ther. Patents* **12**, 621-631.
2. Wild, S., Roglic, G., Green, A., Sicree, R. & King, H. (2004). Global Prevalence of Diabetes. *Diabetes Care* **27**, 1047-1053.
3. Skyler, J.S. (2004). Diabetes Mellitus: Pathogenesis and Treatment Strategies. *J. Med. Chem.* **47**, 4113-4117.
4. Stumvoll, M. Goldstein, B.J. & van Haeften, T.W. (2005). Type 2 diabetes: principles of pathogenesis and therapy. *Lancet* **365**, 1333-1346.
5. Ross, S. A., Gulve, E. A. & Wang, M. (2004). Chemistry and Biochemistry of Type 2 Diabetes. *Chem. Rev.* **104**, 1255-1282.
6. Pfeifer, M. A. & Schumer, M. P. (1995). Clinical Trials of diabetic neuropathy: past, present and future. *Diabetes* **44**, 1355-1361.
7. Suzen S. & Buyukbingol E. (2003). Recent studies of aldose reductase enzyme inhibition for diabetic complications. *Curr. Med. Chem.* **10**, 1329-1352.
8. Yabe-Nishimura, C. (1998). Aldose reductase in glucose toxicity: a potential target for the prevention of diabetic complications. *Pharmacol. Rev.* **50**, 21-33.
9. Brownlee, M. (2001). Biochemistry and molecular cell biology of diabetic complications. *Nature* **414**, 813-820.
10. Evans, J. L., Goldfine, I. D., Maddux, B. A. & Grodsky, G.M. (2002). Oxidative stress and stress-activated signalling pathways: a unifying hypothesis of type 2 diabetes. *Endocrine Rev.* **23**, 599-622.
11. Price, S. A., Agthong, S., Middlemas, A.B. & Tomlinson, D.R. (2004). Mitogen-activated protein kinase p38 mediates reduced nerve conduction

- velocity in experimental diabetic neuropathy. – Interactions with aldose reductase. *Diabetes* **53**, 1851-1856.
12. Suzuki, L. A., Poot, M., Gerrity, R.G. & Bornfeldt, K.E. (2001). Diabetes accelerates smooth muscle accumulation in lesions of atherosclerosis. Lack of direct growth-promoting effects of high glucose levels. *Diabetes* **50**, 851-860.
 13. Nakamura, J., Kasuya, Y., Hamada, Y., Nakashima, E., Naruse, K., Yasuda, Y., Kato, K. & Hotta, N. (2001). Glucose-induced hyperproliferation of cultured rat aortic smooth muscle cells through polyol pathway hyperactivity. *Diabetologica* **44**, 480-487.
 14. Oyama, T., Miyasita, Y., Watanabe, H. & Shirai, K. (2006). The role of polyol pathway in high glucose-induced endothelial cell damages. *Diabetes Res. Clin. Pract.* **73**, 227-234
 15. Dan, Q., Wong, R.L.C., Yin, S., Chung, S.K., Chung, S.S.M. & Lam, K.S.L. (2004). Interaction between the polyol pathway and non-enzymatic glycation on mesangial cell gene expression. *Nephron Exp. Nephrol.* **98**, e89-e99.
 16. Jerums, G., Panagiotopoulos, S., Forbes, J., Osicka, T. & Cooper, M. (2003). Evolving concepts in advanced glycation, diabetic nephropathy, and diabetic vascular disease. *Arch Biochem Biophys.* **419**, 55-62.
 17. Greene, D. A., Arezzo, J. C. & Brown, M. B. (1999). Effect of aldose reductase inhibition on nerve conduction and morphometry in diabetic neuropathy. Zenarestat Study Group. *Neurology* **53**, 580-591.
 18. Constantino, L., Rastelli, G., Vianello, P., Cignarella, G. & Barlocco, D. (1999). Diabetes Complications and their potential prevention: Aldose Reductase Inhibition and other Approaches. *Med. Res. Rev.* **19**, 3-23.
 19. Yagihashi, S., Yamagishi, S. I., Wada, R., Baba, M., Hohman, T. C., Yabe-Nishimura, C. & Kokai, Y. (2001). Neuropathy in diabetic mice overexpressing human aldose reductase and effects of aldose reductase inhibitor. *Brain* **124**, 2448-2458.
 20. Mylari, B. L., Armento, S. J., Beebe, D. A., Conn, E. L., Coutcher, J. B., Dina, M. S., O'Gorman, M. T., Linhares, M. C., Martin, W. H., Oates, P. J., Tess, D. A., Withbroe, G. J. & Zembrowski, W. J. (2003). A highly selective, non-hydantoin, non-carboxylic acid inhibitor of aldose reductase with potent oral activity in diabetic rat models: 6-(5-chloro-3-methylbenzofuran-2-sulfonyl)-2-H-pyridazin-3-one. *J. Med. Chem.* **46**, 2283-2286.

21. Baba, M., Kimura, K., Suda, T. & Yagihashi, S. (2006). Three-year inhibition of aldose reductase on development of symptomatic neuropathy in diabetic patients. *J. Peripher. Nerv. Syst.* **11**, 176-178.
22. Constantino, L., Rastelli, G., Vianello, P., Cignarella, G. & Barlocco, D. (1999). Diabetes Complications and their potential prevention: Aldose Reductase Inhibition and other Approaches. *Med. Res. Rev.* **19**, 3-23.
23. El-Kabbani, O., Darmanin, C., Schneider, T. R., Hazemann, I., Ruiz, F., Oka, M., Joachimiak, A., Schulze-Briese, C., Tomizaki, T., Mitschler, A. & Podjarny, A. (2004). Ultrahigh resolution drug design. II. Atomic resolution structures of human aldose reductase holoenzyme complexed with Fidarestat and Minalrestat: implications for the binding of cyclic imide inhibitors. *Proteins* **55**, 805-813.
24. Van Zandt, M.C., Jones, M.L., Gunn, D.E., Geraci, L.S., Jones, J.H., Sawicki, D.R., Sredy, J., Jacot, J.L., DiCioccio, A.T., Petrova, T., Mitschler, A. & Podjarny A.D. (2005). Discovery of 3-[(4,5,7-Trifluorobenzothiazol-2-yl)methyl]indole-N-acetic acid (Lidorestat) and congeners as highly potent and selective inhibitors of aldose reductase for treatment of chronic diabetic complications. *J.Med.Chem.* **48**, 3141-3152.
25. Howard, E. I., Sanishvili, R., Cachau, R. E., Mitschler, A., Chevrier, B., Barth, P., Lamour, V., Van Zandt, M., Sibley, E., Bon, C., Moras, D., Schneider, T. R., Joachimiak, A. & Podjarny, A. (2004). Ultrahigh resolution drug design I: details of interactions in human aldose reductase-inhibitor complex at 0.66 Å. *Proteins* **55**, 792-804.
26. El-Kabbani, O., Wilson, D.K., Petrash, J.M. & Quioco, F.A. (1998). Structural Features of the aldose reductase and aldehyde reductase inhibitor binding sites. *Mol. Vis.* **4**, 19-25.
27. Sato, S. & Kador, P.F. (1990). Inhibition of aldehyde reductase by aldose reductase inhibitors. *Biochem. Pharmacol.* **40**, 1033-1042.
28. Van Zandt, M.C., Sibley, E.O., McCann, E.E., Combs, K.J., Flam, B., Sawicki, D.R., Sabetta, A., Carrington, A., Sredy, J., Howard, E., Mitschler, A. & Podjarny, A.D. (2004). Design and synthesis of highly potent and selective (2-arylcabamoyl-phenoxy)-acetic acid inhibitors of aldose reductase for treatment of chronic diabetic complications. *Bioorg. Med. Chem.* **12**, 5661-5675.

29. Davydov, V. V., Dobaeva, N. M. & Bozhkov, A. I. (2004). Possible role of alteration of aldehyde's scavenger enzymes during aging. *Exp. Gerontol.* **39**, 11-16.
30. Oka, M., Matsumoto, Y., Sugiyama, S., Tsuruta, N. & Matsushima, M. (2000). A potent aldose reductase inhibitor, (2S,4S)-6-fluoro-2', 5'-dioxospiro[chroman-4,4'-imidazolidine]-2-carboxamide (Fidarestat): its absolute configuration and interactions with the aldose reductase by X-ray crystallography. *J. Med. Chem.* **43**, 2479-2483.
31. Steuber, H., Zentgraf, M., Podjarny, A.D., Heine, A. & Klebe, G. (2006). High resolution crystal structure of aldose reductase complexed with the novel sulfonyl-pyridazinone inhibitor exhibiting an alternative active site anchoring group. *J. Mol. Biol.* **356**, 45-56.
32. Varnai, P., Richards, W. & Lyne, P.D. (1999). Modelling the catalytic reaction in human aldose reductase. *Proteins* **37**, 218-227.
33. Cachau, R., Howard, E., Barth, P., Mitschler, A., Chevrier, B., Lamour, V., Joachimiak, A., Sanishvili, R., Van Zandt, M., Sibley, E., Moras, D. & Podjarny, A.D. (2000). Model of the catalytic mechanism of human aldose reductase based on quantum chemical calculations. *J. Phys. IV France* **10**, 3-13.
34. Iwata, Y., Arisawa, M., Hamada, R., Kita, Y., Mizutani, M.Y., Tomioka, N., Itai, A. & Miyamoto, S. (2001). Discovery of novel aldose reductase inhibitors using a protein-structure-based approach: 3D-database search followed by design and synthesis. *J. Med. Chem.* **44**, 1718-1728.
35. Rastelli, G., Ferrari, A.M., Costantino, L. & Gamberoni, M.C. (2002). Discovery of new inhibitors of aldose reductase from molecular docking and database screening. *Bioorg. Med. Chem.* **10**, 1437-1450.
36. Ferrari, A.M., Wei, B.Q., Costantino, L. & Shoichet, B.W. (2004). Soft docking and multiple receptor conformations in virtual screening. *J. Med. Chem.* **47**, 5076-5084.
37. Krämer, O., Hazemann, I., Podjarny, A.D. & Klebe, G. (2004). Virtual screening for inhibitors of human aldose reductase. *Proteins* **55**, 814-823.
38. Schiffmann, R., Heine, A., Klebe, G. & Klein, C.D. (2005). Metal ions as cofactors for the binding of inhibitors to methionine aminopeptidase: a critical view of the relevance of in vitro metalloenzyme assays. *Angew. Chem. Int. Ed. Engl.* **44**, 3620-3623.

39. Specker, E., Bottcher, J., Lilie, H., Heine, A., Schoop, A., Muller, G., Griebenow, N. & Klebe, G. (2005). An old target revisited: two new privileged skeletons and an unexpected binding mode for HIV-protease inhibitors. *Angew. Chem. Int. Ed. Engl.* **44**, 3140-3144.
40. Shoichet, B.K. (2004). Virtual screening of chemical libraries. *Nature* **432**, 862-865.
41. Lundqvist, T. (2005). The devil is still in the details – driving early drug discovery forward with biophysical experimental methods. *Curr. Opin. Drug Discov. Devel.* **8**, 513-519.
42. Ruiz, F., Hazemann, I., Mitschler, A., Joachimiak, A., Schneider, T., Karplus, M. & Podjarny, A. (2004). The crystallographic structure of the aldose reductase-IDD 552 complex shows direct proton donation from tyrosine 48. *Acta Crystallogr. D* **60**, 1347-1354.
43. Calderone, V., Chevrier, B., Van Zandt, M., Lamour, V., Howard, E., Poterszman, A. et al. (2000). The structure of human aldose reductase bound to the inhibitor IDD 384. *Acta Cryst D* **56**, 536-540.
44. Despite temperature factors of different data sets are not necessarily comparable, the Wilson B-factor for the ALR2-1 and ALR2-2 data sets are 16.1 and 14.3 Å², respectively. This suggests that B-factors derived from model refinement are to some extent comparable.
45. Goodford, P.J. (1985). A computational procedure for determining energetically favourable binding sites on biologically important macromolecules. *J. Med. Chem.* **28**, 849-857.
46. Muzet, N., Guillot, B., Jelsch, C., Howard, E. & Lecomte, C. (2003). Electrostatic complementarity in an aldose reductase complex from ultra-high-resolution crystallography and first-principles calculations. *Proc. Natl. Acad. Sci. USA* **100**, 8742-8747.
47. Lecomte, C., Guillot, B., Muzet, N., Pichon-Pesme, V. & Jelsch, C. (2004). Ultra-high-resolution X-ray structure of proteins. *Cell. Mol. Life Sci.* **61**, 774-782.
48. Auffinger, P., Hays, F.A., Westhof, E. & Ho, P.S. (2004). Halogen bonds in biological molecules. *Proc. Natl. Acad. Sci.* **101**, 16789-16794.

49. Baker, B.M. & Murphy, K.P. (1996). Evaluation of linked protonation effects in protein binding reactions using isothermal titration calorimetry. *Biophys. J.* **71**, 2049-2055.
50. D'Aquino, J.A., Freire, E. & Amzel, L.M. (2000). Binding of small organic molecules to macromolecular targets: evaluation of conformational entropy changes. *Proteins Suppl.* **4**, 93-107.
51. Dunitz, J.D. (1994). The entropic cost of bound water in crystals and biomolecules. *Science* **264**, 670.
52. Yin, F., Cao, R., Goddard, A., Zhang, Y. & Oldfield, E. (2006). Enthalpy versus entropy-driven binding of bisphosphonates to farnesyl diphosphate synthase. *JACS* **128**, 3524-3525.
53. Teague, S.J. (2003). Implications of protein flexibility for drug discovery. *Nat. Rev. Drug Discov.* **2**, 527-540.
54. Homans, S.W. (2005). Probing the binding entropy of ligand-protein interactions by NMR. *ChemBioChem* **6**, 1-8.
55. Ford, D.M. (2005). Enthalpy-entropy compensation is not a general feature of weak association. *JACS* **127**, 16167-16170.
56. Meyer, E.A., Castellano, R.K. & Diederich, F. (2003). Interactions with aromatic rings in chemical and biological recognition. *Angew. Chem. Int. Ed.* **42**, 1210-1250.
57. Cabani, S., Gianni, P., Mollica, V. & Lepori, L. (1981). Group contribution to the thermodynamic properties of non-ionic solutes in dilute aqueous solution. *J. Sol. Chem.* **10**, 563- 595.
58. Barratt, E., Bingham, R.J., Warner, D.J., Laughton, C.A., Phillips, S.E.V. & Homans, S.W. (2005). Van der Waals interactions dominate ligand-protein association in a protein binding site occluded from solvent water. *JACS* **127**, 11827-11834.
59. Chandler, D. (2005). Interfaces and the driving force of hydrophobic assembly. *Nature* **437**, 640-647.
60. Hendlich, M., Bergner, A., Gunther, J. & Klebe, G. (2003). Relibase: Design and development of a database for comprehensive analysis of protein-ligand interactions. *J. Mol. Biol.* **326**, 99-110.
61. The Relibase search was carried out using Relibase + 2.1.1. The distance distribution of contacts between the carbon atom of an aromatic phenyl moiety

- as protein component and the oxygen atom of a nitro group at ligand counterpart was analysed in the range between 2.7 and 4.0 Å.
62. Thomas, K.A., Smith, G.M., Thomas, T.B. & Feldmann, R.J. (1982). Electronic distribution within protein phenylalanine aromatic rings are reflected by the three-dimensional oxygen atom environments. *Proc. Natl. Acad. Sci.* **79**, 4843-4847.
 63. Kleiger, G. & Eisenberg, D. (2002). GXXXG and GXXXA motifs stabilize FAD and NAD(P)-binding Rossmann folds through C^α-H...O hydrogen bonds and van der Waals interactions. *J. Mol. Biol.* **323**, 69-76.
 64. Sarkhel, S. & Desiraju, G.R. (2004). N-H...O, O-H...O, and C-H...O hydrogen bonds in protein-ligand complexes: strong and weak interactions in molecular recognition. *Proteins* **54**, 247-259.
 65. Williams, M.A. & Ladbury, J.E. (2003). Hydrogen bonds in Protein-ligand complexes. In *Protein-Ligand interactions: From Molecular Recognition to Drug Design*. (Boehm, H.-J. & Schneider, G., eds), p. 137-161, Wiley-VCH, Weinheim.
 66. Llorens, O. & Perez, J.J. (2001). Toward the design of chemical libraries for mass screening biased against mutagenic compounds. *J. Med. Chem.* **44**, 2793-2804.
 67. Otwinowski, Z. & Minor, W. (1997). Processing of X-ray Diffraction Data Collected in Oscillation Mode. *Methods Enzymol.* **276**, 307-326.
 68. Brunger, A. T., Adams, P. D., Clore, G. M., DeLano, W. L., Gros, P., Grosse-Kunstleve, R. W., Jiang, J. S., Kuszewski, J., Nilges, M., Pannu, N. S., Read, R. J., Rice, L. M., Simonson, T. & Warren, G. L. (1998). Crystallography & NMR system: A new software suite for macromolecular structure determination. *Acta Crystallogr. D* **54**, 905-921.
 69. Sheldrick, G. M. & Schneider, T. (1997). SHELXL: high-resolution refinement. *Methods Enzymol.* **277**, 319-343.
 70. Jones, T. A., Zou, J. Y., Cowan, S. W. & Kjeldgaard. (1991). Improved methods for building protein models in electron density maps and the location of errors in these models. *Acta Crystallogr. A* **47**, 110-119.
 71. Laskowski, R., MacArthur, M., Moss, D. & Thornton, J. (1993). PROCHECK: a program to check the stereochemical quality of protein structures. *J. Appl. Crystallogr.* **26**, 283-291.

72. DeLano, W. L. (2002). The PyMOL Molecular Graphics System.
<http://www.pymol.org>
73. Fraczekiewicz, R. & Braun, W. (1998). Exact and efficient analytical calculation of the accessible surface areas and their gradients for macromolecules. *J. Comp. Chem.* **19**, 319-333.
74. Shrake, A. & Rupley, J. A. (1973). Environment and exposure to solvent of protein atoms. Lysozyme and insulin. *J. Mol. Biol.* **79**, 351-371.
75. Leatherbarrow, R.J. (1998). GraFit Version 4.0, Erithacus Software, Ltd., Staines, U.K.
76. Holdgate, G. A. & Ward, W.H.J. (2005). Measurements of binding thermodynamics in drug discovery. *Drug Discov. Today* **10**, 1543-1550.

3. High Resolution Crystal Structure of Aldose Reductase Complexed with the Novel Sulfonyl-Pyridazinone Inhibitor Exhibiting an Alternative Active Site Anchoring Group

3.1 Introduction

Aldose reductase (ALR2; EC 1.1.1.21) is a 36 kDa TIM-barrel shaped aldo-keto reductase catalyzing the reaction of a broad range of carbonyl-containing substrates to their corresponding alcohols using NADPH as cofactor for reduction.¹ Even though the physiological function of ALR2 is not completely understood, the enzyme might play a role as detoxifier of various aldehydes produced under conditions of cellular oxidative stress. Representatives of such substrates are, e.g. 4-hydroxy-2-nonenal, methylglyoxal as well as their glutathionylated derivatives.^{1,2}

However, under diabetic conditions accompanied by high cellular levels of glucose, ALR2 is responsible for an enhanced reduction of glucose to sorbitol. In particular, ALR2 is the first and rate-limiting enzyme of the polyol pathway converting glucose to sorbitol followed by the subsequent NADH-dependent oxidation of sorbitol to fructose by sorbitol dehydrogenase. As a consequence, enhanced flux of glucose through the polyol pathway leads to various imbalances with respect to reduction equivalents responsible for oxidative and oxidative-nitrosative stress, osmotic stress, cytokine signalling, regulation of apoptosis as well as activation of kinase cascades.³⁻⁵ Altogether, the pathophysiological activity of aldose reductase plays a key role in the development of diabetic complications such as angiopathy, nephropathy, diabetic retinopathy, and cataract formation.^{6,7} In-vitro and in-vivo studies suggest a clear benefit of the administration of aldose reductase inhibitors (ARIs) in various model systems exposed to high glucose levels as well as in the treatment of diabetic patients.^{5,8-14} Encouraged by these observations extensive efforts have been made within the last two decades to develop appropriate drug candidates. A broad variety of agents inhibiting ALR2 have already been synthesized or extracted from natural sources.⁹ However, in clinical trials most of these inhibitors failed for various

reasons:^{7,10} The first clinically investigated candidate sorbinil, a hydantoin-type inhibitor (**1**, Figure 3.1), led to the occurrence of hypersensitivity reactions independent of the ALR2 inhibition. The carboxylic acid-type inhibitors show a remarkable in-vitro affinity but lack sufficient in-vivo efficiency due to poor bioavailability. Representatives of carboxylic acid inhibitors are depicted in Figure 3.1 (**2**, IDD 594; **3**, tolrestat). It seems to be generally accepted in literature that the decreased in-vivo potency is a consequence of the low pK_a of the carboxylic acid inhibitors (between 3 – 4) which will be almost completely ionized at physiological conditions. Thus, reduced penetration through biological membranes can be expected.^{7,10} In contrast, hydantoin ARIs exhibit a pK_a in the range of approximately 8, accordingly much better potency to cross biological barriers is given due to their essentially uncharged state in aqueous solution. The most promising members of ARIs, the hydantoin fidarestat, and the cyclic imide minalrestat (Figure 3.1, **4** and **5**, respectively) are currently in pre-clinical or clinical trials.^{11-13,15,17,18}

In 2003, Mylari *et al.*¹² reported on the development of a novel non-carboxylic acid, non-hydantoin inhibitor with excellent properties: the compound shows a sub-nanomolar IC_{50} value (840 pM), a more than 1000-fold selectivity advantage for aldose reductase compared to aldehyde reductase, an almost perfect oral bioavailability as well as a pronounced in-vivo efficiency. The ligand consists of a benzofurane moiety, a pyridazinone scaffold, and a sulfonyl group linking these components together (**6**, Figure 3.1). The pK_a of the titratable pyridazinone and the logP of the inhibitor were determined to 6.9 and 3.05, respectively, one prerequisite for good tissue penetration behaviour

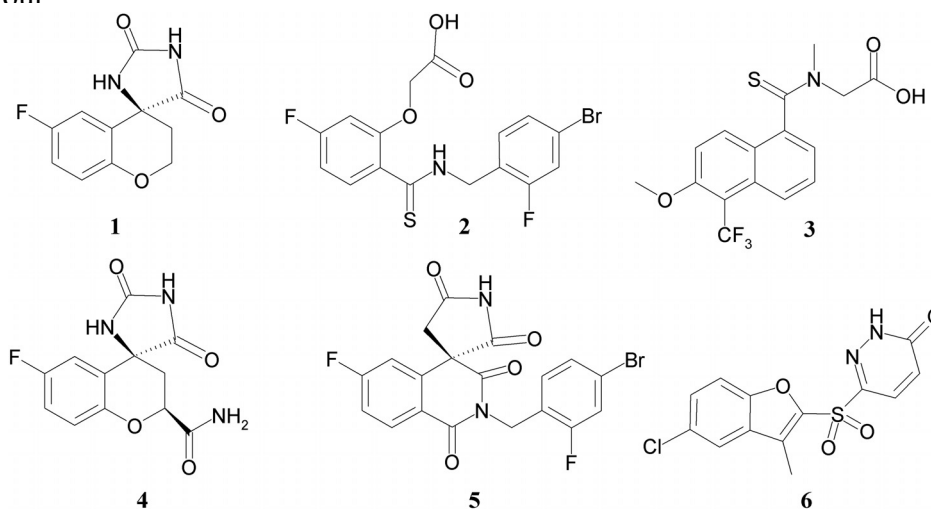


Figure 3.1. Chemical formulae of cyclic imide-type (sorbinil **1**, Fidarestat **4**, Minalrestat **5**), carboxylic-acid-type (IDD 594 **2**, tolrestat **3**) and the novel pyridazinone-type (**6**) inhibitors.

Here, we describe two crystal structures of the ternary complex of ALR2 in complex with the pyridazinone **6** refined to 1.43 and 0.95 Å. As determined previously, the overall topology of the enzyme comprises an (β/α)₈-TIM-barrel with the active site located at the C-terminal region of the protein facilitating binding of charged ligands (in the present case NADP⁺ and inhibitors) possibly stabilized via helix-induced dipole moments.^{15,16} The deeply buried binding pocket is composed by residues presumably involved in catalysis (Tyr 48, Lys 77, His 110), the nicotinamide moiety of NADP⁺ and Trp 111 likely donating an H-bond via its indole portion to most of the described ligand head groups, and hydrophobic contacts formed by the side-chains Trp 20, Val 47, Trp 79, and Trp 219. The part of the binding pocket comprising the residues involved in catalysis is usually addressed by hydrophilic, negatively charged building blocks such as carboxylic acids or deprotonated hydantoins. Inhibitors decorated at the opposing terminal end by appropriate hydrophobic groups showed partially the potential to open distinct pockets referred to as “specificity pockets”. These adaptable pockets are formed by Leu 300, Trp 111, and Phe 122. The present study elucidates the binding mode between aldose reductase and the novel pyridazinone inhibitor **6**. Furthermore, we determined the standard Gibbs free energy of binding by isothermal titration calorimetry (ITC) and compared the binding properties of **6** with those of the known ARIs **1 - 3**.

3.2 Results and Discussion

3.2.1 X-Ray crystallography

The final model (1.43 Å resolution) of a ternary complex of human ALR2 (316 residues) with bound coenzyme NADP⁺ and pyridazinone inhibitor **6** shows a (β/α)₈ barrel fold frequently adopted by enzymes.¹⁵⁻¹⁸ During refinement, split conformations have been assigned to seven amino acids (Glu 60, Gln 93, Glu 120, Glu 193, Glu 267, Ser 282, Arg 293). The electron density maps clearly show the location of the cofactor and the inhibitor. The $F_o - F_c$ density (3σ) of the inhibitor is shown in Figure 3.2. Even though clear-cut electron density was observed for the inhibitor, after assignment of the inhibitor atoms with full population to the model, negative electron density ($-0.28 e/\text{Å}^3$ corresponding to 4.2σ) resulted from refinement in close proximity to the chlorine atom of the inhibitor. We therefore decided to refine the occupancy of the ligand resulting in 74 % presence. The inhibitor occupies the active site of the enzyme with its pyridazinone moiety present in the partly polar anion binding pocket composed by the

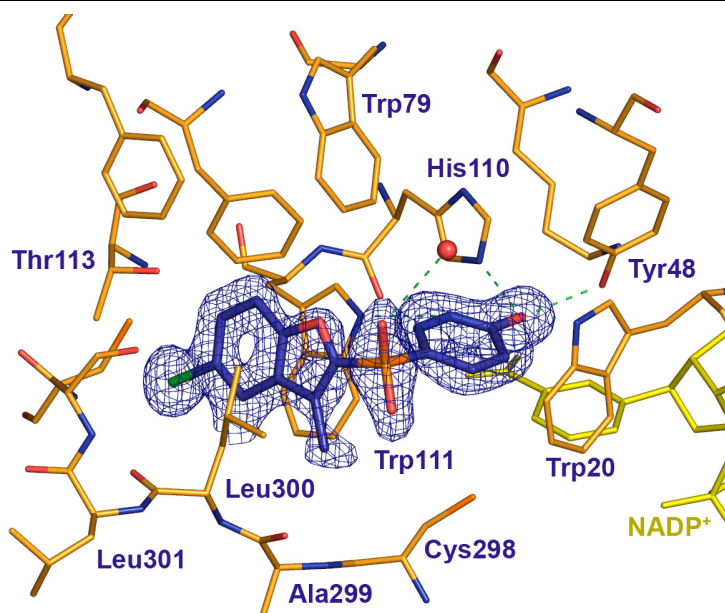
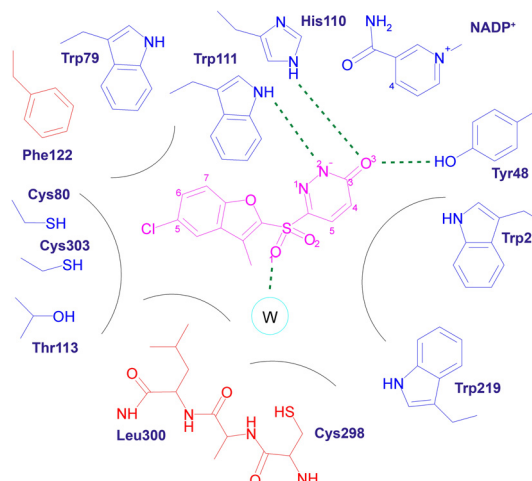


Figure 3.2. Refinement model of the pyridazinone inhibitor **6** bound to ALR2 at 1.43 Å resolution. Residues of the binding pocket are shown in orange, the cofactor is colored in yellow. The inhibitor is depicted in dark blue with the corresponding F_o-F_c density contoured at a level of 3σ . The coordinating water is shown as red sphere. The difference electron density clearly indicates how the inhibitor is accommodated in the active site of ALR2 with its benzofurane moiety occupying the specificity pocket between Leu 300 and Trp 111 and the pyridazinone anchor hosting the catalytic site.

catalytic residues Tyr 48, Lys 77 and His 110. The benzofurane system opens the hydrophobic “specificity” pocket bound by Trp 111, Phe122, and Leu 300. Ligands occupying this specificity pocket of ALR2 have been shown to induce unfavourable rearrangements in aldehyde reductase (ALR1, EC 1.1.1.2) including, e.g. the rupture of the salt bridge between Arg 312 and Asp 313. This might explain to some extent the high selectivity (> 1000 fold)¹² of the studied ligand towards ALR2 in comparison to ALR1. Figure 3.3 shows a schematic representation of the binding pocket and the interaction mode between the ligand and the enzyme-cofactor complex.

Figure 3.3. Schematic representation of the binding mode of **6** to ALR2. The inhibitor is shown in magenta, essential parts of amino acids and cofactor forming the binding pocket are shown. Residues mainly involved in adaptation processes and therefore have to be regarded as flexible are colored in red, the remaining side-chains are represented in blue. Expected H-bond interactions are shown as green dotted lines. Observed distances are given in Table 3.2.



The aromatic pyridazinone moiety binds in a face-to-face-orientation with respect to the nicotinamide moiety of the cofactor. Even though the density corresponding to the pyridazinone head group does not allow to uniquely assign the orientation of the heterocycle with both nitrogens to the same or opposing side with respect to the sulfonyl group, we suggest that the nitrogens point towards Trp 111 adopting optimal geometry to form a H-bond between the side-chain NH of Trp 111 and N2 of the ligand with a contact distance of 3.2 Å. In alternative orientation, a similar interaction to the Trp 20 NH would not be possible for geometrical reasons. An essential prerequisite to form our assumed interaction mode is the binding of the pyridazinone in deprotonated state at N2 to the enzyme. In addition, binding in deprotonated state would allow the ligand to form a charge-assisted interaction between its negatively charged pyridazinone anchor and the positively charged nicotinamide moiety of NADP⁺ (~3.3 Å). Although no information about protonation states can be concluded from the electron density at the available resolution (1.43 Å, for further details, see below), His 110 Nε2 and Tyr 48 OH are in perfect orientation and contact distance (2.7 Å) to act as H-bond donors to the carbonyl oxygen O3 of the pyridazinone (Table 3.1).

Selected contact distances between ALR2-NADP ⁺ and 6 [Å]	1.43 Å crystal structure	0.95 Å crystal structure
C4 (NADP ⁺) – C3	3.3	3.4
Trp 111 Nε1 – N2	3.2	3.1
His 110 Nε2 – O3	2.7	2.7
Tyr 48 OH – O3	2.7	2.7
Cys 80 S – C7	4.0	4.0
Cys 298 S – C5	4.0	3.8 / 4.2
Cys 298 S – O2	4.4	3.9 / 4.6
Cys 303 S – C6	3.9	3.8 / 4.0
Thr 113 OG – C1	3.6	3.5
O1 – WAT1	-	2.7
O1 – WAT2	3.0	3.0
Trp 219 CH2 – O2	3.2	3.2

Table 3.1. Selected contact distances between ALR2-NADP⁺ and the pyridazinone inhibitor **6** at 1.43 and 0.95 Å resolution.

Additionally, the pyridazinone group forms an arene-sulfur contact to Cys 298 and edge-to-face interactions to the aromatic side-chain of Trp 20. The sulfonyl spacer fixes both aromatic systems enclosing a bond angle of 101.6° . This provides an ideal geometry to address both, the catalytic and the specificity pocket. The rigid scaffold might contribute to binding affinity of this ligand: exhibiting only two rotatable bonds, the inhibitor cannot lose pronounced conformational degrees of freedom upon binding to the enzyme. The sulfonyl group remains partly solvent exposed with its O1 oxygen of the sulfon group forming a H-bond to a water molecule. The benzofurane system forms a face-to-face π - π stacking interaction to the aromatic side-chain of Trp 111, hydrophobic contacts to the side-chains of Leu 300 as well as to Trp 79 and Phe 122. Furthermore, arene-sulfur interactions between the thiole group of Cys 80 and Cys 303 and the aromatic benzofurane are observed. In total, there are 109 van der Waals contacts between the ligand and the ALR2-NADP⁺ complex. Upon complex formation, protein (including the cofactor) and ligand bury a solvent-accessible surface area of 636 \AA^2 which can be split into a minor polar (138 \AA^2) and an almost four times larger apolar (498 \AA^2) surface contribution. The relationship is in agreement with previous studies suggesting hydrophobic interactions as an important driving force for the binding process.^{19,20}

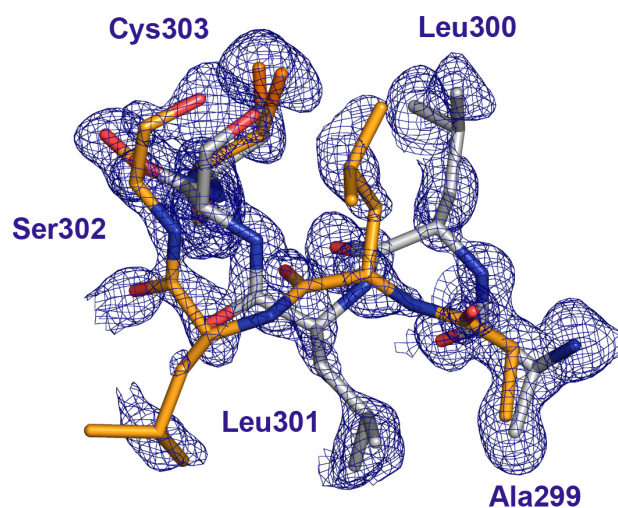


Figure 3.4. Refinement model of the C-terminal ligand-binding region exhibiting two split conformations, the one shown in grey corresponds to the geometry with closed specificity pocket between Leu 300 and Trp 111 (not shown) and the second conformation, shown in orange, describes the open specificity pocket ready to accommodate the bound ligand. The $F_o - F_c$ density (2.0σ) is indicated in blue.

To obtain more detailed insights into the binding mode of the pyridazinone to ALR2 we determined the same complex structure at 0.95 Å resolution. The model was refined to a final R_{cryst} and R_{free} of 12.2 % and 14.2 %, respectively. Interestingly enough, besides the assignment of 22 split conformations, the electron density indicates the presence of two different loop conformations next to the C-terminal ligand-binding region (residue 299 to 303) (Figure 3.4). After fitting a splitted model the occupancy could be refined to 54 % and 46 % for both loop conformations. Conformation 1 represents the specificity pocket of the enzyme in its closed geometry forming direct hydrophobic contacts between the side-chains of Leu 300 and Trp 111. These residues adopt similar conformations in ligand-bound states if the accommodated inhibitor leaves the specificity pocket unoccupied as observed in the case of fidarestat²¹ or in complexes formed with citrate as ligand in the catalytic pocket.²² Conformation 2 corresponds to the open form of the specificity pocket hosting the benzofurane moiety of the ligand. An even better resolved structure of the ternary ALR2-NADP⁺-IDD 594 complex has recently been refined to 0.66 Å.¹⁵ The inhibitor IDD 594 (**2**, Figure 3.1) opens the specificity pocket very similarly to the pyridazinone **6** (rmsd 0.15 and 0.81 Å, calculated for either the backbone atoms of the residues Trp 111, Thr 113, Phe 122, Ala 299, Leu 300, Leu 301, and Ser 302 or for all atoms of these residues, respectively). In addition to the binding site conformations observed in the ALR2-NADP⁺ complexes with IDD 594 and citrate/fidarestat, a third conformer has been found in the complex with tolrestat²³: A detailed comparison of the crystal structures corresponding to these three conformers (Fig. 3.5) reveals that the architecture of the binding site next to the catalytic center and the cofactor location is virtually conserved, but pronounced induced-fit adaptations are observed for the C-terminal loop region (Cys 298 to Cys 303) and the aromatic side-chain of Phe 122 lining up the specificity pockets. In Figure 3.5 a superposition of these binding pockets together with their bound inhibitors is shown.

The backbone trace of conformation 1 in our novel complex structure and the fidarestat-complex superimpose well (rmsd 0.16 Å). Accordingly, this conformation represents the specificity pocket in closed state, adopting very similar side-chain orientations except Cys 298 and Leu 300, where slightly different rotamers are observed. In the fidarestat complex, both split side-chain rotamers place the CH₂S-group towards the nicotinamide moiety of the cofactor, whereas in our complex structure this side-chain is directed in one of the two split orientations towards the

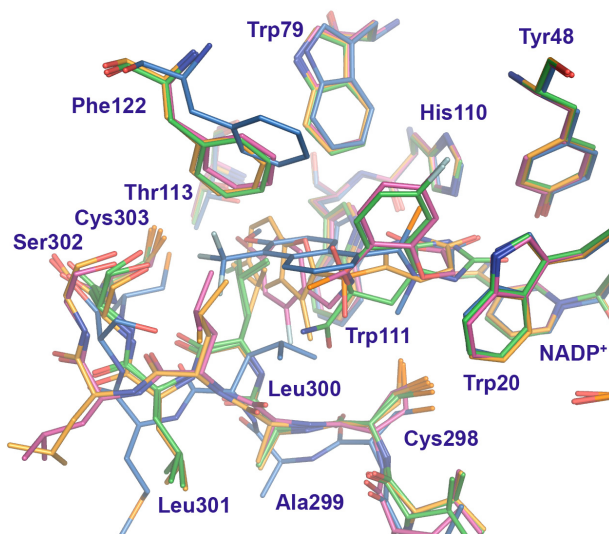


Figure 3.5. Superposition of the 0.95 Å ALR2-pyridazinone complex structure (orange) with the three currently known binding pocket conformations observed for the fidarestat (green), tolrestat (blue) and IDD594 (magenta) complexes.

cofactor and in the second towards the pyridazinone inhibitor. The backbone trace of conformation 2 coincides with that observed for the IDD 594 complex (rmsd 0.12 Å). Slight deviations are observed for the rotameric state of the solvent-exposed Leu 301 side-chain, whereas the geometry of the remaining binding pocket is retained. Compared to the complexes with IDD 594, fidarestat and **6**, remarkable relocations within the C-terminal loop region are observed for the tolrestat complex. For the latter, rmsd values of 5.53 Å and 5.85 Å with respect to the backbone trace and all residue atoms, respectively, are determined for Cys 298 to Cys 303 when compared to conformation 2 found in the 0.95 Å ALR2-**6** complex. Whereas IDD 594 and **6** form face-to-face π - π stacking interactions to Trp 111, the aromatic portion of tolrestat is oriented perpendicularly forming an edge-to-face interaction with Trp 111. Simultaneously, the side-chain of Leu 300 adopts a kinked conformation forming a van der Waals contact to the naphthyl moiety of tolrestat. The trifluoro-methyl substituent is located in a region actually occupied in the IDD 594 and the ALR2-**6** complexes by one of the C δ atoms of Leu 300. As a consequence of this adaptation, the aromatic portion of tolrestat intercalates between the side-chains Leu 300 and Phe 122 with the latter shifted towards Val 47 compared to its orientation present in the IDD 594, fidarestat and **6**-complexes. The atomic positions of the carboxylic groups in IDD 594 and tolrestat superimpose well with N2, C3, and O3 of the pyridazinone moiety in the ALR2-**6** complex. Since binding of **6** requires opening of the specificity pocket, the

occupancy of the inhibitor was set equivalent to the occupancy of the open loop conformation 2 which refined to a 46 % population in the 0.95 Å structure.

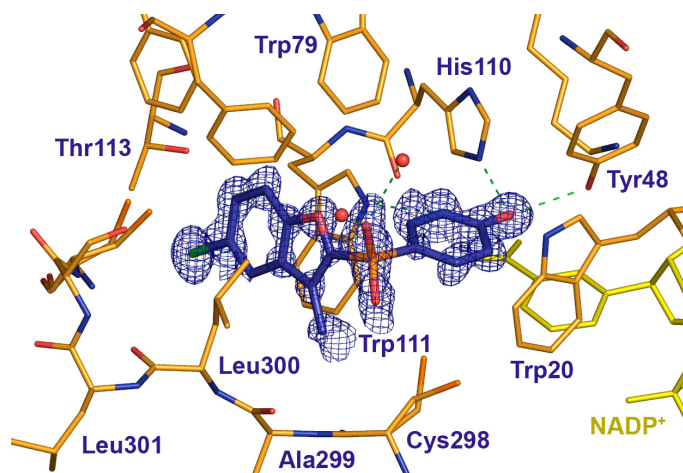


Figure 3.6. Refinement model of the ALR2 binding pocket at 0.95 Å resolution occupied by the pyridazinone inhibitor **6** shown in blue. For clarity, the specificity pocket is only represented in the open conformation. Amino acid residues are shown in orange, water molecules are indicated as red spheres. F_o-F_c density contoured at 3.5σ is shown in blue. It clearly depicts the positions of the inhibitor atoms.

It remains unclear, why in the 1.43 Å structure a higher ligand population has been found, possibly this is due to a difference in ligand soaking time. Nevertheless, the corresponding F_o-F_c difference map (3.5σ) clearly reveals the atomic positions of the inhibitor. A representation of the binding mode, as observed in the 0.95 Å crystal structure, is given in Figure 3.6. The data do not allow to conclude, whether, in agreement with conformation 1 also to some extent a citrate molecule, picked up from the crystallisation buffer, is present in the active site. However, no significant density could be detected that would indicate the presence of a well-ordered citrate molecule in the catalytic pocket. Obviously, our high-resolution structure shows an averaged superposition of the specificity pocket in closed or open state. Both geometries can be regarded as frozen-in snapshots of the conformational adaptation required to accommodate the bound ligand. Previously performed molecular dynamics simulations²⁴ indicate that access to the specificity pocket requires relocation of side-chain together with important backbone atom shifts in this loop region. Table 3.2 shows the ϕ and ψ angles corresponding to the open and closed loop conformation and the observed changes required for opening the pocket. Pronounced differences in $\Delta\phi$ and $\Delta\psi$ are observed for Ala 299 (77.3° , 140.9°) and Leu 300 (161.4° , 64.0°). To quantify backbone atom shifts, Table 3.2 lists the distances of the C_α atoms for the residues

	Conformation 1 [°]		Conformation 2 [°]		Differences [°]		Distances between C α [Å]
	ϕ	ψ	ϕ	ψ	$\Delta\phi$	$\Delta\psi$	
Ala 299	-113.5	9.6	-36.2	150.5	77.3	140.9	1.03
Leu 300	48.2	51.1	-150.4	115.1	161.4	64.0	2.57
Leu 301	-68.3	-18.9	-57.6	-38.6	10.7	19.7	2.47
Ser 302	-79.7	-12.5	-57.5	-152.1	22.2	139.6	1.59
Cys 303	-177.5	29.8	0.7	2.6	178.2	27.2	0.33

Table 3.2. ϕ and ψ angles of the amino acids within the C-terminal ligand-binding loop region. The corresponding values are shown for the closed (conformation 1) and the open conformation (2). Differences are given for comparison. Distances of the C α atoms represent the shift required to open the specificity pocket.

involved in opening of the specificity pocket. Remarkable differences are observed for Leu 300 and 301 being displaced by 2.6 and 2.5 Å, respectively. Thus, significant contributions for the opening of the specificity pocket result from extended backbone atom movements. Table 3.1 lists important interaction distances between the inhibitor and the ALR2-NADP⁺ complex. Whereas in our crystal structure at 1.43 Å resolution only one water molecule was found to coordinate to the solvent exposed O1 oxygen of the inhibitor (distance 3.0 Å), in the 0.95 Å structure two waters are observed next to O1 at a distance of 2.7 and 3.0 Å.

To assign H-bond donors and acceptors at the protein-inhibitor interface, knowledge about the actually adopted protonation states is an essential prerequisite. Therefore, we used the high-resolution data for the calculation of a F_o-F_c difference map neglecting all hydrogens possibly bonded to Tyr 48, Lys 77, His 110, and Trp 111 (Figure 3.7). With some care, the obtained difference density map suggests protonation at Nε2 of His 110, H-bonded to the carbonyl oxygen O3 of the inhibitor. Furthermore, a density peak close to Nε1 of Trp 111 is observed next to a straight line connecting the latter nitrogen with N2 of the inhibitor. This observation suggests protonation of the indole moiety of Trp 111 and supports our hypothesis that the pyridazinone inhibitor binds to the enzyme in deprotonated state. Additionally, the difference electron density gives evidence for a

protonated Tyr 48 hydroxyl function acting as H-bond donor to O3 of the inhibitor. The oxygen of this hydroxyl function is accepting at the same time a H-bond donated by the

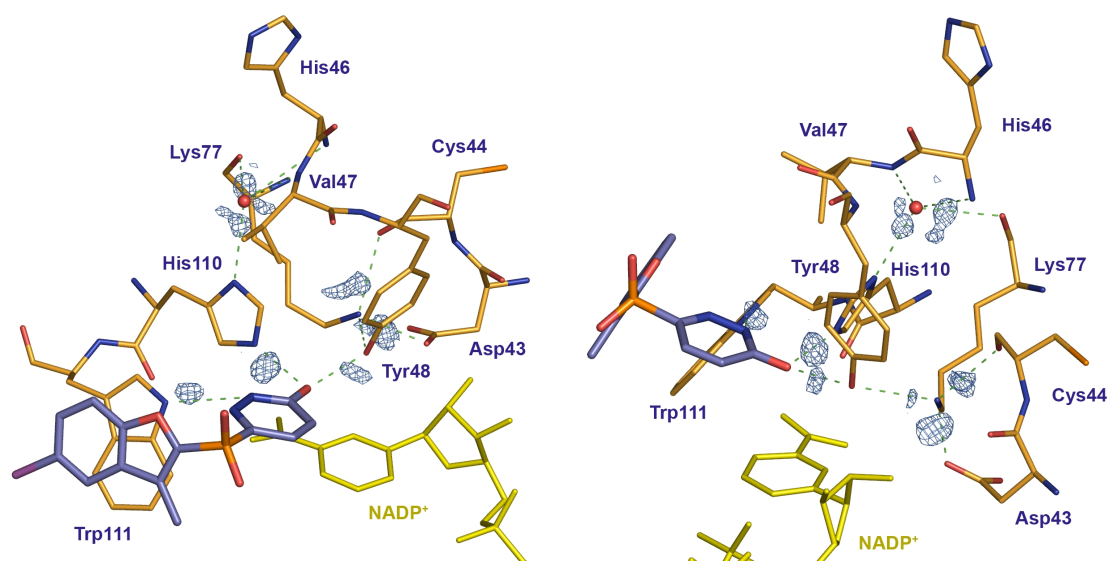


Figure 3.7. Fo-Fc difference map next to residues in the catalytic center provides evidence for the protonation states of Tyr 48, Lys 77, His 110, Trp 111 and the pyridazinone moiety. Furthermore, a water molecule is indicated mediating a hydrogen-bond network to His 110 N δ 2, Lys 77 CO and the backbone NH groups of His 46 and Val 47. H-bonds are shown as green dotted lines and the electron density corresponding to the hydrogen atoms is contoured in blue at 1.8 σ . The inhibitor is shown in blue. The representation presents the binding pocket in two orientations: (a) depicts the H-bond interactions between the inhibitor and Tyr 48 OH, His 110 N ϵ 2 and Trp 111 N ϵ 1; (b) clearly shows the three-fold protonated Lys 77 side-chain nitrogen involved in a H-bond network to Tyr 48 OH, Asp 43 O δ 2 and Cys 44 CO.

three-fold protonated Lys 77. As in the present structure, in several ALR2 crystal structures a water molecule has been found to coordinate to N δ 2 of His 110 and to mediate an interaction to Lys 77. With respect to this site, an interesting feature has been described by El-Kabbani et al.²⁵ They observed in a 0.92 and 1.1 Å resolved crystal structure of human ALR2 complexed by either the hydantoin fidarestat (**4**) or minalrestat (**5**) a similar electron density peak near His 110. Due to an anomalous diffraction signal in case of fidarestat this density peak has been interpreted as 60 % chloride and 40 % water, whereas in the ALR2-minalrestat complex this peak has been assigned to 100 % water occupancy. In our high-resolution crystal structure we also observe difference electron density that can be attributed to a water molecule. However, we do not gain evidence for any additional density that might indicate partial

occupancy by a chloride ion at this site. In our structure, near the water we detect two difference electron density peaks at 2.0σ which, with some care, might be interpreted as the hydrogen atoms of the water molecule pointing towards N δ 2 of His 110 and the backbone carbonyl oxygen of Lys 77. Thus, both neighboring groups act as H-bond acceptors. Furthermore, this tetra-coordinated water molecule accepts H-bonds from the backbone NH groups of His 46 and Val 47. Its B-factor (5.1 \AA^2) corresponds approximately to the B-factors of the coordinating groups (4.7 \AA^2 in average) which supports furthermore the hypothesis of full occupancy by a water molecule. According to these observations, we suggest His 110 to be singly-protonated at N ϵ 2 as previously described for the carboxylic-acid type inhibitor IDD 594. The supposedly deprotonated nature of N2 in **6** in enzyme-bound state suggests either a negative charge on this ligand or a possible hydroxypyridazine tautomer. Close analysis of the binding pattern gives no evidence for a putative interaction of an assumed hydroxyl group at this position for the latter tautomer with any neighbouring group of the protein. Furthermore, unrestrained refinement of the C3-O3 bond length results in $1.19 (0.02) \text{ \AA}$ clearly indicating the presence of a carbonyl double bond. These observations make the presence of the hydroxypyridazine tautomer unlikely.

A further interesting detail concerns the electrostatic polarisation between the 5-chloro substituent at the benzofurane moiety in the specificity pocket and O γ of Thr 113. A similar contact has been described between a bromine and Thr 113 O γ for the ALR2-IDD 594 complex. Multipolar refinement of the diffraction data on the latter complex along with theoretical DFT calculations^{26,27} suggest negative polarisation of O γ involved in a H-bond to the carbonyl oxygen of the same residue. The partial negative charge of O γ polarises the neighbouring IDD 594-bromine substituent resulting in an unusual short bromine-to-oxygen contact of 2.97 \AA . This induced electrostatic interaction is assumed to contribute to affinity and selectivity of IDD 594. The 5-chlorosubstituent at the benzofurane moiety of **6** occupies approximately the same position as the bromine in IDD 594. This fact suggests that similar polarisation effects could possibly matter in the ALR2-**6** complex, even though a chlorine shows reduced polarisability in comparison to a bromine. Closest intermolecular contacts between an alcohol-type oxygen and chlorine bound to an aromatic nucleus are found in small-molecule crystal structures in the range of $2.96 - 2.99 \text{ \AA}$.²⁸ In our complex this O γ to Cl contact amounts to 3.6 and 3.5 \AA for the 1.43 \AA and 0.95 \AA crystal structure, respectively. The larger distance could either be attributed to lower polarisability of the

chlorine or additionally to a non-optimal interaction geometry experienced by the chlorine in **6**: whereas in the crystal structure of IDD 594 the bromine atom points directly towards Thr 113 O γ , in **6** the chlorine is slightly off and orients towards the bottom of the pocket.

3.2.2 Isothermal Titration Calorimetry to Determine Binding Constants

The pyridazinone inhibitor investigated in this study is described as one of the most potent ARIs yet reported in literature¹² based on in-vitro IC₅₀ values and in-vivo dose-response data. In order to compare binding affinity towards ALR2 of **6** with other known ARIs in terms of a pure dissociation constants independent of any superimposed effects resulting from a kinetic enzyme assay we applied isothermal titration calorimetry (ITC). Titration experiments were performed for **6**, IDD 594, sorbinil and tolrestat with human ALR2 in presence of NADP⁺. In structural terms, sorbinil binds to the catalytic pocket of ALR2 without opening the specificity pocket, whereas IDD 594 and tolrestat both open and occupy this pocket, however, as already described, in different fashion. IDD 594, sorbinil, and tolrestat show binding constants of 4.5*10⁶ to 1.5*10⁷ L/mol. Different to **1–3**, **6** turned out to be almost insoluble in 10 mM Hepes buffer at pH 8, even after extensive sonication, when no further pre-treatment of the compound was carried out. However, lyophilisation of **6** dissolved previously in DMSO resulted in a powder soluble up to 150 μ M under the conditions used for the thermodynamic measurements. We determine a binding constant for **6** of 1.1*10⁶ L/mol corresponding to a standard Gibbs free energy of 34.5 kJ/mol. This value is lower than that of IDD 594 and falls into the same range found for sorbinil and tolrestat (Table 3.3).

Inhibitor	Binding constant [10 ⁶ L/mol]	Standard deviation [10 ⁶ L/mol]	Gibbs Free Energy ΔG^0 [kJ/mol]
Sorbinil (1)	4.5	0.7	- 37.9
IDD 594 (2)	14.9	3.7	- 40.9
Tolrestat (3)	4.6	1.2	- 38.0
Pyridazinone (6)	1.1	0.3	- 34.5

Table 3.3. Binding constants and standard deviations of the ARIs investigated in this study as well as the calculated standard Gibbs free energies are shown. All measurements have been carried out at 298 K.

The binding constant observed for **6** by ITC is lower than expected considering the reported IC₅₀ value, however, both values are difficult to compare, as the latter might be affected by various parameters such as enzyme concentration, pH and nature of the buffer, salt content, substrate, substrate concentration and cofactor concentrations used in the kinetic assay. Nevertheless, compared to the carboxylate- and hydantoin-type inhibitors, the in-vivo efficiency obviously benefits from the improved physicochemical properties of **6**, giving rise to higher tissue penetration due to increased lipophilicity.

3.3 Summary and Conclusions

To prevent diabetic complications caused by enhanced glucose flux via the polyol pathway, aldose reductase inhibition provides a promising therapeutic principle to adjust cellular imbalances under pathophysiological high-glucose level conditions. Up to now, most of the carboxylate-type and hydantoin-type ARIs, developed during the last two decades, failed in clinical trials, probably due to insufficient physicochemical or selectivity properties. In 2003, a novel ARI showing a pyridazinone anchor group was reported to possess excellent affinity and tissue penetration properties. The crystal structure of the ternary complex of this pyridazinone inhibitor with ALR2-NADP⁺ has been determined at 1.43 Å and 0.95 Å resolution. The inhibitor binds with its pyridazinone head group to the catalytic center and occupies the selectivity pocket using its benzofurane moiety. Due to the partial occupancy of the inhibitor in the high-resolution structure, our analysis gives evidence for two loop conformations involved in the opening of the specificity pocket. Previously performed molecular dynamics simulations indicated this opening as a concerted movement of backbone atoms as well as side-chain rotations. Soaking times applied to the crystals used for the 0.95 and 1.43 Å resolution structure determination were different. The shorter ligand soak applied for the crystal in the high resolution analysis resulted in only 46 % inhibitor occupancy, whereas the other showed 74%. Nevertheless, both structures exhibit virtually the same binding geometry. Difference electron density of the 0.95 Å data provides some evidence that the pyridazinone moiety binds deprotonated and negatively charged, whereas the neighbouring Tyr 48 and His 110 residues are present in uncharged state.

Furthermore, we determined the binding constant of the pyridazinone inhibitor by ITC to fall into the affinity range of the known inhibitors sorbinil and tolrestat. Even though the inhibitor has been described to possess excellent pharmacokinetic properties, further improvement of the affinity would be desirable. Its poor solubility under the applied crystallisation conditions is probably responsible for the incomplete occupancies after soaking. In case of **1–3**, similar soaking conditions always produced full occupancy. Possibly solubility of the pyridazinone-type inhibitor has to be improved. The recently described in-vitro and in-vivo studies of **6** and other derivatives were carried out in presence of DMSO to increase water solubility. With the knowledge of the detailed interaction pattern between the ligand and the enzyme new ideas how to improve the class of the pyridazinones should be possible. One might consider the electrostatic polarization observed for bromine in IDD 594 and Thr 113 O γ to enhance ligand binding to the specificity pocket. Furthermore, affinity and selectivity of AR-inhibitors have been demonstrated to improve by addressing the backbone NH of Leu 300 with an appropriate H-bond acceptor.^{21,29} Considering the present crystal structure, such acceptor groups should possibly replace the presently attached methyl group at the benzofurane moiety. These modifications might start a subsequent cycle of iterative structure-based drug design in order to combine the beneficial pyridazinone anchor group with affinity-, selectivity- and solubility-enhancing substituents.

3.4 Materials and Methods

Cloning, expression, purification and crystallisation of Aldose Reductase have already been described elsewhere in detail.^{15,17,18,25} Prior to crystallisation, ALR2 solutions were concentrated to 20 mg/ml in 50 mM diammonium hydrogen citrate at pH 5 and mixed with a solution of the cofactor in oxidized state to achieve a molar ratio of ALR2:NADP⁺ of 1:3. Crystals were grown at 277 K using the hanging drop vapor diffusion method. We performed cocrystallisation as well as soaking trials to obtain appropriate crystals of the complex with **6**. Our attempts to cocrystallize **6** with the protein only resulted in crystals which contained, as structure determination showed, the electron density of a citrate molecule accommodated in the active site pocket. Possibly this is due to poor solubility of the pyridazinone inhibitor under the applied crystallization conditions. Therefore, we examined various soaking conditions resulting in a solution of 5% (V/V) isopropanol, 5% (V/V) DMSO, along with 5% (m/V) β -

cyclodextrin (Sigma), 25 % (m/V) PEG 6000 in 50 mM diammonium hydrogen citrate at pH 5, which was used to prepare a saturated solution of the inhibitor. Crystals were soaked for up to three days at 293 K.

Data Collection. Data were collected at 100 K using a solution of 40 % (m/V) PEG 6000 in 50 mM diammonium hydrogen citrate at pH 5 as cryoprotectant. Appropriate crystals were selected to determine a data set (soaking time 3d) at 1.43 Å on our in-house facility. A second data set, based on a crystal soaked for about 2 days was used for data collection at beamline BL1 of the Protein Structure Factory, BESSY synchrotron (Berlin, Germany). The in-house data set was determined with a RIGAKU copper rotating anode (Molecular Structure Cooperation) at 50 kV, 90 mA as X-ray source and a R-AXIS IV image plate system. For each frame the exposure time and oscillation range were set to 5 min and 0.5°, respectively. The BESSY data consist of a low- and a high resolution pass and were collected using a MAR-CCD detector (Marresearch, Norderstedt, Germany).

Exposure time, oscillation range, detector geometry and crystal-detector distance were optimised to obtain a low-resolution data set with a resolution range of 15 – 2.5 Å as well as a high-resolution data set ranging from 2.7 – 0.95 Å. Both sets were processed separately and subsequently mutually scaled to reveal a unique data set. The soaked crystals belong to the monoclinic space group P2₁ with unit cell parameters a=49.4 Å, b=66.9 Å, c=47.4 Å, and β=92.1° and β=91.9° for the in-house and BESSY data, respectively. The structure contains one monomer per asymmetric unit with a Matthews coefficient of 2.2 Å³/Da and 43.2 % solvent content. All data processing and scaling were performed using the HKL2000 package.³⁰ Data collection and processing statistics are given in Table 3.4.

Structure Determination and Refinement. The coordinates of human ALR2 (PDB code 1el3)¹⁷ were used for initial rigid-body refinement of the protein atoms followed by repeated cycles of conjugate gradient energy minimization, simulated annealing and B-factor refinement using the CNS program package.³¹ Refinement at later stages was performed with the program SHELXL.³² Here, at least 20 cycles of conjugate gradient minimization were performed with default restraints on bonding geometry and B-values. Five percent of all data were used for R_{free} calculation. Amino acid side-chains were fitted to sigmaA-weighted 2F_o-F_c and F_o-F_c electron density maps using O.³³ After the first refinement cycle water molecules, and subsequently cofactor and ligand were

located in the electron density and added to the model. Anisotropic conjugate gradient refinement resulted in a significant improvement of the model built for the high-

	Complex structure at 1.43 Å resolution	Complex structure at 0.95 Å resolution
Data collection and Processing		
No. of crystals used	1	1
Wavelength [Å]	1.5418	0.91838
Space group	P2 ₁	P2 ₁
Unit cell parameters		
a, b, c [Å]	49.4, 66.9, 47.4	49.4, 66.9, 47.4
β [°]	92.1	91.9
Diffraction data		
Resolution range [Å]	25 – 1.43 (1.45 – 1.43)	15 – 0.95 (0.97-0.95)*
Unique reflections	55 802	188 551
R(I) _{sym} [%]	4.6 (47.2)	4.5 (37.8)
Completeness [%]	97.8 (92.9)	97.6 (91.6)
Redundancy	2.9 (2.4)	2.9 (2.3)
I/σ(I)	21.7 (1.9)	21.8 (2.4)
Refinement		
Resolution range [Å]	10 – 1.43	20 – 0.95
Reflections used in refinement (work/free)	51 092 / 2735	172 018 / 9067
Final R values for all reflections (work/free) [%]	16.3 / 20.6	12.2 / 14.2
Final R values for reflections with F > 4 σ (work/free) [%]	15.1 / 19.1	11.5 / 12.2
Protein residues	316	315

Coenzyme	1	1
Inhibitor	1	1
Water molecules	345	375
RMSDs		
Bonds [Å]	0.01	0.016
Angles [°]	2.4	2.4
Ramachandran plot		
Residues in most favored regions [%]	91.7	90.6
Residues in additional allowed regions [%]	8.3	9.4
Mean B factor [Å²]		
Protein	19.5	10.9
NADP ⁺	14.1	5.9
Inhibitor	18.4	10.5
Water molecules	28.6	21.1

resolution synchrotron data, which was not observed for the 1.43 Å structure. Restraints were applied to bond lengths and angles, chiral volume, planarity of aromatic rings and van der Waals contacts. Multiple side-chain conformations were built if indicated by appropriate electron density and maintained during the refinement, if the minor populated side-chain rotamer showed at least 10% occupancy. During the last refinement cycles, riding H atoms were introduced for the protein residues without using additional parameters. The riding model was not applied for cofactor and inhibitor. The final models were validated using PROCHECK.³⁴ Data refinement statistics are shown in Table 3.4.

Van der Waals contacts have been detected by the program CONTACTSYM.³⁵ Polar and apolar solvent-accessible surfaces buried upon ligand binding have been calculated with the GETAREA 1.1 web interface³⁶ using an 1.4 Å probe and radii published by Shrake and Rupley.³⁷ Figures were prepared using Isis Draw (MDL, San Leandro, USA) and Pymol.³⁸

RMSD values have been calculated by means of the program suite SYBYL.³⁹

Isothermal Titration Calorimetry. Calorimetric measurements were carried out using a MCS ITC-instrument from MicroCal Inc. (Northampton, USA). In each experiment, the ligand was titrated to the protein solution present in the 1.4 mL sample cell. The reference cell contained 0.1 mM sodium azide dissolved in demineralised water. All measurements were carried out at 298 K. The protein was dissolved in 10 mM HEPES buffer, pH 8 to a concentration of 18.9 μM for the titration of **2**, and 37.8 μM for the measurement of **1**, **3** and **6**. Protein concentrations were determined by UV spectroscopy (280 nm) using the specific absorption calculated by the ProtParam tool (www.expasy.ch). An appropriate amount of **6** was solved in 200 μL DMSO, shock-frozen in liquid nitrogen and subsequently lyophilised over night using a Heraeus lyophilisator. After resolution the saturation concentration of **6** was determined to be 150 μM by UV spectroscopy at 240 nm. The ligand solution contained 252 μM of the corresponding inhibitor dissolved in the same buffer as the protein except in the case of **6**, where, according to the solubility limitations a ligand concentration of 135 μM was used. The protein was saturated with an excess of NADP^+ which was present to the same concentration in the ligand solution to avoid heat effects caused by diluting the cofactor. Solutions were degassed at 293 K under vacuum for 10 min. Upon experimental setup the protein solution present in the sample cell was stirred at 400 rpm. After a stable baseline had been achieved the titration was initiated. The injection sequence started with an initial aliquot of 1.5 μL (to preserve diffusion effects arising from the experimental setup, data not used for fitting) followed by injections of 10 μL in time intervals of 300 s until complete saturation was obtained. In the case of ligand **6**, injections of 15 μL were performed instead of 10 μL . The titrated sample solution was checked for any precipitation by visual microscopic inspection. Heat changes caused by each inhibitor injection were obtained from the integral of the calorimetric signal. Data were analysed using the ORIGIN software (MicroCal Inc.) for fitting the data points to a single-site binding model in agreement with the results from X-ray crystallography.

Experimental heats of the protein-inhibitor titration were corrected for heats of dilution by subtracting the corresponding data of a blank titration (inhibitor into buffer). All measurements have been carried out at least in triplicate. Given energy values, binding constants and standard deviations derive from data fitting and subsequent averaging of

the corresponding measurements. Standard Gibbs free energy values were calculated using the equation $\Delta G^0 = -RT \ln K_b$ (where $R=8.3144 \text{ J/mol}^{-1}\text{K}^{-1}$, K_b binding constant).

Coordinates and structure factor amplitudes of the crystal structures have been deposited at the Protein Database with the PDB code 1Z8A and 1Z89.

3.5 References

1. Yabe-Nishimura, C. (1998). Aldose reductase in glucose toxicity: a potential target for the prevention of diabetic complications. *Pharmacol. Rev.* **50**, 21-33.
2. Davydov, V. V., Dobaeva, N. M. & Bozhkov, A. I. (2004). Possible role of alteration of aldehyde's scavenger enzymes during aging. *Exp. Gerontol.* **39**, 11-16.
3. Obrosova, I. G., Pacher, P., Szabo, C., Zsengeller, Z., Hirooka, H., Stevens, M. J., & Yorek, M. A. (2005). Aldose reductase inhibition counteracts oxidative-nitrosative stress and poly(ADP-ribose) polymerase activation in tissue sites for diabetes complications. *Diabetes* **54**, 234-242.
4. Ishii, H., Tada, H. & Isogai, S. (1998). An aldose reductase inhibitor prevents glucose-induced increase in transforming growth factor-beta and protein kinase C activity in cultured mesangial cells. *Diabetologia* **41**, 362-364.
5. Li, W., Hamada, Y., Nakashima, E., Naruse, K., Kamiya, H., Akiyama, N., Hirooka, H., Takahashi, N., Horiuchi, S., Hotta, N., Oiso, Y. & Nakamura, J. (2004). Suppression of 3-deoxyglucosone and heparin-binding epidermal growth factor-like growth factor mRNA expression by an aldose reductase inhibitor in rat vascular smooth muscle cells. *Biochem. Biophys. Res. Commun.* **314**, 370-376.
6. Jacot, J. L. & Sredy, J. (1999). Emerging therapeutics for diabetic retinopathy: potential therapies for the new millennium. *Emerging Therapeutic Targets* **3**, 1-29.
7. Miyamoto, S. (2002). Recent advances in aldose reductase inhibitors: potential agents for the treatment of diabetic complications. *Expert. Opin. Ther. Patents* **12**, 621-631.

8. Greene, D. A., Arezzo, J. C. & Brown, M. B. (1999). Effect of aldose reductase inhibition on nerve conduction and morphometry in diabetic neuropathy. Zenarestat Study Group. *Neurology* **53**, 580-591.
9. Suzen, S. & Buyukbingol, E. (2003). Recent studies of aldose reductase enzyme inhibition for diabetic complications. *Curr. Med. Chem.* **10**, 1329-1352.
10. Constantino, L., Rastelli, G., Vianello, P., Cignarella, G. & Barlocco, D. (1999). Diabetes Complications and their potential prevention: Aldose Reductase Inhibition and other Approaches. *Med. Res. Rev.* **19**, 3-23.
11. Yagihashi, S., Yamagishi, S. I., Wada Ri, R., Baba, M., Hohman, T. C., Yabe-Nishimura, C. & Kokai, Y. (2001). Neuropathy in diabetic mice overexpressing human aldose reductase and effects of aldose reductase inhibitor. *Brain* **124**, 2448-2458.
12. Mylari, B. L., Armento, S. J., Beebe, D. A., Conn, E. L., Coutcher, J. B., Dina, M. S., O'Gorman, M. T., Linhares, M. C., Martin, W. H., Oates, P. J., Tess, D. A., Withbroe, G. J. & Zembrowski, W. J. (2003). A highly selective, non-hydantoin, non-carboxylic acid inhibitor of aldose reductase with potent oral activity in diabetic rat models: 6-(5-chloro-3-methylbenzofuran- 2-sulfonyl)-2-H-pyridazin-3-one. *J. Med. Chem.* **46**, 2283-2286.
13. Hotta, N., Toyota, T., Matsuoka, K., Shigeta, Y., Kikkawa, R., Kaneko, T., Takahashi, A., Sugimura, K., Koike, Y., Ishii, J. & Sakamoto, N. (2001). Clinical efficacy of Fidarestat, a novel aldose reductase inhibitor, for diabetic peripheral neuropathy. *Diabetes Care* **24**, 10, 1776-1782.
14. Johnson, B. F., Nesto, R. W., Pfeifer, M. A., Slater, W. R., Vinik, A. I., Chyun, D. A., Law, G., Wackers, F. J. T. & Young, L. H. (2004). Cardiac abnormalities in diabetic patients with neuropathy. *Diabetes Care* **27**, 2, 448-454.
15. Howard, E. I., Sanishvili, R., Cachau, R. E., Mitschler, A., Chevrier, B., Barth, P., Lamour, V., Van Zandt, M., Sibley, E., Bon, C., Moras, D., Schneider, T. R., Joachimiak, A. & Podjarny, A. (2004). Ultrahigh resolution drug design I: details of interactions in human aldose reductase-inhibitor complex at 0.66 Å. *Proteins* **55**, 792-804.
16. Wierenga, R. K. (2001). The TIM-barrel fold: a versatile framework for efficient enzymes. *FEBS Lett.* **492**, 193-198.
17. Calderone, V., Chevrier, B., Van Zandt, M., Lamour, V., Howard, E., Poterszman, A., Barth, P., Mitschler, A., Lu, J., Dvornik, D. M., Klebe, G.,

- Kraemer, O., Moorman, A. R., Moras, D. & Podjarny, A. (2000). The structure of human aldose reductase bound to the inhibitor IDD384. *Acta Crystallogr. D* **56**, 536-540.
18. El-Kabbani, O., Darmanin, C., Oka, M., Schulze-Briese, C., Tomizaki, T., Hazemann, I., Mitschler, A. & Podjarny, A. (2004). High-resolution structures of human aldose reductase holoenzyme in complex with stereoisomers of the potent inhibitor Fidarestat: stereospecific interaction between the enzyme and a cyclic imide type inhibitor. *J. Med. Chem.* **47**, 4530-4537.
19. Bohm, H. J. & Klebe, G. (1996). What can we learn from molecular recognition in protein-ligand complexes for the design of new drugs? *Angew. Chem. Int. Ed. Engl.* **35**, 2588-2614.
20. Meyer, E. A., Castellano, R. K. & Diederich, F. (2003). Interactions with aromatic rings in chemical and biological recognition. *Angew. Chem. Int. Ed. Engl.* **42**, 1210-1250.
21. Oka, M., Matsumoto, Y., Sugiyama, S., Tsuruta, N. & Matsushima, M. (2000). A potent aldose reductase inhibitor, (2S,4S)-6-fluoro-2', 5'-dioxospiro[chroman-4,4'-imidazolidine]-2-carboxamide (Fidarestat): its absolute configuration and interactions with the aldose reductase by X-ray crystallography. *J. Med. Chem.* **43**, 2479-2483.
22. Harrison, D. H., Bohren, K. M., Ringe, D., Petsko, G. A. & Gabbay, K. H. (1994). An anion binding site in human aldose reductase: mechanistic implications for the binding of citrate, cacodylate, and glucose 6-phosphate. *Biochemistry* **33**, 2011-2020.
23. Urzhumtzev, A., Tete-Favier, F., Mitschler, A., Barbanton, J., Barth, P., Urzhumtseva, L., Biellmann, J. F., Podjarny, A. & Moras, D. (1997). A "specificity" pocket inferred from the crystal structures of the complexes of aldose reductase with the pharmaceutically important inhibitors tolrestat and sorbinil. *Structure* **5**, 601-612.
24. Sotriffer, C. A., Kramer, O. & Klebe, G. (2004). Probing flexibility and "induced-fit" phenomena in aldose reductase by comparative crystal structure analysis and molecular dynamics simulations. *Proteins* **56**, 52-66.
25. El-Kabbani, O., Darmanin, C., Schneider, T. R., Hazemann, I., Ruiz, F., Oka, M., Joachimiak, A., Schulze-Briese, C., Tomizaki, T., Mitschler, A. & Podjarny, A. (2004). Ultrahigh resolution drug design. II. Atomic resolution

- structures of human aldose reductase holoenzyme complexed with Fidarestat and Minalrestat: implications for the binding of cyclic imide inhibitors. *Proteins* **55**, 805-813.
26. Muzet, N., Guillot, B., Jelsch, C., Howard, E. & Lecomte, C. (2003). Electrostatic complementarity in an aldose reductase complex from ultra-high-resolution crystallography and first-principles calculations. *Proc. Natl. Acad. Sci. U S A* **100**, 8742-8747.
 27. Lecomte, C., Guillot, B., Muzet, N., Pichon-Pesme, V. & Jelsch, C. (2004). Ultra-high-resolution X-ray structure of proteins. *Cell. Mol. Life Sci.* **61**, 774-782.
 28. Cambridge crystallographic data base. Cambridge, UK: Cambridge Crystallographic Data Center; 2003. A CSD search was carried out according to the instructions of the supplier using a chloro-phenyl- and a C^{sp3}-hydroxyl group as search fragments followed by visual inspection of the hits.
 29. Petrova, T., Steuber, H., Hazemann, I., Cousido-Siah, A., Mitschler, A., Chung, R., Oka, M., Klebe, G., El-Kabbani, O., Joachimiak, A. & Podjarny, A. (2005). Factorizing selectivity determinants of inhibitor binding toward aldose and aldehyde reductases: structural and thermodynamic properties of the aldose reductase mutant Leu300Pro-fidarestat complex. *J. Med. Chem.* **48**, 5659-5665.
 30. Otwinowski, Z. & Minor, W. (1997). Processing of X-ray Diffraction Data Collected in Oscillation Mode. *Methods Enzymol.* **276**, 307-326.
 31. Brunger, A. T., Adams, P. D., Clore, G. M., DeLano, W. L., Gros, P., Grosse-Kunstleve, R. W., Jiang, J. S., Kuszewski, J., Nilges, M., Pannu, N. S., Read, R. J., Rice, L. M., Simonson, T. & Warren, G. L. (1998). Crystallography & NMR system: A new software suite for macromolecular structure determination. *Acta Crystallogr. D* **54**, 905-921.
 32. Sheldrick, G. M. & Schneider, T. (1997). SHELXL: high-resolution refinement. *Methods Enzymol.* **277**, 319-343.
 33. Jones, T. A., Zou, J. Y., Cowan, S. W. & Kjeldgaard. (1991). Improved methods for building protein models in electron density maps and the location of errors in these models. *Acta Crystallogr. A* **47**, 110-119.
 34. Laskowski, R., MacArthur, M., Moss, D. & Thornton, J. (1993). PROCHECK: a program to check the stereochemical quality of protein structures. *J. Appl. Crystallogr.* **26**, 283-291.

-
35. Sheriff, S., Silverton, E. W., Padlan, E. A., Cohen, G. H., Smith-Gill, S. J., Finzel, B. C. & Davies, D. R. (1987). Three-dimensional structure of an antibody-antigen complex. *Proc. Natl. Acad. Sci. U S A* **84**, 8075-8079.
 36. Fraczekiewicz, R. & Braun, W. (1998). Exact and efficient analytical calculation of the accessible surface areas and their gradients for macromolecules. *J. Comp. Chem.* **19**, 319-333.
 37. Shrake, A. & Rupley, J. A. (1973). Environment and exposure to solvent of protein atoms. Lysozyme and insulin. *J. Mol. Biol.* **79**, 351-371.
 38. DeLano, W. L. (2002). The PyMOL Molecular Graphics System.
<http://www.pymol.org>
 39. SYBYL 7.0, Tripos Inc., St. Louis, MO.

4. Evidence for a Novel Binding Site Conformer of Aldose reductase in Ligand-Bound State

4.1 Introduction

In structure-based drug design the reliable determination of ligand binding modes between a given target and a series of small-molecule lead compounds is an important prerequisite to understand structure-activity relationships at a molecular level. It stimulates further design hypotheses for ligand optimization with respect to improved affinity and selectivity. In addition, regions of a ligand skeleton can be identified where structural modifications can be performed with respect to an improved ADME/Tox profile, presumably without affecting ligand binding to the target under consideration. Usually, X-ray crystallography is the method of choice to elucidate the detailed binding mode.¹⁻⁴ This technique provides a model of the complexed macromolecule averaged over the time span of the experiment and all unit cells of the crystal contributing to the diffraction pattern. However, in case of rather flexible proteins, exhibiting pronounced adaptability of their binding sites to accommodate different ligands, the information obtained from one single structure determination is limited. To advance structure-based drug design efforts, a more comprehensive view on the accessible binding site conformations seems mandatory. A careful comparison of the available crystal structures can support such an analysis, however, the information will be limited as long as no complete coverage of all representative conformations is achieved by the available experimental structures. To bridge this gap, molecular dynamics simulations can be consulted to probe for the remaining possible conformational sub-states of the binding pocket. The hypothesis has been put forward that the binding site is able to adopt all binding-competent conformations, and a ligand to be bound picks one of these conformers from the ensemble by stabilising it energetically.^{5,6}

Aldose reductase (E.C. 1.1.1.21) is a 36 kDa (β/α)₈-TIM-barrel aldo-keto reductase with the active site located at the C-terminal region of the enzyme. The binding pocket is divided by Trp 111 into the catalytic subpocket and the specificity pocket. The latter is known to adopt multiple conformations depending on the bound ligand. The deeply buried catalytic pocket is comprised by residues presumably involved in the catalytic mechanism (Tyr 48, Lys 77, His 110), the nicotinamide moiety of NADP⁺ and Trp 111

acting via its indole NH group as H-bond donor to most of the presently characterized ligand head groups. Further hydrophobic contacts can be formed by the side chains of Trp 20, Val 47, Trp 79, and Trp 219. This catalytic site is usually addressed by hydrophilic, negatively charged anchor groups. Ligands decorated at the opposing end with appropriate hydrophobic groups frequently provoke “induced-fit” adaptations of the specificity pocket flanked by the Trp 111 indole moiety facing the protein core, and Ala 299, Leu 300, and Phe 122 which adopt different rotameric states.⁷⁻¹⁰

ALR2 is the first enzyme of the polyol pathway and converts various aldehydes to their corresponding non-reactive alcohols using NADPH as reducing cofactor, which donates a hydride ion to the carbonyl carbon of the aldehyde. Most likely, the initial hydride transfer step is followed by a subsequent proton relocation from one of the neighbouring acidic residues accepted by the intermediate substrate anion.^{11,12} ALR2 is of pathophysiological relevance, as under elevated blood glucose levels a remarkable extent of glucose is converted to sorbitol in patients suffering from diabetes mellitus.¹³ This is subsequently oxidized to fructose by the NAD⁺-dependent sorbitol dehydrogenase, the second enzyme of the polyol pathway. Accordingly, increased flux of glucose via the polyol pathway leads to various biochemical imbalances such as osmotic and oxidative stress, pathological interferences with kinase cascades, apoptosis regulation, and cytokine signalling. Altogether, these factors result in diabetic long-term complications.¹⁴⁻¹⁷ The development of ALR2-inhibitors (ARIs) has been proven as a promising therapeutic concept. In consequence a broad variety of inhibitors has been synthesized or extracted from natural sources.¹⁸ Recently, a novel series of naphtho[1,2-*d*]isothiazole acetic acids has been described based on the assumed similarity with the well known inhibitor tolrestat (**1**, Fig. 4.1).¹⁹

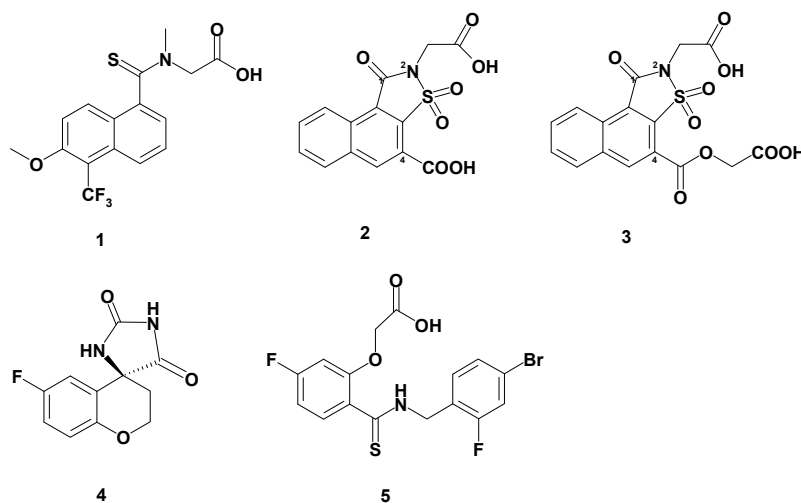


Figure 4.1. Chemical formulae of tolrestat (**1**), two members of the naphtho[1,2-*d*]isothiazole acetic acid series (**2**) and (**3**), sorbinil (**4**), and IDD 594 (**5**).

Besides micromolar and submicromolar binding affinity, these novel ligands exhibited a remarkable selectivity profile for aldose reductase compared to aldehyde reductase, sorbitol dehydrogenase, and glutathione reductase. Here, we report on the binding mode of two members (**2** and **3**, Fig. 4.1) of this series determined by X-ray crystallography, which revealed surprising deviations from the originally predicted binding mode based on a docking study.¹⁹ Interestingly, one of the two ligands stabilizes a binding pocket geometry not yet observed previously in any other ALR2 crystal structure.

4.2 Results and Discussion

Due to its broad substrate promiscuity, the binding pocket of ALR2 exhibits a pronounced adaptability which is also reflected by the multiple crystal structures determined with bound inhibitors. This binding site flexibility is depicted by the residues lining the specificity pocket. In contrast, those residues comprising the catalytic pocket show only minor mobility. Three parent pocket conformations have been characterized so far, represented by the sorbinil-, tolrestat-, and the IDD 594-bound states. The hydantoin sorbinil (**4**, Fig. 4.1) forms hydrogen bonds between its polar head group and the residues of the catalytic pocket (Tyr 48, His 110, and Trp 111, Fig. 4.2a).⁹ Due to its small size and compact scaffold, virtually lacking any conformational degrees of freedom, sorbinil binds to ALR2 with the specificity pocket in closed state. This is indicated by short van der Waals contacts between the side chains of Trp 111 and Leu 300. The second archetypal binding-site conformer is formed with the carboxylate-type inhibitor tolrestat (**1**, Fig. 4.1). It performs similar interactions in the catalytic pocket by means of its carboxylate anchor group, however, the specificity pocket is found in open state. Exhibiting the function of a gate-keeper residue, the side chain of Leu 300 adopts a kinked conformation enabling the inhibitor to form an edge-to-face stacking between its naphthyl moiety and the indole portion of Trp 111 (Fig. 4.2b).⁹ Interestingly, this variant has up to now only found with bound tolrestat.

The third parent conformer is formed with IDD 594 (**5**, Fig. 4.1), which occupies the catalytic pocket with its carboxylate anchor group. Unlike the tolrestat complex, the terminal halogen-substituted aromatic moiety forms a face-to-face stacking to the indole moiety of Trp 111, while the ligand's phenyl ring penetrates between the side chain of Leu 300 and the latter aromatic residue (Fig. 4.2c).⁷ With slight additional

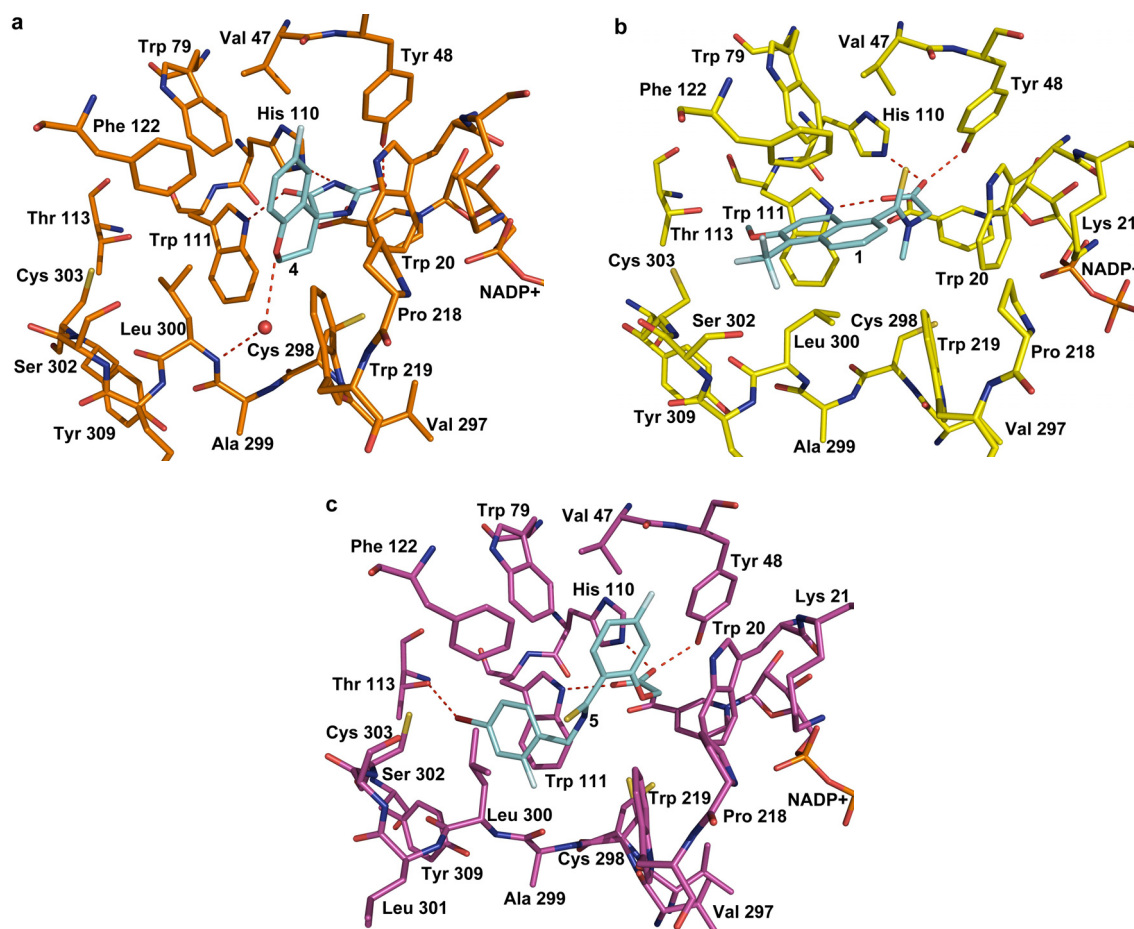


Figure 4.2. Three parent binding pocket conformations of ALR2 observed in complexes with sorbinil, tolrestat, and IDD 594 (shown in light blue). Key interactions are shown as red dotted lines, waters as red spheres. (a) Binding mode of sorbinil with the specificity pocket in closed state; the gating residues Trp 111 and Leu 300 mutually form van der Waals contacts. (b) In the ALR2-1 complex (tolrestat) Leu 300 adopts a kinked conformation and thereby opens the specificity pocket. (c) Binding geometry of **5** (IDD 594) with the enzyme; here, the halogen-substituted aromatic moiety intercalates into the space created between Trp 111 and Leu 300.

adaptations, in particular with respect to the orientation of the Ala 299-Leu 300 peptide region, the latter is the most frequently observed pocket conformer, e.g. also addressed by the ligands zopolrestat,^{20,21} minalrestat,²² zenarestat,²³ IDD 552,²⁴ and a recently published sulfonyl-pyridazinone inhibitor.¹⁰

The novel series of naphtho[1,2-*d*]isothiazole acetic acid derivatives was designed with the idea to freeze the bound conformation of tolrestat by introducing a sulfonlactam ring. A subsequently performed docking study suggested evidence that a tolrestat-like binding mode might be adopted.¹⁹ Nevertheless, with the pronounced adaptability of the ALR2 binding site in mind, we decided to determine the complex structures with **2**

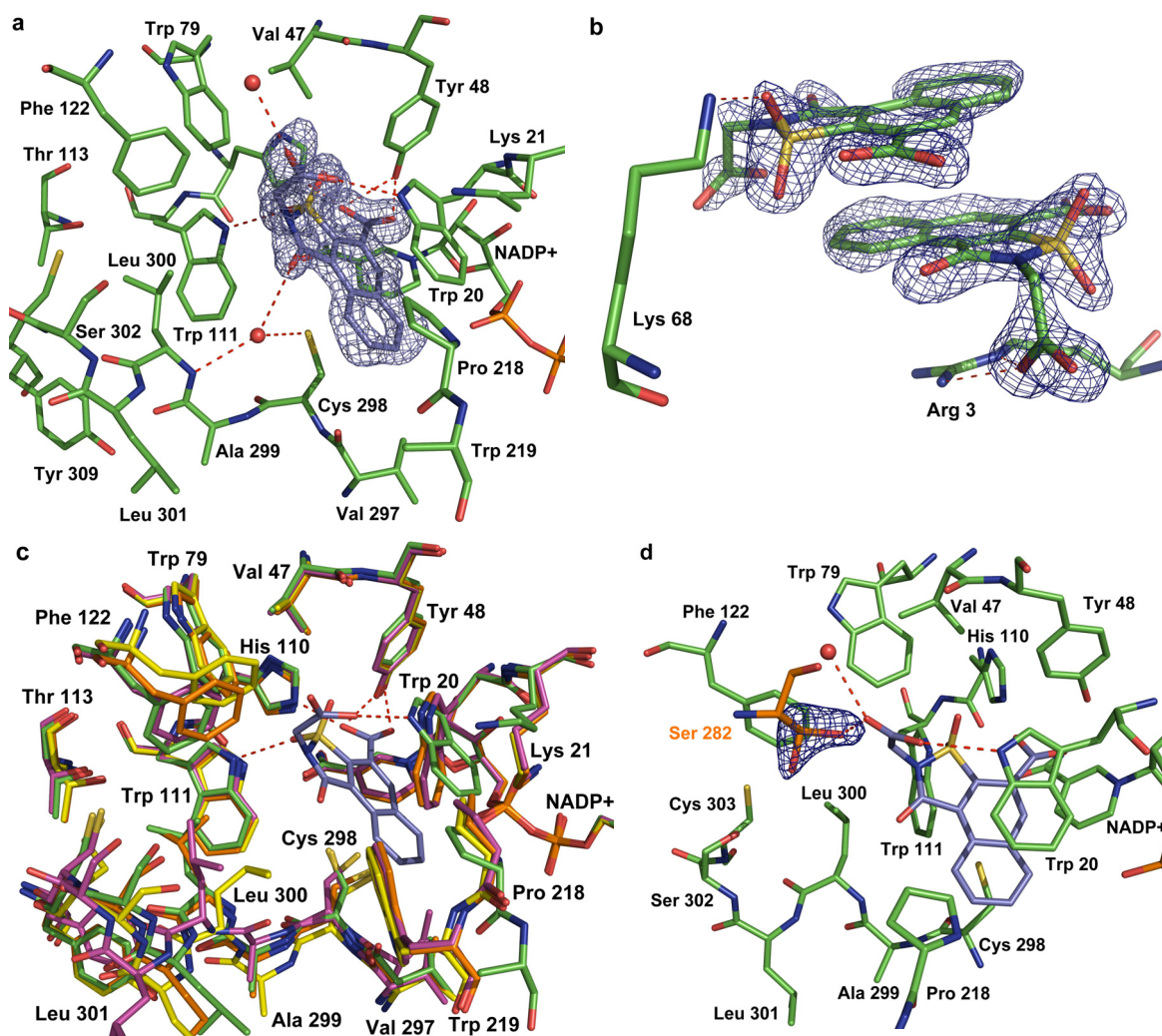


Figure 4.3. Refined model of ALR2 in complex with **2**. Key interactions are shown as red dotted lines and water molecules as red spheres. (a) Binding geometry of **2** within the ALR2 binding site. Protein residues and cofactor are depicted in green, the ligand is shown in dark blue. Omit $F_o - F_c$ difference density for the ligand is represented in blue at 3σ . Remarkably, the ligand acetic acid side chain folds back over the heteroaromatic system imposing pyramidal geometry at the sulfonamide nitrogen. The naphthyl moiety is clamped between the side chains of Trp 20 and Cys 298. In particular, Trp 20 performs an unexpected rotation via its χ_2 ($\sim 35^\circ$) angle creating additional binding pocket space to accommodate **2**. (b) Two additionally incorporated ligand molecules perform a mutual π - π stacking to each other. One of the ligands establishes cation- π interactions to the guanidine group of Arg 3. The omit $F_o - F_c$ difference density for both ligands is shown in blue at 2.5σ . (c) A superposition of ALR2-**2** (green, ligand in blue) with the three known pocket conformations (sorbinil-bound orange, tolrestat-bound yellow, IDD 594-bound magenta, ligands omitted for clarity) depicts the high plasticity in the C-terminal loop region lining the specificity pocket, whereas the catalytic cleft exhibits only minor induced-fit adaptations in the previously determined structures. In our ALR2-**2** complex adaptations extend to the region next to the catalytic center (Trp 20, Lys 21, Pro 218, Trp 219). (d) A hydrogen bond is formed between the ligand's acetic acid carboxylate and Ser 282 O γ of a symmetry-related protein molecule. The latter residue (orange) is found in split orientation and only the minor populated rotamer (43 % occupancy) interacts with the ligand. The omit $F_o - F_c$ difference density for both serine conformations is shown in blue at 3σ . Assuming full occupancy for **2**, this observation suggests the binding geometry to be unaffected by packing effects involving this hydrogen bond.

and **3**. They were refined to a resolution of 1.55 and 1.65 Å, respectively. The complex with the more potent **2** (IC₅₀ 0.14 μM) was obtained by soaking of preformed crystals in an appropriate ligand solution. Crystals soaked with the slightly weaker binding **3** (0.55 μM) showed no appropriate difference electron density for the ligand after one day exposure time. Thus, the ALR2-**3** complex was obtained by cocrystallization.

As expected, both crystal structures represent ALR2 in the typical TIM-barrel fold with bound NADP⁺. Well defined omit F_o-F_c electron density is observed for both inhibitors. The ALR2-**2** complex contains in total three inhibitor molecules, of which one is located in the binding pocket (Fig. 4.3a), whereas two additional molecules are located near the side chain of Arg 3. One of them establishes a cation-π- stacking to the guanidine group of the latter residue (Fig. 4.3b). Furthermore, both ligands interact via π-π-stacking exposing their naphthyl moieties in an face-to-face orientation. In contrast to the expected tolrestat-like binding geometry, the ligand accommodated in the binding site leaves the specificity pocket in closed state. The protein conformer, thus, resembles the sorbinil-bound state. Nevertheless, ligand binding induces surprising changes with respect to Trp 20 (Fig. 4.3c): this residue alters its χ_2 angle by 35° compared to its orientation observed in all three parent pocket conformations. This rotation is accompanied by opening of a novel sub-pocket never observed in any other ALR2-complex structure. It hosts the naphthyl portion of the ligand and forms via the Trp 20 indole moiety a tight face-to-face π-π stacking (3.3 Å between the two aromatic planes). The newly created pocket is further extended by a 90° rotation of the Cys 298 χ_1 moving the side chain of this residue towards the specificity pocket. In most known structures the thiol group points towards Trp 20, or, as indicated in well-resolved structures, it exhibits two split conformations. The observed geometry establishes an arene-sulphur interaction via 3.5 Å (sulphur to aromatic naphthyl distance). Furthermore, in contrast to the expected tolrestat-like binding mode, the catalytic pocket is not occupied by the acetic acid carboxylate side chain present in 2-position, but the second carboxylate group at position 4 directly connected to the naphthyl portion. This is presumably involved in a charge-assisted hydrogen bond network to Tyr 48 OH and His 110 Nε2, whereas the H-bond to Trp 111 Nε1 is not maintained in the present complex (5 Å). Instead, the latter contact is established by one of the sulfolactam oxygens. The carbonyl oxygen at position 1 accepts a hydrogen bond from an interstitial water molecule, which is additionally coordinated by the sulfur atom of Cys 298 and the NH group of Leu 300. The carboxylate group attached at 2-position

via a methylene bridge participates in several interactions: Via one of its carboxylate oxygens it accepts a hydrogen bond from Trp 20 Nε1 (3.0 Å). Therefore, a kinked orientation of the acetic acid side chain is required, which is obviously facilitated by the pyramidal geometry at the sulfonamide nitrogen in order to avoid a clash with the phenyl moiety of Phe 122. This pyramidal geometry is surprising as a planar geometry appears more favourable for an imide-type nitrogen. The question arises, whether this pyramidal geometry is reinforced by the formation of the interactions to the protein. Usually in such cases, a small molecule crystal structure would be evaluated. However, in the present example two additionally incorporated ligand molecules are bound near Arg 3 (Fig. 4.3b), which are less clamped via short distant interactions with the protein. Here, in both ligand molecules the sulfonamide nitrogen clearly exhibits planar geometry. This observation suggests that the pyramidal geometry found for the active-site ligand is obviously reinforced by binding. Finally, it forms a hydrogen bond to a side chain oxygen of Ser 282 of a symmetry-related molecule via a 2.8 Å distance (Fig. 4.3d). Formation of H-bonds in the crystal packing to neighbouring molecules might pretend a binding mode irrelevant under non-crystalline conditions. However, the symmetry-related Ser 282 exhibits two split conformations: the major one (57 % occupancy) is oriented towards the solvent, whereas the minor populated variant points towards the acetic acid carboxylic group of the ligand. Assuming full ligand occupancy, these findings suggest, that the formation of this particular H-bond is not determinant for the adopted binding geometry.

The formation of the novel subpocket is accompanied by further remarkable changes of the binding site environment. A search with Relibase²⁵ retrieves a superposition of all PDB-deposited aldose reductase crystal structures. This search indicates (with exception of two structures) that Lys 21, probably protonated, forms two charge-assisted hydrogen bonds to one of the phosphate groups of the cofactor (~2.8 Å) and to the carboxylate side chain of Asp 216 (~3.0 Å). However, upon the 35°-rotation of the Trp 20 indole portion observed in our structure, these contacts are lost to prevent clashes between Trp 20 and Lys 21 (Fig. 4.3c). Instead, Lys 21 points towards the solvent. This loss of interactions seems non-crucial for cofactor binding, as no elevated temperature factors are observed for NADP⁺ (10.1 Å²) suggesting full occupancy. In addition, the solvent-exposed region Pro 218 to Pro 225 is shifted off from the binding cavity. With respect to the 0.66 Å resolution structure of the ALR2-IDD 594 complex (Fig. 4.2c), this shift results in a C_α RMSD of 0.9 Å for this loop region. In particular,

in ALR2-2 Trp 219 does not only experience a backbone atom shift of ~ 3.0 Å (compared to ALR2-IDD 594) but this rearrangement is accompanied by a rupture of the H-bond between Trp 219 N ϵ 1 and the carbonyl oxygen of Val 297. The latter contact is usually observed in other structures (2.8 Å). The loss of this contact is presumably related to the poorly defined electron-density observed for the indole moiety of Trp 219, which suggests disorder of the side chain to provide space for ligand accommodation. This side chain would otherwise clash with the naphthyl moiety of the inhibitor. Furthermore, the side chains of Pro 218 and Val 297 participate in the formation of the hydrophobic subpocket by providing van der Waals contacts to the naphthyl portion (4.8 and 4.3 Å, respectively).

Facing our ALR2-2 complex to all deposited aldose reductase structures using Relibase,²⁵ the opening of this subpocket becomes evident as a unique pocket conformer not yet described previously. Could this novel geometry be predicted by any other method? A ‘flexibility scale’ has been suggested for active site residues by facing ligand-bound and corresponding uncomplexed binding pockets.²⁶ Statistical evidence could be collected that certain residues (e.g. lysine) experience more frequently a ligand-induced adaptation than others (e.g. cysteine or phenylalanine). Surprisingly, tryptophane exhibited the lowest statistical prevalence for mobility upon ligand binding. According to this investigation, the flexible behaviour of Trp 20 and Trp 219 observed in our ALR2-2 complex appears quite surprising.

Are molecular dynamics (MD) simulations reliable to reveal evidence for the opening of this novel subpocket by providing corresponding snapshots during the regarded trajectory? Recently, we reported an extensive MD analysis of the dynamic properties of complexed and uncomplexed ALR2 at two different temperatures.²⁷ This study suggested enhanced mobility of Trp 219 but pronounced rigidity for all catalytic site residues including Trp 20. Thus, the opening of the novel subpocket could not be sampled by MD simulations, even at elevated temperature and in the uncomplexed state. In consequence, is this pocket conformer only induced by ligand binding? We suppose that the observed binding-site mobility is an inherent property of the protein, also observable in the absence of a bound ligand. Nevertheless, the MD simulation did not indicate this protein conformer. Whether this is due to an insufficient simulation time, an inappropriate setup of the simulation conditions or deficiencies of the force field is difficult to estimate. One has to note that a prerequisite for opening the pocket

consists in the rupture of two charge-assisted hydrogen bonds. This is unlikely to occur frequently along an MD trajectory.

It appears quite surprising that the observed adaptations occur in a region of the binding site that is responsible for the catalytic reaction. Even though the binding site residues have to possess some adaptability for substrate accommodation, it is quite generally postulated that the shape of site where the catalytic elementary steps are accomplished requires a firmly fixed spatial arrangement.

As described above, **2** interacts with the catalytic site using its 4-carboxylate anchor group. In **3**, this carboxylate group is involved in an ester bond formation with glycolic acid. Accordingly, the newly introduced acid functionality is much further remote from the naphthyl moiety. Considering the binding mode of **2** and the interaction pattern involving its 4-carboxylate, a distinct binding mode of **3** with the enzyme can be expected. Accordingly, these considerations prompted us to determine the crystal structure of the ALR2-**3** complex. A well-defined omit F_o-F_c difference electron density within the binding site allowed for an unambiguous ligand placement (Fig. 4.4a). Similarly to ALR2-**2**, in ALR2-**3** the specificity pocket is observed in closed state and the overall shape of the binding pocket resembles the sorbinil-bound state. Apart from this correspondence, the binding mode of **3** is totally different. The basic skeleton shared by **2** and **3** is found in the latter structure with reversed orientation (Fig. 4.4b).

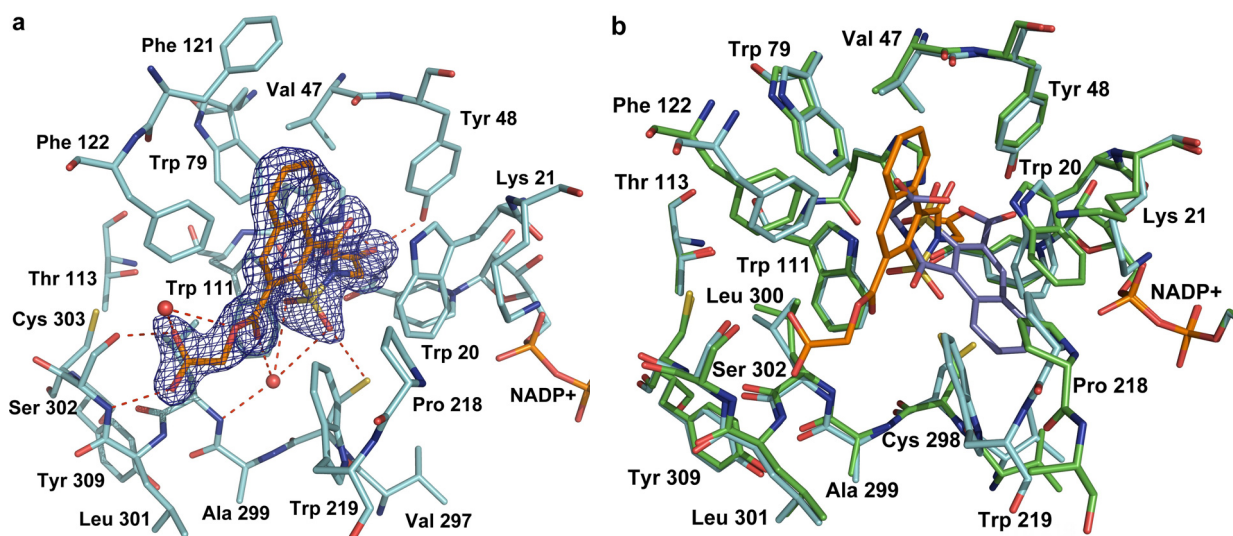


Figure 4.4. Refined model of the ALR2-**3** complex. The ligand is shown in orange, protein and cofactor residues are given in light blue. Water molecules are indicated as red spheres, key interactions are symbolized by red dotted lines. (a) Omit F_o-F_c difference density for the ligand is represented in blue at 3σ . In contrast to **2**, ligand **3** binds to the catalytic cleft via its acetic acid side chain without inducing strong conformational adaptations. (b) Despite **2** and **3** only differ with respect to the extended ester bond at the original 4-carboxylate, both ligands impressively adopt deviating binding modes (**2** in dark blue, protein and cofactor of ALR2-**2** in green, colour-coding for ALR2-**3** as in (a)).

In ALR2-**3**, it is now the acetic acid carboxylate group in position 2 that anchors the ligand in the catalytic site, whereas the extended acidic side chain in 4-position orients towards Ser 302. In the catalytic site Tyr 48 OH, His 110 Nε2, and Trp 111 Nε1 donate hydrogen bonds to the presumably deprotonated carboxylic acid. Interestingly, the sulfonamide nitrogen adopting pyramidal geometry in ALR2-**2**, exhibits planarity in ALR2-**3**. This provides further evidence that the pyramidal geometry of **2** is reinforced by the binding cavity. The sulfonyl group, in the previous complex involved in a H-bond to Trp 111 Nε1, interacts in ALR2-**3** with a water molecule via a distance of 3.4 Å. In addition, this water molecule is coordinated to the backbone NH group of Leu 300 and the carbonyl oxygen of the ester group at position 4. The thiole group of Cys 298 probably forms a weak hydrogen bond to one of the sulfonyl oxygen atoms. The acid group of the glycolic acid moiety accepts a hydrogen bond from Ser 302 Oγ (2.5 Å) and its backbone NH group (2.9 Å). The central heteroaromatic moiety intercalates between Trp 20, Trp 79, and Phe 122. The ester side chain is flanked by Trp 219. “Non-classical” hydrogen bonds are presumably formed between the ligand’s naphthyl moiety and the carbonyl oxygen of Val 47 (3.7 Å) as well as the ligand’s carbonyl oxygen and Tyr 48 Cε1 (3.6 Å). In contrast to the ALR2-**2** complex, the orientation of Trp 20, Lys 21, Pro 218, and Trp 219 are virtually identical to those observed in other crystal structures.

In order to evaluate whether the dramatic deviations with respect to the binding modes observed for **2** and **3** might be attributed to the different protocols used to produce the complexes (soaking or cocrystallization) or to varying crystal packing (P1 versus P2₁), we performed cocrystallization of **2**. The obtained complex crystallized now in the space group P1 (previously P2₁) similarly to ALR-**3** (P1). Nevertheless, it exhibits virtually identical binding geometry for ligand **2**. Accordingly, the different binding properties described for **2** and **3** are not a consequence of deviating crystallization protocols or crystal packing differences.

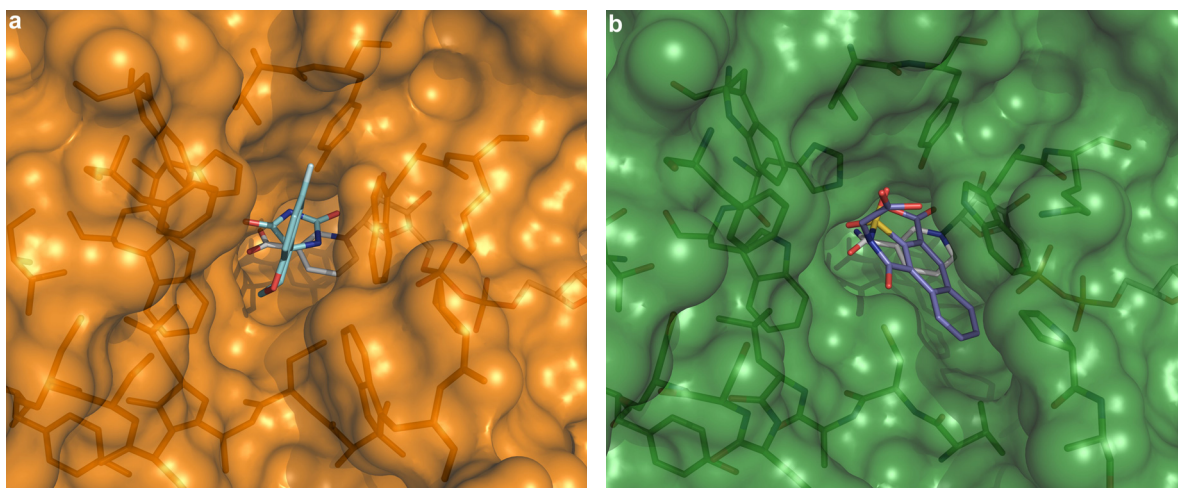


Figure 4.5. (a) Molecular surface representation (orange) of the ALR2 binding pocket conformer in sorbinil-bound state (cofactor in silver, sorbinil in light blue). (b) Molecular surface representation (green) of the binding pocket conformer accommodating **2** (cofactor in silver, **2** in blue). The illustration depicts that ALR2 adopts a novel pocket conformer upon complexation of **2**.

4.3 Conclusions

In the present study, two ALR2 crystal structures complexed with two congeneric ligands of the novel naphtho[1,2-*d*]isothiazole acetic acid series are described. Both ligands adopt a different binding geometry compared to the original design hypotheses. Interestingly enough, **2** selects a conformational state of the binding site opening a previously unknown subpocket (Fig. 4.5 a,b). In addition to the three well-characterized parent pocket conformers (sorbinil-, tolrestat-, and IDD594 bound state), this novel conformer can be exploited for further ligand design and virtual screening campaigns. With respect to the present case studies it would be interesting to probe whether current docking approaches are able to predict relevant binding modes.

In a recent report,²⁸ we used Autodock to place both ligands into either the sorbinil-, tolrestat-, and IDD594-bound pocket conformers. The binding geometry of **3** could be predicted reasonably well, particularly, if information about crystallographically observed water molecules was considered as part of the docking template. The sorbinil-bound state was correctly selected as most likely conformer. On the contrary, for **2**, where extended induced-fit adaptations are involved, the docking approach suggested properly the sorbinil-bound pocket as most likely solution. However, as the opening of a novel subpocket next to Trp 20 was not considered, significant deviations from the experimentally observed binding geometry have been noted. This emphasizes the

importance of including all available knowledge about the conformational space of the binding site residues into the docking campaign. This information should be extracted from all available crystal structures evaluated in a comparative analysis. In addition, elaborate MD simulations should be consulted to complement the crystallographic data by putative binding site conformers not yet seen in any crystalline complex.

The two crystal structures presented in this study provide further evidence to understand the structure-activity relationships of this novel ligand series. Roughly, the members of this congeneric can be divided into three groups. The inhibitors **2** and **3** possess submicromolar affinity and bear a carboxylate group in both, the 2- and the 4-position of the skeleton. The remaining two groups exhibit only one carboxylate attached either to the 2- or to the 4-position. The potency of the latter two groups deviates from **2** and **3** by about one to two orders of magnitude. As indicated in the two complexes, both carboxylates are involved in ligand binding. Thus, their removal or substitution should lead to a loss in affinity. Deletion of the 4-carboxylate results in a ligand with 10 μM affinity (Tab. 2, **6**). Assuming a similar binding mode as observed in ALR2-**3** with the 2-carboxylate serving as anchoring group in the catalytic site, this is presumably due to the loss of the interactions to the Leu 300 NH group mediated by a water molecule and to Ser 302 (Fig. 4.4a). Introduction of nitro or amino groups at the naphthyl moiety lacking the 4-carboxylate leads to a further affinity drop and results in IC_{50} values of 100 to 190 μM (Tab. 2, **7-10**). Again, assuming an ALR2-**3**-like binding mode these nitro or amino substituents should either point into the solvent or to the aromatic moiety of Tyr 48. If no other induced-fit adaptations occur, the binding site cannot provide any appropriate interaction partners for those groups. This provides a rational explanation why the introduction of these substituents is accompanied by an unfavourable desolvation enthalpy as they cannot establish comparable polar contacts in the complex. This results in an imbalanced polar contact inventory and has to be paid by a reduced affinity. Deletion of the 2-carboxylate results in a ligand of 88 μM affinity (Tab. 2, **11**). Assuming a binding mode as observed in ALR2-**2**, these ligands are likely to be bound less fixed and the hydrogen bond to Trp 20 N ϵ 1 will be lost. Finally, removal of the 2-carboxylate and extension of the 4-carboxylate by esterification with glycolic acid leads to an inactive compound (Tab. 2, **12**). The newly created carboxylate group is most likely too far remote from the aromatic skeleton to still interact effectively with the binding pocket.

The two protein-ligand complexes provide a further lesson to drug design: Generally, in order to optimize the binding properties of a given lead scaffold, medicinal chemists embark into a program of systematically modifying substituents. Accordingly, corresponding derivatives are synthesized and binding data are evaluated. Subsequent structure-activity relationships are hypothesized on the assumption that the binding mode of the main scaffold remains unchanged within the series of derivatives. Differences in binding are usually attributed to the varying substituents. However, this study provides an impressive example, that slight changes of the scaffold's decoration at a rather remote position are able to provoke dramatic changes with respect to the binding mode of the entire scaffold. Accordingly, experimental determination of the binding geometry is of utmost importance to develop reliable design hypotheses and to derive accurate structure-activity relationships.

4.4 Materials and Methods

Cloning, expression, purification and crystallisation of Aldose Reductase have already been described elsewhere.^{7-9,22} Prior to crystallisation, ALR2 solutions were concentrated to 20 mg/ml in 50 mM di-ammonium hydrogen citrate at pH 5 and mixed with a solution of the cofactor in oxidized state to achieve a molar ratio of ALR2:NADP⁺ of 1:3. After an equilibration period of one week, microseeding was performed. Crystals were grown at 293 K using the hanging drop vapor diffusion method. For soaking a saturated inhibitor solution in 50 mM di-ammonium hydrogen citrate, pH 5 containing 25 % (m/V) PEG 6000 was prepared. For cocrystallization, 3 μ L of this solution were added to a 15 μ L drop of the protein solution. Crystals were obtained one day after microseeding.

Data Collection. Data were collected at 100 K using a cryoprotectant solution of 40 % (m/V) PEG 6000 in 50 mM di-ammonium hydrogen citrate at pH 5. The data sets were collected on a RIGAKU copper rotating anode (Molecular Structure Cooperation) at 50 kV, 90 mA using a R-AXIS IV++ image plate system. For each frame the exposure time and oscillation range were set to 5 min and 0.5°, respectively. Data processing and scaling were performed using the HKL2000 package.²⁹

PDB entry	ALR2-2 complex	ALR2-3 complex
	2NVD	2NVC
Data collection and Processing		
No. of crystals used	1	1
Wavelength [Å]	1.5418	1.5418
Space group	P2 ₁	P1
Unit cell parameters		
a, b, c [Å]	49.4, 66.6, 47.1	40.0, 47.1, 46.9
α, β, γ [°]	90.0, 91.9, 90.0	76.2, 77.2, 67.8
Matthews coefficient [Å ³ /Da]	2.15	2.17
Solvent content [%]	42.7	43.4
Diffraction data		
Resolution range [Å]	50 – 1.55 (1.58 – 1.55)	50 – 1.65 (1.68- 1.65)
Unique reflections	42 162 (1 413)	32 788 (887)
R(I) _{sym} [%]	3.5 (16.9)	3.0 (24.7)
Completeness [%]	94.9 (63.7)	89.3 (48.3)
Redundancy	3.5 (2.3)	2.0 (1.9)
I/ σ (I)	39.3 (5.3)	27.5 (3.1)
Refinement		
Resolution range [Å]	30 – 1.55	50 – 1.65
Reflections used in refinement (work/free)	31 907 / 2 087	30 631 / 1 596
Final R values for all reflections (work/free) [%]	13.0 / 20.0	15.8 / 21.4
Final R values for reflections with F > 4 σ (work/free) [%]	12.8 / 19.5	15.3 / 20.8
Protein residues	315	315

Coenzyme	1	1
Inhibitor	3	1
Water molecules	214	247
RMSDs		
Bonds [Å]	0.01	0.008
Angles [°]	2.3	2.2
Ramachandran plot		
Residues in most favoured regions [%]	90.6	89.5
Residues in additional allowed regions [%]	9.4	10.1
Residues in generously allowed regions [%]	-	0.4
Mean B factor [Å²]		
Protein	16.1	22.3
NADP ⁺	10.1	15.1
Inhibitor	26.8	26.5
Water molecules	24.4	30.1

Table 4.1 Data collection and refinement statistics.

Structure Determination and Refinement. The coordinates of human ALR2 (PDB code 1el3)³⁰ were used for initial rigid-body refinement of the protein atoms followed by repeated cycles of conjugate gradient energy minimization, simulated annealing and B-factor refinement using the CNS program package.³¹ For ALR2-3, a molecular replacement was carried out previously using Phaser.³² Refinement at later stages was performed with the program SHELXL.³³ Here, at least 20 cycles of conjugate gradient minimization were performed with default restraints on bonding geometry and B-values. Five percent of all data were used for R_{free} calculation. Amino acid side-chains were fitted into sigmaA-weighted $2F_o - F_c$ and $F_o - F_c$ electron density maps using O.³⁴ After the first refinement cycle, water molecules and subsequently cofactor and ligand were located in the electron density and added to the model. Restraints were applied to bond lengths and angles, chiral volume, planarity of aromatic rings and van der Waals

contacts. Multiple side-chain conformations were built if an appropriate electron density was observed and maintained during the refinement, and if the minor populated side-chain showed at least 10% occupancy. During the last refinement cycles, riding H atoms were introduced without using additional parameters. In the ALR2-2 complex, poor electron density for the indole moiety of Trp 219 suggested disorder for this side chain. Accordingly, it was treated as an alanine during refinement. The final models were validated using PROCHECK.³⁵ Data collection, unit cell parameters and refinement statistics are given in Table 4.1. Figures were prepared using Isis Draw (MDL, San Leandro, USA) and Pymol.³⁶

Coordinates and structure factor amplitudes of the crystal structures have been deposited at the Protein DataBank with the PDB codes 2NVC and 2NVD.

4.5 References

1. Davis, A. M., Teague, S. J. & Kleywegt, G. J. (2003). Application and limitations of X-ray crystallographic data in structure-based ligand and drug design. *Angew. Chem. Int. Ed.* **42**, 2718-2736.
2. Blundell, T., Jhoti, H. & Abell, C. (2002). High-throughput crystallography for lead discovery in drug design. *Nature Rev. Drug Discov.* **1**, 45-54.
3. Williams, S. P., Kuyper, L. F. & Pearce, K. H. (2005). Recent applications of protein crystallography and structure-guided drug design. *Curr. Opin. Chem. Biol.* **9**, 371-380.
4. Lundqvist, T. (2005). The devil is still in the details – driving early drug discovery forward with biophysical experimental methods. *Curr. Opin. Drug Discov.* **8**, 513-519.
5. Colletier, J. P., Sanson, B., Nachon, F., Gabellieri, E., Fattorusso, C., Campiani, G. & Weik, M. (2006). Conformational flexibility in the peripheral site of torpedo californica acetylcholinesterase revealed by the complex structure with a bifunctional inhibitor. *J. Am. Chem. Soc.* **128**, 4526-4527.
6. Teague, S.J. (2003). Implications of protein flexibility for drug discovery. *Nat. Rev. Drug Discov.* **2**, 527-540.
7. Howard, E. I., Sanishvili, R., Cachau, R. E., Mitschler, A., Chevrier, B., Barth, P., Lamour, V., Van Zandt, M., Sibley, E., Bon, C., Moras, D., Schneider, T. R.,

-
- Joachimiak, A. & Podjarny, A. (2004). Ultrahigh resolution drug design I: details of interactions in human aldose reductase-inhibitor complex at 0.66 Å. *Proteins* **55**, 792-804.
8. El-Kabbani, O., Wilson, D.K., Petrash, J.M. & Quioco, F.A. (1998). Structural Features of the aldose reductase and aldehyde reductase inhibitor binding sites. *Mol. Vis.* **4**, 19-25.
 9. Urzhumtsev, A., Tete-Favier, F., Mitschler, A., Barbanton, J., Barth, P., Urzhumtseva, L. *et al.* (1997). A 'specificity' pocket inferred from the crystal structures of the complexes of aldose reductase with the pharmaceutically important inhibitors tolrestat and sorbinil. *Structure* **5**, 601-612.
 10. Steuber, H., Zentgraf, M., Podjarny, A.D., Heine, A. & Klebe, G. (2006). High resolution crystal structure of aldose reductase complexed with the novel sulfonyl-pyridazinone inhibitor exhibiting an alternative active site anchoring group. *J. Mol. Biol.* **356**, 45-56.
 11. Varnai, P., Richards, W. & Lyne, P.D. (1999). Modelling the catalytic reaction in human aldose reductase. *Proteins* **37**, 218-227.
 12. Cachau, R., Howard, E., Barth, P., Mitschler, A., Chevrier, B., Lamour, V., Joachimiak, A., Sanishvili, R., Van Zandt, M., Sibley, E., Moras, D. & Podjarny, A.D. (2000). Model of the catalytic mechanism of human aldose reductase based on quantum chemical calculations. *J. Phys. IV France* **10**, 3-13.
 13. Brownlee, M. (2001). Biochemistry and molecular cell biology of diabetic complications. *Nature* **414**, 813-820.
 14. Evans, J. L., Goldfine, I. D., Maddux, B. A. & Grodsky, G.M. (2002). Oxidative stress and stress-activated signalling pathways: a unifying hypothesis of type 2 diabetes. *Endocrine Rev.* **23**, 599-622.
 15. Price, S. A., Agthong, S., Middlemas, A.B. & Tomlinson, D.R. (2004). Mitogen-activated protein kinase p38 mediates reduced nerve conduction velocity in experimental diabetic neuropathy. – Interactions with aldose reductase. *Diabetes* **53**, 1851-1856.
 16. Suzuki, L. A., Poot, M., Gerrity, R.G. & Bornfeldt, K.E. (2001). Diabetes accelerates smooth muscle accumulation in lesions of atherosclerosis. Lack of direct growth-promoting effects of high glucose levels. *Diabetes* **50**, 851-860.
 17. Nakamura, J., Kasuya, Y., Hamada, Y., Nakashima, E., Naruse, K., Yasuda, Y., Kato, K. & Hotta, N. (2001). Glucose-induced hyperproliferation of cultured rat

- aortic smooth muscle cells through polyol pathway hyperactivity. *Diabetologica* **44**, 480-487.
18. Suzen S. & Buyukbingol E. (2003). Recent studies of aldose reductase enzyme inhibition for diabetic complications. *Curr. Med. Chem.* **10**, 1329-1352.
 19. Da Settimo, F., Primofiore, G., La Motta, C., Sartini, S., Taliani, S., Simorini, F., Marini, A.M., Laveccia, A., Novellino, E. & Boldrini, E. (2005). Naphtho[1,2-*d*]isothiazole acetic acid derivatives as a novel class of selective aldose reductase inhibitors. *J. Med. Chem.* **48**, 6897-6907.
 20. Wilson, D. K., Tarle, I., Petrash, J. M. & Quioco, F. A. (1993). Refined 1.8 Å structure of human aldose reductase complexed with the potent inhibitor zopolrestat. *Proc. Natl. Acad. Sci. USA* **90**, 9847-9851.
 21. Steuber, H., Zentgraf, M., Gerlach, C., Sottriffer, C. A., Heine, A. & Klebe, G. (2006). Expect the unexpected or caveat for drug designers: multiple structure determinations using aldose reductase crystals treated under varying conditions. *J. Mol. Biol.*, in press.
 22. El-Kabbani, O., Darmanin, C., Schneider, T. R., Hazemann, I., Ruiz, F., Oka, M., Joachimiak, A., Schulze-Briese, C., Tomizaki, T., Mitschler, A. & Podjarny, A. (2004). Ultrahigh resolution drug design. II. Atomic resolution structures of human aldose reductase holoenzyme complexed with Fidarestat and Minalrestat: implications for the binding of cyclic imide inhibitors. *Proteins* **55**, 805-813.
 23. Kinoshita, T., Miyake, H., Fujii, T., Takakura, S. & Goto, T. (2002). The structure of human recombinant aldose reductase complexed with the potent inhibitor zenarestat *Acta Crystallogr. D* **58**, 622-626.
 24. Ruiz, F., Hazemann, I., Mitschler, A., Joachimiak, A., Schneider, T., Karplus, M. & Podjarny, A. (2004). The crystallographic structure of the aldose reductase-IDD 552 complex shows direct proton donation from tyrosine 48. *Acta Crystallogr. D* **60**, 1347-1354.
 25. Hendlich, M., Bergner, A., Gunther, J. & Klebe, G. (2003). Relibase: Design and development of a database for comprehensive analysis of protein-ligand interactions. *J. Mol. Biol.* **326**, 99-110.
 26. Najmanovich, R., Kuttner, J., Sobolev, V. & Edelman, M. (2000). Side-chain flexibility in proteins upon ligand binding. *Proteins* **39**, 261-268.

27. Sotriffer, C. A., Krämer, O. & Klebe, G. (2004). Probing flexibility and „induced-fit“ phenomena in aldose reductase by comparative crystal structure analysis and molecular dynamics simulations. *Proteins* **56**, 52-66.
28. Zentgraf, M., Steuber, H., Koch C., La Motta, C., Sartini, S., Sotriffer, C. A. & Klebe, G. (2007). How reliable are current docking approaches for structure-based drug design? *Angew. Chem. Int. Ed. Engl.*, in press
29. Otwinowski, Z. & Minor, W. (1997). Processing of X-ray Diffraction Data Collected in Oscillation Mode. *Methods Enzymol.* **276**, 307-326.
30. Calderone, V., Chevrier, B., Van Zandt, M., Lamour, V., Howard, E., Poterszman, A. *et al.* (2000). The structure of human aldose reductase bound to the inhibitor IDD 384. *Acta Crystallogr. D* **56**, 536-540.
31. Brunger, A. T., Adams, P. D., Clore, G. M., DeLano, W. L., Gros, P., Grosse-Kunstleve, R. W., Jiang, J. S., Kuszewski, J., Nilges, M., Pannu, N. S., Read, R. J., Rice, L. M., Simonson, T. & Warren, G. L. (1998). Crystallography & NMR system: A new software suite for macromolecular structure determination. *Acta Crystallogr. D* **54**, 905-921.
32. McCoy, A. J., Grosse-Kunstleve, R. W., Storoni, L. C. & Read, R. J. (2005). Likelihood-enhanced fast translation functions. *Acta Crystallogr. D* **61**, 458-464.
33. Sheldrick, G. M. & Schneider, T. (1997). SHELXL: high-resolution refinement. *Methods Enzymol.* **277**, 319-343.
34. Jones, T. A., Zou, J. Y., Cowan, S. W. & Kjeldgaard. (1991). Improved methods for building protein models in electron density maps and the location of errors in these models. *Acta Crystallogr. A* **47**, 110-119.
35. Laskowski, R., MacArthur, M., Moss, D. & Thornton, J. (1993). PROCHECK: a program to check the stereochemical quality of protein structures. *J. Appl. Crystallogr.* **26**, 283-291.
36. DeLano, W. L. (2002). The PyMOL Molecular Graphics System.
<http://www.pymol.org>

5. Tracing Changes in Protonation: A Prerequisite to Factorize Thermodynamic Data of Inhibitor Binding to Aldose Reductase

5.1 Introduction

Bio-molecular recognition involves the formation of non-covalent interactions that govern biological processes such as substrate binding and conversion by enzymes, or the assembly of protein-protein and protein-ligand complexes.¹ Crystal structure analysis provides detailed insights into the spacial arrangement of such complexes, whereas isothermal titration calorimetry (ITC) elucidates the thermodynamic properties of the binding process. The Gibbs free energy of binding (ΔG^0) can be factorized into enthalpic (ΔH^0) and entropic ($-T\Delta S^0$) contributions to unravel the driving forces of complex formation.²⁻⁵ They can be dominated by an enthalpic or entropic contribution. In due course of ligand optimization, the strategies to be followed can be rather different depending on whether an enthalpic or entropic driving force should be amplified. It has been suggested, that ligands optimized for enthalpic reasons can better escape resistance development caused by rapid mutagenesis of e.g., a viral target protein.^{6,7} In contrast, it can only be speculated that selectivity discrimination among multiple protein isoforms would require perfect protein-ligand shape complementarity usually paralleled by a pronounced optimization of entropic binding factors, e.g. by chemically arresting the ligand in its bioactive conformation, thereby reducing the conformational entropic penalty upon complex formation. One important contribution to binding are hydrogen-bonds formed between functional groups of the ligand and the protein. Depending on their protonation states different types of interactions and strengths will be formed. Particularly, if protonation or deprotonation creates charged species, significant contributions to binding affinity can occur. If the pKa value of a functional group falls next to the pH of the applied buffer conditions, partial protonation will occur. Such groups are referred to as “titratable groups”. Their protonation state depends on the local environment determining the distribution of charges and, in consequence, the adopted pKa value. Protonation states of titratable groups are difficult to determine. The resolution of protein crystal structures is usually

not sufficient to allow for an unambiguous assignment of protonation states. The situation becomes even more complicated by the fact that the accommodation of a ligand may change the local electrostatics in the binding pocket as well and, accordingly, modulate the pKa values.⁸

In consequence, changes of protonation states of ligand and protein functional groups will occur upon ligand binding. They complicate the assignment of H-bond donor or acceptor properties.⁹ Furthermore, the interpretation of ITC measurements is affected by such changes: the experimentally observed heat signal comprises, besides the binding enthalpy, also all ionization enthalpies resulting from the transfer of protons between buffer components, ligand molecules, and titratable protein functional groups. Thus, before a meaningful factorization of the measured binding free energy (ΔG^0) into enthalpic and entropic contributions can be performed, all superimposed contributions from proton transfer reactions have to be subtracted from the measured heat signal.^{5,9,10} In this contribution we report on the application of ITC measurements combined with a mutagenesis approach and Poisson-Boltzmann (PB) calculations to trace changes in protonation states induced upon inhibitor binding to the enzyme human aldose reductase (ALR2). These observations are subsequently exploited to factorize the binding free energy into enthalpic and entropic contributions.

Human aldose reductase (E.C. 1.1.1.21) is a 36 kDa (β/α)₈-TIM-barrel folded aldo-keto reductase. It is the first enzyme of the polyol pathway and converts various aldehydes to their corresponding non-reactive alcohols using NADPH as reducing cofactor. The latter donates a hydride ion to the carbonyl carbon of the aldehyde, most likely followed by a subsequent proton transfer from one of the neighbouring acidic protein residues placed next to the intermediate substrate anion.^{15,16} Along the polyol pathway, ALR2 is of pathophysiological relevance. Under elevated blood glucose levels, present in patients suffering from diabetes mellitus, it converts a remarkable extent of glucose to sorbitol.¹⁷ The latter is subsequently oxidized to fructose by the NAD⁺-dependent sorbitol dehydrogenase, the second enzyme of the polyol pathway. Accordingly, increased flux of glucose via the polyol pathway leads to various biochemical imbalances such as osmotic and oxidative stress, pathological interferences with kinase cascades, apoptotic regulation, and cytokine signalling, altogether resulting in diabetic long-term complications.¹⁸⁻²¹ Thus, the development of ALR2-inhibitors (ARIs) has been proven to be a promising therapeutic concept.

The active site of ALR2 is located at the C-terminal region of the enzyme. The binding pocket is divided by Trp 111 into the catalytic and the specificity subpocket. The latter shows distinct conformational adaptations depending on the bound ligand. The deeply buried substrate binding pocket comprises residues presumably participating in the catalytic reaction mechanism (Tyr 48, Lys 77, His 110), the nicotinamide moiety of NADP⁺, and Trp 111 which forms via its indole NH group an H-bond to most of the described ligand head groups. Further hydrophobic contacts can be formed by the side chains Trp 20, Val 47, Trp 79, and Trp 219 (Fig. 5.1). This catalytic cavity is usually addressed by hydrophilic, negatively charged functional groups of the ligands. Decorated at the opposing end with appropriate hydrophobic groups, these ligands can provoke pronounced “induced-fit” adaptations. A specificity pocket is formed by different rotameric states of Ala 299, Leu 300, and Phe 122 at the solvent exposed site and by the side chain of Trp 111 facing the protein interior.¹¹⁻¹⁴

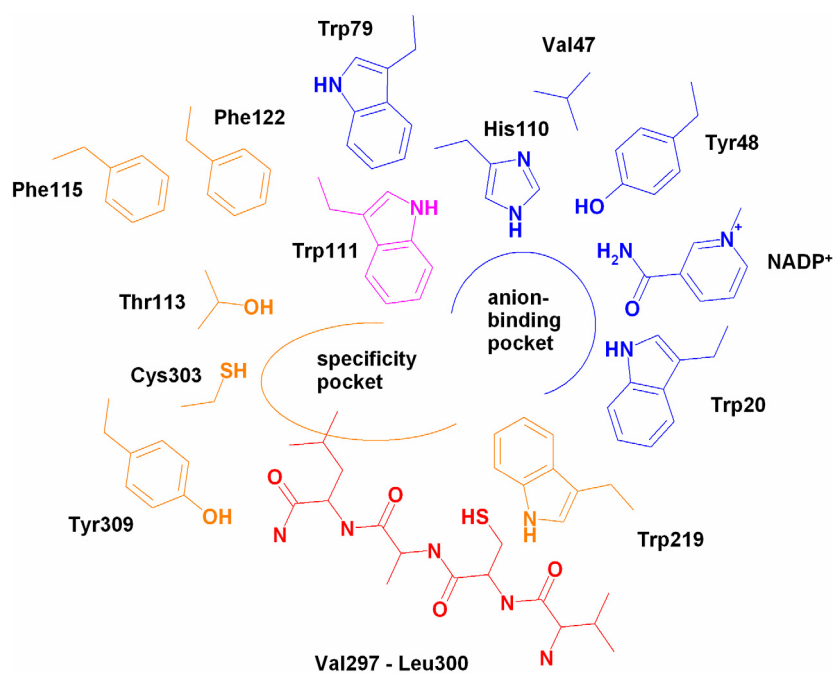


Figure 5.1. Schematic representation of the ALR2 binding pocket.³⁵ The catalytic site is represented in blue, the specificity pocket in orange. Amino acids exhibiting high mobility throughout several crystal structures are shown in red. Trp 111 dividing the entire binding pocket into the two subpockets is shown in magenta.

In order to study the driving forces of inhibitor binding, particularly with respect to the superimposed induced-fit adaptations, we performed ITC measurements paralleled with PB calculations to identify changes in protonation states upon ligand binding. After

correction of the superimposed ionization steps we factorized the binding free energy into enthalpic and entropic contributions.

5.2 Results and Discussion

5.2.1 Analysis of changes of the protonation inventory upon ligand binding

A detailed assignment of protonation states of the titratable groups after complex formation with a carboxylate-type inhibitor has been performed based on the 0.66 Å resolution ALR2-IDD 594 complex structure (**1**, Fig. 5.2).¹¹ The titratable groups of interest comprise the carboxylate function of the inhibitor and the side chains of Asp 43, Tyr 48, Lys 77, and His 110. The difference electron density in this ultra-high resolution structure suggests the carboxylate of IDD 594 (**1**, Fig. 5.2) to bind deprotonated.

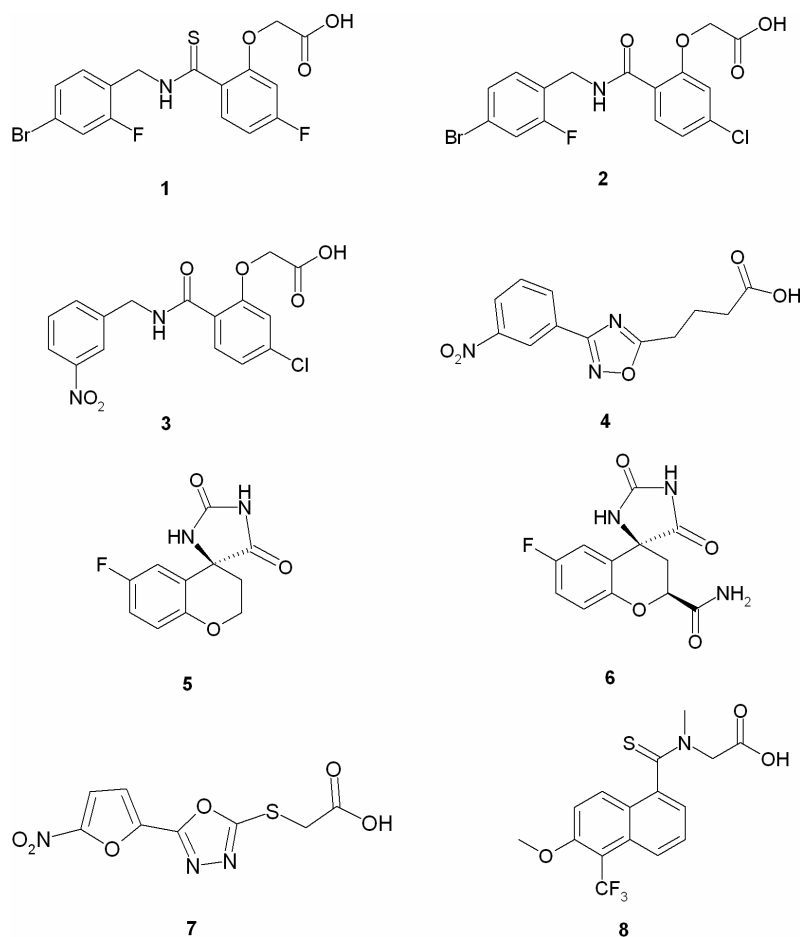


Figure 5.2. Chemical formulae of the studied aldose reductase inhibitors. **1** IDD 594, **2** IDD 388, **3** IDD 393, **4** and **7** lead compounds obtained by virtual screening, **5** sorbinil, **6** fidarestat, **8** tolrestat.

Via its oxygen O1 it accepts an H-bond from Trp 111 N ϵ 1 (3.1 Å). Oxygen O2 forms H-bonds to Tyr 48 OH (O-H bond vector pointing towards O2) and His 110 N ϵ 2 (2.7 Å, Fig. 5.3). Interestingly, the histidine is singly protonated at N ϵ 2, the second nitrogen N δ 1 accepts an H-bond from a neighbouring water molecule (2.9 Å). This geometry is further confirmed by neutron diffraction experiments based on single crystals produced from the fully deuterated protein. The negatively charged carboxylate of IDD 594 performs an electrostatic interaction with the positively charged nicotinamide ring of the cofactor (3.4 Å). Tyr 48 OH accepts a hydrogen bond from Lys 77 NZ, which is threefold protonated. In addition, Lys 77 is involved in a salt bridge to Asp 43 (2.7 and 3.4 Å between NZ and the carboxylate oxygens of Asp 43).

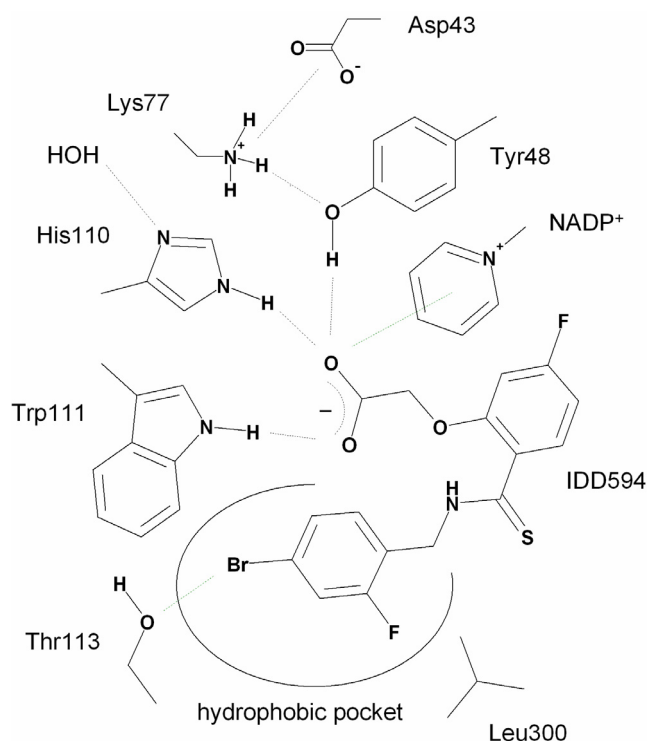


Figure 5.3. Schematic representation of the ALR2 binding pocket complexed with IDD 594 (1). The figure indicates the protonation states of the titratable residues as observed in the 0.66 Å resolution structure. Hydrogen bonds (black) and other polar contacts (green) are depicted as dashed lines.

Although the protonation states are well characterized after ligand binding, no comparable information is available for the uncomplexed holo-enzyme. To trace possible changes, we performed ITC measurements in four buffers of different ionization enthalpies. As the experimentally observed heat signal ΔH^0_{exp} comprises the binding enthalpy ΔH^0_{bind} and the contribution resulting from the ionization of buffer

molecules, a putative net proton uptake or release will be superimposed in the recorded heat signal ΔH_{exp}^0 (Equation 1).^{5,10}

$$\text{Equation 1} \quad \Delta H_{\text{exp}}^0 = \Delta H_{\text{bind}}^0 + n H_{\text{ion,buffer}}^0$$

Three carboxylate-type inhibitors, **2**, **3**, and **4**, were studied (Fig. 5.2): IDD 388 (**2**) exhibits a virtually identical constitution as IDD 594 (**1**) and places its carboxylate moiety almost exactly in the same position as IDD 594. Accordingly, protonation states of protein and ligand after binding to ALR2 can be assumed to be identical for **1** and **2**. The same is valid for IDD 393 (**3**) which is equipped with a meta-nitrophenyl moiety instead of a halogenated aromatic terminus (Fig. 5.4a). Inhibitor (**4**) was identified by virtual screening.²² Its carboxylate group binds to the catalytic site by picking up an interstitial water molecule which mediates an interaction to Trp 111.²³ This is accompanied by a shift of the carboxylate towards Tyr 48 resulting in hydrogen bonds to the latter (2.4 Å) and to His 110 Nε2 (2.5 Å, Fig. 5.4b). These structural deviations and putative changes of the local dielectricity caused by the incorporated water molecule revealed **4** as an interesting candidate for the analysis of protonation state changes.

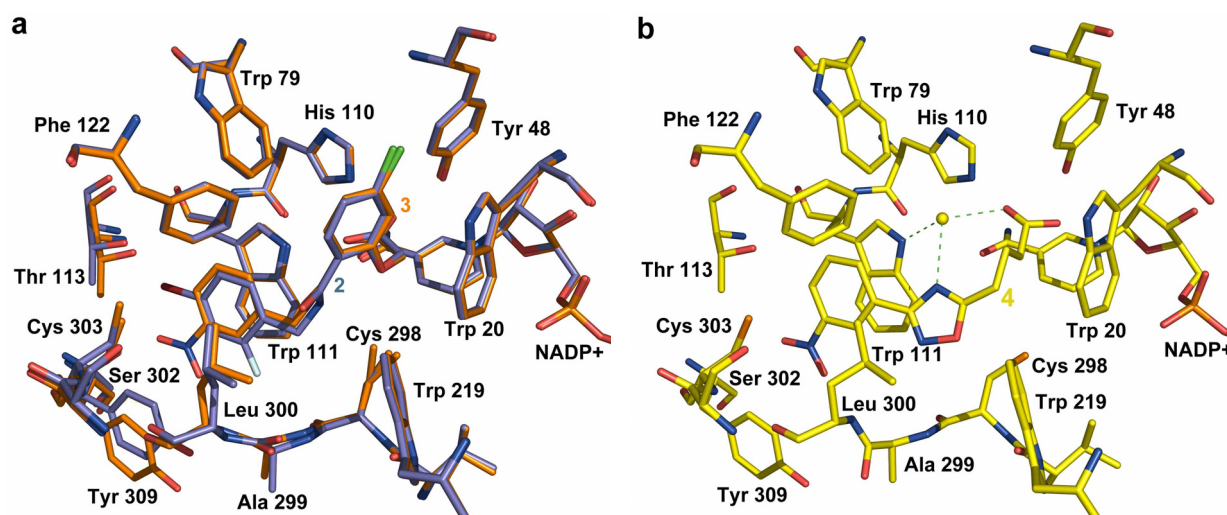


Figure 5.4. Binding mode of the ALR2 inhibitors **2** (blue), **3** (orange, superimposed in a), and **4** (yellow, shown in b). The interstitial water molecule only present in the ALR2-4 complex is shown as yellow sphere.

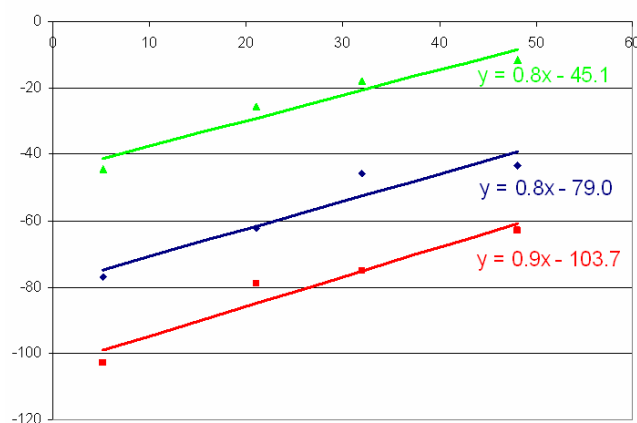


Figure 5.5. ΔH_{exp}^0 (y, in kJ mol^{-1}) versus $\Delta H_{\text{ion,buffer}}^0$ (x, in kJ mol^{-1}) plots for the carboxylate-type inhibitors **2** (blue), **3** (red), and **4** (green) titrated to wild type ALR2 in presence of NADP^+ . The positive slope represents the proton uptake of the protein-ligand complex upon binding.

The positive slope of the linear regression (Fig. 5.5) fitting ΔH_{exp}^0 versus $\Delta H_{\text{ion,buffer}}^0$ at pH 8 in presence of NADP^+ indicates a proton uptake upon complex formation with **2**, **3**, and **4**. In molar ratio, 0.8 ± 0.2 moles of protons are picked-up upon binding of **2**, and 0.9 ± 0.2 upon binding of **3**. Despite deviations in the carboxylate binding geometry, ALR2-**4** exhibits a comparable proton uptake of 0.8 ± 0.1 moles of protons. The low pKa values of the studied carboxylate-type inhibitors, suggest their carboxylate groups as almost completely dissociated in aqueous solution. Thus, the proton pick-up derives from deprotonation of the buffer molecules resulting in the ΔH_{exp}^0 versus $\Delta H_{\text{ion,buffer}}^0$ dependency.

As mentioned, the high-resolution ALR2-IDD 594 complex suggests Tyr 48 OH, Lys 77 NZ, and His 110 Nε2 to be in protonated state, and the ligand's carboxylate in deprotonated situation. Thus, the question remains which titratable residue is responsible for the proton uptake recorded by our ITC measurements. As prior to factorization an appropriate correction for the ionization enthalpy of the involved functional group has to be performed to reveal the net ΔH_{bind}^0 , this issue is of utmost importance. As neither sufficiently resolved crystal structures or neutron structures, nor NMR data for the uncomplexed holo-enzyme are available, we consulted pKa calculations[‡] considering the crucial titratable active site functional groups. We used the PB solver MEAD²⁴ based on our recently developed PEOE_PB charge model.⁹

[‡] All pKa calculations discussed in this chapter were carried out by Dr. Paul Czodrowski, Fachbereich Pharmazie, Philipps-Universität Marburg

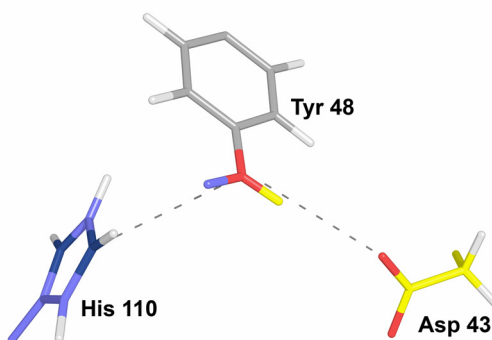
We started from the complexed crystal structures of ALR2 and removed **2-4** from their binding sites to investigate the resulting pKa shifts. The analysis of ligand-deleted structures is a very pragmatic approach, as a geometry for the uncomplexed protein is generated by simply removing the three ligands from the complex neglecting putative adaptations of the binding cavity upon removal of the ligand. However, we applied this approach successfully for other examples.^{25,26} The influence of the dielectric constant by using different values ($\epsilon_{\text{protein}} = 10$ or 20) and the impact of the orientation of the conformationally flexible Tyr 48 OH group with respect to its pKa value were studied (Table 5.1).

Tyr 48 OH towards	ϵ	2	3	4	mean (std dev)
Asp43	10	5.82	6.27	6.79	6.29 (0.49)
His110	10	8.45	8.52	9.09	8.69 (0.35)
Asp43	20	7.70	7.84	8.15	7.90 (0.23)
His110	20	8.72	8.78	9.13	8.88 (0.22)

Table 5.1. Calculated pKa values for Tyr 48 OH of the uncomplexed holo-enzyme (cofactor considered in oxidized state).

For xylanase, we were able to describe a pronounced influence of the Tyr 80 OH orientation on the pKa value of an active site glutamate.⁹ In ALR2, the two Tyr 48 OH orientations shown in Fig. 5.6 were considered for all three ligand-deleted structures. The estimated pKa values for Tyr 48 and His 110 are given in Table 5.1 and 5.2, respectively. For His110, N δ 1 has been defined as sole titratable group. This setting considers the fact that N ϵ 2 is involved in a direct hydrogen bond to the ligand. For the remaining titratable residues of the active site, Asp 43 and Lys 77, no pKa values suggesting strong shifts from the standard values were observed and they are, hence, not listed in the Tables.

Figure 5.6. The two studied orientations of the Tyr 48 OH group: it is either oriented towards Asp 43 (yellow) or His 110 (blue).



The orientation of the Tyr 48 OH-group shows a remarkable influence. Choosing the orientation towards Asp 43 and a dielectric constant of 10 reveals a mean pKa value of 6.29 which corresponds to virtually full deprotonation (Table 5.1) in the uncomplexed state. For His 110, rather low pKa values are suggested indicating an uncharged, singly protonated state of this residue (Table 5.2). The calculations for the considered protein residues in ligand-bound state are listed in Table 5.3. They suggest, in agreement with the crystallographic results, that the carboxylic group of the ligand remains

Tyr 48 OH towards	ϵ	2	3	4	mean (std dev)
Asp43	10	-1.40	-1.70	-1.47	-1.52 (0.16)
His110	10	-1.75	-2.02	-1.80	-1.86 (0.14)
Asp43	20	2.34	2.07	2.36	2.26 (0.16)
His110	20	1.97	1.78	2.02	1.92 (0.13)

Table 5.2. Calculated pKa values for His 110 N δ of the uncomplexed holo-enzyme (cofactor considered in oxidized state).

deprotonated. Furthermore, the calculations indicate a strong pKa shift for Tyr 48 towards basic values, whereas the values for His 110 remain in the acidic range. These findings suggest, in agreement with crystallographic evidence, that Tyr 48 acts as proton acceptor upon complexation and adopts a neutral state in ligand-bound situation. In contrast, His 110 does not experience comparably strong pKa shifts and remains uncharged upon ligand complexation. Considering the value for Tyr 48 before complexation (4 % protonation, $\epsilon = 10$) a net uptake of $n_{\text{calc}} = 0.96$ moles of protons is suggested. This value is in good agreement with experiment. The pKa calculations performed for $\epsilon = 20$ suggest a similar trend, even though agreement with experimental data is less satisfactory.

ϵ	2		3		4		n_{calc}
	pKa		pKa		pKa		
	Tyr48	His110	Tyr48	His110	Tyr48	His110	
10	16.15	1.92	17.16	1.61	31.10	2.54	+0.96
20	13.67	5.48	14.37	5.14	16.33	5.60	+0.51

Table 5.3. Calculated pKa values for Tyr 48 and His 110 of the complexed enzyme (cofactor considered in oxidized state).

Likely, our calculations overestimate the upward pKa shift of Tyr 48, but the trends are correctly suggested. For the ligand-deleted ALR2-2 crystal structure, variants to the standard settings were examined: (a) the explicit consideration of one water molecule which donates a hydrogen-bond from beyond the catalytic site to the N δ 1 atom of His 110, (b) the titration of His 110 N ϵ 2 instead of N δ 1. The effect of the explicit inclusion of the water molecule is rather marginal – it modulates the values by less than 0.1 pKa units for Tyr 48. Also switching to N ϵ 2 as titratable group of His 110 results in pKa values for Tyr 48 which deviate by only 0.5 log units (predicting a higher pKa value for Tyr 48 compared to the N δ 1 titration).

At first glance, our computational results suggest Tyr 48 OH as likely candidate for proton acceptance. This premise appears rather surprising in light of the fact that residues such as histidine, aspartate or lysine are in close neighbourhood which are usually assumed to be responsible for protonation effects in catalytic sites. Nevertheless, the computer simulations prompted us to perform a mutagenesis of Tyr48 to phenylalanine (Y48F). Although kinetic measurements revealed that this mutant is catalytically inactive,²⁷ inhibitor binding should be accessible by ITC. As the affinity of NADP⁺ is virtually not influenced by the mutation ($K_{b(\text{WT}, \text{NADP}^+)} 6.3 \pm 0.7 \cdot 10^5 \text{ L mol}^{-1}$; $K_{b(\text{Y48F}, \text{NADP}^+)} 8.9 \pm 0.1 \cdot 10^5 \text{ L mol}^{-1}$), putative changes of the protonation inventory observed for the Y48F cannot be provoked by a different cofactor binding behaviour or altered population in the pocket. Table 5.4 summarizes the experimentally observed net change of the protonation inventory for WT.

Indeed, repetition of our ITC experiments with Y48F showed no buffer dependence ($n = 0.0 \pm 0.1$) upon binding of **2** (Fig. 5.7, dark blue). In agreement with our pKa calculations, these experimental results suggest the phenolic oxygen of Tyr 48 as proton acceptor. Accordingly, in the NADP⁺ bound state at pH 8, this residue is obviously deprotonated to about 80 % and becomes fully protonated upon inhibitor binding. Otherwise, the crystallographically observed hydrogen bond between the ligand's carboxylate group and Tyr 48 OH could not be established. Possibly, the negative charge of the deprotonated tyrosine in the holo-enzyme compensates to some extent the positive charge of the nicotinamide moiety of the oxidized cofactor (3.2 Å between Tyr 48 OH and C2 of NADP⁺) in absence of a ligand. This compensation will not be given in the uncomplexed Y48F mutant. Obviously, the electrostatic properties of the cofactor strongly influence the protonation state of Tyr 48 OH. These considerations prompted us to repeat the binding study of **2** with the reduced cofactor NADPH (Fig. 5.7, light

	2 (IDD388)		3 (IDD393)	4	5 (sorbiniil)		6 (fidarestat)	
	NADP ⁺	NADPH	NADP ⁺	NADP ⁺	NADP ⁺	NADPH	NADP ⁺	NADPH
ligand pKa value	2.8	2.8	2.8	4.3	8.4	8.4	7.9	7.9
neutral fraction of inhibitor prior to binding [%] ¹	~ 0	~ 0	~ 0	~ 0	71	71	44	44
Net change of protonation inventory (WT) ² [mole /mole complex]	0.8	0.2	0.9	0.8	0.1	- 0.5	0.3	- 0.3
Suggested proton uptake by Tyr 48 OH (WT) [mole / mole complex]	0.8	0.2	0.9	0.8	0.8	0.2	0.8	0.2

Table 5.4. Overview of protonation effects occurring upon ligand binding.

¹The neutral fraction of inhibitor has been calculated according to the Henderson-Hasselbalch equation. ²The net change of the protonation inventory for wild type (WT) has been observed experimentally, based on these results a proton uptake by the deprotonated fraction of Tyr 48 OH is suggested.

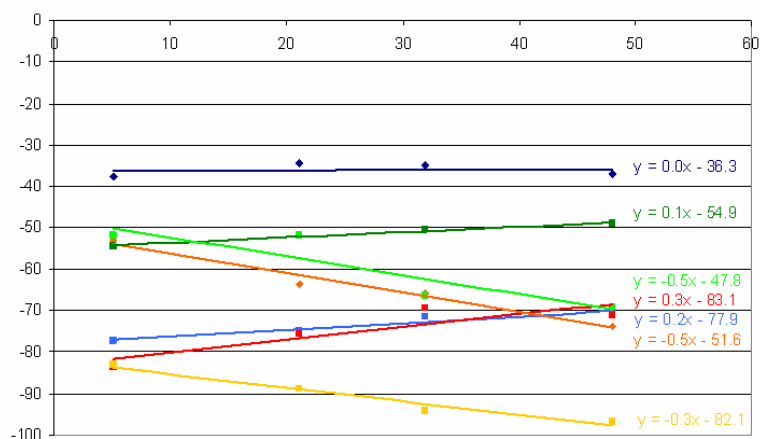


Figure 5.7. ΔH_{exp}^0 (y, in kJ mol^{-1}) versus $\Delta H_{\text{ion,buffer}}^0$ (x, in kJ mol^{-1}) plots for the titration of **2**, **5**, and **6** to ALR2 wild type and Y48F mutant in presence of NADP⁺ or NADPH. The slope indicates the net proton transfer. Titrations to the wild type enzyme are represented by ■, titrations to Y48F are shown as ◆. The titration of **2** to Y48F in presence of NADP⁺ is shown in dark blue, the one of **2** to wild type ALR2 is represented in light blue. Titrations of **5** to ALR2 in presence of NADP⁺ and NADPH are shown in dark green and light green, respectively. The results for **6** titrated to ALR2 in presence of NADP⁺ are given in red, those in presence of NADPH are shown in yellow, and those for Y48F in presence of NADP⁺ are represented in orange.

blue). Now, for the same ligand a proton uptake of 0.2 ± 0.04 moles is observed, suggesting Tyr 48 OH to be 80 % protonated in the uncomplexed NADPH-bound state. Assuming a 1:1 stoichiometry for inhibitor binding, these 0.2 moles of protons would be required to fully protonate Tyr 48 OH. These observations are in agreement with pH-dependent kinetic measurements²⁸ suggesting (for the C298A mutant) a Tyr 48 OH pKa value of 7.6 for the NADP⁺-bound and 8.25 for the WT-NADPH-bound state. Based on these findings, at pH 8 Tyr 48 should be deprotonated to 72 % in presence of NADP⁺, and to 36 % once NADPH is bound. However, these pKa estimations derived from kinetic experiments are to some degree substrate-dependent. In consequence, they do not exactly match with our thermodynamic evaluation.

Besides carboxylate-type inhibitors such as **1-4**, the hydantoin sorbinil (**5**) and its more potent derivative fidarestat (**6**) are well known inhibitors of ALR2. They exhibit strongly deviating pKa values in water compared to the carboxylate-type inhibitors (fidarestat: 7.9, sorbinil: 8.4). Accordingly, 55.8 % of **6** are deprotonated at pH 8 prior to binding. Our ITC experiments indicate a net uptake of 0.3 ± 0.1 moles of protons per mole bound inhibitor upon ALR2-**6** complexation in presence of NADP⁺ (Fig. 5.7, red). Following the assumption that Tyr 48 is to 80% deprotonated in the uncomplexed holo-enzyme, this net proton pick-up results from the superposition of the full protonation of Tyr 48 upon complexation and the release of 0.5 moles of protons by **6** which is to about 50 % protonated in solution and binds to the protein as deprotonated hydantoin. In this negatively charged state it accepts charge-assisted hydrogen bonds from His 110 Nε2 and Tyr 48 OH. This hypothesis is strongly supported by the fact that under the same conditions **6** binds to Y48F with a release of 0.5 ± 0.1 moles of protons per mole bound ligand (Fig. 5.7, orange). As the phenolic oxygen of Tyr 48 is missing in Y48F the entire protonation effect can be attributed to the proton release of the ligand (50 % protonated) to the buffer.

Replacing NADP⁺ by its reduced form under otherwise unchanged conditions results in a net release of $n = -0.3 \pm 0.05$ for the wild type protein (Fig. 5.7, yellow). Assuming Tyr 48 OH to be 80 % protonated in the NADPH-bound holo-state, this net inventory can be factorized into a release of 0.5 moles of protons from the partially protonated **6** superimposed by an uptake of 0.2 moles of protons by the 20 % deprotonated Tyr 48 OH to achieve full protonation.

A similar interpretation can be performed for the hydantoin sorbinil (**5**). According to its pKa value (8.4), at pH 8 the ligand is to 71 % protonated in aqueous solution.

Assuming full deprotonation of the hydantoin upon complexation along with an uptake of 0.8 moles of protons by Tyr48 should mutually compensate to a net pick-up of about 0.1 moles of protons in presence of NADP^+ . Indeed, for **5** we observe an experimental net change of 0.1 +/- 0.02 moles of protons (Fig. 5.7, dark green).

In presence of NADPH, where only about 0.2 moles of protons per mol bound inhibitor are picked up by Tyr 48 OH, a net release of approximately $n = -0.5$ mol protons should be expected. The experimental value of -0.5 +/- 0.2 mol protons (Fig. 5.7, light green) matches well with this interpretation.

5.2.2 Factorization into enthalpic and entropic contributions

In order to factorize the free energy of binding, the standard binding enthalpy ΔH_{bind}^0 has to be determined based on the original heat signal ΔH_{exp}^0 observed from the ITC experiment. According to equation 2, the following contributions superimpose with ΔH_{bind}^0 :

$$\text{Equation 2} \quad \Delta H_{\text{exp}}^0 = \Delta H_{\text{bind}}^0 + n_1 H_{\text{ion,buffer}}^0 + n_2 H_{\text{ion,protein}}^0 + n_3 H_{\text{ion,ligand}}^0$$

Values used for n_1 , n_2 , and n_3 are listed in Table 5.5. The entropic contribution $-T\Delta S^0$ has been calculated as difference between ΔG^0 and ΔH_{bind}^0 according to the Gibbs-Helmholz equation.

5.2.3 Correlation of thermodynamic and structural features

The mutation Y48F was initially performed to confirm Tyr 48 as atypically protonated residue predicted by our pKa calculations. In addition, the thermodynamic analysis reveals the energetic contribution of the Tyr 48 OH - ligand hydrogen bond to binding affinity. Two types of anchor groups, carboxylate (**2**) and hydantoin (**6**), have been studied for WT and Y48F binding. Table 5.6 lists the original heat signal (ΔH_{exp}^0) together with the corrected values (ΔH_{bind}^0) for the different ligands, with respect to wild type ALR2 and Y48F. The cofactor is considered in oxidized and reduced state. Interestingly, binding of the carboxylate-type inhibitor **2** appears to be more affected ($\Delta\Delta G^0 \sim 8.5 \text{ kJ mol}^{-1}$) by the loss of the Tyr 48 OH H-bond compared to the hydantoin **6** ($\Delta\Delta G^0 \sim 1.4 \text{ kJ mol}^{-1}$). Assuming similar architecture for both complexes, WT and Y48F, **6** is obviously better capable to compensate for the loss of the hydrogen bond, possibly by gradually increasing the strength of the remaining contacts to His 110 Nε2

cofactor		ligand	n_1 (buffer contribution)	n_2 (protein contribution)	n_3 (ligand contribution)
WT	NADP+	2, 4	0.8	- 0.8	0
		3	0.9	- 0.9	0
		5	0.1	- 0.8	0.7
		6	0.3	- 0.8	0.5
	NADPH	2	0.2	- 0.2	0
		5	- 0.5	- 0.2	0.7
6		- 0.3	- 0.2	0.5	
Y48F	NADP+	2	0	0	0
		6	- 0.5	0	0.5
	NADPH	2	0	0	0

Table 5.5. Net contributions for the protonation of functional groups in buffer, protein and ligand. Values of n_1 , n_2 , and n_3 are listed for the studied ligands under differing oxidation state of the cofactor for both wild type and Y48F. These values have been used for the calculation of ΔH_{bind}^0 according to equation 2.

and Trp 111 Nε1. This is also reflected by the standard binding enthalpies: the mutational loss of the Tyr 48 OH group is paralleled by a 23 kJ mol⁻¹ reduced binding enthalpy for **2**, whereas **6** experiences only half of this amount ($\Delta\Delta H_{\text{bind}}^0 \sim 11.5$ kJ mol⁻¹). Both, **2** and **6** show a more favourable entropic contribution for Y48F compared to WT ($-T(\Delta\Delta S^0)(\mathbf{2})$ 14.2 kJ mol⁻¹, $-T(\Delta\Delta S^0)(\mathbf{6})$ 10.1 kJ mol⁻¹). This might result from an entropically favourable higher residual mobility of the Phe 48 side chain (and possibly other residues) as a consequence of the Tyr 48 OH group loss as this residue maintains the hydrogen-bond network between Asp 43, Lys 77 and His 110 in the wild type.

The replacement of NADP⁺ by its reduced form decreases the free energy of binding by 2-3 kJ mol⁻¹ as shown for **2**, **5**, and **6**. This drop possibly occurs due to the reduced electrostatic interactions between the negatively charged ligand anchor group and the either positively charged or neutral nicotinamide ring of NADP⁺ or NADPH, respectively. Surprisingly, our factorization suggests a more favourable enthalpic

		K_b [10^6 L mol $^{-1}$]	ΔG^0 [kJ mol $^{-1}$]	ΔH_{exp}^0 [kJ mol $^{-1}$]	ΔH_{bind}^0 [kJ mol $^{-1}$]	$-T\Delta S^0$ [kJ mol $^{-1}$]
WT, NADP $^+$	2	31.5 +/- 8.5	-42.7 +/- 3.1	-79.0 +/- 5.9	-59.0 +/- 5.9	16.3 +/- 9.0
	3	25.0 +/- 4.1	-42.2 +/- 0.8	-103.7 +/- 5.0	-81.2 +/- 5.0	39.0 +/- 5.8
	4	1.65 +/- 0.34	-35.4 +/- 1.0	-45.1 +/- 4.4	-25.1 +/- 4.4	-10.3 +/- 5.4
	5	4.5 +/- 0.6	-37.9 +/- 0.7	-54.9 +/- 0.6	-54.7 +/- 0.7	16.8 +/- 1.4
	6	153.0 +/- 36.6	-46.7 +/- 1.2	-83.1 +/- 3.7	-79.5 +/- 4.0	32.8 +/- 5.2
	7	0.31 +/- 0.1	-31.3 +/- 1.6	-8.7 +/- 1.0	-5.6 +/- 1.0	-25.7 +/- 2.6
	8	4.6 +/- 1.2	-38.0 +/- 1.3	-34.1 +/- 0.8	-31.0 +/- 0.8	-7.0 +/- 2.1
WT, NADPH	2	13.3 +/- 2.0	-40.6 +/- 0.8	-77.9 +/- 1.2	-72.9 +/- 1.2	32.3 +/- 2.0
	5	1.3 +/- 0.2	-34.9 +/- 0.7	-47.8 +/- 5.1	-62.6 +/- 5.6	27.7 +/- 6.3
	6	61.7 +/- 15.9	-44.4 +/- 1.3	-82.1 +/- 1.5	-93.5 +/- 1.7	49.1 +/- 3.0
Y48F, NADP $^+$	2	1.0 +/- 0.2	-34.2 +/- 1.0	-36.3 +/- 1.5	-36.3 +/- 1.5	2.1 +/- 2.5
	6	86.9 +/- 16.5	-45.3 +/- 0.9	-51.6 +/- 1.7	-68.0 +/- 2.0	22.7 +/- 2.9
Y48F, NADPH	2	0.16 +/- 0.04	-29.7 +/- 1.2	-39.6 +/- 1.9	-39.6 +/- 1.9	9.9 +/- 3.1

Table 5.6. Thermodynamic parameters of the studied inhibitors.

contribution ΔH_{bind}^0 for inhibitor binding to the NADPH-bound enzyme compared to the oxidized state (**5**: ~ 8 kJ mol $^{-1}$, **2** and **6**: ~ 14 kJ mol $^{-1}$). At first glance, this is unexpected, as a loss of electrostatic interactions is assumed to be accompanied by a loss in binding enthalpy. However, the present case might be more complex. The positive charge on the nicotinamide moiety NADP $^+$ compared to the neutral system of NADPH will polarize the neighbouring groups involved in hydrogen bonding. This redistribution of charges can alter the strength of such hydrogen bonds^{30,31} resulting in an overall enthalpic advantage with the cofactor in the reduced state. The hypothesis of an enthalpically more favourable hydrogen-bond network involving the carboxylate group of, e.g., **2** in presence of NADPH compared to NADP $^+$ is also reflected by the binding thermodynamics to Y48F. In the mutant, the hydrogen bond to Tyr 48 cannot be established. In presence of NADP $^+$, the binding enthalpy drops by 22.7 kJ mol $^{-1}$ in

consequence of the mutation, whereas in presence of NADPH the corresponding drop in binding enthalpy amounts to 33.3 kJ mol⁻¹. This indicates that the H-bond loss in presence of NADPH demands an even larger enthalpic penalty. Overall, the difference in ΔG^0_{bind} of 8.5 kJ mol⁻¹ for WT-**2** and Y48F-**2** with bound NADP⁺ indicates a ΔG^0_{bind} contribution for the hydrogen bond. The corresponding pair in reduced state indicates a slightly larger value of 10.9 kJ mol⁻¹. The affinity difference for binding of **2** to the oxidized and reduced cofactor present in WT or Y48F amounts to 2.1 or 4.5 kJ mol⁻¹, respectively.

In order to analyse the deviating thermodynamic profiles, ΔG^0 , ΔH^0_{bind} , and $-T\Delta S^0$ are shown in Fig. 5.8 for the NADP⁺-bound WT enzyme. Two representatives of the IDD series (**2**, **3**), two ligands identified by a virtual screening campaign (**4**, **7**), tolrestat (**8**) and two hydantoin (**5**, **6**) are studied.

5.2.4 Thermodynamic consequences of substituent effects

Comparing the thermodynamic profiles of ligands sharing the same scaffold, a meaningful correlation between substituent patterns and thermodynamic driving forces becomes apparent. Whereas in **2** the terminal phenyl ring bears an ortho-fluoro and a para-bromo substituent, in **3** a meta-nitro group is present. The binding modes of **2** and **3** are displayed in Fig. 5.4. The aromatic portions of both ligands occupy the specificity pocket. **2** forms an electrostatic interaction between its bromo substituent and the side chain oxygen of Thr 113.

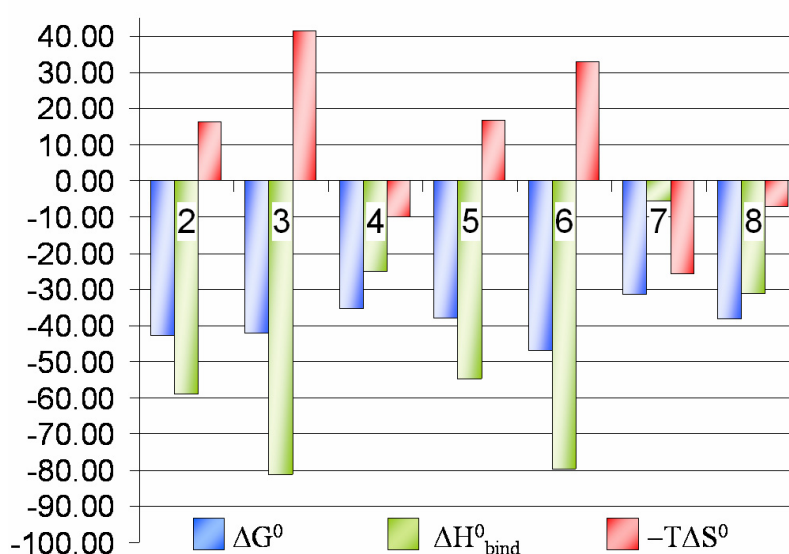


Figure 5.8. Bar diagram of the standard free energies of binding (blue) and its factorisation into enthalpic (green) and entropic (red) contributions for the inhibitors **2-8** in presence of NADP⁺. All values are given in kJ mol⁻¹.

In contrast to the latter complex, **3** induces structural changes in the Ala 299-Leu 300 peptide region, thus facilitating hydrogen-bond formation between Leu 300 NH and one of the nitro oxygens. Furthermore, the side chain of Tyr 309 is shifted and the nitro group accepts two non-classical hydrogen bonds from the aromatic dipolar C-H groups of Tyr 309.²³ This is obviously accompanied by a more favourable enthalpic contribution ($\sim 22 \text{ kJ mol}^{-1}$) paralleled by a compensating entropic penalty. The latter might be the price which has to be paid due to a more pronounced spatial arrest of the ligand provoked by these additional interactions and the required adaptations of the protein. Despite this deviating thermodynamic factorization, both ligands share a virtually identical free energy of binding.

The ligands **4** and **7** (Fig. 5.2) both possess a terminal nitro-aromatic tail linked to an oxadiazole ring which is further connected by a two- or three-membered alkyl spacer to the carboxylate anchor group. Even though both share a similar overall topology, their thermodynamic profiles differ remarkably. In contrast to the pairs **2**, **3** and **5**, **6**, their binding is favoured by either enthalpic and entropic contributions, nevertheless to varying extent. **4** picks-up a water molecule mediating the hydrogen bond between its carboxylate and Trp 111 N ϵ 1. Furthermore, it exhibits one additional rotatable bond compared to **7** and, thus, becomes likely more restrained upon binding compared to its solvated state. The incorporation of a water molecule is enthalpically favourable and entropically unfavourable. Furthermore, the immobilization of one additional rotatable bond in **4** should be entropically detrimental. Therefore, binding of **7** shows an entropic advantage compared to **4**. Both ligands, **4** and **7**, possess an oxadiazole ring with deviating topology. In the ALR2-**4** complex, the oxygen and one nitrogen are saturated by polar contacts to the sulfur atom of Cys 298 (3.5 Å) and the interstitial water molecule (2.8 Å), respectively. However, none of the heteroatoms in the oxadiazole of **7** finds appropriate binding partners. In addition, **7** possesses a furan ring as terminal aromatic moiety and a sulfur atom incorporated into the aliphatic spacer. Also these heteroatoms are poorly saturated by polar contacts in the complex, as only the sulfur atom forms a weak hydrogen bond to a bulk water (3.5 Å). These polar heteroatoms which remain unsaturated in the complex contribute enthalpically unfavourable, as they implicate an imbalanced solvation/desolvation inventory. In summary, for **7** more polar groups remain unsatisfied compared to **4** resulting in a $\sim 4 \text{ kJ mol}^{-1}$ reduced binding affinity. Likely, also in case of **4** the replacement of non-saturated heteroatoms would improve the enthalpic binding contribution.

The carboxylate-type inhibitor tolrestat (**8**) possesses a similar thermodynamic profile as **4**, with a 6 kJ mol⁻¹ more favourable binding enthalpy and a 3 kJ mol⁻¹ less favourable entropic contribution resulting in a 3 kJ mol⁻¹ more favourable ΔG^0 . This observation is to some extent surprising, as **8** does not pick-up a water molecule upon complex formation and exhibits a more rigid skeleton. However, it induces a distinct protein binding pocket conformer up to now only observed for **8** and adopts a different binding geometry. Besides polar contacts involving the carboxylate head group, a hydrogen bond between Ser 302 O γ and one fluorine atom of the ligand is formed (2.9 Å). A comparison of the nonpolar surface buried upon binding of **4** and **8** reveals that in the latter complex about 150 Å² additional nonpolar surface area is buried, whereas in ALR2-**4** about 50 Å² additional polar surface are removed (ALR2-**4**: buried polar surface: 240.3 Å², buried apolar surface: 373.2 Å²; ALR2-**8**: buried polar surface 187.2 Å², buried nonpolar surface 519.7 Å²). Due to the different protein conformations induced by accommodation of both ligands, the thermodynamic data are difficult to compare. The more enthalpic binding of **8** compared to **4** could possibly be explained by a more favourable desolvation of **8** following the concept of the ‘non-classical hydrophobic effect’.³²

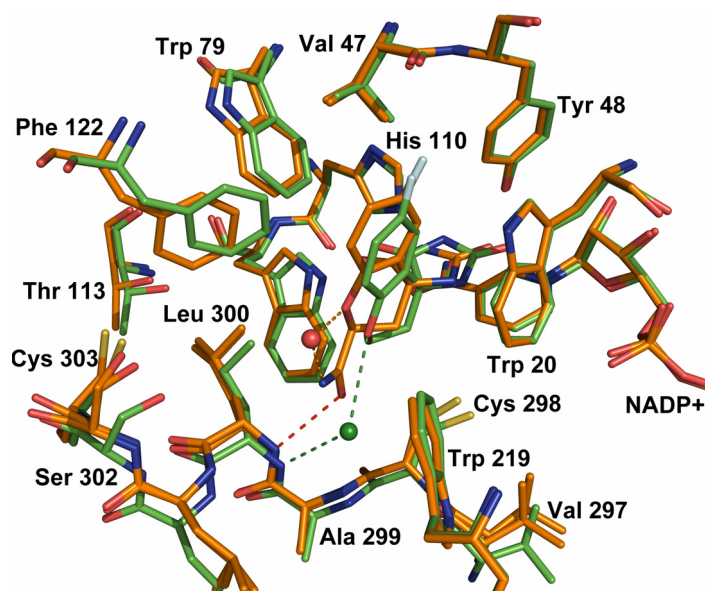


Figure 5.9. Superposition of the ALR2 binding pocket complexed with **5** (green), and **6** (orange). The interstitial water molecule only present in the ALR2-**5** complex is shown in green, whereas the water captured by fidarestat is given in red. Corresponding H-bonds are shown as dashed lines. The hydrogen bond directly formed between the amide group of fidarestat (**6**) and Leu 300 NH is shown in red.

In contrast to all other inhibitors studied in this contribution the hydantoins **5** and **6** exhibit a different anchor group and bind to ALR2 keeping the specificity pocket in closed state (Fig. 5.9).^{13,29,33} Both ligands share an identical scaffold. In addition, **6** possesses an exocyclic amide group which forms a direct H-bond to the Leu 300 NH group (3.0 Å). Ligand **5** also establishes a contact to the Leu 300 NH group, however mediated via an interstitial water molecule picked-up upon complex formation. The presence of the exocyclic amide function in **6** is obviously attributed to a gain in binding free energy of 8.8 kJ mol⁻¹ (Tab. 5.6). The free energy of binding factorizes into a 25 kJ mol⁻¹ more favourable enthalpy of **6** over **5**, and an entropic advantage of **5** (-TΔΔS⁰:16 kJ mol⁻¹). The enthalpic gain of **6** can presumably be attributed to the formation of a direct H-bond to the protein which results in an entropically less favourable arrest of either the ligand and the C-terminal loop of the protein. As mentioned above, the pick-up of a water molecule should be enthalpically favourable and entropically unfavourable. In both complexes, ALR2-**5** and ALR2-**6**, the ligands are associated with a water molecule (Fig. 5.9). Thus, at first glance, the thermodynamic inventory due to water incorporation should be balanced. However, the water molecule observed in ALR2-**6** mediates an intra-ligand H-bond between its ether oxygen and the amide nitrogen (3.2 Å), presumably also present in uncomplexed state. In case of **5**, the H-bond is only mediated through a water molecule, and this contact might be enthalpically of comparable strength to the situation in water. Furthermore, the special arrest of protein and ligand reinforced by a water-mediated contact might be less pronounced compared to the situation observed for **6**, revealing a residual entropic benefit for **5**.

Ligands **3** and **6** exhibit deviating scaffolds and induce different adaptations to the protein. Both show strong enthalpic binding paralleled by a pronounced entropic penalty of almost equal size. The matching thermodynamic profiles are particularly surprising as they bind to the enzyme either in the specificity pocket-closed or opened state. Assuming that no intricate and mutually compensating effects are in operation, this observation suggests the energy barrier between open and closed state to be rather small. Possibly, water takes a significant influence on the opening process. In non-crystalline phase the dynamic properties of the C-terminal loop region might allow the specificity pocket to adopt an open conformation which is in due course filled by water molecules demanding an entropic penalty. Subsequent desolvation of the partly

hydrophobic pocket upon ligand binding could compensate to some extent for the entropic penalty along with enthalpy contributions required for the opening process.

5.3 Conclusions

In the present study, we investigated the binding thermodynamics of different aldose reductase inhibitors to better understand the driving forces of ligand binding in the light of their adopted binding modes. However, prior to any meaningful factorization of the free energy of binding into enthalpic and entropic contributions, a detailed analysis of putative changes in the protonation inventory is required to correct for any superimposed heat contributions resulting from ionization effects. By means of ITC measurements we were able to detect an uptake of approximately 0.8 moles of protons per mole formed complex upon binding of carboxylate-type inhibitors to the enzyme with the cofactor in oxidized state. Several titratable groups are present in the catalytic pocket that might pick-up this proton. As the likely candidates for proton acceptance (e.g. Lys 77 instead of Tyr 48) show strongly deviating heats of ionization, correct assignment is essential (e.g. Tyr OH: 25 kJ mol⁻¹; Lys NZ: 45 kJ mol⁻¹).³⁴ We performed PB-based pKa calculations using our PEOE-PB charge model, recently developed in our laboratory.⁹ This computational approach suggested Tyr 48 as likely proton acceptor. Subsequently, this could be experimentally confirmed by mutating Tyr 48 to Phe. Binding of carboxylate-type inhibitors to the mutant leads to the absence of any buffer-dependent proton transfer. On the contrary, hydantoins, partially protonated prior to binding, release their protons whereas Tyr 48 picks-up a similar amount as observed for the carboxylate-type inhibitors.

Our measurements suggest that the protonation inventory and the binding thermodynamics strongly depend on the oxidation state of the cofactor. This knowledge is essential in order to apply appropriate corrections of the superimposed ionization contributions. It further indicates that the energetics of the hydrogen-bonds formed between the ligand anchor group and the catalytic site residues are dependent on the oxidation state. Such properties might be essential for the accommodation of substrate and release of product along a reaction pathway.

Our factorization also indicates the influence of different substituents attached to a given ligand scaffold on the thermodynamic binding profile. For example, an imbalanced inventory of polar ligand atoms which do not find appropriate polar

contacts within the complex are penalized by an unfavourable desolvation enthalpy. This is detrimental to the binding enthalpy and should be avoided.

Entropic contributions are more difficult to interpret, particularly, if only limited information about the dynamic properties of ligand and protein prior and after binding is available. Recent NMR studies of ligand binding to major urinary protein (MUP)¹ suggested changes of ordering parameters of protein residues partly remote from the actual binding site. Such changes of the residual entropy are essentially difficult to predict and to interpret if only the crystal structure of a protein-ligand complex is available. However, these contributions can take strong influence towards the entropic term, particularly, if they are affected by the complexation. In case of adaptive proteins such as ALR2, it is in question, how much energy is required to transform the enzyme between different pocket conformers. Such knowledge would presumably be helpful to estimate whether binding affinity of a given ligand scaffold will profit from the decoration with appropriate groups opening subpockets of the protein. A comparison of the thermodynamic profiles observed for **3** and **6** suggests that the energetic barrier which separates the open from the closed specificity pocket is rather low, as postulated earlier on the basis of molecular dynamics simulations.³⁵ These properties likely determine the accommodation of substrates and agree with the broad substrate promiscuity of ALR2.

5.4 Materials and Methods

Compounds **4** (BTB02809) and **7** (JFD00882) were purchased from Chempur, Karlsruhe, Germany. Expression and purification of Aldose Reductase have already been described elsewhere.¹¹⁻¹³ The mutation of tyrosine 48 to phenylalanine was introduced by PCR, using the Pfu Turbo polymerase (Stratagene), to amplify the entire plasmid. In order to construct the mutant, the primer with the following sequence was obtained from MWG-Biotech (Ebersberg, Germany):

5'- CCTCATTCTCATTCTGGAACACATGGGCACAGTCGATGTGG – 3'. After 20 cycles of PCR, the initial plasmid was digested by DpnI enzyme for 30 minutes at 37°C. After amplification (in XL2 Blue *E.Coli* strain), purification with the Quiagen Miniprep kit and sequencing (MWG-Biotech) to confirm the mutation, the mutated plasmid was transformed into the *E. coli* strain BL21 Gold for protein production. The mutated protein was then expressed and purified by the same procedures as used to obtain the wild type protein.

Isothermal Titration Calorimetry. Calorimetric measurements were carried out using an MCS ITC-instrument from MicroCal Inc. (Northampton, USA). In each experiment, the ligand was titrated to the protein solution present in the 1.4 mL sample cell. The reference cell contained 0.1 mM sodium azide dissolved in demineralised water. All measurements were carried out at 298 K. In order to detect changes in protonation state, all measurements were performed in phosphate, hepes, tricine, and tris buffer. The corresponding buffer ionization enthalpies were taken from literature.^{36,37} The wild type protein was dissolved in a 10 mM solution of the appropriate buffer at pH 8 to a concentration of 18.9 μM for the titration of **2**, **3**, **6**, and **8** and 37.8 μM for the measurements of **4**, **5**, and **7**. For the Y48F mutant, all measurements were performed with a protein concentration of 37.8 μM . Protein concentrations were determined by UV spectroscopy (280 nm) using the specific absorption calculated by the ProtParam tool (www.expasy.ch). The ligand solution contained 252 μM of the corresponding inhibitor dissolved in the same buffer as the protein. The protein was saturated with an excess of NADP^+ which was present at the same concentration in the ligand solution to avoid heat effects caused by diluting the cofactor. Solutions were degassed at 293 K under vacuum for 10 min. Upon experimental setup, the protein solution present in the sample cell was stirred at 400 rpm. After a stable baseline had been achieved, the titration was initiated. The injection sequence started with an initial aliquot of 1.5 μL (to preserve diffusion effects arising from the experimental setup, data not used for fitting) followed by injections of 10 μL in time intervals of 300 s until complete saturation was obtained. Heat changes caused by each inhibitor injection were obtained from the integral of the calorimetric signal. Data were analysed using the ORIGIN software (MicroCal Inc.) for fitting the data points to a single-site binding model in agreement with the results from X-ray crystallography.

Experimental heats of the protein-inhibitor titration were corrected for heats of dilution by subtracting the average heat of the last three measurements after saturation of the protein binding sites has been achieved. All measurements have been carried out at least in duplicate. Energy values, binding constants, and standard deviations were derived from data fitting and subsequent averaging of the corresponding measurements. Standard Gibbs free energy values were calculated using the equation $\Delta G^0 = -RT \ln K_b$ (where $R=8.3144 \text{ J mol}^{-1}\text{K}^{-1}$, K_b binding constant). The determination of ΔH_{exp}^0 was performed for **2** – **6** using the linear regression of experimentally observed enthalpies

and subsequent extrapolation towards the y-axis, whereas ΔH_{exp}^0 for **7** and **8** was calculated using the enthalpy value observed in Hepes buffer. For the determination of the ionization enthalpies of **5** and **6** a 2 mM solution of each inhibitor in purified water has been prepared and the pH has been adapted to the pKa value of both compounds. This solution was titrated with 10 μL injections of 1 mM HCl. The corresponding ionization enthalpies were obtained by subtraction of the heats determined by a blank titration followed by subsequent averaging of the heats obtained from at least 10 injection peaks. The ionization enthalpies observed (**5**: 28.3 \pm 2.5 kJ mol⁻¹; **6**: 32.8 \pm 3.1 kJ mol⁻¹) are in agreement with the corresponding value reported for the first ionization of an appropriate hydantoin analogue (32.6 kJ mol⁻¹).³⁸ The ligand binding enthalpy ΔH_{bind}^0 was calculated using the experimental heat ΔH_{exp}^0 according to equation 2. To obtain ΔH_{bind}^0 , the ionization enthalpy of buffer, protein residue (tyrosine) and, if present, of the ligand were subtracted from ΔH_{exp}^0 using the coefficients given in Tab. 5.4.

pKa calculations. The crystal structures of ALR2 in complex with **2** (IDD388), **3** (IDD393) and **4** have recently been determined in our laboratory.²³ The experimentally determined pKa value of **1** (IDD594) is 2.9.¹¹ The structural similarity of **1**, **2**, and **3** tempted us to perform the pKa calculations based on the pKa value of **1** for all carboxylate head groups. For the sake of consistency, a pKa value of 3.0 was also assumed for **4** in our calculations. However, changing the pKa value by \pm 1 unit does not suggest different protonation effects. For the pKa calculations, we applied the same methodology as recently described elsewhere.⁹ MEAD was employed as PB solver.²⁴ We performed the calculations with a dielectric constant of 20 and 10 to elucidate its influence. REDUCE was used to generate hydrogens for the residues of the protein.³⁹ For the calculations of the complexes, the orientation of the Tyr48 OH group was chosen to point towards the ligand. SYBYL was applied to add hydrogens to the cofactor and the ligands.⁴⁰ To study the protonation effects upon ligand binding, two pKa calculations are required: One without ligand and a second with the bound ligand. Only the titratable residues within a 12 Å sphere around the active site were selected for evaluation of the site-site interactions in order to reduce the computational effort (in total, there are 91 titratable residues in hAR). This results in the following 26 titratable residues: Lys21, Asp43, Cys44, His46, Tyr48, Glu51, Lys77, Cys80, Tyr82, His83, His110, Lys116, Lys119, Glu120, Glu185, Cys186, Tyr209, Asp216, Lys262, Cys298, Cys303, His306, Lys307, Asp308, Tyr309, His312. We used the higher populated

amino acid conformer in case a split conformation has been assigned in the crystal structure. In contrast to our standard settings for the titration of histidine residues, the N δ atom of His110 was titrated.

pK_a values of **2-6** were determined in an aqueous solution of 0.15 M KCl at 296 K using a photometric procedure. Figures were prepared using Isis Draw (MDL, San Leandro, USA) and Pymol.⁴¹ Calculations of the solvent-accessible surface buried upon complex formation were performed with the web-accessible tool GETAREA 1.1⁴² using an 1.4 Å probe and radii published by Shrake and Rupley.⁴³

5.5 References

1. Homans, S. W. (2005). Probing the binding entropy of ligand protein interactions by NMR. *ChemBioChem* **6**, 1-8.
2. Ladbury, J. E. & Ababou, A. (2005). Survey of the year 2004: literature on applications of isothermal titration calorimetry. *J. Mol. Recognit.* **1**, 79-89.
3. Holdgate, G. A. & Ward, W. H. J. (2005). Measurements of binding thermodynamics in drug discovery. *Drug Discov Today* **10**, 1543-1550.
4. Ruben, A. J., Kiso, Y. & Freire, E. (2006). Overcoming roadblocks in lead optimization: a thermodynamic perspective. *Chem. Biol. Drug Res.* **67**, 2-4.
5. Dullweber, F., Stubbs, M. T., Musil, D., Stürzebecher, J. & Klebe, G. (2001). Factorizing ligand affinity: a combined thermodynamic and crystallographic study of trypsin and thrombin inhibition. *J. Mol. Biol.* **313**, 593-614.
6. Velazquez-Campoy, A, Todd, M.J. & Freire, E. (2000). HIV-1 protease inhibitors: enthalpic versus entropic optimization of the binding affinity. *Biochemistry* **39**, 2201-2207.
7. Velazquez-Campoy, A, Kiso, Y. & Freire, E. (2001). The binding energetics of first- and second-generation HIV-1 protease inhibitors: implications for drug design. *Arch. Biochem. Biophys.* **390**, 169-175.
8. Warshel, A., Sharma, P. K., Kato, M. & Parson, W. W. (2006). Modeling electrostatic effects in proteins. *BBA –Proteins and Proteomics*, in press.
9. Czodrowski, P., Dramburg, I., Sottriffer, C. A. & Klebe, G. (2006). Development, validation and application of adapted PEOE charges to estimate

- pK(a) values of functional groups in protein-ligand complexes. *Proteins* **65**, 424-437.
10. Baker, B M. & Murphy, K. P. (1996). Evaluation of linked protonation effects in protein binding reactions using isothermal titration calorimetry. *Biophys. J.* **71**, 2049-2055.
 11. Howard, E. I., Sanishvili, R., Cachau, R. E., Mitschler, A., Chevrier, B., Barth, P., Lamour, V., Van Zandt, M., Sibley, E., Bon, C., Moras, D., Schneider, T. R., Joachimiak, A. & Podjarny, A. (2004). Ultrahigh resolution drug design I: details of interactions in human aldose reductase-inhibitor complex at 0.66 Å. *Proteins* **55**, 792-804.
 12. El-Kabbani, O., Wilson, D.K., Petrash, J.M. & Quioco, F.A. (1998). Structural Features of the aldose reductase and aldehyde reductase inhibitor binding sites. *Mol. Vis.* **4**, 19-25.
 13. Urzhumtsev, A., Tete-Favier, F., Mitschler, A., Barbanton, J., Barth, P., Urzhumtseva, L. *et al.* (1997). A 'specificity' pocket inferred from the crystal structures of the complexes of aldose reductase with the pharmaceutically important inhibitors tolrestat and sorbinil. *Structure* **5**, 601-612.
 14. Steuber, H., Zentgraf, M., Podjarny, A.D., Heine, A. & Klebe, G. (2006). High resolution crystal structure of aldose reductase complexed with the novel sulfonyl-pyridazinone inhibitor exhibiting an alternative active site anchoring group. *J. Mol. Biol.* **356**, 45-56.
 15. Varnai, P., Richards, W. & Lyne, P.D. (1999). Modelling the catalytic reaction in human aldose reductase. *Proteins* **37**, 218-227.
 16. Cachau, R., Howard, E., Barth, P., Mitschler, A., Chevrier, B., Lamour, V., Joachimiak, A., Sanishvili, R., Van Zandt, M., Sibley, E., Moras, D. & Podjarny, A.D. (2000). Model of the catalytic mechanism of human aldose reductase based on quantum chemical calculations. *J. Phys. IV France* **10**, 3-13.
 17. Brownlee, M. (2001). Biochemistry and molecular cell biology of diabetic complications. *Nature* **414**, 813-820.
 18. Evans, J. L., Goldfine, I. D., Maddux, B. A. & Grodsky, G.M. (2002). Oxidative stress and stress-activated signalling pathways: a unifying hypothesis of type 2 diabetes. *Endocrine Rev.* **23**, 599-622.
 19. Price, S. A., Agthong, S., Middlemas, A.B. & Tomlinson, D.R. (2004). Mitogen-activated protein kinase p38 mediates reduced nerve conduction

- velocity in experimental diabetic neuropathy. – Interactions with aldose reductase. *Diabetes* **53**, 1851-1856.
20. Suzuki, L. A., Poot, M., Gerrity, R.G. & Bornfeldt, K.E. (2001). Diabetes accelerates smooth muscle accumulation in lesions of atherosclerosis. Lack of direct growth-promoting effects of high glucose levels. *Diabetes* **50**, 851-860.
 21. Nakamura, J., Kasuya, Y., Hamada, Y., Nakashima, E., Naruse, K., Yasuda, Y., Kato, K. & Hotta, N. (2001). Glucose-induced hyperproliferation of cultured rat aortic smooth muscle cells through polyol pathway hyperactivity. *Diabetologica* **44**, 480-487.
 22. Krämer, O., Hazemann, I., Pojarny, A.D. & Klebe, G. (2004). Virtual screening for inhibitors of human aldose reductase. *Proteins* **55**, 814-823.
 23. Steuber, H., Heine, A. & Klebe, G. (2006). Structural and thermodynamic characterization of aldose reductase inhibitors reveals a nitro-substituent as strong enthalpic contributor to ligand affinity. *J. Mol. Biol.*, accepted.
 24. Bashford, D. (1997). An object-oriented programming suite for electrostatic effects in biological molecules. In: Ishikawa, Y., Oldehoeft, R. R., Reynders, J. V. W., Tholburn, M., editors. Lecture notes in computer science. Berlin: Springer; 1997. pp. 233-240. ISCOPE97.
 25. Czodrowski, P., Sotriffer, C. A. & Klebe, G. (2007). Protonation changes upon ligand binding to trypsin and thrombin: structural interpretation based on pKa calculations and ITC experiments. *In press*.
 26. Czodrowski, P., Sotriffer, C. A. & Klebe, G. (2006). Atypical protonation states in the active site of HIV-1 protease: A computational study. *submitted*.
 27. Tarle, I., Borhani, D. W., Wilson, D. K., Quioco, F. A. & Petrash, J. M. (1993). Probing the active site of human aldose reductase. *J. Biol. Chem.* **268**, 25687-25693.
 28. Grimshaw, C. E., Bohren, K. M., Lai, C.-J. & Gabbay, K. H. (1995). Human aldose reductase: pK of tyrosine 48 reveals the preferred ionization state for catalysis and inhibition. *Biochemistry* **34**, 14374-14384.
 29. El-Kabbani, O., Darmanin, C., Schneider, T. R., Hazemann, I., Ruiz, F., Oka, M., Joachimiak, A., Schulze-Briese, C., Tomizaki, T., Mitschler, A. & Podjarny, A. (2004). Ultrahigh resolution drug design. II. Atomic resolution structures of human aldose reductase holoenzyme complexed with fidarestat and

- minalrestat: implications for the binding of cyclic imide inhibitors. *Proteins* **55**, 805-813.
30. Williams, M.A. & Ladbury, J.E. (2003). Hydrogen bonds in protein-ligand complexes. In *Protein-Ligand interactions: From Molecular Recognition to Drug Design*. (Boehm, H.-J. & Schneider, G., eds), p. 137-161, Wiley-VCH, Weinheim.
 31. Meot-Ner, M. (2005). The ionic hydrogen bond. *Chem. Rev.* **105**, 213-284.
 32. Meyer, E.A., Castellano, R.K. & Diederich, F. (2003). Interactions with aromatic rings in chemical and biological recognition. *Angew. Chem. Int. Ed.* **42**, 1210-1250.
 33. Petrova, T., Steuber, H., Hazemann, I., Cousido-Siah, A., Mitschler, A., Chung, R., Oka, M., Klebe, G., El-Kabbani, O., Joachimiak, A. & Podjarny, A. (2005). Factorizing selectivity determinants of inhibitor binding toward aldose and aldehyde reductases: structural and thermodynamic properties of the aldose reductase mutant Leu300Pro-fidarestat complex. *J. Med. Chem.* **48**, 5659-5665.
 34. Chaplin, M. (2002). <http://www.sbu.ac.uk/biology/enztech/ph.html>.
 35. Sotriffer, C. A., Krämer, O. & Klebe, G. (2004). Probing flexibility and „induced-fit“ phenomena in aldose reductase by comparative crystal structure analysis and molecular dynamics simulations. *Proteins* **56**, 52-66.
 36. Fukada, H. & Takahashi, K. (1998). Enthalpy and heat capacity changes for the proton dissociations of various buffer components in 0.1 M potassium chloride. *Proteins* **33**, 159-166.
 37. Christensen, J.J., Hansen, L. D. & Izatt, R. M. (1976). Handbook of proton ionization heats and related thermodynamic quantities. Wiley, New York.
 38. Lennette, E. P. & Plapp, B. V. (1979). Kinetics of carboxymethylation of histidine hydantoin. *Biochemistry* **18**, 3933-3938.
 39. Word, J. M., Lovell, S. C., Richardson, J. S. & Richardson, D. C. (1999). Asparagine and glutamine: using hydrogen atom contacts in the choice of side-chain amide orientation. *J. Mol. Biol.* **285**, 1735-1747.
 40. SYBYL 6.6, Tripos, Inc., Missouri, USA.
 41. DeLano, W. L. (2002). The PyMOL Molecular Graphics System. <http://www.pymol.org>

-
42. Fraczekiewicz, R. & Braun, W. (1998). Exact and efficient analytical calculation of the accessible surface areas and their gradients for macromolecules. *J. Comp. Chem.* **19**, 319-333.
 43. Shrake, A. & Rupley, J. A. (1973). Environment and exposure to solvent of protein atoms. Lysozyme and insulin. *J. Mol. Biol.* **79**, 351-371.

6. Merging the Binding Sites of Aldose and Aldehyde Reductase for Detection of Inhibitor Selectivity-Determining Features

6.1 Introduction

The development of potent drug candidates with sufficient selectivity for a given target is one of the major goals in modern drug discovery. Suitable lead compounds have to discriminate between the binding pocket of the desired target and related isoforms possessing similar binding properties. Nature often succeeds to achieve the required selectivity simply because the involved biochemical processes are evolved in well-defined physiological compartments, separated from other sites that may host putative isoforms. The situation is quite different with respect to orally administered therapeutic xenobiotics because they flood the whole body and distribute over the entire organism. Thus, save drug candidates have to be optimized not only with respect to maximum potency, but also for the required target selectivity to minimize undesired side effects. Therefore, insights into the principles determining target selectivity are of utmost importance.¹ However, even in cases, where structural information about the target and putative competitive isoforms is available, it is still a major challenge to endow a ligand with sufficient selectivity, particularly, if the binding site performs pronounced adaptations upon ligand accommodation.² Irritatingly enough, even slight deviations of the binding site constitution can induce dramatic effects towards the selectivity profile. An impressive achievement has been reported for the design of selective cyclooxygenase (COX) inhibitors discriminating between the isoforms I and II, where the subtle substitution of a valine by an isoleucine has been exploited to develop compounds with a selectivity advantage by more than three orders of magnitude.³ The recently developed “bump-and-hole” approach in the field of protein kinases is another example highlighting the relevance of inhibitor selectivity in structure-guided ligand design: here, functionally silent mutations are introduced next to the ATP-binding site.

This creates artificial inhibitor sensitivity and allows to study the biochemical role of a certain kinase particularly with respect to its validity as a putative drug target.⁴

In the present contribution we probe the binding site of human aldose reductase (hALR2, E.C. 1.1.1.21) by site-directed mutagenesis in order to elucidate its selectivity-determining features over human aldehyde reductase (ALR1, E.C. 1.1.1.2). Both enzymes are widely distributed in various tissues and catalyze the reduction of reactive aldehydes derived from the oxidative degradation of fatty acids, amino acids and carbohydrates.⁵ In addition to this detoxifying role, ALR2 catalyzes, under hyperglycaemic conditions, the rate-limiting step of the polyol pathway, which converts glucose to fructose via sorbitol as intermediate. Enhanced turnover along this pathway relates to various biochemical imbalances, such as a perturbed NAD^+/NADH ratio, oxidative and osmotic stress, formation of advanced glycosylated endproducts (AGEs) and activation of kinase signalling. These imbalances have been made responsible for diabetic late complications such as retinopathy, angiopathy, cataract and nerve conduction deficiencies.⁵⁻⁷ Accordingly, in various pre-clinical and clinical trials ALR2 inhibition evolved as a promising therapeutic concept.⁸⁻¹² Whereas ALR2 converts glucose with K_m values in the range of 100-200 mM, the corresponding value of ALR1 is about two orders of magnitude higher, rendering glucose as a poorer substrate even under hyperglycaemic conditions.¹³ On the contrary, it is widely known that various ALR2 inhibitors can also interfere with ALR1 thereby affecting its capability to detoxify reactive aldehydes such as methylglyoxal or 3-deoxyglucosone.¹⁴⁻¹⁶ Accumulation of these endogenous aldehydes has been reported to induce oxidative stress, aging, apoptosis and atherosclerosis.^{5,17-19} Accordingly, insufficient selectivity of ALR2 inhibitors may account for undesirable side effects,²⁰ in consequence of a reduced detoxifying activity of ALR1.

Both enzymes share a sequence identity of ~ 65 % and adopt a TIM barrel fold.²¹⁻²³ Even though there are characteristic deviations with respect to their kinetic properties, the overall binding site architecture is conserved between both enzymes. In both isoforms, the binding cavity comprises two subpockets. The catalytic subpocket is formed by the nicotinamide ring of the cofactor and in ALR1 by the side chains of Tyr 50, His 113 and Trp 114, and in ALR2 by the side chains of Tyr 48, His 110 and Trp 111. The second subpocket ("specificity pocket") is flanked by the latter Trp moiety and the C-terminal loop region of the enzymes (Fig. 6.1). In case of ALR2, this loop region exhibits high plasticity throughout the known crystal structures, particularly

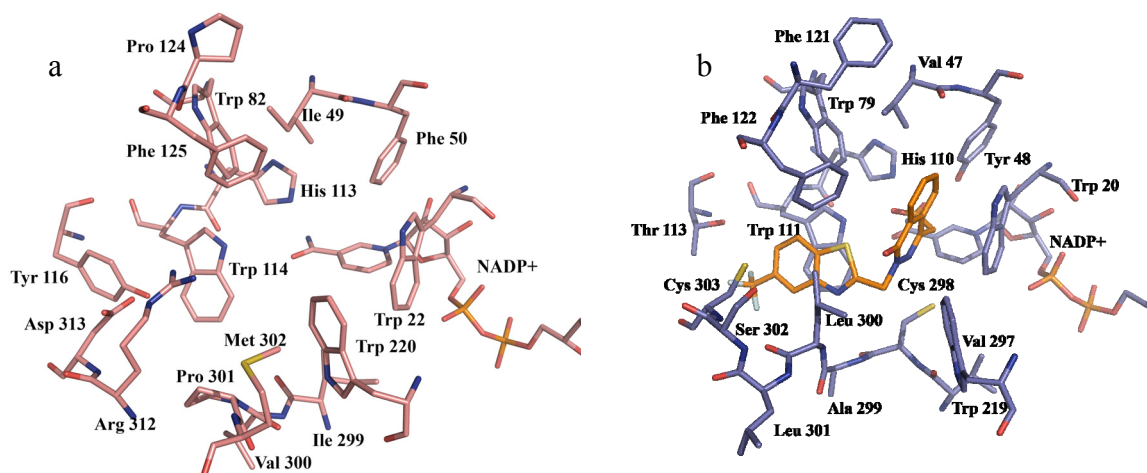


Figure 6.1. Comparative representation of the related ALR1 (a) and ALR2 (b) inhibitor binding pockets.

provoked by the less restrained dynamic properties of Phe 122, Ala 299 and Leu 300. These residues populate deviating rotameric states and thereby produce differently shaped subpockets.^{24,25} The most remarkable ALR1/2 differences involve the replacement of the C-terminal loop region Ala 299, Leu 300, Leu 301, Ser 302 and Cys 303 in ALR2 by Val 300, Pro 301, Met 302, Arg 312 and Asp 313 in ALR1. ALR1 possesses a loop insertion of ten amino acids between Met 302 and Arg 312 which does not directly contribute to the shape of the binding pocket, but is likely involved in the modulation of the dynamic properties. Pronounced induced-fit adaptations have been observed for ALR2, in particular with respect to the specificity pocket. In ALR1, the establishment of a similar pocket upon ligand binding appears rather unfavourable as its formation would involve the rupture of the salt bridge between Arg 312 and Asp 313 and slight relocations of Tyr 116. Even though in principle these rearrangements in ALR1 should be prerequisite for binding of each inhibitor equipped with appropriate hydrophobic groups usually occupying the ALR2-specificity pocket, such a relocation of Arg 312 accompanied by a salt link rupture has been up to now uniquely reported for the ALR1-tolrestat complex.²⁶ Additional differences in the binding pocket constitution are given by the substitution of Val 47 (ALR2) against Ile 49 (ALR1), Thr 113 (ALR2) against Tyr 116, and Phe 121 (ALR2) against Pro 124 (ALR1). A further deviation between both isoforms resides in the substitution of Cys 298 (ALR2) by an isoleucine (ALR1). However, substitution of Cys 298 in ALR2 strongly interferes with cofactor binding,^{27,28} possibly, because the sulfur atom of this cysteine forms a van der Waals interaction to the nicotinamide moiety throughout most of the determined crystal structures.

In order to probe and to quantify the structural and thermodynamic consequences of these differences between ALR1 and ALR2 with respect to ligand binding, we performed a step-by step mutagenesis study using ALR2 as parent enzyme accompanied by crystal structure analysis and isothermal titration calorimetry. As the presence of Cys 298 appeared crucial for ALR2 cofactor binding, the mutational studies were not extended to this residue.

6.2 Results and Discussion

The inhibitory profile with respect to wild type and hybrid ALR2 has been studied for at least two ligands given in Fig. 6.2. IC_{50} values for both parent enzymes ALR1 and ALR2 are listed in Tab. 6.1. The latter values are only rough estimates for the inhibitory potency as they have been determined in different laboratories, partly with deviating substrates, enzyme concentrations and varying buffer conditions. In the following, mutants are referred to by the amino acid substitution in one letter code at the corresponding ALR2 position (e. g. V47I represents the ALR2 mutant with Val 47 replaced by isoleucine). Thermodynamic data for binding to the wild type and mutant enzymes have been corrected for the heat of ionization enthalpies involved in changes of protonation states (Table 6.2 a). For clarity, the differences of the thermodynamic values for WT and mutant species are listed in Table 6.2 b. The results observed for the slightly deviating set of ligands used for the mutant L301M are given in Table 6.3. Data collection and refinement statistics of the determined crystal structures are listed in the appendix of this chapter.

Ligand	ALR1 [mol L ⁻¹]	ALR2 [mol L ⁻¹]
1	27 10 ⁻⁶	1.9 10 ⁻⁸
2	> 10 ⁻⁴ (r)	5.7 10 ⁻⁹ (r)
3	14 10 ⁻⁶	30 10 ⁻⁹
4	34 10 ⁻⁶ *	6 10 ⁻⁹ *
5	5.4 10 ⁻⁶	2 10 ⁻⁶
6	1.2 10 ⁻⁶	9 10 ⁻⁹
7	0.72 10 ⁻⁶	0.01 10 ⁻⁶

Table 6.1. Overview of selected published affinity data observed from kinetic measurements.^{15,16,32,48-50} (p) rat enzyme * 2-fluoro derivative

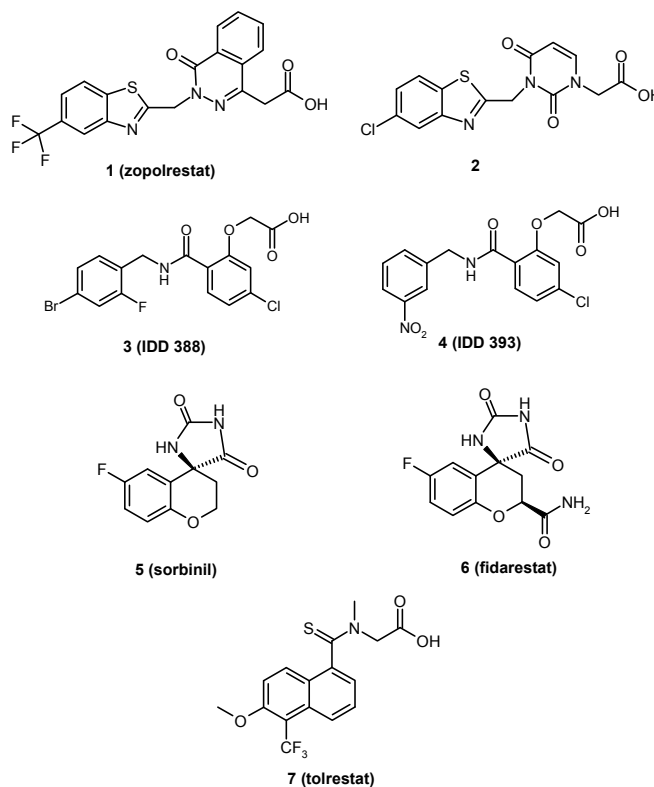


Figure 6.2. Chemical formulae of the ALR2 inhibitors investigated in this study.

Val 47 to Ile mutation (V47I)

The side chain of Val 47 caps the catalytic site of ALR2 and forms van der Waals contacts to bound ligand portions accommodated between the aromatic moieties of Tyr 48 and Phe 122. In ALR1, an isoleucine is present at the corresponding position. It forms van der Waals contacts to the indole portion of Trp 82 (Fig. 6.1a) with the C δ carbon pointing towards Pro 121 in either complexed and uncomplexed states as observed in all known crystal structures. In order to determine the impact of the V47I substitution towards selectivity, binding of **1**, **2**, **3**, and **6** was probed against the mutant. Crystal structures were determined for V47I-**1** and V47I-**6** (Fig. 6.3a and b, respectively). In these complexes, the binding modes of the ligands remain virtually unchanged. The introduced additional methyl group in V47I forms contacts to Trp 79 with C δ either pointing away from the binding pocket (in V47I-**1**, similar to the situation in ALR1) or into the cavity (in V47I-**6**). In V47I-**1**, Ile 47 pushes the neighbouring Phe 121 side chain slightly out of space compared to WT (van der Waals contact to Ile 47 of 3.3 Å). Without this rearrangement, a contact of 2.5 Å would be present. In V47I-**6**, C δ of Ile 47 forms additional van der Waals interactions to Phe 122 and to the aromatic moiety of the ligand. Binding of **1** to V47I

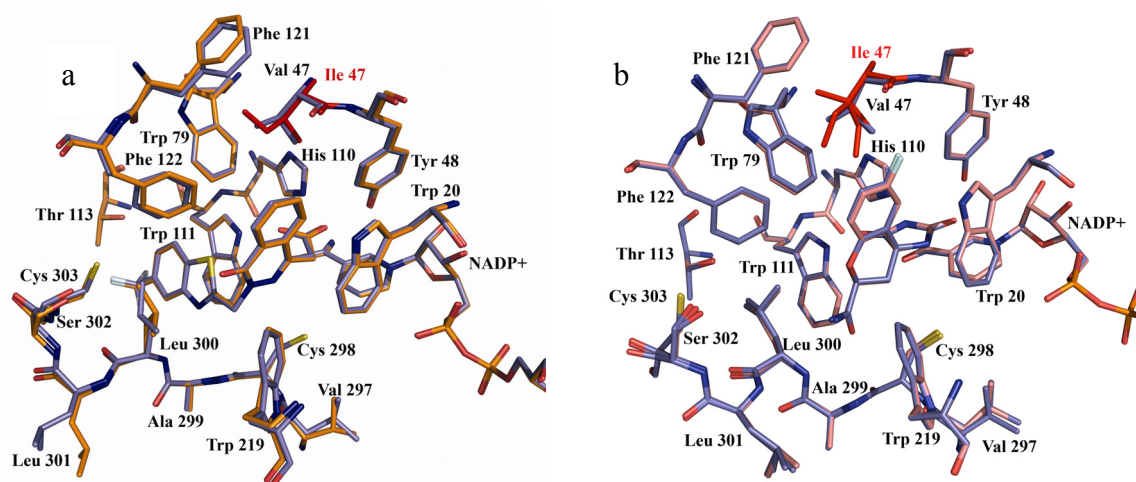


Figure 6.3. (a) Superposition of ALR2 wild type (blue sticks) and V47I mutant (orange sticks) complexed with **1**. The mutation site is shown in red. (b) Superposition of ALR2 wild type (blue sticks) and V47I (light red) in complex with **6**. The split conformation of the introduced Ile 47 is shown in red.

is accompanied by an affinity drop of one order of magnitude compared to the wild type. This is reflected by a 3.6 kJ mol^{-1} loss concerning the Gibbs Free Energy of binding. It can be attributed to a less favourable binding enthalpy ($\sim 7 \text{ kJ mol}^{-1}$), compensated to some extent by a more favourable entropic contribution ($\sim 3 \text{ kJ mol}^{-1}$). As the binding mode of **1** is virtually identically for WT and V47I, these thermodynamic deviations are possibly provoked by relocations of Phe 121 and other changes of the dynamic properties. Conceivably, they involve significant changes in the rotameric states of terminal groups such as methyl groups as recently stated by Homans et al.²⁹ In summary, these affects translate into a small selectivity advantage of WT over V47I for **1**. Surprisingly, for **6**, the binding free energy remains nearly unchanged upon mutation. However, it factorizes differently and suggests a more favourable enthalpic contribution ($\sim 5 \text{ kJ mol}^{-1}$) for binding to V47I, compensated by an entropically less beneficial contribution for the mutant compared to WT. The binding mode of **6** is nearly unchanged in both species, however the fluoro substituent approaches quite closely to the mutation site. The larger Ile residue can possibly experience more favourable van der Waals interactions with the bound ligand which advocates for the enthalpic advantage. On the contrary, Ile 47 is disordered over two states in V47I-**6**, whereas it populates only one orientation in V47I-**1**. This disorder should be entropically favourable, thus conflicting with the observed thermodynamic data. However, to fully interpret these changes, the ordering of this residue in the

uncomplexed situation would have to be known. As the structural information for V47I-2 and V47I-3 are missing due to the absence of appropriate cocrystals, the interpretation of the thermodynamic data remains even more speculative. In **2**, the phthalazinone moiety of **1** is replaced by a smaller uracil portion (Fig. 6.2 and 6.4). Accordingly, **2** reveals weaker van der Waals interactions in the WT complex with Val 47, as suggested by longer van der Waals distances (6.0 and 6.7 Å). Likely, the Val/Ile exchange will not take dramatic influence on these contacts. Nevertheless, binding free energy of **2** drops by 5 kJ mol⁻¹ for V47I compared to WT.

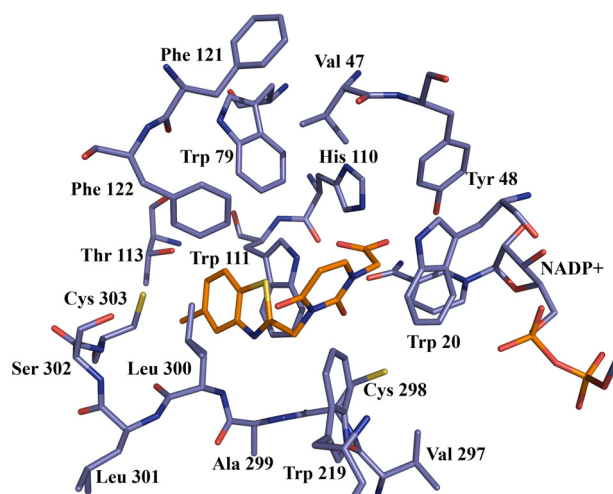


Figure 6.4. Binding geometry of **2** (orange) to ALR2 (blue). The carboxylic anchoring group occupies the catalytic cleft, whereas the benzothiazol moiety penetrates into the specificity pocket of ALR2.

It even factorizes in an enthalpic loss and a slight entropic gain. In that respect, its thermodynamic profile resembles that of **1**. Finally, **3** exhibits similar thermodynamic data as **6**. Its binding free energy remains nearly unchanged for the V47I exchange. Furthermore, it experiences a very similar factorization as **6** exhibiting a favourable $\Delta\Delta H_{\text{bind}}^0$ and an unfavourable $-T\Delta\Delta S^0$. Assuming a WT-like binding mode for **3** to V47I (such as observed for V47I-1 and V47I-6), the central chloro substituent in **3** experiences a similar placement compared to the fluoro group in **6**. Both approach quite closely the position of Val 47. At least this structural similarity suggests alike thermodynamic profiles for both inhibitors.

Phe 121 to Pro mutation (F121P)

In ALR2, Phe 121 is located closely to Val 47 and forms van der Waals contacts to the latter residue. In ALR1, a proline is located at the corresponding position. Even though neither in ALR1 nor in ALR2 this amino acid forms any relevant direct contact to bound ligands, this hydrophobic amino acid might be involved in the integrity, dynamics and the water accessibility of the subpocket between Phe 122 and Tyr 48 (ALR2). Accordingly, we analysed the binding properties of **1**, **2**, **4** and **6** to the mutant F121P. The crystal structures of F121P in complex with **1** and **4** were determined. In both complexes, no remarkable relocations of amino acids or ligands could be observed compared to the corresponding wild type crystal structures (Fig. 6.5). Even though the mutation site is quite solvent-exposed, the additional space created by the F121P mutation becomes only poorly solvated by ordered water molecules as suggested by the electron density. This is in agreement with the situation in ALR1, where almost no water molecules are assigned next to Pro 124 in most of the determined crystal structures. However, as the presence or absence of water molecules in this region will most likely be independent on ligand binding, the thermodynamic properties of the binding process should, in principle, not be influenced by the solvent structure in this region. Ligands **1** and **4**, both occupying the subpocket formed by Val 47, Tyr 48 and Phe 122 experience a loss in affinity of about 5 kJ mol^{-1} . In both cases, this drop is provoked by a less favourable binding enthalpy ($\Delta\Delta H_{\text{bind}}^0 \sim 15 \text{ kJ mol}^{-1}$), compensated by a more beneficial entropic gain for binding to the mutant compared to WT. The binding free energy of **2**, which does not occupy the corresponding pocket (Fig. 6.4), remains unaffected. However, the trend towards modulated factorization into enthalpic and entropic contributions as observed for **1** and **4** is similarly recorded for **2** ($\Delta\Delta H_{\text{bind}}^0 \sim 6 \text{ kJ mol}^{-1}$, $-T\Delta\Delta S^0 \sim 7 \text{ kJ mol}^{-1}$). Even though, the replacement of Phe 121 by Pro obviously affects the binding affinity of **1** and **4**, these changes and the modulated factorization are by no way simply to explain. The complex structures of WT and mutant reveal virtually identical interaction geometries. This suggests that the deviating binding profiles between WT and mutant complexes have to be attributed to changes in dynamic or solvation properties. Inhibitor **6** also occupies the referenced subpocket but leaves the specificity pocket between Trp 111 and Leu 300 in closed state.³⁰ Surprisingly, all thermodynamic properties recorded for binding of **6** appear virtually unchanged for F121P and WT. These results suggest a deviation thermodynamic profile depending whether the bound ligand penetrates into both, the specificity pocket and the

subpocket near Val 47-Tyr 48, or whether the former pocket remains in closed state. Ligands such as **1** or **4**, which occupy both of these pockets, exhibit a higher drop in affinity with respect to F121P.

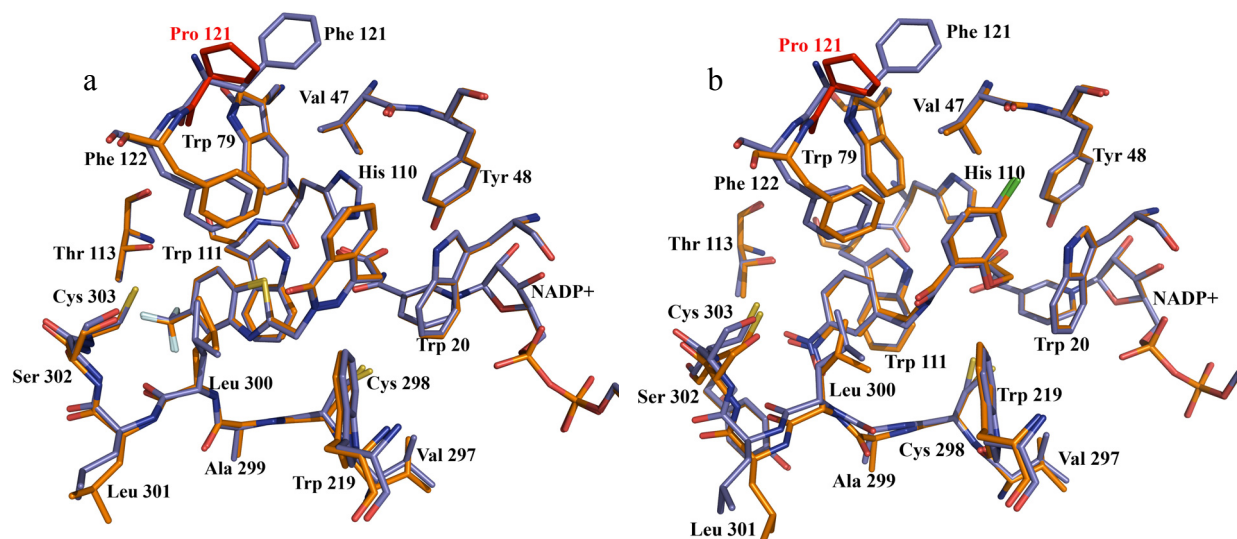


Figure 6.5. (a) Superposition of ALR2 (blue) and F121P (orange) complexed with **1**. The mutation site is shown in red. (b) Superposition of ALR2 (blue) and F121P (orange) complexed with **4**.

Ligand	WT ALR2				V47I				F121P				T113Y				L300P			
	k_b [10 ⁶ L/mol]	ΔG^0 [kJ mol ⁻¹]	ΔH_{bind}^0 [kJ mol ⁻¹]	$-T\Delta S^0$ [kJ mol ⁻¹]	k_b [10 ⁶ L/mol]	ΔG^0 [kJ mol ⁻¹]	ΔH_{bind}^0 [kJ mol ⁻¹]	$-T\Delta S^0$ [kJ mol ⁻¹]	k_b [10 ⁶ L/mol]	ΔG^0 [kJ mol ⁻¹]	ΔH_{bind}^0 [kJ mol ⁻¹]	$-T\Delta S^0$ [kJ mol ⁻¹]	k_b [10 ⁶ L/mol]	ΔG^0 [kJ mol ⁻¹]	ΔH_{bind}^0 [kJ mol ⁻¹]	$-T\Delta S^0$ [kJ mol ⁻¹]	k_b [10 ⁶ L/mol]	ΔG^0 [kJ mol ⁻¹]	ΔH_{bind}^0 [kJ mol ⁻¹]	$-T\Delta S^0$ [kJ mol ⁻¹]
1	115.6 +/- 16.4	- 46.0 +/- 0.7	-58.1 +/- 1.0	12.1 +/- 1.7	27.0 +/- 8.7	- 42.4 +/- 1.7	- 51.6 +/- 1.5	9.2 +/- 3.3	10.3 +/- 3.6	-40.0 +/- 1.9	-42.1 +/- 1.5	2.1 +/- 3.4	0.66 +/- 0.1	-33.2 +/- 0.8	-50.7 +/- 1.3	17.5 +/- 2.1	4.9 +/- 2.2	-38.2 +/- 2.4	- 75.7 +/- 3.1	37.5 +/- 5.5
2	28.2 +/- 4.2	- 42.5 +/- 0.7	- 48.5 +/- 1.1	6.0 +/- 1.8	3.7 +/- 0.6	- 37.5 +/- 0.8	- 41.1 +/- 1.7	3.6 +/- 2.5	11.6 +/- 5.2	-40.3 +/- 2.4	- 42.3 +/- 1.3	2.0 +/- 3.7	0.36 +/- 0.06	-31.7 +/- 0.9	- 40.1 +/- 2.3	8.4 +/- 3.2	4.4 +/- 0.9	-37.9 +/- 1.1	- 57.3 +/- 1.3	19.4 +/- 2.4
3	31.5 +/- 8.5	- 42.7 +/- 3.1	- 59.0 +/- 1.4	16.3 +/- 9.0	51.6 +/- 5.9	- 44.0 +/- 0.6	- 65.7 +/- 0.9	21.7 +/- 1.5	-	-	-	-	0.95 +/- 0.2	-34.1 +/- 1.1	- 76.0 +/- 4.6	41.9 +/- 5.7	0.37 +/- 0.06	-31.8 +/- 0.8	- 53.3 +/- 2.0	21.5 +/- 2.8
4	25.0 +/- 4.1	- 42.2 +/- 0.8	- 81.2 +/- 1.4	39.0 +/- 5.8	-	-	-	-	3.9 +/- 0.6	-37.6 +/- 0.8	- 66.2 +/- 0.9	28.6 +/- 1.7	0.5 +/- 0.1	-32.5 +/- 1.0	- 64.9 +/- 3.3	32.4 +/- 4.3	2.3 +/- 0.4	-36.3 +/- 0.9	- 84.6 +/- 2.2	48.3 +/- 3.1
5	4.5 +/- 0.6	- 37.9 +/- 0.7	- 54.7 +/- 0.7	16.8 +/- 1.4	-	-	-	-	*	*	*	*	*	*	*	*	6.1 +/- 0.1	-38.7 +/- 0.2	- 48.6 +/- 0.7	9.9 +/- 0.9
6	153.3 +/- 36.6	- 46.7 +/- 1.2	-79.5 +/- 0.4	32.8 +/- 5.2	120.4 +/- 30.6	- 46.1 +/- 1.3	- 84.3 +/- 2.0	38.2 +/- 3.3	94.5 +/- 26.5	-45.5 +/- 1.4	- 79.6 +/- 0.6	34.1 +/- 2.0	4.8 +/- 1.9	-38.1 +/- 2.0	- 102.5 +/- 4.7	64.4 +/- 6.7	6.5 +/- 1.7	-38.9 +/- 1.3	- 71.3 +/- 1.4	32.4 +/- 2.7

Ligand	L300A				S302R				C303D				DM (S302R-C303D)			
	k_b [10 ⁶ L/mol]	ΔG^0 [kJ mol ⁻¹]	ΔH_{bind}^0 [kJ mol ⁻¹]	$-T\Delta S^0$ [kJ mol ⁻¹]	k_b [10 ⁶ L/mol]	ΔG^0 [kJ mol ⁻¹]	ΔH_{bind}^0 [kJ mol ⁻¹]	$-T\Delta S^0$ [kJ mol ⁻¹]	k_b [10 ⁶ L/mol]	ΔG^0 [kJ mol ⁻¹]	ΔH_{bind}^0 [kJ mol ⁻¹]	$-T\Delta S^0$ [kJ mol ⁻¹]	k_b [10 ⁶ L/mol]	ΔG^0 [kJ mol ⁻¹]	ΔH_{bind}^0 [kJ mol ⁻¹]	$-T\Delta S^0$ [kJ mol ⁻¹]
1	18.8 +/- 2.2	- 41.5 +/- 0.6	- 58.4 +/- 0.8	16.9 +/- 1.4	2.5 +/- 0.9	-36.5 +/- 1.9	- 81.1 +/- 5.5	50.6 +/- 7.4	4.4 +/- 0.9	- 37.9 +/- 1.1	- 76.0 +/- 1.4	38.1 +/- 2.5	0.42 +/- 0.08	-32.1 +/- 0.9	- 81.9 +/- 6.7	49.8 +/- 7.6
2	42.1 +/- 6.9	- 43.5 +/- 0.8	- 47.9 +/- 0.4	4.4 +/- 1.2	0.26 +/- 0.07	-30.9 +/- 1.4	- 68.0 +/- 10.7	37.1 +/- 12.1	0.5 +/- 0.12	- 32.5 +/- 1.2	- 37.7 +/- 1.7	5.2 +/- 2.9	0.28 +/- 0.07	- 31.1 +/- 1.2	- 67.2 +/- 10.2	36.1 +/- 11.4
4	11.6 +/- 2.7	- 40.3 +/- 1.2	- 61.9 +/- 0.9	21.6 +/- 2.1	0.36 +/- 0.13	-31.7 +/- 1.9	- 61.8 +/- 3.0	30.1 +/- 4.9	0.4 +/- 0.1	- 31.9 +/- 1.3	- 80.5 +/- 4.3	48.6 +/- 5.6	0.4 +/- 0.1	- 31.9 +/- 1.3	- 57.6 +/- 8.4	25.7 +/- 9.7
5	-	-	-	-	*	*	*	*	*	*	*	*	*	*	*	*
6	71.2 +/- 6.1	- 44.8 +/- 0.4	- 71.0 +/- 0.8	26.2 +/- 1.2	*	*	*	*	27 +/- 11.2	- 42.4 +/- 2.1	- 84.7 +/- 3.5	42.3 +/- 5.6	6.3 +/- 0.5	- 38.8 +/- 0.4	- 76.5 +/- 6.2	37.7 +/- 6.6

Table 6.2a. Thermodynamic binding data for WT and ALR2 mutants.

- not determined; * no appropriate binding isotherm obtained for data fitting

	V47I			F121P			T113Y			L300P		
Ligand	$\Delta\Delta G^0$ [kJ mol ⁻¹]	$\Delta\Delta H_{\text{bind}}^0$ [kJ mol ⁻¹]	$-\Delta\Delta S^0$ [kJ mol ⁻¹]	$\Delta\Delta G^0$ [kJ mol ⁻¹]	$\Delta\Delta H_{\text{bind}}^0$ [kJ mol ⁻¹]	$-\Delta\Delta S^0$ [kJ mol ⁻¹]	$\Delta\Delta G^0$ [kJ mol ⁻¹]	$\Delta\Delta H_{\text{bind}}^0$ [kJ mol ⁻¹]	$-\Delta\Delta S^0$ [kJ mol ⁻¹]	$\Delta\Delta G^0$ [kJ mol ⁻¹]	$\Delta\Delta H_{\text{bind}}^0$ [kJ mol ⁻¹]	$-\Delta\Delta S^0$ [kJ mol ⁻¹]
1	-3.6	-6.5	2.9	-6	-16	10	-12.8	-7.4	-5.4	-7.8	17.6	-25.4
2	-5	-7.4	2.4	-2.2	-6.2	4	-10.8	-8.4	-2.4	-4.6	8.8	-13.4
3	1.3	6.7	-5.4	-	-	-	-8.6	17	-25.6	-10.9	-5.7	-5.2
4	-	-	-	-4.6	-15	10.4	-9.7	-16.3	6.6	-5.9	3.4	-9.3
5	-	-	-	-	-	-	-	-	-	0.8	-6.1	6.9
6	-0.6	4.8	-5.4	-1.2	0.1	-1.3	-8.6	23	-31.6	-7.8	-8.2	0.4
	L300A			S302R			C303D			DM (S302R-C303D)		
Ligand	$\Delta\Delta G^0$ [kJ mol ⁻¹]	$\Delta\Delta H_{\text{bind}}^0$ [kJ mol ⁻¹]	$-\Delta\Delta S^0$ [kJ mol ⁻¹]	$\Delta\Delta G^0$ [kJ mol ⁻¹]	$\Delta\Delta H_{\text{bind}}^0$ [kJ mol ⁻¹]	$-\Delta\Delta S^0$ [kJ mol ⁻¹]	$\Delta\Delta G^0$ [kJ mol ⁻¹]	$\Delta\Delta H_{\text{bind}}^0$ [kJ mol ⁻¹]	$-\Delta\Delta S^0$ [kJ mol ⁻¹]	$\Delta\Delta G^0$ [kJ mol ⁻¹]	$\Delta\Delta H_{\text{bind}}^0$ [kJ mol ⁻¹]	$-\Delta\Delta S^0$ [kJ mol ⁻¹]
1	-4.5	0.3	-4.8	-9.5	23	-38.5	-8.1	17.9	-26	-13.9	23.8	-37.7
2	1.0	-0.6	1.6	-11.6	19.5	-31.1	-10	-10.8	0.8	-11.4	18.7	-30.1
4	-1.9	-19.3	17.4	-10.5	-19.4	8.9	-10.3	-0.7	-9.6	-10.3	-23.6	13.3
6	-1.9	-8.5	6.6	-	-	-	-4.3	5.2	-9.5	-7.9	-3	-4.9

Table 6.2b. Differences between the thermodynamic profiles of wild type ALR2 and the indicated mutant. The values have been calculated by subtracting the corresponding value observed for the mutant (Table 2a) from those for the wild type. Accordingly, negative values indicate a more beneficial contribution for binding to WT, whereas positive values represent a more favourable contribution for binding to the corresponding mutant compared to WT.

Thr 113 to Tyr mutation (T113Y)

All mutations discussed in the following contribute to the composition of the specificity pocket. The first investigated site, Thr 113, is located at the far end of the ALR2 specificity pocket. Its O_{γ} oxygen presumably forms a (weak) hydrogen-bond to one of the fluorine atoms of the ligand's terminal tri-fluoro-methyl group (as present in **1**). Bromo-substituted inhibitors as **3** form a short electrostatic contact between their polarisable bromine atom and Thr 113 O_{γ} , which itself H-bonds to the backbone carbonyl oxygen of the same residue. This electrostatic contact has been argued to contribute to inhibitor selectivity for ALR2 over ALR1, as the latter isoenzyme exposes a more bulky tyrosine residue at this position to the ligand.^{31,32} In consequence, in ALR1 the corresponding region is barred, and a similar electrostatic contact can presumably not be established. Therefore, we replaced Thr 113 by a tyrosine in order to probe the influence of this substitution. Whereas our thermodynamic data suggest binding to T113Y in micromolar range, no successful cocrystallization or soaking could be achieved to structurally characterize ligand binding to the mutant. All inhibitors studied with this mutant (**1-4**, **6**) exhibited a remarkable drop in affinity of 7 – 13 kJ mol⁻¹. Interestingly, even **6**, which does not occupy the ALR2 specificity pocket,³⁰ drops in affinity by about 8 kJ mol⁻¹. This suggests that the properties of the opened and closed specificity pocket did not remain unaffected by the Thr113/Tyr mutation. Furthermore, no evidence is available for conserved ligand binding geometries of WT and mutant. However, the thermodynamic data observed for T113Y do not suggest any selectivity advantage of the bromo-substituted **3** for binding to ALR2. At least the affinity drop affects **3** to similar extent compared to the nitro-substituted analogue **4**. Ligand **1** experiences the strongest loss in affinity (~ 13 kJ mol⁻¹), next to steric influences additionally provoked by the loss of the fluorine-Thr 113 O_{γ} hydrogen-bond. Ligand **2**, bearing an bioisosteric chlorine instead of the CF₃ group, experiences a drop in ΔG^0 of 11 kJ mol⁻¹. In summary, the replacement of Thr 113 by a tyrosine influences ligand binding unfavourably and might contribute to the affinity discrimination between ALR2 and ALR1.

Leu 300 to Pro mutation (L300P)

Whereas the sites of the binding pocket considered so far only comprise single point mutations between ALR1 and ALR2, the lowest degree of sequence identity is observed, however, in the C-terminal loop region lining the solvent-exposed site of the specificity pocket in ALR2 (Fig. 6.1). Here, the switch from opened or closed state is triggered by an outward movement of the C-terminal loop region next to Leu 300. In addition, appropriate rotameric states are adjusted to accommodate ligands in between the side chains of Trp 111, Phe 122 and Leu 300. In particular, the latter amino acid appeared of outstanding interest, as ALR2 inhibitors, appropriately substituted with hydrogen-bond acceptors, form an immediate contact to the backbone NH group of Leu 300 after the required adaptations of the protein. This is observed for example for the nitrogen of the benzothiazole moiety of **1** and **2**, for the nitro substituent of **4**, or for the exocyclic amide group of **6**.^{25,30-34} In ALR1, a proline is present at the corresponding position, thereby changing the dynamic properties of the loop region and disqualifying the backbone nitrogen for hydrogen-bonding. By mutating Leu 300 to proline, we recently collected evidence for the contribution of this replacement to selectivity with respect to the hydantoins **5** and **6**. Both ligands differ only with respect to the presence of an exocyclic amide function.³⁵ Whereas **6** hydrogen-bonds to Leu 300 NH, **5** is incompetent to form a similar direct hydrogen-bond due to lacking of this amide group. However, in ALR2-**5** an analogous contact is mediated via an interstitial water molecule (Fig. 6.6a). Facing the binding of **6** to L300P and WT, the loss of the hydrogen bond correlates with a drop in ΔG^0 of $\sim 8 \text{ kJ mol}^{-1}$, whereas for **5** virtually identical affinities are observed for WT and L300P. This loss in affinity of **6** is mainly enthalpically sacrificed and is presumably attributed to the absence of the hydrogen bond. The entropic contribution for binding of **6** to either WT or L300P remains virtually unchanged. On the contrary, the unchanged binding free energy for L300P-**5** factorizes differently compared to WT: a less favourable enthalpy for binding to L300P ($\Delta\Delta H_{\text{bind}}^0 \sim 6 \text{ kJ mol}^{-1}$) is compensated by a more favourable entropic contribution ($\sim 7 \text{ kJ mol}^{-1}$). Presumably, this can be attributed to the interaction between the chroman ring oxygen of **5** and Leu 300 NH in ALR2-**5** mediated by the interstitial water molecule, which is not established for L300P-**5**. Both ligands, **5** and **6**, are located in the catalytic pocket and leave the specificity pocket unoccupied. Thus, it appeared interesting to study whether ligands such as **1-4**, penetrating into this pocket, experience further effects. Complex structures were determined for L300P for **1** and **2** (Fig. 6.6 b

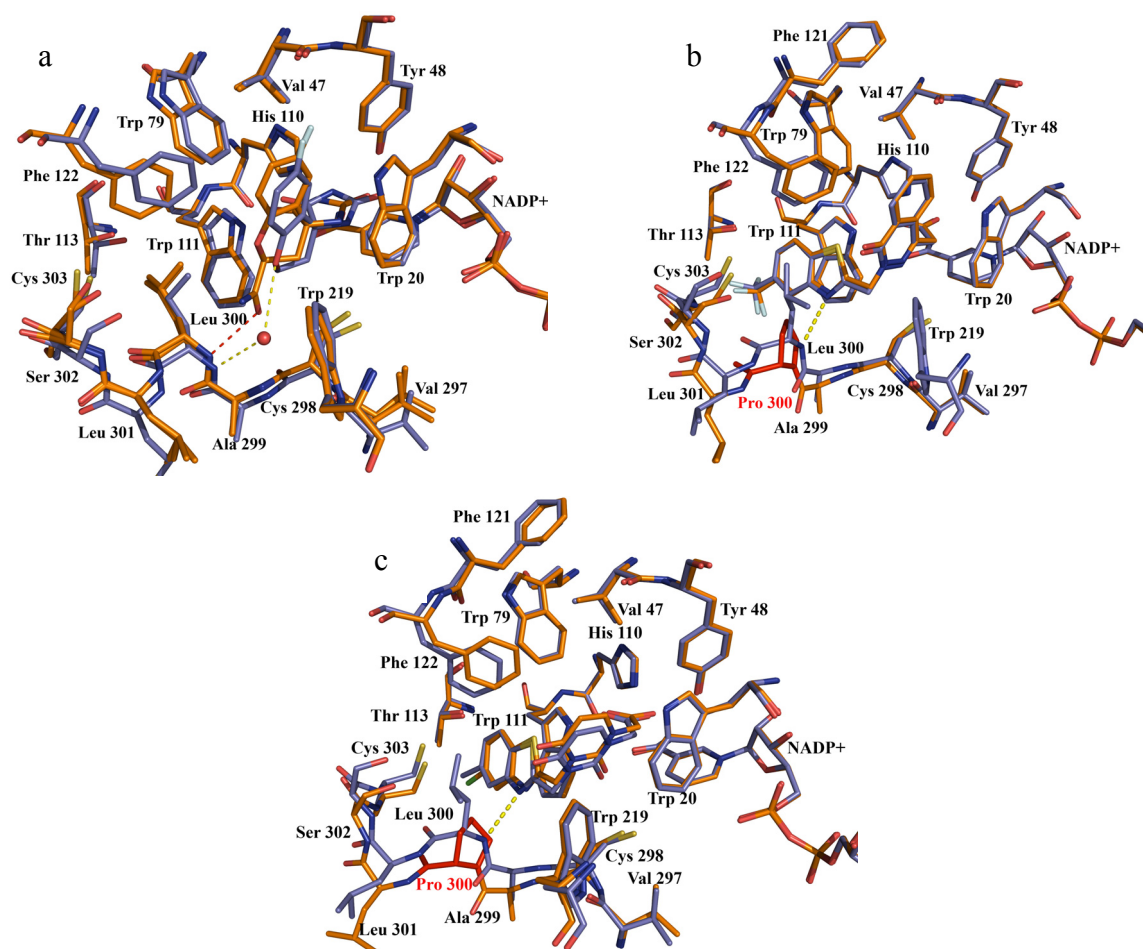


Figure 6.6. (a) Superposition of porcine ALR2 with bound **5** (blue) and human ALR2 complexed with **6** (orange). The exocyclic amide group of **6** directly hydrogen-bonds to Leu 300 NH, whereas this contact in the **5**-complex is mediated by an interstitial water molecule. (b) Superposition of the wild type ALR2 (blue) and L300P (orange) binding pocket complexed with **1**. (c) Superposition of the wild type ALR2 (blue) and L300P (orange) binding pocket complexed with **2**.

and c, respectively). As in L300P-**6** and ALR1, the proline adopts trans configuration. In contrast to the L300P-**6** complex, binding of **1** and **2** induces an outwards movement of the Pro 300 backbone atoms of up to 1.9 Å. The ligand atoms are located virtually identically compared to the corresponding wild type complexes. Facing the wild type complexes with the corresponding L300P structures, a slight shift of the backbone atoms becomes evident for the loop region Cys 298 – Ser 302. In both complexes, L300P-**1** and L300P-**2**, the proline C δ carbon forms a close van der Waals contact to the ligand's benzothiazole nitrogen (3.1 and 2.8 Å, respectively). All ligands **1-4** experience a strong drop in affinity of about 6-10 kJ mol⁻¹. Interestingly enough, also **3**, which does not interact via a hydrogen-bond to Leu 300 NH in the ALR2-**3** complex,³⁴

losses affinity ($\sim 10 \text{ kJ mol}^{-1}$). This suggests further contributions involved in ligand binding to L300P apart from the formation of the abovementioned hydrogen bond. In contrast to **5** and **6**, L300P complexation by the ligands penetrating into the specificity pocket is paralleled by a remarkable gain in binding enthalpy. This appears surprising, as the loss of one hydrogen-bond for **1,2** and **4** in L300P compared to the wild type should be penalized enthalpically as observed for **6**. Other contributions must countervail the inventory. The crystal structures of L300P-1 and L300P-2 do not provide evidence for the formation of any additional formed polar interaction or hydrogen bonds in the complexes. Differences in ligand desolvation also appear unlikely. In contrast, the solvent reorganization of the binding pocket upon ligand accommodation could be different for the wild type and L300P mutant. In uncomplexed state, the specificity pocket of ALR2 will be in closed state and the side chain of Leu 300 forms van der Waals contacts to Trp 111. Access of water molecules to the pocket will be hampered. The sterically less bulky proline in L300P cannot form as efficiently as Leu such van der Waals contacts to Trp 111. Thus, the repelling of water access might be less pronounced. This assumption is supported by the fact that in the L300P-**6** complex, a water molecule is observed coordinating to Thr 113 O γ and to the sulfur of Cys 303 in the virtually hydrophobic specificity pocket. Presumably, even further water molecules occupy the binding pocket in uncomplexed state. According to the non-classical hydrophobic effect, removal of water molecules from hydrophobic surfaces is accompanied by an enthalpic gain.³⁶ This might serve as an explanation for the unexpected favourable enthalpic contribution for L300P-binding of **1**, **2**, and **4**. Even though the presence of a proline imposes additional restraints compared to a leucine, the C-terminal loop region next to position 300 is shifted (see above). Possibly, this can be attributed to the less favourable binding entropy observed for ligands penetrating into the specificity pocket, but not for **5** or **6**. To study the influence of Leu 300 more deeply we also constructed the corresponding alanine mutant and studied its complexation by **1**, **2**, **4** and **6**. Crystal structures were determined of L300A-1 and L300A-4 (Fig. 6.7 a and b, respectively). In the L300A-1 complex, the position of the alanine 300 residue is virtually identical with that of leucine in the wild type complex. The hydrogen bond length between the alanine NH group and the benzothiazole nitrogen amounts 3.0 Å (compared to 3.2 Å in ALR2-1). Facing ALR2-4 and L300A-4 (Fig. 6.7b), the mutant exhibits a more favourable hydrogen-bonding geometry to the nitro-group, as the ψ angle of Ala 299 deviates by $\sim 40^\circ$ (ALR2-4: 140.9° , L300A-4:

by the missing Leu 300 side chain removed in L300A might be attributed to the less favourable binding enthalpy of **1**, as a larger hydrophobic surface becomes solvent-exposed. Whereas the loss of this contact is to some extent compensated in L300A-4 by appropriate adaptation of Phe 122, this is not observed for L300A-1. In case of the L300P mutant a more enthalpic binding of the ligands penetrating into the specificity pocket has been observed. This trend is not confirmed for L300A. According to the abovementioned hypothesis of non-classical hydrophobic effects related to solvation/desolvation differences for ligand binding to L300P, data obtained for L300A implicate a more effective prevention of water entrance into the specificity pocket for latter mutant, as otherwise the enthalpic gain found throughout ligand binding to L300P should also become evident for L300A.

Leu 301 to Met mutation (L301M)

A further site of interest comprises Met 302 of ALR1, which is replaced by Leu 301 in ALR2. In the latter isoform, Leu 301 is solvent-exposed throughout all known crystal structures and does not directly interact with a bound ligand. Even though the corresponding region of ALR1 is assumed to be more rigid compared to ALR2, in the former isoform Met 302 adopts multiple conformational states next to the binding site: it points either to Trp 220 and, thus, away from the binding pocket, or towards Phe 125 thereby lining the binding cavity (Fig. 6.8a). Interestingly, binding of **7** to ALR1 induces an arene-sulfur interaction (4.2 Å) of the methionine sulfur and the ligand's naphthyl portion, presumably assisted by an sulfur-cation interaction to Arg 312 (3.2 Å), which is relocated upon binding of **7**.²⁶ Is the arene-sulfur contact also formed once a Met is introduced at position 301 in ALR2 ? To obtain some insights into this question the crystal structures of L301M-5 and L301M-7 together with the thermodynamic binding data of **1**, **5**, **6** and **7** towards L301M were determined (Tab. 6.3). Both complex structures, reveal no evidence for the formation of an arene-sulfur interaction as observed in ALR1-7. Instead, the introduced methionine side chain remains largely solvent-exposed similarly to leucine in the ALR2 wild type. These structural results are in agreement with those derived from porcine ALR2 complexed with **5** and **7**, which possesses a Met at the corresponding position (Fig. 6.8 b and c, respectively).²⁴ The absence of putative adaptations is consistent with the

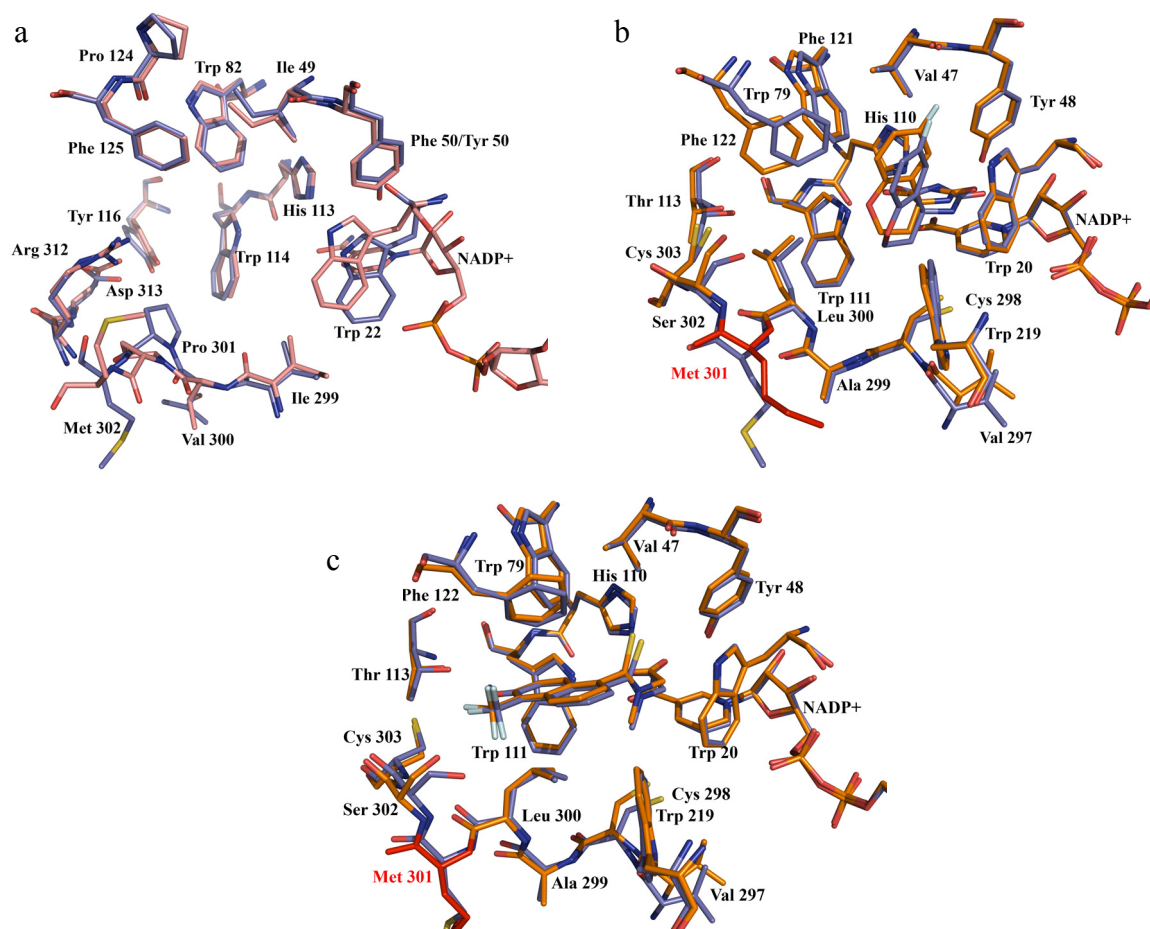


Figure 6.8. (a) Overview of two ALR1 crystal structures (pdb entries 1hqt and 2alr) demonstrating the remarkable dynamic properties of the C-terminal loop region around Met 302. (b) and (c) Superposition of porcine wild type ALR2 and human L301M mutant complexed with **5** and **7**, respectively. The introduced methionine remains solvent-exposed and does not interact with the ligand bound.

thermodynamic profiles observed for **5**, **6** and **7**: for WT and L301M, thermodynamic properties of binding remain nearly unchanged.

Ser 302 to Arg mutation (S302R)

The next series of exchanged amino acids which appear to modulate ligand binding selectivity comprises Arg 312 and Asp 313 in ALR1, which form a salt bridge with each other. The latter has been observed in uncomplexed and fidarestat-bound state. These bulky and interconnected residues impede the formation of an ALR2-like specificity pocket. However, as observed in the ALR1-**7** complex, ligands can rupture

Ligand	WT ALR2				L301M						
	k_b [10 ⁶ L/mol]	ΔG^0 [kJ mol ⁻¹]	ΔH_{bind}^0 [kJ mol ⁻¹]	$-T\Delta S^0$ [kJ mol ⁻¹]	k_b [10 ⁶ L/mol]	ΔG^0 [kJ mol ⁻¹]	ΔH_{bind}^0 [kJ mol ⁻¹]	$-T\Delta S^0$ [kJ mol ⁻¹]	$\Delta\Delta G^0$ [kJ mol ⁻¹]	$\Delta\Delta H_{bind}^0$ [kJ mol ⁻¹]	$-\Delta\Delta S^0$ [kJ mol ⁻¹]
1	115.6 +/- 16.4	-46.0 +/- 0.7	-58.1 +/- 1.0	12.1 +/- 1.7	15.4 +/- 1.0	-41.0 +/- 0.4	-69.5 +/- 3.6	28.5 +/- 4.0	-5.0	11.4	-16.4
5	4.5 +/- 0.6	-37.9 +/- 0.7	-54.7 +/- 0.8	16.8 +/- 1.4	3.7 +/- 0.7	-37.5 +/- 0.9	-54.4 +/- 1.4	16.9 +/- 2.3	-0.4	-0.3	-0.1
6	153.3 +/- 36.6	-46.7 +/- 1.2	-79.5 +/- 0.4	32.8 +/- 5.2	47.6 +/- 17.3	-43.8 +/- 1.9	-77.7 +/- 2.0	33.9 +/- 3.9	-2.9	-1.8	-1.1
7	4.6 +/- 1.9	-38.0 +/- 1.3	-31.0 +/- 1.0	-7.0 +/- 2.1	1.7 +/- 0.4	-35.5 +/- 1.2	-32.3 +/- 2.4	-3.2 +/- 3.6	-2.5	1.3	-3.8

Table 6.3. Thermodynamic binding data for **1**, **5**, **6**, and **7** to WT and L301M.

this salt bridge and thereby provoke a relocation of Arg 312.²⁶ As a result of this rearrangement, **7** is accommodated in a similar region as the specificity pocket in ALR2. Point mutation of the bulky arginine by alanine in ALR increases the affinity of **7** by about two orders of magnitude compared to wild type ALR1.²⁶ In the following, we transform this study to ALR2. In this isoform the smaller and uncharged residues Ser 302 and Cys 303 are located at corresponding positions. We therefore constructed the two ALR2 single mutants S302R, C303D, and the corresponding double mutant (DM). With respect to S302R, crystal structures and thermodynamic data were determined for **1**, **2** and **4** (Fig. 6.9 a-c).

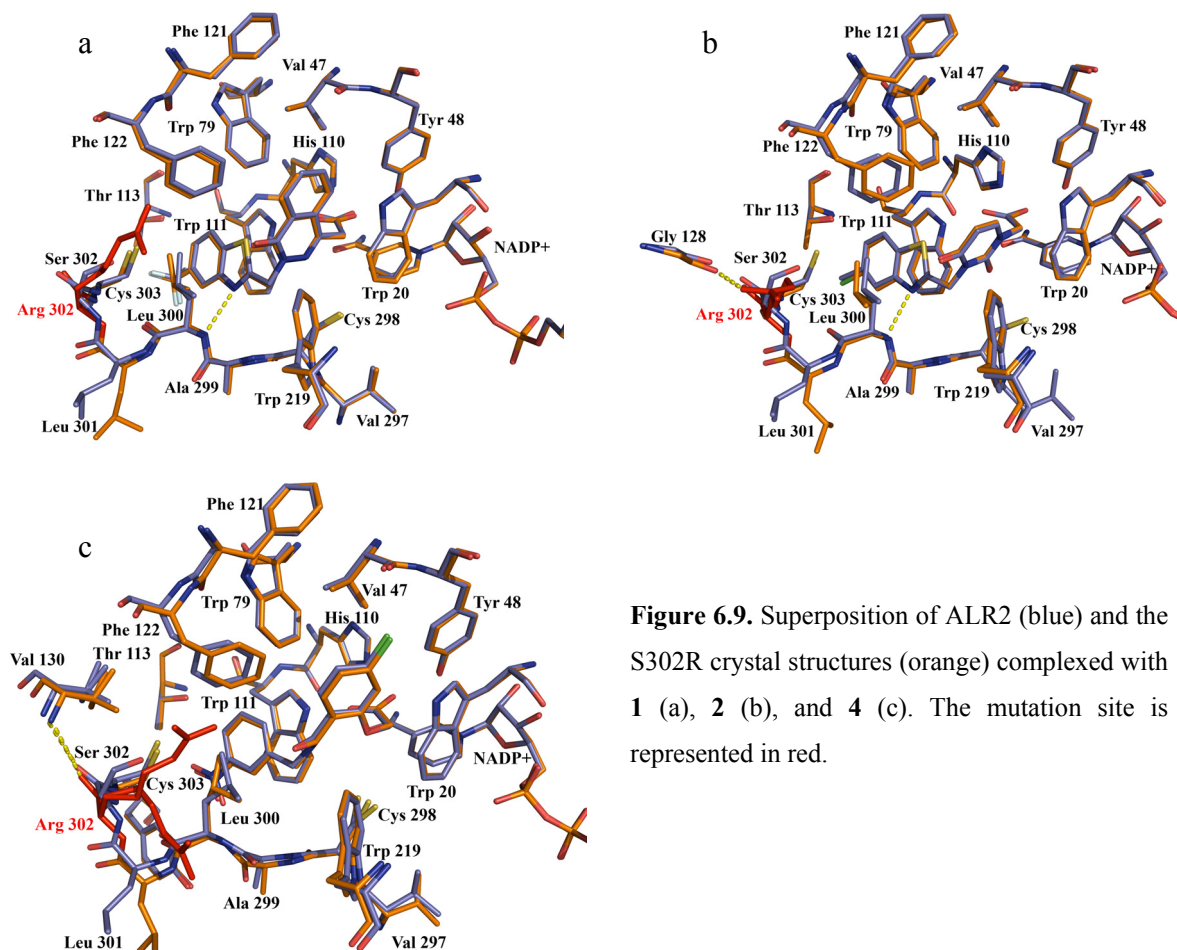


Figure 6.9. Superposition of ALR2 (blue) and the S302R crystal structures (orange) complexed with **1** (a), **2** (b), and **4** (c). The mutation site is represented in red.

For all three mutant complexes the backbone atoms of WT and S302R are hardly relocated. Only the backbone region of Leu 301 and Arg 302 are slightly shifted away from Val 130 compared to the corresponding WT complexes, presumably to avoid close contacts clash to the arginine side chain. In S302R-1 and S302R-2, the arginine residue orients towards the solvent, in S302R-4 it adopts a split conformation. One conformer forms a cation- π interaction with Phe 122 (3.4 Å), the other is oriented towards Leu 300 (3.8 Å) forming van der Waals contacts. The first split conformer establishes a water-mediated hydrogen-bond to the amide carbonyl group of the ligand. In S302R-2, the arginine NH1 nitrogen hydrogen-bonds to the backbone carbonyl oxygen of Gly 128. In all three S302R complexes the arginine side chain is located similarly to the corresponding Arg 312 in ALR1 after binding of **7**. Interestingly, all three studied inhibitors experience a drop in affinity of about 10 kJ mol⁻¹ corresponding to a change of two orders of magnitude in binding constant. Obviously, the introduction of the arginine side chain into ALR2 reduces ligand affinity to similar extent as the affinity to ALR1-R312A²⁶ is enhanced after removal of the arginine side chain. The factorization of the binding free energy into enthalpic and entropic contributions has been performed assuming that ligand binding is not affected by any superimposed changes of protonation states involving the arginine side chain. Whereas **1** and **2** experience a remarkable gain in binding enthalpy, complexation of **4**, the strongest enthalpic WT-binder, encounters a less favourable enthalpic contribution in case of S302R. Likely, ligand-induced relocation towards the solvent and subsequent change in solvation of the arginine residue is determinant for the overall thermodynamic profile resulting in an enthalpic gain for **1** and **2**. For S302R-4, where the arginine is disordered and involves a water molecule into ligand binding, a deviating thermodynamic behaviour is recorded. In total, this leads to an entropic advantage for complex formation with S302R compared to WT. Possibly, this also involves the more pronounced conformational disorder of the arginine. Regarding the WT and S302R-complexes of **4**, the guanidinium groups of both arginine conformers in S302R-4 are placed to positions occupied by water molecules in the WT complex. Their release will putatively also contribute to the observed entropic advantage of S302R-4 compared to ALR2-4. The thermodynamic consequences of the water-mediated H-bond between one Arg 302 split conformer and the amide carbonyl oxygen of **4** is presumably rather low, as such a water molecule is also present in the ALR2-4 complex. In summary, the

structural and thermodynamic properties of ligand binding to S302R are strongly affected by the Ser 302 to Arg replacement.

Cys 303 to Asp mutation (C303D)

The single replacement of Cys 303 by Asp has been studied for **1**, **2**, **4** and **6**. In most WT crystal structures Cys 303 is involved in arene-sulfur interactions with ligands occupying the specificity pocket. Crystal structures of this mutant have been determined **2**, **4** and **6** (Fig. 6.10 a-c). In C303D-**2** and C303D-**4**, Asp 303 points towards the imidazole moiety of His 306. One carboxylate oxygen of Asp 303 forms a polar contact to Thr 113 O γ (3.8 Å). Van der Waals contacts are established to the chlorine substituent of **2** or one nitro oxygen in **4** (both 3.3 Å). In C303D-**4**, the carboxylate group additionally interacts with the carbonyl oxygen of Val 130 via an interstitial water molecule.

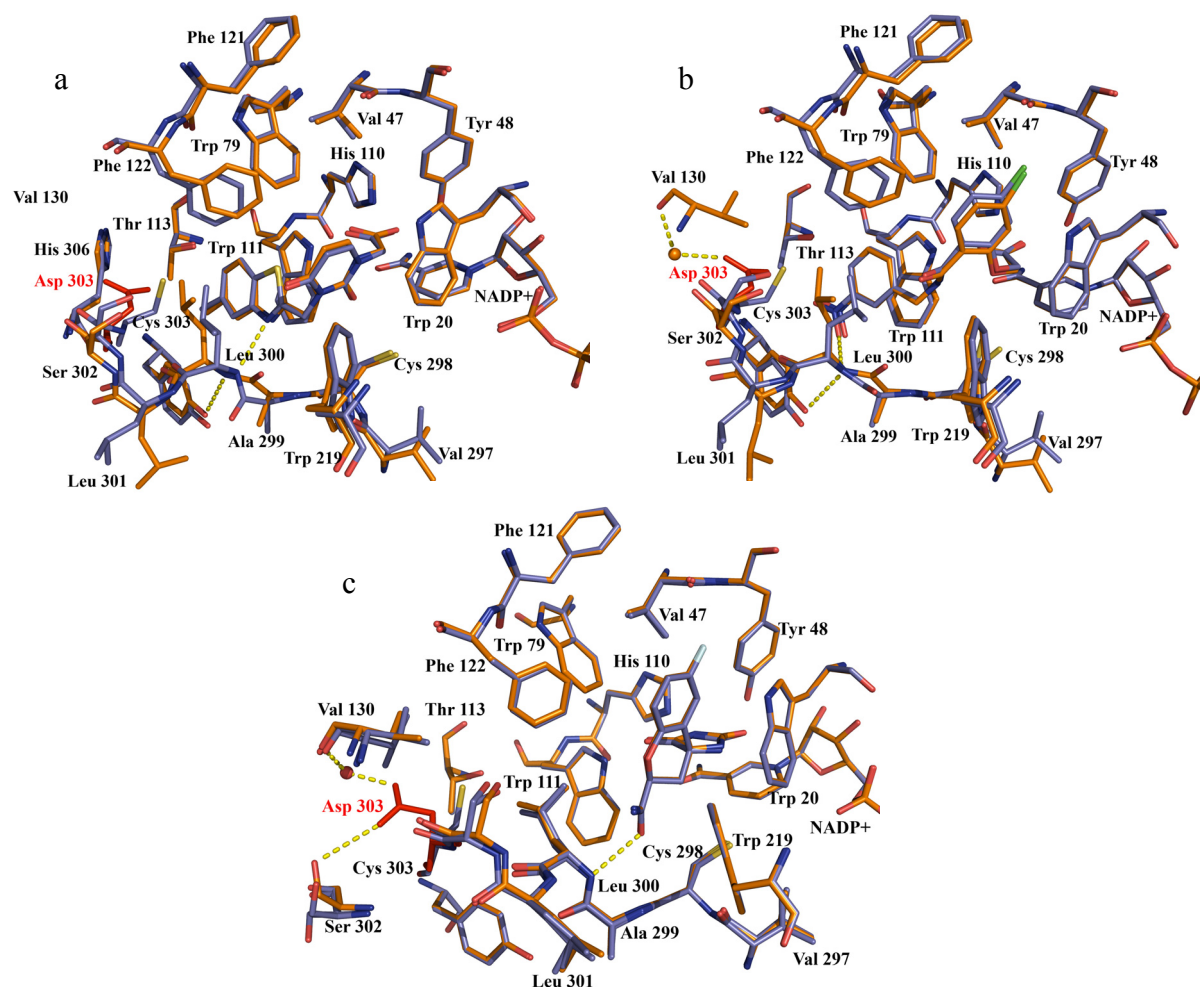


Figure 6.10. Superposition of ALR2 (blue) and the C303D crystal structures (orange) complexed with **2** (a), **4** (b), and **6** (c). The mutation site is represented in red.

For both ligands, **2** and **4**, a remarkable deviation between WT and C303D complexes is observed: In the WT crystal structures the Ala 299-Leu 300 peptide region orients in a way to form a hydrogen bond via its NH group to the benzothiazole nitrogen of **2** or the nitro group of **4**. Interestingly, in the C303D-**2** and -**4** complexes, this H-bond is lost, as the NH group forms a weak hydrogen bond to the side-chain oxygen of Tyr 309 (3.7 Å). The occupation of the ALR2 specificity pocket by ligands substituted by nitro substituent (such as **4**) has been shown to induce a slight rotation of the Tyr 309 χ_1 angle to accommodate this nitro group. In addition, polar interactions between the aromatic tyrosine side chain and both nitro oxygens (3.4 and 3.6 Å) has been attributed to an enhanced enthalpic contribution to binding affinity for ALR2-**4**.³³ In C303D-**4**, the displacement of this Tyr 309 side chain is also recorded and produces slightly closer contacts (3.2 and 3.5 Å). In C303D-**6**, the specificity pocket is found in closed state. Similar to the wild type complex, Leu 300 NH hydrogen-bonds to the exocyclic amide group of **6**. Asp 303 points away from the binding cavity and interacts with the backbone carbonyl oxygen of Val 130 and Ser 305 O γ . The former of these contacts is mediated via an interstitial water molecule. With respect to the thermodynamic properties, **1**, **2** and **4**, which bind next to the mutation site, experience all a remarkable drop in binding free energy of ~ 10 kJ mol⁻¹. In contrast, **6** which leaves the specificity pocket unoccupied, loses only 4 kJ mol⁻¹ in affinity towards C303D compared to WT. In case of **1** and **4**, this loss translates into a less favourable entropic contribution, however, the binding entropy of **2** remains virtually unchanged. Here, the drop in ΔG^0 is nearly exclusively of enthalpic origin (~ 10 kJ mol⁻¹). This correlates with the lost hydrogen-bond between the Leu 300 NH group and the benzothiazole moiety of **2**. This H-bond is lost in the C303D-**4** complex. As no drop in ΔH_{bind}^0 can be experienced between WT and C303D, some compensating effects must be in operation. Possibly, the closer contact between nitro group and Tyr 309, or, more likely, the incorporation of the water molecule next to Asp 303 can be attributed to this compensation. Binding of **6** to C303D compared to WT is accompanied by a more favourable enthalpy, overcompensated by a less beneficial entropic contribution. Also here, the pick-up of the water molecule could be determinant for the resulting thermodynamic profile as the arrest of water should be enthalpically favourable but entropically disfavoured.

Ser 302 to Arg and Cys 303 to Asp double mutation (DM)

As both single substitutions at position 302 and 303 in ALR2 result in a remarkable loss of binding free energy, also the double mutant was studied as it could possibly initiate the salt bridge observed in ALR1. Ligand binding to the double mutant (DM) was studied in structural terms for **1** and **6** and thermodynamically for **1**, **2**, **4** and **6**. Whereas the overall binding pocket geometry of the DM-**1** complex remains virtually unchanged, dramatic structural changes are observed for the C-terminal loop region hosting the mutation site (Fig. 6.11 a). In DM-**1**, the benzothiazole moiety of the ligand is shifted by about 1 Å away from Trp 111 (compared to ALR2-**1**) resulting in a less well fit to the binding site. The hydrogen bond formed by the Ala 299-Leu 300 peptide NH group to the ligand's benzothiazole nitrogen shows comparable length in WT and DM (ALR2-**1**: 3.2 Å, DM-**1**: 3.1 Å). However, the solvent-exposed site of the specificity pocket, formed in the WT complex by Leu 300 and Cys 303, is replaced in DM-**1** by Leu 300 and Leu 301. Both mutated neighbouring amino acids Arg 302 and Asp 303 are not interconnected via a salt bridge, but the oppositely charged functional groups remain solvent exposed with a mutual distance of about 10 Å. The guanidinium group of Arg 302 forms a water-mediated hydrogen bond to the Arg 296 backbone nitrogen. In addition, direct H-bonds are formed to the carbonyl oxygens of the latter amino acid (2.7 Å) and of Ala 299 (3.0 Å). The Asp 303 carboxylate accepts a hydrogen bond from the backbone NH group of the same residue (2.7 Å).

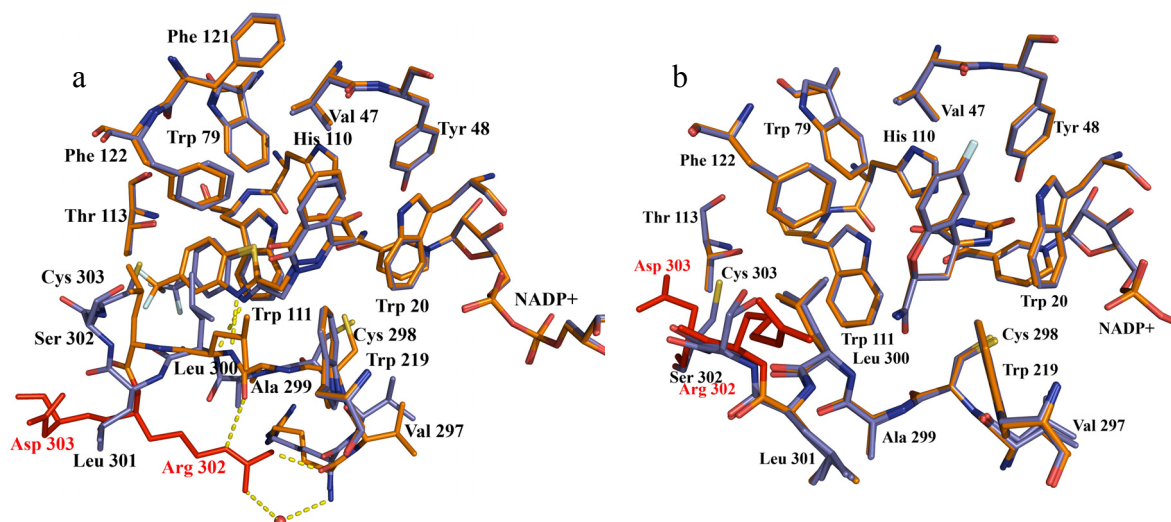


Figure 6.11. Superposition of ALR2 (blue) and the DM mutant crystal structures (orange) complexed with **1** (a), and **6** (b). The mutation sites are represented in red, hydrogen bonds involving the mutation are given as yellow dashes.

No further interactions are performed by this side chain carboxylate, as it orients directly into a solvent channel. It does not participate in any contacts to neighbouring symmetry-related molecules. The conformation observed for the two mutated residues in DM-1 has no relationship to the conformers detected in the S302R and C303D complexes. It reinforces a novel conformation of the C-terminal loop. Surprisingly, the contrary is observed for DM-6. Here, the overall geometry of the binding site and the bound ligand are similar to the corresponding WT complex (Fig. 6.11b). In particular, backbone and side chain atoms (apart from Arg 302) of the C-terminal loop are located virtually identically in DM-6 and ALR2-6. **6** binds to ALR2 without penetrating into the specificity pocket. Presumably, this explains the rather different adaptations of the C-terminal loop of the DM mutant upon ligand binding. In uncomplexed and **6**-bound state, crystal structures of ALR1 show a salt bridge between Arg 312 and Asp 313. In the DM-6 complex such a salt bridge is not observed. As no appropriate uncomplexed holo-structure of DM is currently available, it is difficult to estimate whether a salt bridge will be formed in the ligand-free protein. This has, however, consequences for the interpretation of our thermodynamic data, as a rupture of the salt bridge cannot be fully excluded occurring upon ligand binding. The solvent-exposed orientation adopted by Arg 302 in DM-6 is similar to the one observed in ALR1-7 and in S302R-2. Likewise, the conformation of Asp 303 in DM shows a water-mediated interaction to the Val 130 backbone nitrogen and carbonyl oxygen similar to C303D-6. The mutation of the two amino acids in DM dramatically alters the thermodynamic profile of ligand binding. The affinity of the investigated ligands directly interacting with the mutated region is significantly reduced: **2** and **4** lose about 10 kJ mol⁻¹ in affinity, in case of **1** even a decrease of about 14 kJ mol⁻¹ is recorded. The corresponding loss for **6**, not directly interacting to the specificity pocket, amounts to about 8 kJ mol⁻¹. The pronounced $\Delta\Delta G^0$ losses for **1**, **2**, and **4** factorize into even larger, partially compensating enthalpic and entropic contributions. Considering the dramatic changes of the complex structure observed in DM-1 as representative for ligands occupying the specificity pocket hardly allows for a conclusive interpretation of the thermodynamic data. The crystal structures of ALR2-6 and DM-6 suggest similar interactions of the ligand with the protein, yet a decrease in affinity (8 kJ mol⁻¹) is recorded as a result of less favourable enthalpic (3 kJ mol⁻¹) and entropic (5 kJ mol⁻¹) contributions. Possibly, this can be attributed to changes of solvation and protein dynamics upon binding.

6.3 Summary and Conclusions

Depending on their mode of action drugs must be endowed with the required selectivity profile towards a particular target and its related isoforms. Usually these isoforms differ to varying extent in the amino-acid composition in or next to the ligand binding pocket. In order to obtain a more detailed insight into the selectivity determining features we embarked into a systematic study of replacing crucial residues next to the binding site of aldose reductase (ALR2) by the corresponding ones found in its isoform aldehyde reductase (ALR1). To obtain a comprehensive overview, we applied protein crystallography and isothermal titration calorimetry to a set of inhibitors, originally developed for ALR2. Crystallography provides a detailed view on the static binding geometry, whereas microcalorimetry supplies energetic data on the wholesale binding process. The former conveys only limited information about the residual mobility of the binding partners and changes of the inherent dynamics upon complex formation. The latter can be superimposed by several association – related processes.^{29,37} We tried to correct for any concurrent changes in the heat of ionization resulting from overlaid protonation steps prior to factorization in enthalpy and entropy. This correction has been based on evidence collected in a previous study.³⁸ Nevertheless, as the results show, hardly ever the mutation of one residue in a binding site can be tight to the change of one structural and in consequence one enthalpic or entropic factor. Usually several changes superimpose which make the interpretation difficult. Furthermore, neither of the two methods can pinpoint the changes in residual mobility and/or dynamics, e.g. of rotational and vibrational degrees of freedom between two complexes. Admittedly, our view on mutational studies with respect to selectivity and structural conservation has been too simple. For some mutations very clear-cut and conclusive correlations can be observed (e.g. V47I, L300P). In other cases, we failed dramatically, e.g. with the constructed double mutant that should introduce a crucial salt bridge present in ALR1 into ALR2. Even though very interesting complex structures result from this exchange, they contribute little to the understanding of the selectivity determinants between both isomers. Site-directed mutagenesis is a popular tool to study protein function and binding properties towards ligand. But is the mutated protein conserved enough to still extract reasonable information, e.g. about altered

binding data? Without repeatedly determined crystals structures such interpretations will have to remain rather speculative.

A number of important messages can be learnt from the present study. In nearly all of the cases the actual binding mode of the bound ligands remains quite similar in WT and mutated species. The ligands studied can be grouped into those penetrating the specificity pocket (**1-4**) and those leaving the specificity pocket in close state (**5,6**). With respect to the studied point mutations only V47I and F121P are not involved in the specificity pocket, the others contribute directly to its composition. Apart from the V47I mutant the two groups of ligands mostly show distinct thermodynamic behaviour. Only in those cases where hardly any influence (L300A, L301M) can be detected or where the amino acid exchange creates locally too dramatic modifications (S302R, C303D, double mutant: S302R/C303D) to allow for a simple correlation, the distinct behaviour of the two groups of ligands cannot be observed.

For V47I the discrimination among the ligands seems to correlate with the fact whether a given ligand creates short contacts with the residue at the mutation site or not. Obviously, short contacts are detrimental for affinity, but enthalpically a gain and entropically a loss is experienced.

The F121P replacement affects binding of the specificity-pocket occupants by an affinity loss which factorizes in an enthalpic expense and an entropic benefit. The ligands not penetrating into the specificity pocket exhibit virtually unchanged thermodynamic binding profile.

Leu300 appears to be the crucial residue for triggering the opening of the specificity pocket. Furthermore, it potentially exposes its backbone NH as putative interaction site to bound ligands. It has been exchanged to Pro and Ala. Surprisingly, the Ala exchange takes not dramatic effect on the ligand binding profiles. This is quite different for the Pro mutation. For the non-penetrating ligands **5** and **6** an interesting series can be observed demonstrating that the loss of a hydrogen bond can be attributed to a decrease in $\Delta\Delta G^0$ of about 8 kJ mol⁻¹. This value matches well with those found in other studies.^{35,39} Furthermore, the pick-up of a water molecule to mediate protein-ligand interactions is enthalpically favourable and entropically disfavorable. Both effects mutually compensate to a fairly large extent. Also this result matches well with evidence collected for similar case studies.^{34,38} For the specificity-pocket occupants (**1-4**) a general loss in affinity (6-10 kJ mol⁻¹) is observed which factorizes in an enthalpic gain. It is overcompensated by an entropic loss. This observation points to a complex

correlation involving changes in the solvation properties of the opening specificity pockets which is altered in size by the Leu to Pro replacement. Furthermore, the flexibility of the C-terminal loop will be affected by the introduction of the restrained Proline residue.

The replacements of Ser and Cys by Arg and Asp at the position 302 and 303, respectively, create dramatic local changes in the protein, even more if both residues are exchanged at one time. Interestingly, the binding geometry of the studied ligands is not strongly perturbed, however their affinity drops in all cases by about one order of magnitude. Seemingly, those not penetrating the specificity pocket are less affected. The deviating factorization of these $\Delta\Delta G^0$ losses across the series of complexes indicates a complicated superposition of various effects involving hydrogen-bond formation to the ligands, partial disorder of the mutated residues in some complexes, pick-up of H-bonds mediating water molecules and deviating (partial) solvation/desolvation of the protein residues. The multiplicity of these contributions hampers a meaningful interpretation of the results.

The latter residue exchanges also points to the limitations of such a subsequent point mutational study. Clearly, only rather conserved exchanges can be discussed in terms of a clear-cut relationship. Nevertheless, one has to note that nearly all modifications on the molecular level create a response in an enthalpy and entropy change. Often they mutually compensate, pretending that the system or an important property has not been altered. Thus, they get easily neglected in the interpretation. This is of no consequences as long as these changes are similar for all examples in the studied series. If one entry, however, does not obey this “similar behaviour”, it falls out of the series. Possibly, even though our study has collected a fairly large amount of complementary information about the studied complexes, we still miss to record properties which could take substantial influence on the thermodynamic binding profile. These properties could possibly involve changes in the protein-internal degrees of freedom (e.g. rotational and vibrational state) or differences in the solvation/desolvation of the binding pockets of the various mutants along with the ligand binding process.

Further investigations of these processes will contribute to our understanding of the driving forces responsible for making a protein binding pocket attractive for a ligand, and subsequently will provide insights for the design of novel drug candidates.

6.4 Materials and Methods

Mutagenesis and enzyme expression. Expression and purification of Aldose Reductase have already been described elsewhere.^{24,30,31,35} The mutation of the tyrosine 48 into phenylalanine was introduced by PCR, using the Pfu Turbo polymerase (Stratagene), to amplify the entire plasmid. In order to construct the mutant enzymes, primer with the following and the corresponding complementary sequences were obtained from MWG-Biotech (Ebersberg, Germany): V47I: 5'-CCTCATTCTCATTCTGGTAGATATGGGCACAGTCGATGTGG- 3', T113Y: 5'-CCTTCCCAGGCTTAAAGCCATACGGCCAGTGAATAAGG- 3', F121P: 5'-CCGACTCATCCAATGGGAAAGGTTCCCTCCAGGC- 3', L300P: 5'-GGAGGTACAGCTCAACGGGGCACAGACCCTCC- 3', L300A: 5'-GGAGGTACAGCTCAACGCGGCACAGACCCTCC- 3', L301M: 5'-GGAGGTACAGCTCATCAAGGCACAGAC- 3', S302R: 5'-CCTTGTGGGAGGTACACCTCAAGGCACAGACCC-3', C303D: 5'-CCTTGTGGGAGGTATCGCTCAACAAGGCACAGACCC- 3', DM (S302R-C303D): 5'-CCTTGTGGGAGGTATCCCTCAACAAGGCACAGACCC-3'. After 20 cycles of PCR, the initial plasmid was digested by DpnI enzyme for 30 minutes at 37°C. After amplification (in XL2 Blue *E.Coli* strain), purification with the Quiagen Miniprep kit and sequencing (MWG-Biotech) to confirm the mutation, the mutated plasmid was transformed into the *E. coli* strain BL21 Gold for protein production. The mutated protein was then expressed and purified via the same procedures as for the wild type protein.

Isothermal Titration Calorimetry. Calorimetric measurements were carried out using a MCS ITC-instrument from MicroCal Inc. (Northampton, USA). In each experiment, the ligand was titrated to the protein solution present in the 1.4 mL sample cell. The reference cell contained 0.1 mM sodium azide dissolved in demineralised water. All measurements were carried out at 298 K in 10 mM Hepes buffer at pH 8. The wild type protein was used at a concentration of 18.9 μ M or 37.8 μ M, depending on the affinity of the protein-ligand pair. Protein concentrations were determined by UV spectroscopy (280 nm) using the specific absorption calculated by the ProtParam tool (www.expasy.ch). The ligand solution contained 252 μ M of the corresponding inhibitor dissolved in the same buffer as the protein. The protein was saturated with an excess of NADP⁺ which was present at the same concentration in the ligand solution to avoid

heat effects caused by diluting the cofactor. Solutions were degassed at 293 K under vacuum for 10 min. Upon experimental setup, the protein solution present in the sample cell was stirred at 400 rpm. After a stable baseline had been achieved the titration was initiated. The injection sequence started with an initial aliquot of 1.5 μL (to preserve diffusion effects arising from the experimental setup, data not used for fitting) followed by injections of 10 μL in time intervals of 300 s until complete saturation was obtained. Heat changes caused by each inhibitor injection were obtained from the integral of the calorimetric signal. Data were analysed using the ORIGIN software (MicroCal Inc.) for fitting the data points to a single-site binding model in agreement with the crystallographic results.

Experimental heats of the protein-inhibitor titration were corrected for heats of dilution by subtracting the average heat of the last three measurements after saturation of the protein binding sites has occurred. All measurements have been carried out at least in duplicate. Given energy values, binding constants and standard deviations were derived from data fitting and subsequent averaging of the corresponding measurements. Standard Gibbs free energy values were calculated using the equation $\Delta G^0 = -RT \ln K_b$ (where $R=8.3144 \text{ J mol}^{-1}\text{K}^{-1}$, K_b binding constant). The ligand binding enthalpy ΔH^0_{bind} , from the experimental binding enthalpy ΔH^0_{exp} the ionization enthalpy of buffer, protein residue (tyrosine) and, if present, of the ligand were deducted as described elsewhere.³⁸

Crystallization. The detailed crystallisation procedure has been reported elsewhere.^{24,30,31,35} Prior to crystallisation, ALR2 solutions were concentrated to 20 mg/ml in 50 mM di-ammonium hydrogen citrate at pH 5 and mixed with a solution of the cofactor in oxidized state to achieve a molar ratio of ALR2:NADP⁺ of 1:3. All complex structures determined in this study were obtained by cocrystallization (inhibitor concentration 2 mM in protein drop), as no appropriate holo crystals of the mutants were obtained in absence of any inhibitor. After an equilibration period of one week, a microseeding was performed. Crystals were grown at 293 K using the hanging drop vapor diffusion method. Initial crystals were obtained one day after microseeding.

Data Collection. Data were collected at 100 K using a cryoprotectant solution of 40 % (m/V) PEG 6000 in 50 mM di-ammonium hydrogen citrate at pH 5. The data sets were collected on a RIGAKU copper rotating anode (Molecular Structure Cooperation) at 50 kV, 90 mA using a R-AXIS IV++ image plate system. For each frame the exposure time and oscillation range were set to 5 min and 0.5°, respectively. Data processing and scaling were performed using the HKL2000 package.⁴⁰

Structure Determination and Refinement. The coordinates of human ALR2 (PDB code 1e13)⁴¹ were used for initial rigid-body refinement of the protein atoms followed by repeated cycles of conjugate gradient energy minimization, simulated annealing and B-factor refinement using the CNS program package.⁴² Refinement at later stages was performed with the program SHELXL.⁴³ Here, at least 20 cycles of conjugate gradient minimization were performed with default restraints on bonding geometry and B-values. Five percent of all data were used for R_{free} calculation. Amino acid side-chains were fitted into sigmaA-weighted $2F_o-F_c$ and F_o-F_c electron density maps using O and COOT.^{44,45} After the first refinement cycle, water molecules and subsequently cofactor and ligand were located in the electron density and added to the model. Restraints were applied to bond lengths and angles, chiral volume, planarity of aromatic rings and van der Waals contacts. Multiple side-chain conformations were built in case an appropriate electron density was observed and maintained during the refinement, and if the minor populated side-chain showed at least 10% occupancy. During the last refinement cycles, riding H atoms were introduced without using additional parameters. The final models were validated using PROCHECK.⁴⁶ Data collection, unit cell parameters and refinement statistics are given in the appendix of this chapter. Figures were prepared using Isis Draw (MDL, San Leandro, USA) and Pymol.⁴⁷

6. 5 References

1. Rauh, D., Klebe, G. & Stubbs, M. T. (2004). Understanding protein-ligand interactions: the price of protein flexibility. *J. Mol. Biol.* **335**, 1325-1341.
2. Teague, S. T. (2003). Implications of protein flexibility for drug discovery. *Nat. Rev. Drug Discov.* **2**, 527-541.
3. Kurumbail, R. G., Stevens, A. M., Gierse, J. K., McDonald, J. J. et al. (1996). Structural basis for selective inhibition of cyclooxygenase-2 by anti-inflammatory agents. *Nature* **384**, 644-648.
4. Bishop, A. C., Buzko, O. & Shokat, K. M. (2001). Magic bullets for protein kinases. *Trends Cell Biol.* **11**, 167-172.

5. Davydov, V. V., Dobaeva, N. M. & Bozhkov, A. I. (2004). Possible role of alteration of aldehyde's scavenger enzymes during aging. *Exp. Gerontol.* **39**, 11-16.
6. Yabe-Nishimura, C. (1998). Aldose reductase in glucose toxicity: a potential target for the prevention of diabetic complications. *Pharmacol. Rev.* **50**, 21-33.
7. Brownlee, M. (2001). Biochemistry and molecular cell biology of diabetic complications. *Nature* **414**, 813-820.
8. Greene, D. A., Arezzo, J. C. & Brown, M. B. (1999). Effect of aldose reductase inhibition on nerve conduction and morphometry in diabetic neuropathy. Zenarestat Study Group. *Neurology* **53**, 580-591.
9. Suzen, S. & Buyukbingol, E. (2003). Recent studies of aldose reductase enzyme inhibition for diabetic complications. *Curr. Med. Chem.* **10**, 1329-1352.
10. Constantino, L., Rastelli, G., Vianello, P., Cignarella, G. & Barlocco, D. (1999). Diabetes Complications and their potential prevention: Aldose Reductase Inhibition and other Approaches. *Med. Res. Rev.* **19**, 3-23.
11. Yagihashi, S., Yamagishi, S. I., Wada Ri, R., Baba, M., Hohman, T. C., Yabe-Nishimura, C. & Kokai, Y. (2001). Neuropathy in diabetic mice overexpressing human aldose reductase and effects of aldose reductase inhibitor. *Brain* **124**, 2448-2458.
12. Mylari, B. L., Armento, S. J., Beebe, D. A., Conn, E. L., Coutcher, J. B., Dina, M. S., O'Gorman, M. T., Linhares, M. C., Martin, W. H., Oates, P. J., Tess, D. A., Withbroe, G. J. & Zembrowski, W. J. (2003). A highly selective, non-hydantoin, non-carboxylic acid inhibitor of aldose reductase with potent oral activity in diabetic rat models: 6-(5-chloro-3-methylbenzofuran-2-sulfonyl)-2-H-pyridazin-3-one. *J. Med. Chem.* **46**, 2283-2286.
13. Bohren, K. M., Grimshaw, C. E. & Gabbay, K. H. (1992). Catalytic effectiveness of human aldose reductase. *J. Biol. Chem.* **267**, 20965-20970.
14. Sato, S. & Kador, P.F. (1990). Inhibition of aldehyde reductase by aldose reductase inhibitors. *Biochem. Pharmacol.* **40**, 303-307.
15. Barski, O. A., Gabbay, K. H., Grimshaw, C. E. & Bohren, K. M. (1995). Mechanism of human aldehyde reductase: characterization of the active site pocket. *Biochemistry* **34**, 11264-11275.

16. Barski, O. A. Gabbay, K. H. & Bohren, K. M. (1996). The C-terminal loop of aldehyde reductase determines the substrate and inhibitor specificity. *Biochemistry* **35**, 14276-14280.
17. Jay, D., Hitomi, H. & Griendling, K. K. (2006). Oxidative stress and diabetic complications. *Free Radic. Biol. Med.* **40**, 183-192.
18. Chang, T., Wang, R. & Wu, L. (2005). Methylglyoxal-induced nitric oxide and peroxynitrite production in vascular smooth muscle cells. *Free Radic. Biol. Med.* **38**, 286-293.
19. Oya, T., Hattori, N., Mizuno, Y., Miyata, S., Maeda, S., Osawa, T. & Uchida, K. (1999). Methylglyoxal modification of protein. Chemical and immunochemical characterization of methylglyoxal-arginine adducts. *J. Biol. Chem.* **274**, 18492- 18502.
20. El-Kabbani, O., Ruiz, F., Darmanin, C. & Chung, R.P.-T. (2004). Aldose reductase structures: implications for mechanism and inhibition. *Cell. Mol. Life Sci.* **61**, 750-762.
21. Darmanin, C., Chevreux, G., Potier, N., Dorsselaer, A. et al. (2004). Probing the ultra-high resolution structure of aldose reductase with molecular modelling and noncovalent mass spectrometry. *Bioorg. Med. Chem.* **12**, 3797-3806.
22. El-Kabbani, O., Old, S. E., Ginell, S. L. & Carper, D. A. (1999). Aldose and aldehyde reductases: structure-function studies on the coenzyme and inhibitor-binding sites. *Mol. Vis.* **5**, 20-25.
23. El-Kabbani, O., Wilson, D. K., Petrash, J. M. & Quioco, F. A. (1998). Structural features of the aldose reductase and aldehyde reductase inhibitor-binding sites. *Mol. Vis.* **4**, 19-25.
24. Urzhumtsev, A., Tete-Favier, F., Mitschler, A., Barbanton, J. et al. (1997). A 'specificity' pocket inferred from the crystal structures of the complexes of aldose reductase with the pharmaceutically important inhibitors tolrestat and sorbinil. *Structure* **5**, 601-605.
25. Podjarny, A., Cachau, R. E., Schneider, T., Van Zandt, M. & Joachimiak, A. (2004). Subatomic and atomic crystallographic studies of aldose reductase: implications for inhibitor binding. *Cell. Mol. Life Sci.* **61**, 763-773.
26. El-Kabbani, O., Carper, D., McGowan, M. H., Devedjiev, Y. et al. (1997). Studies on the inhibitor-binding site of porcine aldehyde reductase: crystal structure of the holoenzyme-inhibitor ternary complex. *Proteins* **29**, 186-192.

27. Petrash, J. M., Harter, T. M., Devine, C. S., Olins, P. O., Bhatnagar, A. et al. (1992). Involvement of cysteine residues in catalysis and inhibition of human aldose reductase. *J. Biol. Chem.* **267**, 24833-24840.
28. Grimshaw, C. E., Bohren, K. M., Lai, C.-J. & Gabbay, K. H. (1995). Human aldose reductase: Subtle effects revealed by rapid kinetic studies of the C298A mutant enzyme. *Biochemistry* **34**, 14366-14373.
29. Homans, S. W. (2005). Probing the binding entropy of ligand protein interactions by NMR. *ChemBioChem* **6**, 1-8.
30. El-Kabbani, O., Darmanin, C., Schneider, T. R., Hazemann, I., Ruiz, F., Oka, M., Joachimiak, A., Schulze-Briese, C., Tomizaki, T., Mitschler, A. & Podjarny, A. (2004). Ultrahigh resolution drug design. II. Atomic resolution structures of human aldose reductase holoenzyme complexed with Fidarestat and Minalrestat: implications for the binding of cyclic imide inhibitors. *Proteins* **55**, 805-813.
31. Howard, E. I., Sanishvili, R., Cachau, R. E., Mitschler, A., Chevrier, B., Barth, P., Lamour, V., Van Zandt, M., Sibley, E., Bon, C., Moras, D., Schneider, T. R., Joachimiak, A. & Podjarny, A. (2004). Ultrahigh resolution drug design I: details of interactions in human aldose reductase-inhibitor complex at 0.66 Å. *Proteins* **55**, 792-804.
32. Van Zandt, M.C., Sibley, E.O., McCann, E.E., Combs, K.J., Flam, B., Sawicki, D.R., Sabetta, A., Carrington, A., Sredy, J., Howard, E., Mitschler, A. & Podjarny, A.D. (2004). Design and synthesis of highly potent and selective (2-arylcabamoyl-phenoxy)-acetic acid inhibitors of aldose reductase for treatment of chronic diabetic complications. *Bioorg. Med. Chem.* **12**, 5661-5675.
33. Steuber, H., Zentgraf, M., Gerlach, C., Sotriffer, C. A., Heine, A. & Klebe, G. (2006). Expect the unexpected or caveat for drug designers: Multiple structure determinations using aldose reductase crystals treated under varying soaking and co-crystallization conditions. *J. Mol. Biol.* **363**, 174-187.
34. Steuber, H., Heine, A. & Klebe, G. (2007). Structural and thermodynamic characterization of Aldose Reductase inhibitors reveals a nitro substituent as strong enthalpic contributor to ligand affinity. *J. Mol. Biol.* *In press*.
35. Petrova, T., Steuber, H., Hazemann, I., Cousido-Siah, A., Mitschler, A., Chung, R., Oka, M., Klebe, G., El-Kabbani, O., Joachimiak, A. & Podjarny, A. (2005). Factorizing selectivity determinants of inhibitor binding toward aldose and

- aldehyde reductases: Structural and thermodynamic properties of the aldose reductase mutant Leu300Pro-fidarestat complex. *J. Med. Chem.* **48**, 5659-5665.
36. Meyer, E.A., Castellano, R.K. & Diederich, F. (2003). Interactions with aromatic rings in chemical and biological recognition. *Angew. Chem. Int. Ed.* **42**, 1210-1250.
37. Ruben, A. J., Kiso, Y. & Freire, E. (2006). Overcoming roadblocks in lead optimization: a thermodynamic perspective. *Chem. Biol. Drug Des.* **67**, 2-4.
38. Steuber, H., Czodrowski, P., Sottriffer, C. A. & Klebe, G. Tracing changes in protonation: A prerequisite to factorize thermodynamic data of inhibitor binding to aldose reductase. *To be submitted*.
39. Dullweber, F., Stubbs, M. T., Musil, D., Stürzebecher, J. & Klebe, G. (2001). Factorizing ligand affinity: a combined thermodynamic and crystallographic study of trypsin and thrombin inhibition. *J. Mol. Biol.* **313**, 593-614.
40. Otwinowski, Z. & Minor, W. (1997). Processing of X-ray Diffraction Data Collected in Oscillation Mode. *Methods Enzymol.* **276**, 307-326.
41. Calderone, V., Chevrier, B., Van Zandt, M., Lamour, V., Howard, E., Poterszman, A. et al. (2000). The structure of human aldose reductase bound to the inhibitor IDD 384. *Acta Cryst D* **56**, 536-540.
42. Brunger, A. T., Adams, P. D., Clore, G. M., DeLano, W. L., Gros, P., Grosse-Kunstleve, R. W., Jiang, J. S., Kuszewski, J., Nilges, M., Pannu, N. S., Read, R. J., Rice, L. M., Simonson, T. & Warren, G. L. (1998). Crystallography & NMR system: A new software suite for macromolecular structure determination. *Acta Crystallogr. D* **54**, 905-921.
43. Sheldrick, G. M. & Schneider, T. (1997). SHELXL: high-resolution refinement. *Methods Enzymol.* **277**, 319-343.
44. Jones, T. A., Zou, J. Y., Cowan, S. W. & Kjeldgaard. (1991). Improved methods for building protein models in electron density maps and the location of errors in these models. *Acta Crystallogr. A* **47**, 110-119.
45. Emsley, P. & Cowtan, K. (2004). Coot: model-building tools for molecular graphics. *Acta Crystallogr.* **D60**, 2126-2132.
46. Laskowski, R., MacArthur, M., Moss, D. & Thornton, J. (1993). PROCHECK: a program to check the stereochemical quality of protein structures. *J. Appl. Crystallogr.* **26**, 283-291.
47. DeLano, W. L. (2002). The PyMOL Molecular Graphics System.

<http://www.pymol.org>

48. Mylari, B. L., Larson, E. R., Beyer, T. A., Zembrowski, W. J., Aldinger, C. E. et al. (1991). Novel, potent aldose reductase inhibitors: 3,4-Dihydro-4-oxo-3-[[5-(trifluoromethyl)-2-benzothiazolyl]methyl]-1-phthalazine-acetic acid (Zopolrestat) and congeners. *J. Med. Chem.* **34**, 108-122.
49. Kotani, T., Nagaki, Y., Ishii, A., Konishi, Y., Yago, H., Suehiro, S., Okukado, N. & Okamoto, K. (1997). Highly selective aldose reductase inhibitors. 3. Structural diversity of 3-(Arylmethyl)-2,4,5-trioxoimidazolidine-1-acetic acids. *J. Med. Chem.* **40**, 684-694.
50. Mizuno, K., Yamaguchi, T., Unoue, A., Tomiya, N., Unno, R., Miura, K. et al. (1990). Profile of a new aldose reductase inhibitor (2S,4S)-6-fluoro-2'.5'-dioxyspiro[chroman-4,4'-imidazoline]-2-carboxamide. *Excerpta Med.* **913**, 89-96.

6.6 Appendix: Data collection and Refinement statistics

PDB entry	V47I-1 2PD5	V47I-6 2PD9	ALR2-2 2PDG	F121P-1 2PDB	F121P-4 2PDC
Data collection and Processing*					
No. of crystals used	1	1	1	1	1
Wavelength [Å]	1.5418	1.5418	1.5418	1.5418	1.5418
Space group	P1	P2 ₁	P2 ₁	P1	P1
Unit cell parameters					
a, b, c [Å]	40.5 47.3 47.4	49.4 66.9 47.3	49.3 66.9 47.1	40.3 47.2 47.4	40.5 47.1 47.2
α, β, γ [°]**	75.8 67.3 76.3	92.1	92.7	75.8 67.4 77.0	76.1 76.3 67.6
Solvent content [%]	44.6	43.1	2.2	2.2	2.2
Matthews coefficient [Å ³ /Da]	2.2	2.1	42.7	44.3	44.3
Diffraction data					
Resolution range [Å]	50-1.6 (1.63-1.6)	50-1.55 (1.58-1.55)	30-1.42 (1.44-1.42)	50-1.6 (1.63-1.6)	50-1.65 (1.68-1.65)
Unique reflections	37 079 (1 257)	43 127 (1 337)	54 379 (2 186)	36 978 (1 244)	28 734 (1 347)
R(I) _{sym} [%]	3.2 (11.5)	3.4 (5.3)	4.3 (44.1)	2.6 (6.4)	2.0 (4.7)
Completeness [%]	90.0 (59.6)	96.1 (60.2)	94.4 (76.1)	90.5 (59.9)	77.1 (72.5)
Redundancy	2.2 (2.2)	3.7 (2.4)	2.4 (1.7)	2.2 (2.2)	1.8 (1.8)
I/σ(I)	26.7 (10.6)	56.6 (24.4)	20.7 (2.1)	41.9 (17.9)	39.7 (19.2)

* Numbers in parentheses characterize the highest resolution shell.

** For space group P2₁ only the β angle is given.

	L300P-1	L300P-2	L300A-1	L300A-4	L301M-5
PDB entry	2PDF	2PDH	2PDI	2PDJ	2PDK
Data collection and Processing*					
No. of crystals used	1	1	1	1	1
Wavelength [Å]	1.5418	1.5418	1.5418	1.5418	1.5418
Space group	P1	P1	P2 ₁	P1	P2 ₁
Unit cell parameters					
a, b, c [Å]	40.4 47.0 47.3	40.2 47.3 47.0	49.4 66.9 47.3	40.4 47.1 46.2	49.4 66.6 47.4
α, β, γ [°]**	76.1 67.5 76.9	75.9 77.1 67.5	93.0	76.1 76.7 67.9	91.9
Solvent content [%]	44.2	43.9	43.1	43.1	43.0
Matthews coefficient [Å ³ /Da]	2.2	2.2	2.2	2.2	2.2
Diffraction data					
Resolution range [Å]	30-1.56 (1.59-1.56)	20-1.45 (1.47-1.45)	50-1.55 (1.58-1.55)	50-1.6 (1.63-1.6)	50-1.55 (1.58-1.55)
Unique reflections	39 048 (1 505)	46 661 (1 178)	41 753 (1 036)	35 579 (1 218)	42 955 (1 379)
R(I) _{sym} [%]	3.2 (8.2)	3.7 (29.8)	2.6 (6.3)	3.1 (22.0)	5.1 (27.2)
Completeness [%]	88.9 (68.6)	85.8 (42.9)	93.3 (46.9)	87.1 (58.0)	96.2 (62.5)
Redundancy	1.6 (1.6)	1.9 (1.8)	2.5 (1.7)	1.5 (1.3)	2.9 (1.9)
I/ σ (I)	22.3 (10.4)	24.6 (2.2)	36.6 (13.2)	25.6 (7.7)	23.7 (2.7)

	L301M-7	S302R-1	S302R-2	S302R-4	C303D-2
PDB entry	2PDL	2PDM	2PDN	2PDP	2PDQ
Data collection and Processing*					
No. of crystals used	1	1	1	1	1
Wavelength [Å]	1.5418	1.5418	1.5418	1.5418	1.5418
Space group	P2 ₁	P2 ₁	P1	P1	P1
Unit cell parameters					
a, b, c [Å]	49.4 67.0 47.0	49.5 66.4 47.4	40.5 47.2 47.2	40.4 47.3 47.2	40.3 47.1 47.4
α, β, γ [°]*	92.4	92.2	76.0 67.5 76.3	76.3 67.6 76.7	76.1 67.2 76.9
Solvent content [%]	42.8	42.9	44.3	44.5	44.2
Matthews coefficient [Å ³ /Da]	2.2	2.2	2.2	2.2	2.2
Diffraction data					
Resolution range [Å]	30-1.47 (1.5-1.47)	50-1.75 (1.78-1.75)	50-1.7 (1.73-1.70)	50-1.65 (1.68-1.65)	50-1.73 (1.76-1.73)
Unique reflections	46 195 (1 954)	29 405 (1 008)	30 010 (758)	34 170 (1 627)	27 792 (875)
R(I) _{sym} [%]	5.7 (30.6)	9.0 (34.9)	2.8 (7.7)	3.2 (7.7)	4.9 (24.2)
Completeness [%]	88.7 (75.4)	94.5 (66.9)	88.3 (45.4)	91.6 (86.3)	86.2 (53.3)
Redundancy	2.0 (1.6)	3.0 (1.9)	2.0 (2.0)	1.9 (1.8)	1.5 (1.7)
I/σ(I)	13.9 (1.9)	17.1 (2.0)	25.6 (12.0)	36.6 (10.2)	18.6 (3.6)

	C303D-4	C303D-6	DM-1	DM-6
PDB entry	2PDU	2PDW	2PDX	2PDY
Data collection and Processing*				
No. of crystals used	1	1	1	1
Wavelength [Å]	1.5418	1.5418	1.5418	1.5418
Space group	P1	P2 ₁	P2 ₁	P2 ₁
Unit cell parameters				
a, b, c [Å]	40.1 47.3 47.3	49.5 67.0 47.5	49.3 67.3 47.8	49.4 66.7 47.5
α, β, γ [°]**	76.3 67.4 77.1	91.4	91.4	91.6
Solvent content [%]	44.2	43.6	43.9	43.2
Matthews coefficient [Å ³ /Da]	2.2	2.2	2.2	2.2
Diffraction data				
Resolution range [Å]	50-1.55 (1.58-1.55)	50-1.55 (1.58-1.55)	50-1.65 (1.68-1.65)	50-1.65 (1.68-1.65)
Unique reflections	38 314 (1550)	43 220 (1 346)	35 600 (1 037)	34 105 (949)
R(I) _{sym} [%]	2.9 (12.6)	3.1 (5.4)	7.0 (46.3)	6.2 (35.3)
Completeness [%]	85.2 (68.3)	95.9 (60.3)	94.5 (56.0)	91.3 (51.4)
Redundancy	1.8 (1.6)	3.5 (2.5)	3.5 (2.1)	2.8 (1.9)
I/ σ (I)	29.0 (6.2)	37.0 (19.6)	21.2 (1.8)	22.0 (2.7)

	V47I-1	V47I-6	ALR2-2	F121P-1	F121P-4
Refinement					
Resolution range used in refinement [Å]	30-1.6	30-1.55	30-1.42	30-1.6	30-1.65
Reflections used in refinement (work/free)	35 014 / 1 839	40 911 / 2 166	50 718 / 2 687	35 041 / 1 846	27 250 / 1 400
Final R values for all reflections (work/free) [%]	17.2 / 21.4	15.5 / 20.4	14.3 / 20.0	15.6 / 20.7	16.3 / 22.8
Final R values for reflections with $F > 4 \sigma$ (work/free) [%]	17.1 / 21.1	15.4 / 20.3	13.9 / 19.4	15.5 / 20.5	16.2 / 22.7
Protein residues	315	315	314	315	315
Coenzyme	1	1	1	1	1
Inhibitor	1	1	1	1	1
Water molecules	301	396	286	318	291
RMSDs					
Bonds [Å]	0.009	0.011	0.011	0.011	0.008
Angles [°]	2.2	2.5	2.5	2.5	2.2

	L300P-1	L300P-2	L300A-1	L300A-4	L301M-5
Refinement					
Resolution range used in refinement [Å]	30-1.56	20-1.45	30-1.55	30-1.6	50-1.55
Reflections used in refinement (work/free)	36 950 / 1 945	43 074 / 2 257	39 532 / 2 073	33 464 / 1 743	39 931 / 2 098
Final R values for all reflections (work/free) [%]	17.9 / 22.8	17.5 / 22.3	15.4 / 19.5	17.6 / 22.6	15.9 / 20.1
Final R values for reflections with $F > 4 \sigma$ (work/free) [%]	17.7 / 22.4	16.5 / 21.3	15.3 / 19.2	17.1 / 21.8	15.3 / 19.4
Protein residues	314	315	315	315	315
Coenzyme	1	1	1	1	1
Inhibitor	1	1	1	1	1
Water molecules	254	251	349	269	348
RMSDs					
Bonds [Å]	0.009	0.009	0.011	0.009	0.01
Angles [°]	2.2	2.3	2.5	2.3	2.2

	L301M-7	S302R-1	S302R-2	S302R-4	C303D-2
Refinement					
Resolution range used in refinement [Å]	30-1.47	30-1.75	30-1.7	30-1.65	30-1.73
Reflections used in refinement (work/free)	42 166 / 2 226	27 372 / 1 399	28 420 / 1 481	32 238 / 1 687	25 829 / 1 329
Final R values for all reflections (work/free) [%]	18.3 / 23.3	17.1 / 24.7	16.8 / 24.2	17.1 / 24.1	18.2 / 24.8
Final R values for reflections with $F > 4 \sigma$ (work/free) [%]	17.5 / 22.1	16.4 / 23.6	16.7 / 23.8	16.9 / 23.8	17.3 / 23.6
Protein residues	315	315	315	315	315
Coenzyme	1	1	1	1	1
Inhibitor	1	1	1	1	1
Water molecules	295	329	289	270	180
RMSDs					
Bonds [Å]	0.009	0.007	0.008	0.008	0.006
Angles [°]	2.4	2.0	2.1	2.1	1.9

	C303D-4	C303D-6	DM-1	DM-6
Refinement				
Resolution range used in refinement [Å]	30-1.55	30-1.55	30-1.65	30-1.65
Reflections used in refinement (work/free)	35 872 / 1 892	40 960 / 2 168	32 396 / 1 691	31 716 / 1 650
Final R values for all reflections (work/free) [%]	15.7 / 21.2	16.1 / 20.3	17.4 / 22.2	16.0 / 22.4
Final R values for reflections with $F > 4 \sigma$ (work/free) [%]	15.3 / 20.5	16.0 / 20.1	16.1 / 21.0	15.4 / 21.3
Protein residues	315	315	312	315
Coenzyme	1	1	1	1
Inhibitor	1	1	1	1
Water molecules	306	323	275	315
RMSDs				
Bonds [Å]	0.009	0.010	0.008	0.008
Angles [°]	2.2	2.5	2.1	2.2

	V47I-1	V47I-6	ALR2-2	F121P-1	F121P-4
Ramachandran plot					
Most favoured [%]	91.0	91.3	91.3	91.3	90.6
Additionally allowed [%]	9.0	8.7	8.7	8.7	8.7
Generously allowed [%]	0	0	0	0	0.7
Mean B factors [Å²]					
Protein	22.2	14.3	18.6	17.1	19.4
NADP ⁺	15.2	9.0	12.4	10.9	12.5
Inhibitor	20.5	10.5	14.2	13.6	17.0
Water molecules	31.5	24.1	29.9	27.0	29.0

	L300P-1	L300P-2	L300A-1	L300A-4	L301M-5
Ramachandran plot					
Most favoured [%]	91.3	91.7	91.7	90.3	91.3
Additionally allowed [%]	8.3	8.0	8.3	9.4	8.7
Generously allowed [%]	0.4	0.4	0	0.4	0
Mean B factors [Å²]					
Protein	20.5	22.8	11.3	19.2	19.2
NADP ⁺	14.1	15.2	6.8	12.7	14.2
Inhibitor	16.2	17.3	7.9	14.4	35.9
Water molecules	28.1	31.1	19.5	27.9	28.9

	L301M-7	S302R-1	S302R-2	S302R-4	C303D-2
Ramachandran plot					
Most favoured [%]	89.9	91.0	91.3	91.7	91.0
Additionally allowed [%]	9.7	9.0	8.7	8.3	9.0
Generously allowed [%]	0.4	0	0	0	0
Mean B factors [Å²]					
Protein	19.7	26.7	22.0	23.2	26.3
NADP ⁺	12.8	18.6	14.2	15.9	19.8
Inhibitor	15.7	33.8	17.2	21.0	23.7
Water molecules	28.6	36.7	30.2	31.5	30.6

	C303D-4	C303D-6	DM-1	DM-6
Ramachandran plot				
Most favoured [%]	91.3	91.7	88.7	91.7
Additionally allowed [%]	8.3	8.3	11.3	8.3
Generously allowed [%]	0.4	0	0	0
Mean B factors [Å²]				
Protein	15.4	13.0	16.6	19.4
NADP ⁺	9.7	7.8	10.2	14.0
Inhibitor	11.7	8.5	12.8	15.1
Water molecules	24.3	20.7	24.7	26.6

7. Expect the Unexpected or Caveat for Drug

Designers: Multiple Structure Determinations

Using Aldose Reductase Crystals Treated under varying Soaking and Cocrystallization Conditions

7.1 Introduction

During the last four decades protein crystallography emerged as an essential tool to elucidate the binding geometry and interaction patterns of protein-protein and protein-ligand complexes. Especially as prerequisite for drug design accurate crystal structure determinations are of utmost importance.^{1,2} Novel leads are either discovered experimentally by screening existing compound libraries (high-throughput screening) or computationally by enumerating virtual libraries against a given target.³ For the latter strategy, X-ray crystallography is essential as it provides the structure of the target protein allowing detailed insights into the binding characteristics of a bound ligand. Prerequisite for such a structure-based approach are correct model building and error-free interpretation of electron-density maps.⁴ However, even in the case of successful crystal structure determination a unique and definite answer with respect to the binding mode resembling the in-vivo situation is not necessarily provided. One explanation for the observed complexity most likely originates from protein flexibility resulting in different geometries in deviating environments. Protein adaptability is an important prerequisite for biological function.^{2,3,5} Nevertheless, it also provides special challenge to inhibitor design as flexibility complicates the prediction of the binding mode of a small molecule ligand.⁶ Crystallographic B-factors provide evidence for the local atomic displacements, and, in case they are refined anisotropically, even information about the directionality is available. It has often been discussed whether B-factors provide information about local dynamic mobility or whether crystal structures only represent a static frozen-in picture, thereby underestimating the dynamic properties of the crystallized molecules.^{1,7}

In the first part of this study we analyse the dynamic properties of a protein-ligand complex using a molecular dynamics simulation based on the binding geometry observed in a crystal structure determined in our laboratory. Characteristic changes of the binding geometry observed during the MD simulation prompted us to collect multiple data sets of crystals obtained by different soaking or cocrystallization conditions in order to investigate whether the computationally indicated flexibility is also reflected by different states in the crystalline phase. Actually, distinct protein conformers are observed, which underline agreement between experimentally observed and computationally predicted adaptability of the protein binding pocket. In a second example, the intricate interplay between flexibility experienced by some amino-acid side-chains and cooperative packing effects caused by symmetry-equivalent molecules enable binding of more than one ordered ligand within and close-by the binding pocket. The studied target protein is human aldose reductase (ALR2; E.C. 1.1.1.21), a 36 kDa-sized enzyme that exhibits pronounced flexibility and adaptability with respect to its active site. The enzyme adopts a TIM-barrel fold and is probably involved in severe diabetic complications such as retinopathy and angiopathy. It is therefore believed to be a promising drug target.⁸ It converts various aldehydes (including glucose under diabetic conditions) to their corresponding alcohols using NADPH as reducing cofactor. Even though the exact mechanism is currently under discussion, NADPH donates a hydride ion to the carbonyl carbon of the aldehyde resulting in a negatively charged intermediate. Most likely, this step is followed by a subsequent transfer of a proton from one of the neighbouring acidic active site residues. The binding site consists of two sub-pockets, one comprising the residues probably involved in catalysis (Tyr 48, Lys 77, and His 110) along with the nicotinamide moiety of the cofactor, while the second so-called specificity pocket is formed by Trp 111, Ala 299, Leu 300 and Phe 122 (Fig. 7.1). These latter residues can adopt several conformations depending on the size and properties of the accommodated ligand. Thereby, they form differently shaped sub-pockets. However, upon binding of, e.g., a small-molecule ligand to a protein, the residual dynamic properties of the resulting complex are difficult to predict. The binding event imposes additional restraints onto the formed complex that can either increase or decrease the mobility of one or both partners.^{5,9} Thus, deeper understanding of dynamic properties with respect to protein-ligand interactions is of utmost importance. Here, we address these questions by means of multiple crystal structure determination and MD simulations.

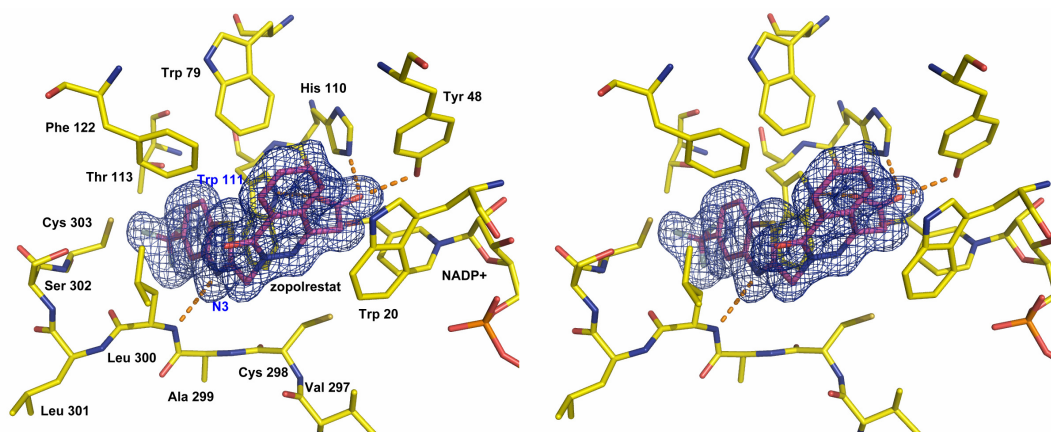


Figure 7.1. Stereo view of the refined crystal structure obtained after one day soaking of the ligand zopolrestat into aldose reductase crystals (**1day_soaked**). Residues comprising the binding pocket are shown as sticks coloured in yellow, the ligand is shown in magenta. H-bond interactions are represented in orange. The benzothiazole moiety penetrates the specificity pocket formed by Trp 111, Phe 122, and Leu 300. The phthalazinone system intercalates between Trp 20, Trp 79, and Phe 122, whereas the carboxylic head group penetrates into the catalytic cleft. An H-bond is formed donated by Leu 300 NH to the ligand's N3. Electron density of the $F_o - F_c$ omit map is depicted in blue at 2σ .

7.2 Results and Discussion

7.2.1 An unexpected backbone flip in the ALR2-zopolrestat complex

Human ALR2 is studied in complex with zopolrestat (Fig. 7.2, **1**), a potent carboxylic-acid type inhibitor formerly investigated in clinical trials. A crystal structure was obtained from preformed crystals soaked for one day with zopolrestat (**1day_soaked**, Fig. 7.1). It could be refined to a resolution of 1.48 Å and shows the following binding mode:¹⁰ The benzothiazole moiety of the inhibitor occupies the specificity pocket. It penetrates between Leu 300 and Trp 111, and its phthalazinone part intercalates with Phe 122, Trp 111 and Trp 20.

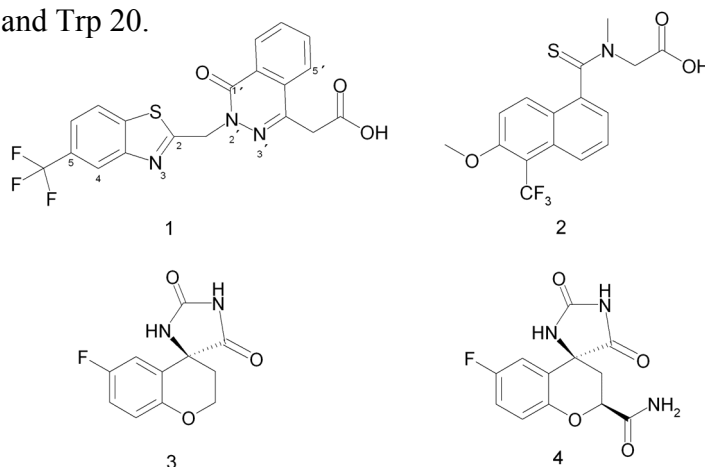


Figure 7.2. Chemical formulae of the aldose reductase inhibitors zopolrestat (**1**), tolrestat (**2**), sorbinil (**3**), and fidarestat (**4**).

Remarkably, Trp 20 N ϵ 1 forms a contact of 3.1 Å to the 5'-carbon atom of the phthalazinone system which is exceptionally short for a hydrophobic van der Waals contact. The carboxyl group of zopolrestat is likely deprotonated and forms electrostatic interactions with the positively charged nicotinamide moiety of the cofactor. Furthermore, it participates in a charge-assisted H-bond network to Tyr 48, His 110, and Trp 111. For the following discussion it has to be emphasized that the nitrogen atom of the benzothiazole moiety accepts an H-bond from the backbone NH group of Leu 300 facilitated by an appropriate orientation of the amide bond connecting Ala 299 and Leu 300. The electron density observed for **1day_soaked** gave no evidence for any structural disorder resulting in a split conformation of the binding site residues. The formation of the above-mentioned hydrogen bond is to some degree surprising as in the ultra-high resolution crystal structure of ALR2 complexed with IDD 594¹² such a contact is not present and the peptide bond adopts a different orientation which would not be suited to evolve the hydrogen bond to the ligand. Accordingly, the question arises whether the hydrogen bond observed in the crystals soaked for one day represents a frozen-in situation in the crystal packing and whether it is also relevant under conditions that allow to evolve dynamic properties.

In order to obtain some insights into the latter properties, MD simulations of the described complex were carried out.**

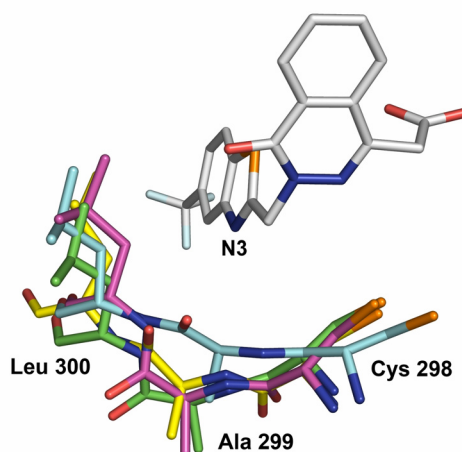


Figure 7.3. Selected conformational snapshots obtained from the MD simulation of the ALR2-zopolrestat complex are represented for the residues Cys 298, Ala 299, and Leu 300. These snapshots suggest enhanced mobility in this region: while the conformations shown in green or magenta enable H-bond formation to the ligand's N3, this H-bond is ruptured in the conformations coloured in light blue or yellow. The inhibitor as observed in **10days_cocryst** is represented as grey sticks after superimposing this crystal structure with the MD snapshots using a C α -fit.

** All MD simulations discussed in this chapter were carried out by Dr. Matthias Zentgraf, Fachbereich Pharmazie, Philipps-Universität Marburg.

Analysis of subsequent frames collected along the trajectory in terms of RMS deviations to detect conformational families (Fig. 7.3) clearly indicates the occurrence of several distinct states differing in the orientation of the residues Ala 299 and Leu 300 which reside in the C-terminal loop.

Conformation 1 resembles the geometry observed in the crystal structure which served as starting geometry. It shows the described H-bond between Leu 300 NH and the inhibitor's N3. Interestingly, conformation 2 displays a situation where this H-bond is ruptured as a result of the backbone flip of Ala 299. This conformation is similar to the one observed in the crystal structure of the ALR2-IDD594 complex.¹² Furthermore, Fig. 7.3 represents two additional intermediate conformers that were collected along the trajectory. The dominant conformation throughout the MD is the one with the lacking hydrogen bond. Nevertheless, is this indicated mobility an artefact of our MD simulation or does it correctly suggest enhanced flexibility in this region?

In consequence, we decided to perform further crystallisation attempts under slightly varied conditions.

In particular, we studied the influence of the soaking exposure time and compared the results to cocrystallization trials. In total, data sets for eight crystal structure determinations were collected and refined independently. After only two hours soaking, no appropriate electron density for zopolrestat could be detected in the F_o-F_c difference map. Instead, a citrate molecule picked up from the crystallisation buffer is observed in the active site. The specificity pocket is present in closed state characterized by short van der Waals contacts between the side-chains of Leu 300 and Trp 111. The backbone carbonyl group of Ala 299 likely accepts an H-bond from Tyr 309 OH via a 2.5 Å distance. The corresponding NH group of Leu 300 points towards the binding pocket and donates a H-bond to the solvent-exposed carboxylate of the citrate.¹³

Surprisingly, expanding the soaking period to three or even six days showed remarkable signs of flexibility or even conformational changes according to the dynamic behaviour suggested by MD simulations: two of three crystal structures based on data collected after a soaking period of three days (**3days_soaked_1**, **3days_soaked_2**) showed disrupted F_o-F_c electron density at $> 3.2 \sigma$ level in between the $C\alpha$ -atom and the carbonyl group of Ala 299. This indicates disorder phenomena possibly evidenced by extended mobility present in this region. However, the conformation found in the latter structures (Fig. 7.4b) resembles the one observed in

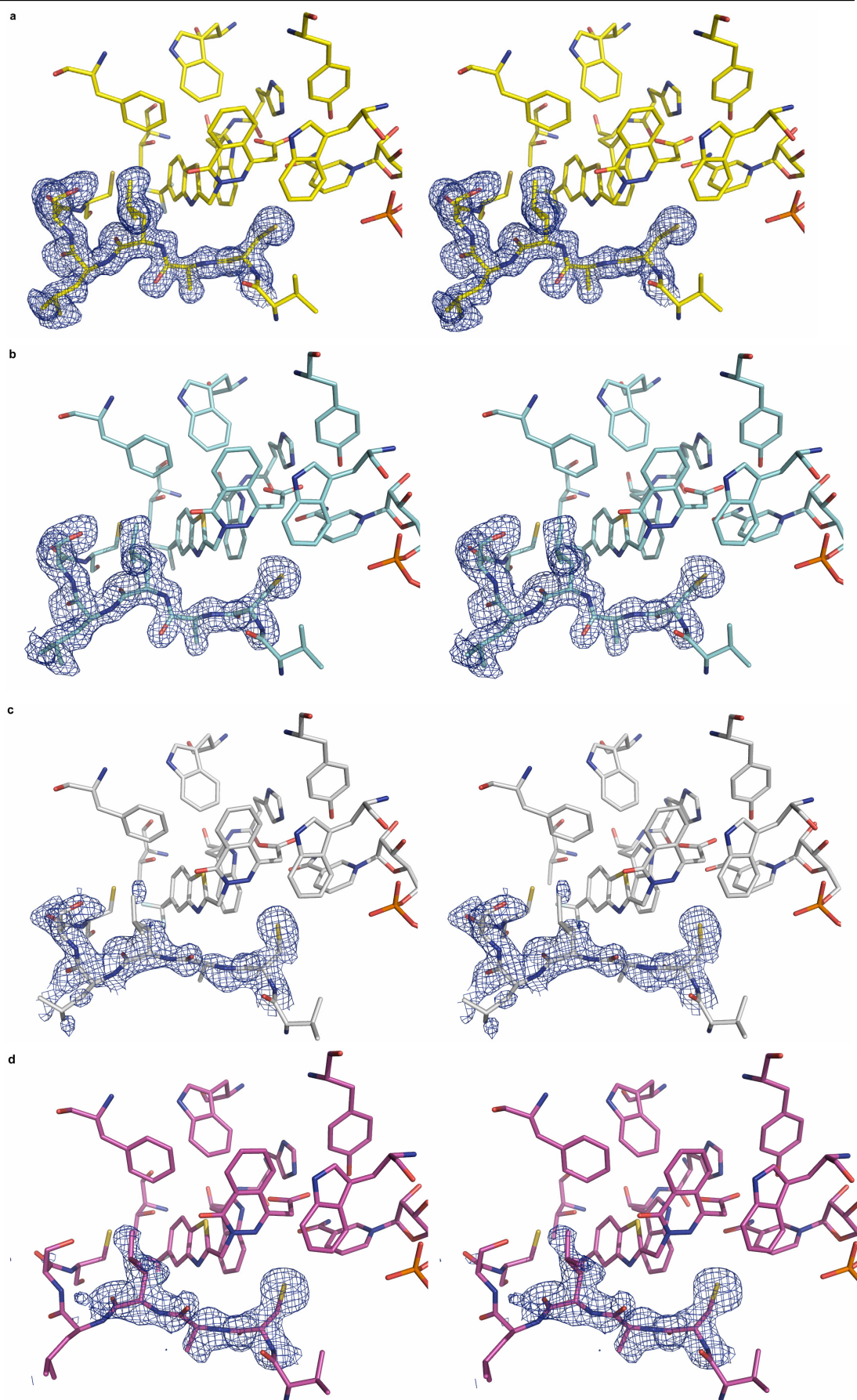


Figure 7.4. (p. 174) Stereo representation of the binding pocket occupied by the inhibitor zopolrestat. F_o-F_c omit difference densities observed for the C-terminal loop conformation after exclusion of the corresponding residues from the model are shown in blue contoured at 2.0σ . (a) The clear-cut electron density shows the conformation of the loop residues of **1day_soaked**. (b) The electron density observed for **3days_soaked_1** confirms the same loop conformation as represented in Fig. 1 and Fig. 4a. However, at higher σ -level (> 3.2) a discontinuity of the electron density becomes evident (not shown). (c) Representation of the loop conformation found in a third crystal soaked for three days (**3days_soaked_3**). Surprisingly, a backbone flip of the Ala 299-Leu 300 peptide bond accompanied by a rupture of the H-bond to the ligand is observed in this crystal structure. (d) Binding pocket representation obtained from crystals soaked for six days (**6days_soaked_1**). Even though the difference density is poorly defined for some parts of the C-terminal loop, it clearly shows a flip of the Ala 299-Leu 300 peptide bond similar to the conformation found in **3days_soaked_3** as well as rupture of the backbone electron density near Ala 299.

1day_soaked. We therefore concluded, that the H-bond donated by the Leu 300 amide group to N3 of the ligand is maintained. Surprisingly, in the third crystal structure obtained from a crystal soaked for three days (**3days_soaked_3**) a backbone flip of the amide bond next to Ala 299 is observed, accordingly accompanied by a rupture of the respective H-bond to the ligand. To assess the relevance of our refinement model, the F_o-F_c difference electron density was examined as obtained after excluding the residues 298-302 from the model (Fig. 7.4c). Conformational changes and a possible distribution over multiple conformational states is suggested by the poorly defined electron density next to Ala 299 in **3days_soaked_3**.¹⁴ Two additional crystal structures determined after a soaking period of six days (**6days_soaked_1** and **6days_soaked_2**) confirmed the binding geometry as observed in **3days_soaked_3**, underlining the occurrence of the backbone flip observed for Ala 299: whereas the ϕ angle is found nearly unchanged in all structures ($-167.8 \pm 6.6^\circ$), the ψ angle, representing the flip of the Ala 299 carbonyl group, undergoes a change of about 120° by rotating from $66.7 \pm 2.5^\circ$ in **1day_soaked**, **3days_soaked_1**, and **3days_soaked_2** to $-175.2 \pm 6.9^\circ$ found in **3day_soaked_3**, **6days_soaked_1**, and **6days_soaked_2**.

In order to examine which of the observed binding geometries is obtained under cocrystallisation conditions, two additional structures of the same complex were determined: one set, **1day_cocryst**, was collected using a crystal grown within one day, and a second data set, **10days_cocryst**, after crystals were exposed for ten days to the

mother liquid. In contrast to long-term soaking, for both structures obtained by cocrystallisation the electron density clearly indicates the conformation resembling that in **1day_soaked**. No ill-defined electron density is observed next to Ala 299. Interestingly, as shown in Fig. 7.5, long-term ligand soaking of preformed crystals provokes the conformational changes which are not observed after short-term soaking or cocrystallisation. Figure 7.6 visualises the differences between the families of structures representing the two conformers of the peptide bond. They are indicating by representing the backbone chain as tube diagram coloured by average B-factors. In particular, within the ligand-binding C-terminal loop a remarkable increase of the B-factors is observed when comparing, e.g., the crystal structures **10days_cocryst** and **6days_soaked_1**.¹⁵ In both complexes, the averaged B-factors for Ala 299 and Leu 300 amount to 14.8 Å² and 31.4 Å², respectively.

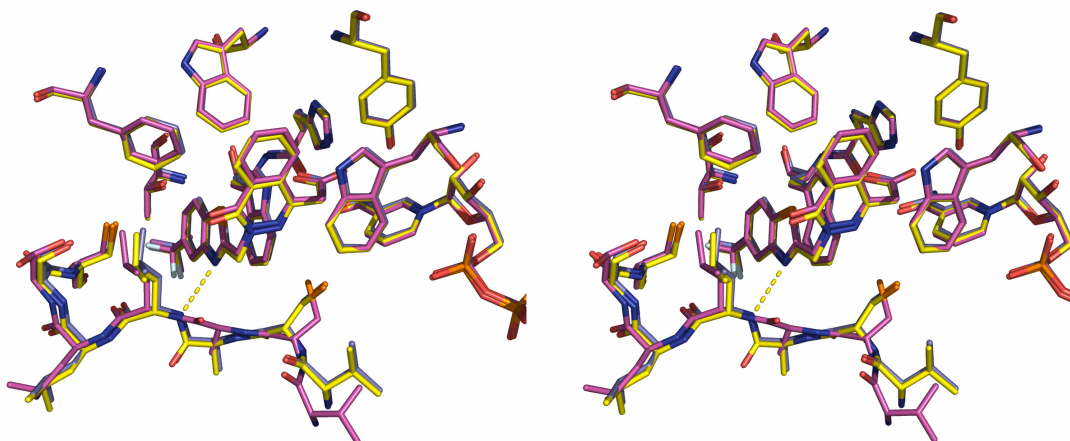


Figure 7.5. Superposition of the refinement models obtained for **10days_cocryst** (blue), **6days_soaked_1** (magenta) and **1day_soaked** (yellow). This representation clearly shows **1day_soaked** and **10days_cocryst** being virtually identical, whereas in **6days_soaked_1** the C-terminal loop adopts a different conformation.

In order to assess whether the collected evidence for an enhanced mobility indicated in the MD simulation depends on the starting conformation, a second MD run was performed, now using **3days_soaked_3** with the ruptured H-bond as initial model. Again, the conformer lacking this hydrogen bond is more frequently adopted, but the backbone flip, which triggers the H-bond formation is also observed. Thus, the enhanced flexibility in this region, suggested by the MD simulation, is not dependent on the starting geometry.

Our crystallographically observed Ala 299-Leu 300 backbone flip is accompanied by an H-bond rupture to the ligand. The enhanced mobility of this backbone stretch

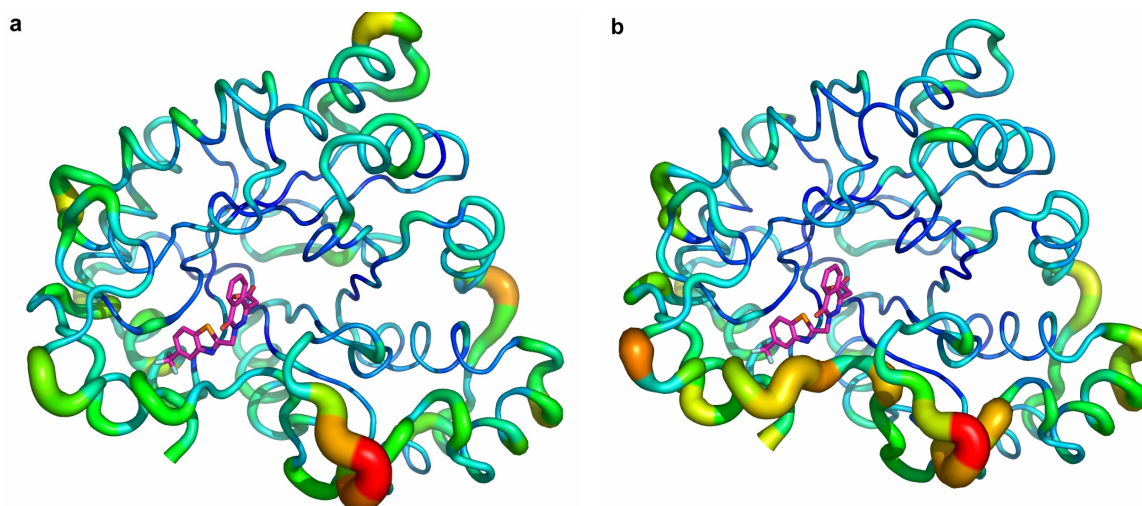


Figure 7.6. TIM-barrel of ALR2 represented as tube, emphasizing the local mobility with respect to the refined B-factors. The tube is coloured by B-factor: blue regions correspond to low temperature factors, whereas green, yellow and red colour characterize regions of subsequently increasing B-factor. In particular, dark blue represents B-values in the single-digit range, whereas red depicts regions with average B-factors of 40 \AA^2 and higher. Additionally, gain of temperature factor is represented by increasing diameter of the tube. The inhibitor zopolrestat is shown in magenta: (a) represents the corresponding tube representation for **10days_cocryst**, in (b) the one for **6days_soaked_1** is given. Note the remarkable gain of local mobility within the C-terminal loop region lining the ligand binding pocket observed in **6days_soaked_1** ($\sim 31 \text{ \AA}^2$, shown in yellow) compared to **10days_cocryst** ($\sim 15 \text{ \AA}^2$, represented in light blue). This comparison suggests that extended soaking exposure times provoke increasing mobility with respect to distinct regions represented by higher B-factors.

suggested by MD simulations indicates that this H-bond possibly contributes little to the binding affinity of this particular ligand. In order to evidence this issue, affinity data of zopolrestat analogues¹⁶ were analysed: No affinity data are available for derivatives only lacking the H-bond accepting nitrogen in the benzothiazole moiety. The study of Mylari et al.¹⁶ corroborates with some care the consequence for the presence or absence of an H-bond acceptor at this position. Assuming conserved binding mode for zopolrestat and its analogues, substitution of a 5-chloro-benzoxazole ($IC_{50} 7.8 * 10^{-8} \text{ M}$) by a 5-chloro-benzothiophene ($IC_{50} 2.5 * 10^{-7} \text{ M}$) or a 5-chloro-benzofuran moiety ($IC_{50} 1.5 * 10^{-7} \text{ M}$) at this site corresponds to an approximately twofold affinity drop. These kinetic inhibition data suggest a slight affinity advantage of derivatives capable to form this particular H-bond. Nevertheless, for this series of ligands, it appears as non-crucial for binding affinity. Its rupture along with enhanced mobility is apparently not paralleled by a dramatic loss in binding. Possibly it is determined by various other

interactions that compensate to some extent for the loss of this H-bond. In contrast, we recently collected evidence that the formation of this hydrogen bond is an important contributor to ligand affinity.¹⁷ Binding affinity and its factorization into enthalpic and entropic contributions were analysed for binding of the two related hydantoin-type inhibitors sorbinil and fidarestat (**3** and **4**, Figure 7.2) towards wild-type ALR2 and its Leu300Pro mutant. Whereas in the wild-type ALR2-fidarestat complex the exocyclic amide group of the ligand accepts an H-bond from Leu 300 NH, in the Leu300Pro mutant a similar H-bond cannot be formed due to lacking NH functionality in proline. Comparing the thermodynamic data for wild-type and mutant, the loss of this H-bond provokes a drop in ΔG^0 of about 8 kJ/mol, entirely determined by enthalpy loss. These results support the design hypothesis that addressing the Leu 300 NH group by appropriate H-bond accepting groups present in a ligand is important for ligand binding.

In the present study, two different protein conformations were found by crystal structure analysis for a complex formed with the same ligand, obviously depending on the protocol used to prepare the crystals or to form the protein-ligand complex. In drug design this has to be regarded as a caveat. For example, naively taking the two distinct structures to estimate the binding affinity for the two alternative complexes by consulting a scoring function, as e.g. implemented into FlexX¹⁸, a difference of 18 % between both geometries (e.g. **1day_soaked** over **3days_soaked_3**) is suggested. Applying a docking tool in lead discovery to develop novel leads, the results obtained by such a program will highly depend on whether or not the formation of a particular hydrogen bond is assumed. However, this is exactly the difference between both crystal structures determined according to the varying crystallization protocols. Even though crystal structure analysis is the most powerful tool to learn about the spatial structure of molecules, ambiguities may exist that could be misleading. Correctly considered, they also provide insights into the dynamic properties of a protein-ligand complex.

7.2.2 ALR2 complexed with one or several tolrestat molecules

In the second part of this study we report on deviating ligand stoichiometry with respect to the protein during complex formation. It is accompanied by cooperative structural adaptations of residues participating in the crystal packing. The structure of tolrestat (Fig. 7.2) has been previously determined in complex with pig aldose reductase (pdb

code: 1ah3) to a resolution of 2.30 Å by Urzhumtsev et al. in 1997 (Fig. 7.7).¹⁹ In order to elucidate the crystal structure with the corresponding human enzyme, crystals of the

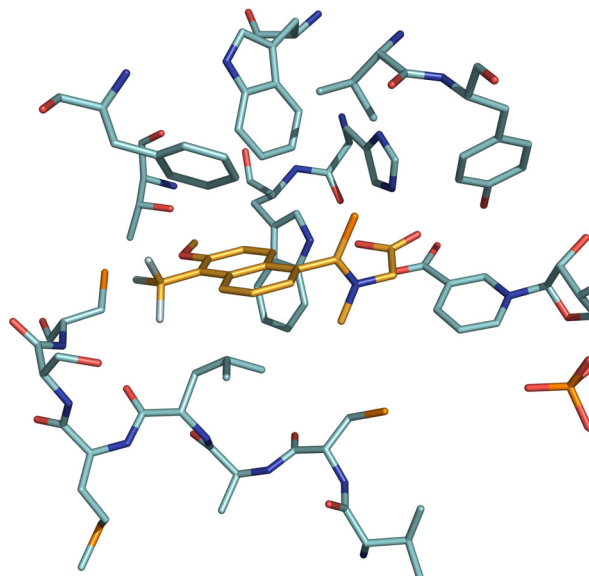


Figure 7.7. Binding mode of tolrestat in pig ALR2 as described.¹⁹ The carboxylic-acid head group occupies the catalytic pocket, whereas the naphthyl moiety forms hydrophobic contacts to Trp 111, Phe 122, and Leu 300. Note the kinked conformation of Leu 300 allowing the aromatic system of the ligand to form an edge-to-face interaction.

complex were obtained by soaking for three days. The crystal structure was refined to 1.48 Å. Data collection and refinement statistics are given in Table 7.1. The overall structure is very similar to the complex with pig aldose reductase, showing a C α rmsd of 0.37 Å. Surprisingly, the final structure comprises four bound ligand molecules in and around the binding pocket (Fig. 7.8). One ligand, L1 adopts the same binding mode as the single ligand found in the deposited pig aldose reductase structure (0.1 Å rmsd). In our complex, a second tolrestat molecule, L2, is placed in front of the binding pocket perpendicular to L1. The carboxylate group of this molecule forms two hydrogen bonds to the backbone NH groups of Leu 301 and Ser 302. The naphthalin moiety adopts a T-shaped aromatic π - π stacking geometry with respect to the corresponding part of ligand L1. The two additional ligands L3 and L4 are placed in a small pocket formed at the crystal packing interface. They create hydrophobic contacts with each other, most likely further stabilizing their binding modes. The carboxylate moiety of L3 forms a salt bridge to Lys 194 of a symmetry equivalent molecule, while the carboxylate group of L4 accepts an H-bond from Asn 292 ND2 of the same symmetry equivalent. In order to further analyse whether the incorporation of additional molecules depends on the crystallization conditions selected in this case, two further datasets were collected for

crystals with soaking exposure times of two hours and four days, keeping all other parameters invariant. The long-term soaked crystal was measured at a synchrotron

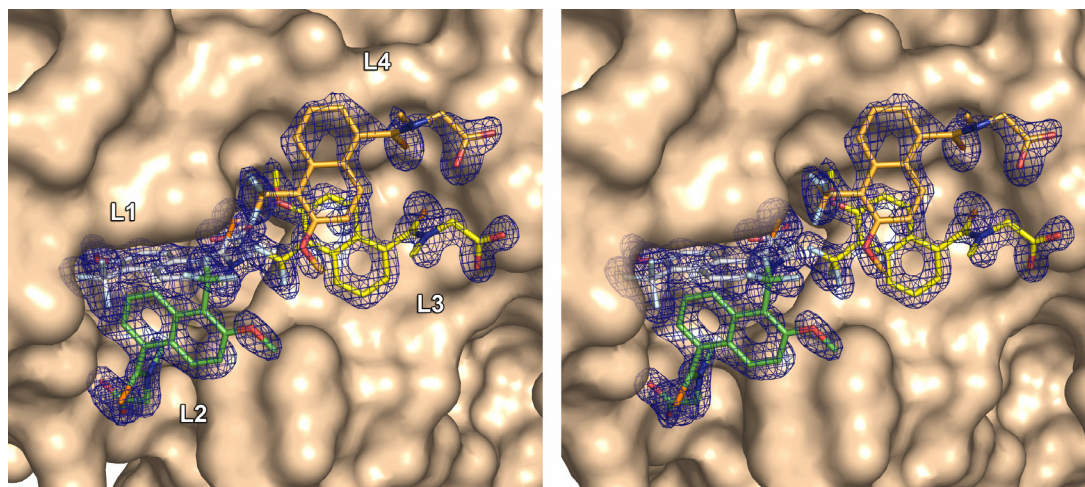


Figure 7.8. Stereo representation of ALR2 in complex with four tolrestat molecules, $F_o - F_c$ densities are coloured in blue and contoured at 1.5σ . Ligand L1 occupies the binding pocket as observed in the 1:1 complex with the enzyme. However, in the present complex, a second ligand, L2 is placed in front of the binding site of L1, forming an edge-to-face interaction with each other. Two additional tolrestat molecules, L3 and L4, occupy a binding cleft formed by crystal contacts.

beamline to improve data quality and resolution of the putative multi-ligand complex. As expected the structure determined for crystals of a short-term soak comprised only one ligand. It is placed in the binding pocket as already found in the singly complexed tolrestat crystal structure (Fig. 7.7). Surprisingly, also the crystal structure derived from the four-day soak reveals only one bound ligand. Obviously our four ligand-bound structure exhibits an unique observation. The most striking difference between the crystals of deviating stoichiometry is a change in the length of the b axis of the unit cell of about 2 \AA , obviously one characteristic resulting from the incorporation of the additional ligands. Screening for further crystals with similarly expanded cell dimensions was not successful as based on data collected for 5 different crystals soaked for three days.

A close comparison of the one and four ligand-bound structure reveals how the additional ligands are accommodated in a cleft formed between the protein molecules (Fig. 7.9). The interactions experienced between the ligands and the protein (see above) are accompanied by additional changes. The C-terminal residues Glu 313 – Phe 315, in the one-ligand structure only represented by poorly defined electron density, become

more clearly defined upon incorporation of the additional ligands. The C-terminal carboxylate oxygens of Phe 315 form an interaction with the backbone NH group of

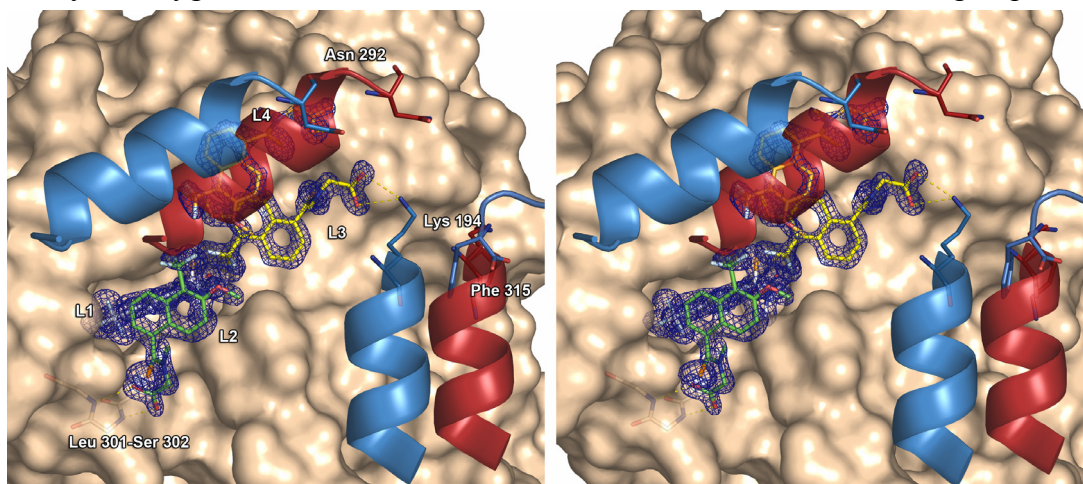


Figure 7.9. Interactions of the additional ligands with ALR2 and its symmetry related molecules. Omit $F_o - F_c$ densities of the inhibitor molecules are coloured in blue and contoured at 1.5σ . The carboxylate moiety of L3 forms a salt bridge to Lys 194 of one symmetry equivalent, while the carboxylate group of L4 accepts an H-bond from Asn 292 ND2 of this symmetry equivalent. The accommodation of the additional ligands requires significant changes of the protein structure: The helix formed by the residues Ser 282 - Tyr 291 performs a $C\alpha$ shift of about 7.0 \AA RMSD away from the binding site, whereas the helix Lys 194 - Lys 202 moves 6.2 \AA towards L3. For comparison these helices representing the conformation observed in the four-ligand complex are coloured in blue, whereas the spatial location of these helices known from the one-ligand structure is shown by red ribbons.

His 163, while the phenyl moiety is involved in a π - π stacking interaction with the imidazole moiety of the latter residue. The residues which directly interact with L3 and L4 adopt different conformations compared to the one-ligand structure to facilitate these interactions. In order to expand the pocket to accommodate L3 and L4 the helix formed by the residues Ser 282 - Tyr 291 undergoes a shift of about 7.0 \AA as indicated by the rmsd of the C_α atoms. The spatial location of this helix found in the one-ligand structure would clash with the positions of L3 and L4. Additionally, the helix comprised by residues Lys 194 to Lys 202 moves approximately 6 \AA towards L3 and, thus, facilitates the salt bridge between Lys 194 and the carboxylate group of L3. During this process the otherwise disordered residue Lys 194 becomes ordered. The space created by the rearrangement of the helix is occupied by the C-terminal residue Phe 315, which also becomes ordered (see above). These features clearly show that remarkable conformational changes apart from the induced-fit adaptations of the

binding pocket take place in order to create enough volume to accommodate the additional ligands. Even though the occurrence of two ligands, both located within the binding pocket, has been reported for a double mutant of ALR2,²⁰ a similar phenomenon as described in this study has not yet been reported for any other Aldose Reductase crystals.

7.3 Conclusions

Several conclusions can be drawn from our study. It is well known that modified crystallization conditions with respect to the composition of the mother liquid can result in different crystal forms and, in consequence, in deviating ligand binding modes. However, it is widely assumed that the same binding mode will be produced for a protein-ligand complex independent of the applied protocol concerning the soaking exposure time or the cocrystallization procedure. To our best knowledge, this is the first systematic study analysing the influence of different soaking and cocrystallization protocols with respect to the produced binding poses observed in protein-ligand complexes. As we observe deviating results this immediately provokes the question under which conditions the most relevant geometry resembling the in-vivo situation may be obtained in order to develop meaningful ligand design hypotheses. Even though we cannot provide an explanation for the obtained results, it points to a caveat for structural studies. Usually, crystallization conditions are screened and one or several turn out to be successful. The best diffracting crystal is subjected to data collection and the data are evaluated. Once the structure has been determined successfully, usually no further analysis of this structure in dependence of the crystal growth conditions is performed. This is a quite acceptable strategy, in particular, since the systematic re-evaluation of a structure can be rather tedious. For the present case study, in total 17 complete data sets had to be collected, 10 of those were subsequently refined. However, as indicated, the relevance of the resulting structures with respect to drug design can be different. This has been shown by the studied zopolrestat example where the presence or absence of a hydrogen bond to the protein will influence the drug design hypothesis. On the other hand, such multiple structure determinations can indicate the intrinsic flexibility of some portions of a protein that are in particular influenced and modified upon ligand binding. The present multiple structure determinations have been combined

with MD simulations to generate a conclusive picture. It clearly relates the different crystal structures as contiguous frozen-in snapshots of a dynamic process probably evolved in solution.

Appropriate handling of protein flexibility in structure-based drug design remains one of the major challenges. Even though a generally applicable protocol is not yet available, this study suggests that more relevant hypotheses can be produced if crystal growth and protein-ligand complex formation is studied under varying conditions and crystal structure analysis is combined with MD simulations. This is in particular important if only one crystal structure is available. Visual inspection and thorough comparison of multiple crystal structures and NMR studies complemented by the analysis of frames generated by MD simulations can help to estimate, in which regions enhanced protein mobility can affect ligand binding.

7.4 Materials and Methods

Cloning, expression, purification and crystallisation of Aldose Reductase have already been described elsewhere.^{12,21,22} Prior to crystallisation, ALR2 solutions were concentrated to 20 mg/ml in 50 mM di-ammonium hydrogen citrate at pH 5 and mixed with a solution of the cofactor in oxidized state to achieve a molar ratio of ALR2:NADP⁺ of 1:3. After an equilibration period of one week, a microseeding was performed. Crystals were grown at 293 K using the hanging drop vapor diffusion method. For the soaking process of zopolrestat a saturated solution in 50 mM di-ammonium hydrogen citrate, pH 5 containing 25 % (m/V) PEG 6000 was prepared. For cocrystallisation, 5 μ L of this soaking suspension were added to 20 μ L of the protein solution prior to crystallization, equilibrated over one week at 277 K. After one day incubation microseeding was performed. Crystals were obtained one day after microseeding. For soaking of tolrestat a ligand concentration of 40 mM in the described soaking buffer was used. For all soaking experiments, the same soaking solutions were used. All crystals were taken from the same crystallization plate, and the protein used for growing the crystals was obtained from the same expression and purification batch.

Data Collection. Data were collected at 100 K using a cryoprotectant solution of 40 % (m/V) PEG 6000 in 50 mM di-ammonium hydrogen citrate at pH 5. The data sets were

collected on a RIGAKU copper rotating anode (Molecular Structure Cooperation) at 50 kV, 90 mA using a R-AXIS IV++ image plate system. For each frame the exposure time and oscillation range were set to 5 min and 0.5° , respectively. Data processing and scaling were performed using the HKL2000 package.²³ The data set of the tolrestat complex at 1.08 Å resolution was collected at the beamline X06SA at SLS, Switzerland.

Structure Determination and Refinement. The coordinates of human ALR2 (PDB code 1el3)²⁴ were used for initial rigid-body refinement of the protein atoms followed by repeated cycles of conjugate gradient energy minimization, simulated annealing and B-factor refinement using the CNS program package.²⁵ Refinement at later stages was performed with the program SHELXL.²⁶ Here, at least 20 cycles of conjugate gradient minimization were performed with default restraints on bonding geometry and B-values. Five percent of all data were used for R_{free} calculation. Amino acid side-chains were fitted into sigmaA-weighted $2F_o-F_c$ and F_o-F_c electron density maps using O.²⁷ After the first refinement cycle, water molecules and subsequently cofactor and ligand were located in the electron density and added to the model. Restraints were applied to bond lengths and angles, chiral volume, planarity of aromatic rings and van der Waals contacts. Multiple side-chain conformations were built if an appropriate electron density was observed and maintained during the refinement, if the minor populated side-chain showed at least 10% occupancy. During the last refinement cycles, riding H atoms were introduced without using additional parameters. The final models were validated using PROCHECK.²⁸ Data collection, unit cell parameters and refinement statistics are given in Table 7.1. Figures were prepared using Isis Draw (MDL, San Leandro, USA) and Pymol.²⁹ RMS deviations were calculated using SYBYL.³⁰

Molecular Dynamics. All preparing steps and simulations were carried out with the AMBER 8.0³¹ suite of programs, using the Cornell et al.³² force field in the variant of the parm99 parameter set.³³ Parameters for the ligand were taken from the GAFF force field³⁴ using antechamber. Parameters for the cofactor NADP^+ were taken from a previous MD study.³⁵ The carboxylic group of the ligand was treated as deprotonated. Atomic charges for both the ligand and the cofactor were calculated by fitting to the HF/6-31G* electrostatic potential using the conformation observed in the crystal structure. The corresponding ab initio calculations were performed with GAUSSIAN98³⁶, the restrained electrostatic potential fit with the RESP program.^{37,38} Hydrogen atoms were added using Amber templates. The simulated protein system thus consisted of 316

amino acids or 5071 atoms, plus the cofactor with 73 atoms and the ligand with 40 atoms.

The crystal structure served as starting model was subjected to a short initial energy minimization in vacuo using 20 steps of steepest descent followed by 180 steps conjugate gradient minimization. After addition of two sodium counterions to ensure neutrality (placed at minima of the electrostatic potential), the systems were solvated in a box of TIP3P³⁹ water molecules, which resulted in box sizes of $\sim 80 \text{ \AA} \times 65 \text{ \AA} \times 77 \text{ \AA}$ and a total of ~ 9000 water molecules. The MD simulation was then started by heating the solvent to 300K over a period of 20 ps and cooling to 100 K over a period of 5 ps, keeping the solute fixed. After this procedure, the entire system was gradually brought to 300 K over a period of 25 ps. The simulation was then carried on for 6050 ps under constant temperature and pressure (NPT), applying periodic boundary conditions.

The temperature was kept constant by coupling to a heat bath through the Berendsen algorithm.⁴⁰ Pressure was adjusted by isotropic position scaling using a Berendsen-like algorithm. Covalent bonds to hydrogen atoms were constrained by the SHAKE⁴¹ algorithm and a time step of 2 fs was used. A cutoff of 8 Å was applied to the van der Waals interactions, while the electrostatics were treated by the Particle Mesh Ewald method.⁴² The simulations were carried out with the SANDER MD module of AMBER 8.0.

For analysis, energy data were saved every 10 time steps, solvent and solute coordinates every 0.5 ps. All results presented refer to the 6.0 ns trajectories which exclude the first 100 ps required for temperature adjustment and equilibration (an equilibrated state with respect to the total potential energy in the system was reached within the first 100 ps).

Coordinates and structure factor amplitudes of all crystal structures have been deposited at the Protein Databank with the PDB entries given in Table 7.1. Despite some redundancy may have been generated by our depositions, we intended to satisfy the referee's request.

PDB entry	1day_soaked 2FZS	3days_soaked_1 2DUX	3days_soaked_2 2DUZ	3days_soaked_3 2HV5	6days_soaked_1 2FZ9	6days_soaked_2 2DV0	1day_cocryst 2HVN	10days_cocryst 2HVO	Tolrestat four_ligands 2FZB	Tolrestat_sync 2FZD
<i>Data collection and processing</i>										
No. of crystals used	1	1	1	1	1	1	1	1	1	1
Wavelength (Å)	1.5418	1.5418	1.5418	1.5418	1.5418	1.5418	1.5418	1.5418	1.5418	0.97920
Space group	<i>P</i> 2 ₁	<i>P</i> 2 ₁	<i>P</i> 2 ₁	<i>P</i> 2 ₁	<i>P</i> 2 ₁	<i>P</i> 2 ₁	<i>P</i> 2 ₁	<i>P</i> 2 ₁	<i>P</i> 2 ₁	<i>P</i> 2 ₁
<i>Unit cell parameters</i>										
<i>a</i> , <i>b</i> , <i>c</i> (Å)	49.3, 66.9, 47.2	49.4, 67.0, 47.2	49.4, 67.1, 47.2	49.6, 67.0, 47.3	49.4, 67.1, 47.3	49.5, 67.1, 47.1	49.4, 66.9, 47.2	49.5, 67.2, 47.3	49.2, 68.1, 46.7	49.5, 66.7, 47.1
β (°)	92.9	92.8	92.8	92.2	92.4	93.0	93.0	92.8	92.8	92.5
<i>Diffraction data^a</i>										
Resolution range (Å)	35–1.48 (1.51–1.48)	50–1.6 (1.63–1.6)	50–1.6 (1.63–1.6)	30–1.59 (1.62–1.59)	50–1.6 (1.63–1.6)	20–1.62 (1.65–1.62)	30–1.58 (1.61–1.58)	40–1.65 (1.68–1.65)	50–1.5 (1.53–1.5)	30–1.08 (1.1–1.08)
Unique reflections	46, 784 (1272)	36, 163 (1324)	35, 051 (1265)	36, 929 (1794)	35, 630 (1639)	27, 889 (1283)	38, 031 (1128)	35, 822 (1773)	43, 631 (1920)	123, 403 (5449)
<i>R</i> (I) _{sym} (%)	5.7 (49.7)	5.2 (34.0)	4.9 (27.0)	4.7 (51.1)	7.1 (35.7)	7.2 (40.8)	9.4 (40.2)	5.3 (40.2)	8.3 (22.5)	5.2 (8.7)
Completeness (%)	91.7 (50.2)	89.0 (64.6)	86.3 (62.1)	89.0 (88.3)	87.5 (80.4)	71.1 (65.7)	90.1 (53.8)	96.5 (95.1)	88.2 (78.7)	94.5 (83.3)
Redundancy	2.9 (1.8)	2.5 (2.1)	2.5 (2.1)	2.4 (2.4)	2.8 (2.1)	1.9 (1.7)	3.7 (3.2)	2.2 (2.1)	2.4 (2.3)	2.8 (1.9)
<i>I</i> / σ (<i>I</i>)	21.7 (2.0)	19.3 (2.8)	23.2 (3.4)	17.4 (1.8)	16.5 (2.4)	13.2 (2.0)	20.4 (3.6)	16.8 (2.3)	10.2 (3.9)	17.9 (8.9)
<i>Refinement</i>										
Resolution range used in refinement (Å)	25–1.48	50–1.6	50–1.6	25–1.59	50–1.6	20–1.62	30–1.58	10–1.65	20–1.5	10–1.08
Reflections used in refinement (work/free)	43, 783/2 286	33, 568/1 755	32, 672/1 696	33, 653/1 768	32, 719/1 711	25, 777/1 298	35, 603/1 879	32, 789/1 690	41, 439/2 163	116, 227/6 130
Final <i>R</i> values for all reflections (work/free) (%)	15.6/19.7	16.1/22.7	16.2/22.1	16.7/22.8	16.2/22.3	18.7/27.0	16.3/20.8	15.3/21.7	16.9/22.0	11.2/13.9
Final <i>R</i> values for reflections with <i>F</i> >4 σ (work/free) (%)	15.0/18.8	14.7/20.7	15.3/20.8	15.8/21.5	15.1/20.8	18.0/25.9	15.8/20.1	14.0/19.9	16.2/21.0	11.0/13.6
Protein residues	315	315	315	314	315	314	315	315	316	316
Coenzyme	1	1	1	1	1	1	1	1	1	1
Inhibitor	1	1	1	1	1	1	1	1	4	1
Water molecules	377	342	337	227	308	223	360	386	344	350
<i>rmsd values</i>										
Bonds (Å)	0.011	0.009	0.01	0.009	0.009	0.008	0.008	0.009	0.011	0.017
Angles (°)	2.6	2.2	2.5	2.2	2.1	2.3	2.2	2.3	2.3	2.4
<i>Ramachandran plot</i>										
Most favoured (%)	91.7	92.1	91.3	90.9	92.4	91.7	91.0	91.3	91.7	90.2
Additionally allowed (%)	7.9	7.9	8.3	9.1	7.6	8.3	9.0	8.7	8.3	9.8
Generously allowed (%)	0.4	–	0.4	–	–	–	–	–	–	–
<i>Mean B factors (Å²)</i>										
Protein	15.4	12.7	13.5	19.9	16.3	23.8	18.6	14.2	19.4	11.7
NADP ⁺	9.8	6.0	6.7	13.0	9.8	18.6	13.5	8.6	15.0	5.5
Inhibitor	10.9	8.3	8.3	18.0	13.9	21.8	14.2	10.4	26.1	8.2
Water molecules	25.1	21.3	21.5	27.1	26.0	30.1	27.5	25.2	29.1	21.7
Loop region Cys298–Ser302	16.1	13.3	15.6	42.2	26.8	26.2	19.3	15.0	–	–
<i>Distance rmsd in comparison to 1day_soaked</i>										
Whole protein (all atoms)	–	0.5	0.5	0.6	0.7	0.7	0.4	0.4	–	–
Loop region Cys298–Ser302 (all atoms)	–	0.1	0.1	1.0	0.7	1.0	0.6	0.1	–	–
Whole protein (C ^α)	–	0.2	0.1	0.3	0.3	0.3	0.1	0.1	–	–
Loop region Cys298–Ser302 (C ^α)	–	0.1	0.1	0.6	0.4	0.5	0.1	0.1	–	–

^a Numbers in parentheses characterize the highest resolution shell.

Table 7.1. Data collection and Refinement statistics.

7.5 References

1. Blundell, T.L. & Jhoti, H.; Abell, C. (2002). High-throughput crystallography for lead discovery in drug design. *Nat. Rev. Drug Discov.* **1**, 45-54.
2. Davis, A.M., Teague, S.J. & Kleywegt, G.J. (2003). Application and limitations of X-ray crystallographic data in structure-based ligand and drug design. *Angew. Chem. Int. Ed. Engl.* **42**, 2718-2736.
3. Shoichet, B.K. (2004). Virtual screening of chemical libraries. *Nature* **432**, 862-865.
4. Jones, T. & Kjeldgaard, M. (1997). Electron-density map interpretation. *Methods Enzymol.* **277**, 173-208.
5. Teague, S.J. (2003). Implications of protein flexibility for drug discovery. *Nat. Rev. Drug Discov.* **2**, 527-541.
6. Kitchen, D.B., Decornez, H., Furr, J.R. & Bajorath, J. (2004). Docking and scoring in virtual screening for drug discovery: methods and applications. *Nat. Rev. Drug Discov.* **3**, 935-949.
7. Schmidt, A. & Lamzin, V.S. (2002). Veni, vidi, vici - atomic resolution unravelling the mysteries of protein function. *Curr. Opin. Struct. Biol.* **6**, 698-703.
8. Brownlee, M. (2001). Biochemistry and molecular cell biology of diabetic complications. *Nature* **414**, 813-820.
9. Homans, S.W. (2005). Probing the binding entropy of ligand-protein interactions by NMR. *ChemBioChem* **6**, 1585-1591.
10. A similar binding geometry for the same complex obtained by cocrystallisation was described by Wilson et al.,^[11] however neither structure factors nor complete protein coordinates, but only the C α trace was deposited. Thus, this complex structure was redetermined in our laboratory.
11. Wilson, D.K., Tarle, I., Petrash, J.M. & Quioco, F.A. (1993). Refined 1.8 Å structure of human aldose reductase complexed with the potent inhibitor zopolrestat. *Proc. Natl. Acad. Sci. U S A* **90**, 9847-9851.
12. Howard, E.I., Sanishvili, R., Cachau, R.E., Mitschler, A., Chevrier, B., Barth, P., Lamour, V., Van Zandt, M., Sibley, E., Bon, C., Moras, D., Schneider, T.R., Joachimiak, A. & Podjarny, A. (2004). Ultrahigh resolution drug design I:

- details of interactions in human aldose reductase-inhibitor complex at 0.66 Å. *Proteins* **55**, 792-804.
13. As several ALR2-citrate complexes have already been described and deposited in the PDB, this citrate complex is not further described here.
 14. No significant electron density is observed for Leu 300 C γ , C δ , and C ϵ , indicating high flexibility for this side-chain.
 15. Despite these representations do not base on normalized B-factors, the Wilson B-factor for the **co_10** and **6d_a** data sets are 17.7 and 16.9 Å², respectively. This suggests that B-factors derived from model refinement are to some extent comparable.
 16. Mylari, B.L., Beyer, T.A., Scott, P.J., Aldinger, C.E., Dee, M.F., Siegel, T.W. & Zembrowski, W.J. (1992). Potent, orally active aldose reductase inhibitors related to zopolrestat: surrogates for benzothiazole side chain. *J. Med. Chem.* **35**, 457-465.
 17. Petrova, T., Steuber, H., Hazemann, I., Cousido-Siah, A., Mitschler, A., Chung, R., Oka, M., Klebe, G., El-Kabbani, O., Joachimiak, A. & Podjarny, A. (2005). Factorizing selectivity determinants of inhibitor binding toward aldose and aldehyde reductases: Structural and thermodynamic properties of the aldose reductase mutant Leu300Pro-fidarestat complex. *J. Med. Chem.* **48**, 5659-5665.
 18. Böhm, H.J. (1994). The development of a simple empirical scoring function to estimate the binding constant for a protein-ligand complex of known three-dimensional structure. *J. Comput. Aided Mol. Des.* **8**, 243-256.
 19. Urzhumtsev, A., Tete-Favier, F., Mitschler, A., Barbanton, J., Barth, P., Urzhumtseva, L., Biellmann, J.F., Podjarny, A.D. & Moras, D. (1997). A 'specificity' pocket inferred from the crystal structures of the complexes of aldose reductase with the pharmaceutically important inhibitors tolrestat and sorbinil. *Structure* **5**, 601-612.
 20. Harrison, D.H., Bohren, K.M., Petsko, G.A., Ringe, D. & Gabbay, K.H. (1997). The alrestatin double-decker: binding of two inhibitor molecules to human aldose reductase reveals a new specificity determinant. *Biochemistry* **51**, 16134-16140.
 21. Lamour, V., Barth, P., Rogniaux, H., Poterszman, A., Howard, E., Mitschler, A., Van Dorsselaer, A., Podjarny, A. & Moras, D. (1999). Production of crystals

- of human aldose reductase with very high resolution diffraction. *Acta Cryst. D* **55**, 721-723.
22. El-Kabbani, O., Darmanin, C., Schneider, T.R., Hazemann, I., Ruiz, F., Oka, M., Joachimiak, A., Schulze-Briese, C., Tomizaki, T., Mitschler, A. & Podjarny, A.(2004). Ultrahigh resolution drug design. II. Atomic resolution structures of human aldose reductase holoenzyme complexed with Fidarestat and Minalrestat: implications for the binding of cyclic imide inhibitors. *Proteins* **55**, 805-813.
 23. Otwinowski, Z. & Minor, W. (1997). Processing of X-ray diffraction data ^ collected in oscillation mode. *Methods Enzymol.* **276**, 307-326.
 24. Calderone, V., Chevrier, B., Van Zandt, M., Lamour, V., Howard, E., Poterszman, A., Barth, P., Mitschler, A., Lu, J., Dvornik, D.M., Klebe, G., Kraemer, O., Moorman, A.R., Moras, D. & Podjarny, A. (2000). The structure of human aldose reductase bound to the inhibitor IDD384. *Acta Cryst. D* **56**, 536-540.
 25. Brunger, A.T., Adams, P.D., Clore, G.M., DeLano, W.L., Gros, P., Grosse-Kunstleve, R.W., Jiang, J.S., Kuszewski, J., Nilges, M., Pannu, N.S., Read, R.J., Rice, L.M., Simonson, T. & Warren, G.L. (1998). Crystallography & NMR system: A new software suite for macromolecular structure determination. *Acta Cryst. D* **54**, 905-921.
 26. Sheldrick, G.M. & Schneider, T. (1997). SHELXL: high-resolution refinement. *Methods Enzymol.* **277**, 319-343.
 27. Jones, T.A., Zou, J.Y., Cowan, S.W. & Kjeldgaard, M. (1991). Improved methods for building protein models in electron density maps and the location of errors in these models. *Acta Cryst. A* **47**, 110-119.
 28. Laskowski, R., MacArthur, M., Moss, D. & Thornton, J.(1993). PROCHECK: a program to check the stereochemical quality of protein structures. *J. Appl. Crystallogr.* **26**, 283-291.
 29. DeLano, W.L. 2002. <http://www.pymol.org>
 30. SYBYL Molecular Modeling Software, 7.0 ed.; Tripos Inc., St. Louis, MO, 2004.
 31. Case, D.A., Darden, T.A., Cheatham, III, T.E., Simmerling, C.L., Wang, J., Duke, R.E., Luo, R., Merz, K.M., Wang, B., Pearlman, D.A., Crowley, M., Brozell, S., Tsui, V., Gohlke, H., Mongan, J., Hornak, V., Cui, G., Beroza, P.,

- Schafmeister, C., Caldwell, J.W., Ross, W.S. & Kollman, P.A. **2004**, AMBER 8, University of California, San Francisco.
32. Cornell, W.D.; Cieplak, P.; Bayly, C.I.; Gould, I.R.; Merz Jr., K.M.; Ferguson, D.M.; Spellmeyer, D.C.; Fox, T.; Caldwell, J.W.; Kollman, P.A. A second generation force field for the simulation of proteins, nucleic acids, and organic molecules. *J. Am. Chem. Soc.* **1995**, *117*, 5179.
33. Wang, J., Cieplak, P. & Kollman, P.A. (2000). How well does a restrained electrostatic potential (RESP) perform in calculating conformational energies of organic and biological molecules. *J. Comput. Chem.* **21**, 1049-1074.
34. Wang, J., Wolf, R.M., Caldwell, J.W., Kollman, P.A. & Case, D.A. (2004). Development and testing of a general amber force field. *J. Comput. Chem.* **25**, 1157-1174.
35. Sotriffer, C.A., Kraemer, O. & Klebe, G. (2004). Probing flexibility and "induced-fit" phenomena in aldose reductase by comparative crystal structure analysis and molecular dynamics simulations. *Proteins* **56**, 52-66.
36. Frisch, M.J., Trucks, G.W., Schlegel, H.B., Scuseria, G.E., Robb, M.A., Cheeseman, J.R., Zakrzewski, V.G., Montgomery, J.A., Stratmann, R.E., Burant, J.C., Dapprich, S., Millam, J.M., Daniels, A.D., Kudin, K.N., Strain, M.C., Farkas, O., Tomasi, J., Barone, V., Cossi, M., Cammi, R., Mennucci, B., Pomelli, C., Adamo, C., Clifford, S., Ochterski, J., Petersson, G.A., Ayala, P.Y., Cui, Q., Morokuma, K., Malick, D.K., Rabuck, A.D., Raghavachari, K., Foresman, J.B., Cioslowski, J., Ortiz, J.V., Stefanov, B.B., Liu, G., Liashenko, A., Piskorz, P., Komaromi, I., Gomperts, R., Martin, R.L., Fox, D.J., Keith, T., Al-Laham, M.A., Peng, C.Y., Nanayakkara, A., Gonzalez, C., Challacombe, M., Gill, P.M.W., Johnson, B.G., Chen, W., Wong, M.W., Andres, J.L., Head-Gordon, M., Replogle, E.S. & Pople, J.A. (1998). Gaussian98; Gaussian, Inc., Pittsburgh PA.
37. Bayly, C.I., Cieplak, P., Cornell, W.P. & Kollman, P.A. (1993). A well-behaved electrostatic potential based method using charge restraints for deriving atomic charges: the RESP model. *J. Phys. Chem.* **97**, 10269-10280.
38. Cornell, W.P., Cieplak, P., Bayly, C.I. & Kollman, P.A. (1993). Application of RESP charges to calculate conformational energies, hydrogen bond energies, and free energies of solvation. *J. Am. Chem. Soc.* **115**, 9620-9631.

-
39. Jorgensen, W.L., Chandrasekhar, J., Madura, J.P., Impey, R.W. & Klein, M.L. (1983). Comparison of simple potential functions for simulating liquid water. *J. Chem. Phys.* **79**, 926-935.
 40. Berendsen, H.J.C., Postma, J.P.M., van Gunsteren, W.F., Di Nola, A. & Haak, J.R. (1984). Molecular dynamics with coupling to an external bath. *J. Chem. Phys.* **81**, 3684-3690.
 41. Ryckaert, J.P., Ciccotti, G. & Berendsen, H.J.C. (1977). Numerical integration of the cartesian equations of motion of a system with constraints: molecular dynamics of *n*-alkanes *J. Comput. Phys.* **23**, 327-341.
 42. Darden, T., York, D. & Pedersen, L. (1993). Particle mesh Ewald: An $N \cdot \log(N)$ method for Ewald sums in large systems. *J. Chem. Phys.* **98**, 10089-10092.

8. Summary / Zusammenfassung

Even though profound understanding of protein-ligand recognition provides the basis for successful structure-guided ligand design and optimization, currently only limited knowledge is available about the principles driving ligands to bind to their targets. In particular protein flexibility, the role of water for ligand affinity and binding geometry, as well as changes in protonation of protein residues or ligand functional groups is difficult to consider in the design process in absence of appropriate experimental data, and even more difficult to predict. The TIM-barrel folded enzyme Aldose reductase (ALR2) is a valuable model system to study structural and thermodynamic features of inhibitor binding and, furthermore, represents an excellent drug target. To prevent diabetic complications derived from enhanced glucose flux via the polyol pathway the development of aldose reductase inhibitors (ARIs) has been established as a promising therapeutic concept. Its attraction as a test system consists furthermore in the high mobility and adaptivity properties of its active site residues, giving rise to various distinct binding pocket conformers and pronounced induced-fit adaptations upon ligand binding.

In order to identify novel lead compounds, a virtual screening was performed successfully prior to this thesis suggesting carboxylate-type inhibitors of sub-micromolar to micromolar affinity. In chapter 2, we combine a structural characterization of the experimental binding modes observed for these hits with isothermal titration calorimetry (ITC) measurements providing insights into the driving forces of inhibitor binding. Characteristic features of this novel inhibitor type include a carboxylate head group connected via an alkyl spacer to a heteroaromatic moiety, which is linked to a further nitro-substituted aromatic portion. The crystal structures of two enzyme-inhibitor complexes have been determined at resolutions of 1.43 and 1.55 Å. Surprisingly, the carboxylic group of the most potent lead occupies the catalytic pocket differently compared to the interaction geometry observed in almost all other crystal structures with structurally related ligands and obtained under similar conditions, as an interstitial water molecule is picked up upon ligand binding. The nitro-aromatic moiety of both leads occupies the specificity pocket of the enzyme, however, adopting a different geometry compared to the original docking prediction. The nitro group binds to the bottom of the specificity pocket and provokes remarkable induced-fit adaptations. A peptide group located at the active site orients in such a way

that H-bond formation to one nitro group oxygen is enabled, whereas a neighbouring tyrosine side chain performs a slight rotation off from the binding cavity to accommodate the nitro group. Identically constituted ligands, lacking this nitro group, exhibit an affinity drop of one order of magnitude. In addition, thermodynamic data suggest a strongly favourable contribution to binding enthalpy in case the inhibitor is equipped with a nitro group at the corresponding position. To further investigate this phenomenon, we determined crystal structures and thermodynamic data of two similarly constituted IDD-type inhibitors addressing the specificity pocket with either a nitro- or halogen-substituted aromatic moiety. As these data suggest, the nitro group provokes the enthalpic contribution, in addition to the H-bond mentioned above, by accepting two “non-classical” H-bonds donated by the aromatic tyrosine side chain.

In chapter 3, we report on the crystal structures of a novel sulfonyl-pyridazinone inhibitor in complex with aldose reductase, determined at 1.43 and 0.95 Å resolution. Supposedly due to low solubility in the crystallisation buffer, in both structures the inhibitor shows reduced occupancy of 74 and 46 % population, respectively. The inhibitor occupies with its pyridazinone head group the catalytic site whereas the chloro-benzofurane moiety penetrates into the opened specificity pocket. The high resolution structure provides some evidence that the pyridazinone group binds in a negatively charged deprotonated state whereas the neighboring His 110 residue most likely adopts a neutral uncharged state. Since the latter structure is only to 46 % populated by the ligand a second conformation of the C-terminal ligand binding region can be detected. This conformation corresponds to the closed state of the specificity pocket when no or only small ligands are bound to aldose reductase. Both geometries, superimposed as average in the crystal structure, correspond to snapshots of the ligand bound and unbound state.

In chapter 4, we probed the ALR2 binding site with a novel structural class of inhibitors in order to identify putative pocket adaptations. The determined binding geometries help to understand structure-activity relationships. We elucidated two ALR2 crystal structures at 1.55 and 1.65 Å resolution, each complexed with a member of the recently described naphtho[1,2-d]isothiazole acetic acid series. In contrast to the original design hypothesis based on the binding mode of tolrestat, both inhibitors leave the specificity pocket in closed state. Unexpectedly, the more potent ligand extends the catalytic pocket by opening of a novel subpocket. Access to this novel subpocket is mainly attributed to the rotation of a neighbouring indole moiety by about 35°. The newly

formed subpocket provides accommodation of the naphthyl portion of the ligand. The second studied inhibitor differs from the first only by an extended glycolic ester functionality added to one of its carboxylic groups. However, despite this slight structural modification, its binding mode differs dramatically from that of the first inhibitor, but provokes less pronounced induced-fit adaptations of the binding cavity. For the more potent inhibitor a novel binding site conformation has been identified in a region where previous complex structures suggested only low adaptability of the binding pocket. Furthermore, the two ligand complexes represent an impressive example, how the slight change of a chemically extended side chain at a given ligand scaffold can result in a dramatically altered binding mode. In addition, our study emphasizes the importance of crystal structure analysis for the translation of affinity data into structure-activity relationships.

In chapter 5, we study the binding process of inhibitors to ALR2 with respect to changes of the protonation inventory upon complex formation. Knowledge of such processes is a prerequisite to factorize the binding free energy into enthalpic and entropic contributions on an absolute scale. Our ITC measurements suggest a proton uptake upon complex formation with carboxylate-type inhibitors. As the protonation event will strongly contribute to the enthalpic signal recorded during ITC experiments, knowledge about the proton-accepting and -releasing functional groups of the system is of utmost importance. However, this is intricate to retrieve, if, as in the present case, both, binding site and ligand possess several titratable groups. Here, we present pKa calculations complemented by mutagenesis and thermodynamic measurements suggesting a tyrosine residue located in the catalytic site (Tyr 48) as likely candidate to act as proton acceptor upon inhibitor binding, as it occurs deprotonated to remarkable extent if only the cofactor NADP⁺ is bound. We furthermore provide evidence that protonation state and binding thermodynamics strongly depend on the oxidation state of the cofactor's nicotinamide moiety. Binding thermodynamics of IDD 388, IDD 393, tolrestat, sorbinil, and fidarestat are discussed in the context of substituent effects.

In chapter 6, the ALR2 binding site is probed for selectivity determining features, which make binding of certain ligands to ALR2 more attractive than to the concurrent isoform aldehyde reductase (ALR1). The resulting mutational constructs of ALR2 (eight point mutations and one double mutant) are probed for their influence towards ligand selectivity by X-ray structure analysis of the corresponding complexes and ITC. The binding properties of these mutants were evaluated using a ligand set of

zopolrestat, a related uracil derivative, IDD388, IDD393, sorbinil, fidarestat and tolrestat.

Our study reveals induced-fit adaptations within the mutated binding site as an essential prerequisite for ligand accommodation related to the selectivity discrimination of the ligands. However, our study also highlights the limits of the present understanding of protein-ligand interactions. Interestingly, binding site mutations not involved in any direct interaction to the ligands in various cases show significant effects towards their binding thermodynamics. Furthermore, our results suggest the binding site residues deviating between ALR1 and ALR2 to influence ligand affinity in a complex interplay presumably involving changes of dynamic properties and deviations of the solvation/desolvation balance upon ligand binding.

In structure-based drug design, accurate crystal structure-determination of protein-ligand complexes is of utmost importance in order to elucidate the binding characteristics of a putative lead to a given target. It is the starting point for further design hypotheses to predict novel leads with improved properties. Often, crystal structure determination is regarded as ultimate proof for ligand binding providing detailed insight into the specific binding mode of the ligand to the protein. This widely accepted practise relies on the assumption that the crystal structure of a given protein-ligand complex is unique and independent of the protocol applied to produce the crystals. In chapter 7, we present two examples indicating that this assumption is not generally given, even though the composition of the mother liquid for crystallization was kept unchanged: Multiple crystal structure determinations of aldose reductase complexes obtained under varying crystallization protocols concerning soaking and crystallization exposure times were performed resulting in total 17 complete data sets and 10 refined crystal structures, eight in complex with zopolrestat and two complexed with tolrestat. In the first example, a flip of a peptide bond is observed, obviously depending on the crystallization protocol with respect to soaking and cocrystallization conditions. This peptide flip is accompanied by a rupture of an H-bond formed to the bound ligand zopolrestat. The indicated enhanced local mobility of the complex is in agreement with the results of molecular dynamics simulations. As a second example, the aldose reductase-tolrestat complex is studied. Unexpectedly, two structures could be obtained: one with one, and a second with four inhibitor molecules bound to the protein. They are located in and near the binding pocket facilitated by crystal packing

effects. Accommodation of the four ligand molecules is accompanied by pronounced shifts concerning two helices interacting with the additional ligands.

In summary, valuable experimental structural and thermodynamic insights into inhibitor binding to ALR2 were collected. The crystal structures determined in this thesis provide the platform for further ligand optimization strategies, insights into structure-activity relationships, or, in case of the novel pocket conformer, a further template for virtual screening. A consistent picture for ligand-induced changes of protonation states could be suggested and experimentally proved. The general assumption that the ligand binding mode is independent on the complexation protocol could be shown to be not valid.

Zusammenfassung

Ein profundes Verständnis über Protein-Ligand-Wechselwirkungen stellt zwar die Voraussetzung für eine erfolgreiche Leitstruktur-Findung und Optimierung dar, jedoch sind die Vorstellungen über die grundlegenden Prinzipien, die die Bindung eines Liganden an ein biologisches Makromolekül attraktiv erscheinen lassen, noch sehr lückenhaft. Insbesondere die Flexibilität von Proteinen, die Rolle des Wassers für die Affinität von Liganden sowie die eingenommene Bindungsgeometrie und Änderungen von Protonierungszuständen der funktionellen Gruppen von Protein und Ligand sind in Abwesenheit geeigneter experimenteller Daten noch schwer in den Designprozess mit einzubeziehen und erst recht schwierig vorherzusagen. Das Enzym Aldose Reduktase (ALR2), das eine *TIM-barrel* Faltung besitzt, stellt ein wertvolles Testsystem dar, um strukturelle und thermodynamische Eigenschaften der Inhibitorbindung zu charakterisieren und ist darüber hinaus ein geeignetes Zielenzym für eine Arzneistoff-Intervention. Um diabetischen Spät komplikationen entgegen zu wirken, die durch eine verstärkte Metabolisierung von Glucose über den Polyol-Weg hervorgerufen werden, hat sich die Entwicklung von Inhibitoren der ALR2 als vielversprechendes Konzept erwiesen. Zudem ist das Enzym ein hervorragendes Testsystem für Strategien zur Leitstrukturfindung, da es aufgrund der hohen Mobilität der Aminosäure-Reste in der Bindetasche in der Lage ist, verschiedene Konformere einzunehmen und sich ausgesprochen vielseitig an Liganden anzupassen.

Um neue Leitstrukturen zu identifizieren, wurde vor Beginn dieser Arbeit ein virtuelles Screening durchgeführt, aus dem submikromolare bis mikromolare Inhibitoren vom Carbonsäure-Typ hervorgingen. Zu Beginn dieser Arbeit wird die Strukturbestimmung

der Bindungsmoden dieser Liganden ergänzt durch Isothermale Titrationskalorimetrie (ITC), um Einblicke in die Triebkräfte des Bindungsprozesses zu erhalten. Der durch das Screening erhaltene neue Inhibitor-Typ ist gekennzeichnet durch eine Carbonsäure-Ankergruppe, die über eine Alkylkette mit einem Heteroaromaten verbunden ist. Letzterer ist verknüpft mit einem nitro-aromatischen System. Die Kristallstrukturen der beiden affinsten dieser Inhibitoren konnten mit Auflösungen von 1,43 und 1,55 Å bestimmt werden. Überraschenderweise interagiert die Carbonsäure-Gruppe der affinsten Leitstruktur anders mit der katalytischen Tasche, als von nahezu allen anderen Strukturen mit verwandten Liganden bekannt, die unter vergleichbaren Bedingungen erhalten worden waren: ein verbrückendes Wasser-Molekül wird bei der Ligandbindung inkorporiert. Der nitro-aromatische Teil beider Leitstrukturen besetzt die Spezifitätstasche des Enzyms, allerdings in abweichender Weise, als durch die Einpassung am Rechner vorhergesagt. Die Nitro-Gruppe bindet in den unteren Teil der Spezifitätstasche und ruft dort bemerkenswerte Änderungen hervor. Eine nahe der Bindetasche gelegene Peptid-Gruppe ordnet sich so an, dass sie eine H-Brücke zu einem der Nitro-Sauerstoff-Atome bilden kann, während ein nahegelegenes Tyrosin sich leicht von der Tasche wegbewegt, um das Einpassen der Nitro-Gruppe zu ermöglichen. Gleichartige Liganden, denen diese Nitro-Gruppe fehlt, zeigen einen Affinitätsverlust von einer Größenordnung. Darüber hinaus deuten thermodynamische Daten auf einen deutlich günstigen Beitrag zur Bindungsenthalpie hin, falls der Ligand an geeigneter Stelle eine Nitro-Gruppe trägt. Um diesem Phänomen weiter nachzugehen, wurden Kristallstrukturen und thermodynamische Bindungsdaten von zwei weiteren Liganden des IDD-Typs bestimmt, die die Spezifitätstasche mit entweder einem Halogenatom oder einer Nitro-Gruppe adressieren. Diese Daten unterstützen die Interpretation, dass die Nitro-Gruppe für den günstigen enthalpischen Beitrag verantwortlich ist, zum einen durch die erwähnte H-Brücke, zum anderen durch die Ausbildung von zwei nichtklassischen H-Brücken zur Tyrosin-Seitenkette.

In Kapitel 3 werden die Kristallstrukturen eines neuartigen Sulfonyl-Pyridazinons im Komplex mit ALR2, bestimmt bei 1,43 und 0,95 Å, beschrieben. Vermutlich ist die geringe Löslichkeit der Verbindung im Kristallisationspuffer dafür verantwortlich, dass die Besetzung des Liganden in den beiden Strukturen nur 74 bzw. 46 % aufweist. Der Inhibitor besetzt mit seiner Pyridazinon-Kopfgruppe die katalytische Tasche, während der chlor-substituierte Benzofuran-Teil die Spezifitätstasche belegt. Die hochaufgelöste Struktur legt nahe, dass die Pyridazinon-Gruppe in deprotoniertem, negativ geladenem

Zustand bindet, während das benachbarte Histidin einen ungeladenen Zustand einnimmt. Da der Ligand in letzterer Struktur nur zu 46 % populiert ist, konnte in der Elektronendichte eine zweite Konformation der C-terminalen ligand-bindenden Region ausgemacht werden. Diese Konformation entspricht dem Zustand mit geschlossener Spezifitätstasche, den das Enzym im Komplex mit kleinen Liganden oder ohne Ligand einnimmt. Beide Geometrien, deren gemittelttes Bild in der Kristallstruktur gefunden wird, entsprechen Momentaufnahmen des komplexierten und nicht-komplexierten Zustandes.

In Kapitel 4 wird die Bindetasche der ALR2 mit einer neuartigen Strukturklasse von Inhibitoren sondiert, um mögliche neue Adaptationsvorgänge des Enzyms sowie den Bindungsmodus der Liganden zu bestimmen und deren Struktur-Wirkungs-Beziehungen zu verstehen. Zwei Kristallstrukturen, aufgelöst bis 1,55 und 1,65 Å, wurden bestimmt. Beide stellen einen Komplex mit einem Liganden der kürzlich veröffentlichten Naphtho[1,2-*d*]isothiazol-essigsäuren dar. Im Gegensatz zur ursprünglichen Designhypothese, die auf dem Bindungsmodus von Tolrestat basierte, zeigt sich die Spezifitätstasche in den Strukturen in geschlossenem Zustand. Überraschenderweise erweitert der potentere der beiden Liganden die katalytische Tasche, indem eine neue Subtasche geöffnet wird. Dies wird in erster Linie dadurch ermöglicht, dass sich eine benachbarte Indol-Seitenkette eines Tryptophans um ca. 35° dreht. Die so entstandene neue Subtasche wird vom Naphthyl-Rest des Liganden belegt. Der zweite Ligand unterscheidet sich vom ersten nur durch einen angefügten Glycolsäure-Teil, mit dem eine der Carboxylgruppen des Liganden verestert ist. Trotz dieser nur geringfügigen Modifikation unterscheidet sich der Bindungsmodus in dramatischer Weise von dem des zuerst untersuchten Liganden. Jedoch werden weniger ausgeprägte Anpassungsvorgänge in der Bindetasche beobachtet. Es konnte also im Falle des affineren Liganden eine neue Taschenkonformation in einer Proteinregion identifiziert werden, in der die zuvor bekannten Strukturen nur geringe Anpassungsfähigkeit erwarten liessen. Darüber hinaus stellen die beiden Komplexstrukturen ein beeindruckendes Beispiel dar, wie die geringfügige Veränderung an einem Grundgerüst des Liganden zu einem deutlich veränderten Bindungsmodus führen kann. Daher unterstreicht diese Bindungsstudie die Bedeutung der Kristallstrukturbestimmung für den Prozess, aus Affinitätsdaten Rückschlüsse auf Struktur-Wirkungsbeziehungen zu ziehen.

In Kapitel 5 wird der Bindungsprozess von Inhibitoren an ALR2 im Hinblick auf Änderungen von Protonierungszuständen untersucht. Das Wissen über solche Prozesse stellt die Basis dar, um die Freie Bindungsenthalpie erfolgreich auf einer absoluten Skala in enthalpische und entropische Beiträge zu zerlegen. Die durchgeführten ITC-Messungen legen eine Protonenaufnahme bei der Bindung von Liganden des Carbonsäure-Typs nahe. Da solche Prozesse das bei einer ITC-Messung registrierte enthalpische Signal stark überlagern, ist genaue Kenntnis über protonen-aufnehmende und freisetzende funktionelle Gruppen des Systems von hoher Bedeutung. Dennoch ist diese schwierig zu erhalten, wenn, wie im vorliegenden Fall, Bindetasche und Ligand zusammen mehrere titrierbare Gruppen besitzen. Zu diesem Ziel werden in diesem Kapitel pKa-rechnungen zusammen mit ortsspezifischer Mutagenese und thermodynamischen Messungen eingesetzt. Diese lassen ein in der katalytischen Tasche befindliches Tyrosin (Tyr 48) für die Protonenaufnahme bei der Ligandbindung als wahrscheinlich erscheinen, da diese Seitenkette im NADP^+ -gebundenen Zustand zu bemerkenswertem Ausmaß deprotoniert vorliegt. Weiterhin wird gezeigt, dass Protonierungszustand und Bindungs-Thermodynamik deutlich vom Oxidationszustand des Kofaktors abhängig sind. In diesem Zusammenhang wird die Bindung von IDD 388, IDD 393, Tolrestat, Sorbinil und Fidarestat diskutiert.

In Kapitel 6 werden selektivitätsbestimmende Eigenschaften identifiziert, die die Bindung von Liganden an ALR2 energetisch günstiger erscheinen lassen als an die konkurrierende Isoform Aldehyd Reduktase (ALR1). Die zu diesem Zweck erstellten mutierten ALR2-Konstrukte (8 Punktmutationen und eine Doppelmutante) wurden mit Hilfe von Kristallstrukturbestimmung und ITC auf ihre Einflussnahme bezüglich der Ligandenselektivität untersucht. Dazu diente ein Ligandensatz, der aus Zopolrestat, einem verwandten Uracil-Derivat, IDD 388, IDD 393, Sorbinil, Fidarestat und Tolrestat zusammengestellt wurde. Es konnte gezeigt werden, dass das Auftreten von Anpassungsvorgängen in der mutierten Bindetasche essentiell für die Einpassung der Liganden ist. Dieses lässt Rückschlüsse auf das Selektivitätsverhalten der Liganden zu. Dennoch zeigt diese Studie auch, dass unserem Verständnis über Protein-Ligand-Wechselwirkungen noch deutliche Grenzen gesetzt sind. Interessanterweise haben Mutationen, die nicht in direktem Kontakt zum Liganden stehen, trotzdem einen deutlichen Einfluss auf seine Bindungsthermodynamik. Darüber hinaus zeigen die Ergebnisse, dass diejenigen Aminosäuren, in denen sich die Bindetaschen von ALR1 und ALR2 unterscheiden, die Bindung von Liganden in einem komplexen

Zusammenspiel beeinflussen, wahrscheinlich unter Beteiligung von Änderungen dynamischer Eigenschaften und der Solvatisierungs/Desolvatisierungs-Beiträge.

Für strukturbasiertes Wirkstoff-Design ist akkurate Kristallstrukturbestimmung von Protein-Ligand-Komplexen von großer Bedeutung, um Einblicke in den genauen Bindungsmodus einer Leitstruktur an ein Zielprotein zu erhalten. Diese bilden den Startpunkt für den Entwurf neuer Liganden mit potentiell verbesserten Eigenschaften. In vielen Fällen ist die Kristallstrukturbestimmung als schlussendlicher Beleg für die spezifische Wechselwirkung des Liganden mit dem Zielmolekül angesehen, da sie das genaue Wechselwirkungsmuster beider Bindungspartner repräsentiert. Diese weit verbreitete Vorgehensweise beruht auf der Annahme, dass eine Kristallstruktur eines gegebenen Protein-Ligand-Komplexes einzigartig und unabhängig von dem Protokoll ist, die zur Erzeugung der komplexierten Kristalle diente. In Kapitel 7 werden zwei Beispiele diskutiert, die zeigen, dass diese Annahmen nicht allgemein gültig sind, obwohl die Zusammensetzung der Kristallisationsbedingung unverändert blieb. Mehrfache Kristallstrukturbestimmung von ALR2-Komplexen, die unter verschiedenen Komplexierungsprotokollen bezüglich Soaking und Kokristallisation bei variierender Expositionsdauer durchgeführt wurden, erbrachte insgesamt siebzehn Datensätze und zehn schlussendlich verfeinerte Kristallstrukturen, davon acht im Komplex mit Zopolrestat und zwei im Komplex mit Tolrestat. Im ersten Fall wird der Flip einer Peptidbindung beobachtet, der offenbar von den gewählten Komplexierungsbedingungen abhängig ist. Bei diesem Peptid-Flip bricht eine H-Brücke zum Liganden Zopolrestat. Die so gezeigte lokal erhöhte Mobilität stimmt gut mit Ergebnissen aus Molekulardynamik-Simulationen überein. Im zweiten Fall wird der ALR2-Tolrestat-Komplex untersucht. Überraschenderweise wurden zwei verschiedene Strukturen erhalten: eine mit einem gebundenen Liganden, und eine weitere mit vier Liganden. Letztere sind unter Veränderung von Packungseffekten in und neben der Bindetasche untergebracht. Diese Einpassung der vier Ligand-Moleküle wird begleitet von bemerkenswerten Verschiebungen bezüglich zwei Helices, die mit den zusätzlichen Liganden wechselwirken.

Zusammenfassend konnten im Rahmen dieser Arbeit wertvolle Erkenntnisse über die Ligandenbindung an ALR2 gesammelt werden. Die in dieser Arbeit bestimmten Kristallstrukturen bilden die Grundlage für das Verständnis von Struktur-Wirkungs-Beziehungen sowie weitere Optimierungsschritte. Im Fall der neuartigen Taschenkonformation wird ein bisher unbekanntes Konformer für ein erweitertes

virtuelles Screening bereitgestellt. Für die beobachteten Protonenübergänge bei der Ligandbindung wird ein konsistentes Bild vorgeschlagen und experimentell belegt. Die allgemeine Annahme, dass der für einen Liganden kristallographisch erhaltene Bindungsmodus unabhängig vom Komplexierungsprotokoll ist, konnte in dieser Arbeit kritisch hinterfragt und widerlegt werden.

Danksagungen

Mein Herzlicher Dank gilt:

- Prof. Dr. Gerhard Klebe für die permanente wissenschaftliche und finanzielle Förderung dieser Arbeit, für die gewährte Freiheit, Forschungsvorhaben eigenständig bearbeiten und publizieren zu dürfen, sowie für viele lehrreiche Diskussionen und (meist farbenfrohe) Manuskript-Korrekturen.
- Dr. Andreas Heine für seine fundierte Einführung in die Welt der Kristallographie, seine ständige Diskussionsbereitschaft sowie viele erheiternde wissenschaftliche (und nicht-wissenschaftliche) Gespräche in den vergangenen Jahren.
- Prof. Dr. Christoph Sotriffer für die Betreuung von MD-Simulationen und zahlreiche Diskussionen um die Aldose Reduktase
- Dr. Alberto Podjarny und Isabel Hazeman danke ich für die Überlassung des Überexpressionsvektors der Aldose Reduktase, des initialen Aufreinigungsprotokolls, sowie diverse Liganden.
- Herrn Michael Eisenmann und Prof. Dr. Martin Schlitzer für zahlreiche Diskussionen und die gute Zusammenarbeit beim Entwurf und die Synthese neuer Inhibitoren.
- Dr. Concettina LaMotta und Dr. Stefania Sartini danke ich herzlich für die gute Zusammenarbeit auf dem Gebiet der Naphthoisothiazole und deren Synthese. Ohne diese wäre ein neues ALR2-Taschenkonformer sicher noch lange verborgen geblieben.
- Dr. Markus Böhm und Pfizer, Inc., Connecticut für die Bereitstellung des Pyridazinon-Liganden sowie Proben von Sorbinil und Zopolrestat.
- Dr. Matthias Zentgraf danke ich für zahlreiche Diskussionen auf dem Gebiet der Aldose Reduktase und die erfolgreiche Zusammenarbeit sowie seine Einführung in ITC-Messungen und die Auswertung thermodynamischer Daten.
- Dr. Paul Czodrowski gebürt mein Dank für viele unterhaltsame Autofahrten von Marburg nach München und zurück, neben anderen Dingen ging es dabei manchmal auch über Protonierungszustände der Aldose Reduktase.
- Dr. Christof Gerlach danke ich für seine Einführung in zahlreiche Modellierung-Tools sowie seine tatkräftige Unterstützung bei der Durchführung eines virtuellen Screenings einer FeatureTree-vorselektierten Molekül-Library.

-
- Herrn Christian Sohn bin ich sehr dankbar für seine Bemühungen, dass der Röntgengenerator zu nahezu jeder Tages- und Nachtzeit einsetzbar war.
 - Frau Angela Scholz danke ich herzlich für ihre entgegenkommende Aufopferung und ihr offenes Ohr, sich jeglichen (auch bürokratischen und administrativen) Problemen aller AG-Mitglieder anzunehmen, sowie für die permanente Versorgung mit Süßigkeiten bei jedem Besuch im Sekretariat und ihre herzerfrischende, verständnisvolle und erheiternde Art.
 - Dem Administratorenteam sei herzlich gedankt für einsatzfähige Rechner, Support in vielen Linux-Fragen („Was muss ich denn da sourcen??“) und Verständnis für die vielen OSC-Files im Home-Directory.
 - Herrn Alexander Hillebrecht danke ich für zahlreiche Ratschläge im Bereich des Modellings, viele wissenschaftliche (und „nicht-wissenschaftliche“) Diskussionen, sowie die Erweiterung meines Österreichisch-Vokabulars u.a. beim abendlichen Pizza-Essen.
 - Meinen Literaturarbeitern und Vertiefern Judith Haselhoff, Diana Fladerer, Maria Thomas und Heike Rohrbacher danke ich herzlich für die geleistete Arbeit bei der Aufreinigung von AR-Mutanten.
 - Allen Mitgliedern der AG Klebe sei gedankt für die allseits gute und kollegiale Arbeitsatmosphäre.
 - Der Deutschen Forschungsgemeinschaft (DFG) sowie dem Graduiertenkolleg „Proteinfunktion auf atomarer Ebene“ danke ich für die finanzielle Förderung und einige angenehme Hirschegg-Aufenthalte.
 - Meiner Freundin Mareike danke ich herzlich für ihre Unterstützung während meiner Doktorarbeit, ihre Geduld und viele erholsame Wochenenden in München sowie für das Korrekturlesen dieser Arbeit.

ERKLÄRUNG

Ich versichere, daß ich meine Dissertation

**Structural and Thermodynamic Characterization of Inhibitor Binding to
Aldose Reductase: Insights into Binding Modes, Driving Forces,
and Selectivity Determinants**

selbständig ohne unerlaubte Hilfe angefertigt und mich dabei keiner anderen als den von mir ausdrücklich bezeichneten Quellen bedient habe.

Die Dissertation wurde in der jetzigen oder einer ähnlichen Form noch bei keiner anderen Hochschule eingereicht und hat noch keinen sonstigen Prüfungszwecken gedient.

Marburg, den 29.04.2007

Holger Steuber

Curriculum vitae

Full name: Holger Magnus Steuber

Date of birth: April, 4 1977

Place of birth: Hagen, Germany

Nationality: German

2003-2006 PhD student at the Institute for Pharmaceutical Chemistry,
Philipps-University, Marburg, in the research group of Prof. G. Klebe

2003-2006 Fellow of the Research Training Group “Protein function at the
atomic level”

2001-2002 Obligatory practical training student in pharmacy

11/01-04/02 First half (public pharmacy): Bären-Apotheke, Regensburg,
Germany

05/02-10/02 Second half: Research internship with Prof. G. Folkers and Prof.
L. Scapozza, Department of Pharmaceutical Chemistry, Swiss
Federal Institute of Technology (ETH) Zürich, Switzerland

1997-2001 Studies of Pharmacy, University of Regensburg

1996-1997 Military Service, aid-man at the naval base List, Sylt

1987-1996 Albrecht-Dürer-Gymnasium, Hagen
Abitur (majors: Maths, Biology)